UNIVERSIDAD DE CHILE
FACULTAD DE CIENCIAS FÍSICAS Y MATEMÁTICAS
DEPARTAMENTO DE GEOLOGÍA

MINERALOGY AND GEOCHEMISTRY OF APATITE AND MAGNETITE IN IRON OXIDE-APATITE DEPOSITS: IMPLICATIONS FOR ORE GENESIS IN THE ANDEAN IOCG PROVINCE

TESIS PARA OPTAR AL GRADO DE DOCTORA EN CIENCIAS, MENCIÓN GEOLOGÍA

GISELLA FRANCISCA PALMA LIRA

PROFESOR GUÍA:
FERNANDO BARRA PANTOJA

MIEMBRO DE LA COMISIÓN:
MARTIN REICH MORALES
DIEGO MORATA CÉSPEDES
PEDRO CORDEIRO DE OLIVEIRA

Este trabajo ha sido financiado por el Núcleo Milenio Trazadores de Metales y el proyecto FONDECYT-1140780.

SANTIAGO DE CHILE
2020

RESUMEN DE LA TESIS PARA OPTAR AL GRADO DE: Doctora en Ciencias, Mención Geología.
POR: Gisella Palma Lira
FECHA: Enero 2020
PROFESOR GUÍA: Fernando Barra Pantoja
PROFESOR CO-GUÍA: Martin Reich Morales

MINERALOGY AND GEOCHEMISTRY OF APATITE AND MAGNETITE IN IRON OXIDE-APATITE DEPOSITS: IMPLICATIONS FOR ORE GENESIS IN THE ANDEAN IOCG PROVINCE

Los depósitos denominados de tipo magnetita apatito o *iron-oxide apatite* (IOA) son una fuente importante de Fe, P y REE a nivel mundial. En los últimos años, la magnetita ha sido utilizada como un indicador petrogenético de los ambientes geológicos de formación y como un trazador de la fuente de Fe y otros metales. Por su parte, el apatito se utiliza como un monitor de los volátiles (F, Cl, H_2O y S) en los sistemas magmáticos-hidrotermales.

Este estudio se centra en los depósitos Carmen, Fresia y Mariela, correspondientes a cuerpos de vetas y brechas de magnetita masiva, ricos en apatito (~20-40 % modal), con texturas pegmatíticas, y fuertemente controlados por estructuras asociadas al Sistema de Falla de Atamana. Se presentan datos de química-mineral de apatitos y magnetitas, obtenidos mediante microsonda electrónica (EMPA) y ablación láser (LA-ICP-MS), e isótopos de Sr y Nd en apatito, los cuales han sido acoplados con estudios microtexturales para su interpretación.

Posterior a su formación, los apatitos y magnetitas de Carmen y Fresia, habrían sido reequilibrados/reemplazados producto de procesos de disolución-reprecipitación asociados a la infiltración de fluidos tardíos (< 500°C), oxidados y ricos en Cl y S (e.g., salmueras de cuenca). Los apatitos se encuentran zonados con respecto a F y Cl, mostrando un comportamiento desacoplado entre dominios microtexturales y composicionales de fluorapatito y chlorapatito. Asimismo, los núcleos de F-apatito son compatibles con una signatura magmática, mientras que Cl- y Cl-OH-apatito con un origen hidrotermal. Por el contrario, los datos de la brecha Mariela reflejan una fuente con una signatura puramente magmática y primitiva (> 500°C), de la cual se formó magnetita con altas concentraciones de V, Ti y Ga. Dichas magnetitas, provendrían desde una porción más profunda de Mariela y habrían sido emplazadas hacia niveles más someros de la corteza. Esta fuente magmática habría dado origen a fluidos salinos y ricos en Cl, a partir de los cuales habría cristalizado principalmente Cl-apatito (> 3,5 wt.% Cl).

Por otra parte, se presenta una discusión crítica sobre el uso de la geoquímica de elementos traza en magnetita (Al, Ti, V, Cr, Mn, Ni, Cu y Ga) para determinar condiciones de formación, el origen ígneo vs. Hidrotermal, y la evolución de una serie de depósitos IOA de la Franja Ferrífera Chilena de la Cordillera de la Costa y el Laco (Altiplano Chileno). La geoquímica y las microtexturas revelan distintas condiciones de formación, desde un ambiente netamente ígneo a un ambiente transicional magmático-hidrotermal/hidrotermal. El *modelo de flotación* explica plausiblemente dichas características, permitiendo la definición de subtipos IOA. Las diferencias observadas entre los distintos estilos, i.e., con una componente ígnea relevante (tipo "intrusivo", Los Colorados), fuertemente hidrotermal (Cerro Negro Norte), pegmatítico (Carmen, Fresia y Mariela) y somero/subaereo (El Laco), dependen fundamentalmente de la profundidad de formación, la presencia de estructuras y fallas, la composición de la roca hospedante, la fuente de los fluidos hidrotermales y la relación fluido/roca.

En todos los grandes hombres de ciencia
existe el soplo de la fantasía.
GIOVANNI PAPINI

A mis padres

AGRADECIMIENTOS

El presente trabajo se llevó a cabo gracias al apoyo de muchas personas durante mi estadía en el programa de Doctorado. En primer lugar, quisiera agradecer a mi Profesor guía, Fernando Barra, por los años de aprendizajes, por las oportunidades que me dio de aprender y ampliar mis conocimientos en geoquímica, así como por su sincera preocupación y soporte para sacar adelante este trabajo. También quisiera agradecer a mi profesor co-guía Martin Reich, por darme la oportunidad de ser parte de NMTM, por los conocimientos y herramientas entregadas, además de encaminarme a realizar un buen trabajo. A los profesores Adam Simon, Diego Morata y Pedro Cordeiro, por sus aportes, comentarios, correcciones al contenido y presentación de esta investigación.

Un especial agradecimiento a mis padres y mis hermanas. Por todo el apoyo y por siempre confiar en mí, incluso mucho más de lo que yo confío en mi misma. A Ignacio, por apoyarme de manera incondicional y por creer siempre en mí. Gracias por jugártela, por todo el esfuerzo y amor que has puesto para lograr todos nuestros planes. Tan importante fue esta etapa, que hasta nos casamos durante la realización de mi Doctorado. Gracias a Frida y Bennu, por todo su amor, compañía, y por los muchos *homeoffice* que tuvimos.

Agradecer a quienes contribuyeron a la obtención de datos para este trabajo, en especial a Victor Valencia, Jeff Vervoort, Chao Zhang y Diane Wilford, durante mi pasantía por Washington State University (Pullman, EEUU), por su apoyo en los análisis químicos en apatito; a Rurik Romero y Mathieu Leisan del CEGA, Universidad de Chile, por su apoyo con los análisis de LA-ICP-MS en apatito y magnetita; y al Laboratorio LAMARX de la Universidad Nacional de Córdoba (Argentina) por el apoyo en los análisis de EPMA en magnetita.

No quisiera dejar de agradecer a las personas con las que compartí día a día la *vida del estudiante de postgrado*. En primer lugar, a mis grandes amigos desde el pregrado, Eduardo y Rurik, quienes hicieron sin duda mis días de estudiante mucho más entretenidos e inolvidables. Un especial reconocimiento a RR quien compartió conmigo hasta el final del Doctorado. Agradecer también a mis compañeros del NMTM y algunos del CEGA que conocí en este periodo, con quienes tuve el gusto de compartir una buena conversación, un café de grano, un terreno y/o un congreso fuera de Chile. En especial a: Paula y Andrés, en los inicios del NMTM; Tomás, Jorge, Cinthia y Andrea, los doctores y futuros doctores con los que compartí casi toda mi estadía en el NMTM; Nelson, Antonia y Aldo, la mejor época Milenio, los mejores cafés, y las mejores jornadas de reflexión; Fran Aguilera, mi vecina de La Reina, por siempre estar ahí cuando la necesité; y Lorrana y Ricardo, en la recta final del Doctorado, cuando ya no esperaba conocer a nadie nuevo, me llevé una linda sorpresa. Gracias a todos por el apoyo, contención, los buenos momentos y risas. Me llevo grandes amigos.

Reconozco también el soporte de algunos funcionarios del Departamento de Geología, en especial, a Luis Acevedo, por su buena disposición y toda su ayuda en cualquier aspecto computacional, y a Maritza Acuña por su ayuda en la parte más administrativa y burocrática del Doctorado.

Finalmente agradezco el apoyo financiero del proyecto FONDECYT #1140780; el Núcleo Milenio Trazadores de Metales; y de CONICYT por financiar mis estudios mediante la beca de Doctorado Nacional (CONICYT-PFCHA/Doctorado Nacional/2016-2116001).

TABLA DE CONTENIDO

ÍNDICE DE TABLAS

ÍNDICE DE FIGURAS

CAPÍTULO 1

INTRODUCCIÓN

1.1. PRESENTACIÓN

Los depósitos de magnetita-apatito, *iron oxide-apatite* (IOA) o tipo Kiruna representan el miembro extremo, deficiente en cobre, del clan de depósitos tipo óxidos de hierro-cobre-oro o *iron oxide-copper-gold* (IOCG) y son una fuente importante de hierro (Sillitoe, 2003). La mineralización tipo IOA se encuentra dominada por magnetita maciza con baja concentración de titanio, la cual puede ocurrir acompañada de cantidades variables (1-50 % modal) de apatito, actinolita, piroxeno, epidota y sulfuros (Williams et al., 2005). Por otra parte, los depósitos IOCG son explotados por sus concentraciones en cobre, y en ocasiones con sub-productos relevantes tales como oro, uranio, tierras raras, fósforo, cobalto, bismuto y niobio (Hitzman et al., 1992; Sillitoe, 2003; Williams et al., 2005; Groves et al., 2010; Barton, 2014). La mineralización tipo IOCG se caracteriza por sulfuros de cobre y hierro (calcopirita y menor bornita), acompañados de abundantes óxidos de hierro (magnetita y/o hematita especular). La alteración hidrotermal se encuentra representada por asociaciones sódica-cálcica (albita, actinolita, epidota) y potásica (biotita, ortoclasa) con menor clorita, sericita y calcita tardía.

Los depósitos IOCG e IOA se han descrito por todo el mundo y se reportan edades desde el Arcaico (e.g., Provincia de Carajás, Brasil; de Melo et al., 2017); Proterozoico temprano (e.g., distrito Kiruna, Suecia, y distrito Olympic Dam, Australia; Westhues et al., 2017; Apukhtina et al., 2017); Proterozoico medio (e.g., depósitos Pea Ridge y Pilot Knob, USA, y distrito Cloncurry, Australia; Rusk et al., 2010; Day et al., 2016; Childress et al., 2016), Cretácico (e.g., Los Colorados, El Romeral, Candelaria y Mantoverde, Chile; Benavides et al., 2007; Rieger et al., 2010; 2012; Knipping et al., 2015a, b; Rojas et al., 2018a) y Plioceno (e.g., El Laco, Chile; Maksaev et al., 1998; Nyström y Henríquez, 1994; Naranjo et al., 2010).

En Chile, la mayoría de los depósitos IOCG e IOA ocurren de manera espacial y temporalmente asociados, unos con otros, en la Franja Ferrífera Chilena del Jurásico-Cretácico Temprano de la Cordillera de la Costa entre las latitudes 25° S y 31°S (**Figura 1**). Estos depósitos son aledaños a intrusiones del Mesozoico y se encuentran estructuralmente controlados por el Sistema de Falla de Atacama (Sillitoe, 2003; Williams et al., 2005). La Franja Ferrífera Chilena, conocida como la provincia IOCG-IOA más joven del mundo, sin evidencias de metamorfismo ni deformación (Sillitoe, 2003), es una zona ideal para estudiar los procesos involucrados en la formación de estos depósitos y refinar los modelos genéticos actuales. No obstante, el complejo volcánico El Laco, ubicado más al norte (23° 48´S), en el Altiplano Chileno (**Figura 1**), hospeda los depósitos IOA más jóvenes, menos alterados y mejor preservados que se han descubierto hasta la fecha (Naranjo et al., 2010). En un área de alrededor 35 km^2 se describen seis cuerpos de magnetita: Laco Norte, Laco Sur, San Vicente Alto, Rodados Negros, Cristales Grandes y San Vicente Bajo. Estos cuerpos de magnetita presentan notables características volcánicas y subvolcánicas que han instado la controversia con respecto a un origen magmático (modelo de inmiscibilidad) o metasomático para los depósitos IOA (Frutos and Oyarzún, 1975; Nyström and Henriquez 1994; Sillitoe and Burrows, 2002; Naranjo et al., 2010; Tornos et al., 2016; Velasco et al., 2016; Ovalle et al., 2018).

Es un hecho que los depósitos IOCG se forman principalmente por procesos hidrotermales (Sillitoe, 2003; Williams et al., 2005; Mumin et al 2007; Groves et al., 2010; Barton 2014). Sin embargo, el origen de los depósitos IOA continúa siendo un tema controversial e, históricamente, se han propuesto dos hipótesis "clásicas" y contrapuestas. La primera, postula un origen netamente magmático, es decir, la separación de un fundido inmiscible rico en hierro y fósforo de un fundido silicatado, con la consecuente intrusión y cristalización de un cuerpo de hierro en los niveles superiores de la corteza (e.g., Nyström and Henriquez, 1994; Naslund et al., 2002; Chen et al., 2010; Velasco et al., 2016). La segunda hipótesis postula un origen netamente hidrotermal, donde la mineralización de hierro se forma del reemplazo metasomático de la roca de caja por fluidos ricos en hierro de procedencia magmática o no-magmática (e.g., Rhodes and Oreskes, 1995, 1999; Sillitoe and Burrows, 2002; Barton and Johnson 1996, 2004; Pollard, 2006; Dare et al, 2015; Westhues et al., 2016, 2017a, b). Por otra parte, la mayor parte del debate actual sobre el origen de los depósitos IOA se ha centrado en el depósito El Laco. Los investigadores a favor de un origen magmático argumentan que los cuerpos de magnetita conservan sus características netamente ígneas/volcánicas tales como flujos de lava tipo *pahoehoe* y *aa*, flujos de lavas contorsionados, magnetita esferulítica y dendrítica, distintos grados de textura vesicular y estructuras verticales que se interpretan como tubos de escape de gases (Nyström and Henríquez, 1994, 1995; Naslund, et al., 2002). Sin embargo, otros investigadores han interpretado estas texturas como relictos de los flujos de lavas andesíticos que fueron reemplazados por oxidos de hierro de origen hidrotermal, con base en la observación de vetas, cuerpos de brechas y asociaciones minerales de alteración hidrotermal alrededor de los cuerpos de magnetita (Rhodes et al., 1999; Sillitoe and Burrows, 2002).

En los últimos años, y a luz de un gran interés en el estudio de la geoquímica de la magnetita, Knipping et al. (2015a, b) propusieron un nuevo modelo genético para explicar la formación de los depósitos IOA. Con base en una serie de observaciones de terreno, la geoquímica de elementos traza y la composición de los isótopos estables de Fe y O en las magnetitas del depósito Los Colorados, estos autores propusieron que los depósitos IOA se formarían mediante una combinación de procesos ígneos y magmáticos-hidrotermales. En el *modelo de flotación,* los microlitos de magnetita que cristalizan desde un fundido silicatado, gatillan la nucleación de burbujas, con la consiguiente formación de una suspensión de magnetita-fluido, la cual transporta la magnetita hacia profundidades más someras a través de fallas/estructuras pre-existentes, que son reactivadas por extensión de la corteza. Este modelo no solo concilia ambas hipótesis genéticas contrarias (i.e., inmiscibilidad líquida vs. reemplazo metasomático), asimismo, proporciona una explicación plausible a la formación de los depósitos IOCG como parte de un mismo sistema en evolución (Reich et al., 2016; Barra et al., 2017; Simon et al., 2018). Dicha conexión genética, donde los IOA (empobrecidos en sulfuros) representarían las raíces o las porciones más profundas de los sistemas IOCG (enriquecidos en sulfuros), fue propuesta anteriormente para los depósitos IOA e IOCG de la Cordillera de la Costa (Espinoza et al., 1996; Sillitoe, 2003).

La discusión actual sobre la génesis de los depósitos IOA se encuentra arraigada a la geoquímica de la magnetita (Fe_3O_4), entre otros *proxies*, que es el mineral más abundante en los depósitos IOA. Para esto, se han utilizado las técnicas analíticas de microsonda electrónica (EMPA) y ablación láser (LA-ICP-MS) para medir la composición química de los elementos mayores y traza en magnetita, respectivamente. Por una parte, la microsonda electrónica permite analizar un número limitado de elementos (e.g., Mg, Al, Ca, Ti, V, Cr y Mn), por medio de un haz de tamaño de unas pocas micras (< 5µm), con límites de detección de decenas a cientos de ppm (e.g., Dupuis and Beaudoin, 2011). Por otra parte, la ablación láser permite analizar puntos *in-situ*,

entre 20 y 50 µm de diámetro, de una gran cantidad de elementos traza (> 40) a niveles de ppm o sub-ppm. Estos avances analíticos han conducido a un creciente interés por el estudio de la magnetita como un indicador petrogenético y una herramienta de identificación de los ambientes geológicos de formación o *fingerprint* de distintos tipos de depósitos minerales (Dupuis and Beaudoin, 2011; Dare et al., 2012, 2014; Nadoll et al., 2012, 2014; Huang and Beaudoin, 2019; Huang et al., 2019). Asimismo, Knipping et al. (2015a, b) revelaron una zonación química particular en los cristales de magnetita de Los Colorados. En donde los centros de estos cristales, enriquecidos en Ti, Al, Mn y Mg, cristalizarían a partir de un fundido silicatado; mientras que los bordes de grano, muestran un pronunciado empobrecimiento en dichos elementos, consistente con el crecimiento de magnetita a partir de fluidos acuosos ricos en hierro de origen magmático-hidrotermal (Knipping et al., 2015b).

Nuevos estudios geoquímicos y texturales, tanto en magnetitas y otras fases minerales, tales como pirita, actinolita y apatito, se han llevado a cabo posterior al trabajo de Knipping et al. (2015a, b), en una serie depósitos IOCG e IOA Andinos: El Romeral (Rojas et al., 2018a, b), Los Colorados (Bilenker et al., 2016; Reich et al., 2016; Deditius et al., 2018; La Cruz et al., 2019; Knipping et al., 2019a,b), El Laco (Ovalle et al., 2018; La Cruz et al., 2019), Cerro Negro Norte (Salazar et al., 2019). Cabe destacar, que en ninguno de estos trabajos el foco principal ha sido el estudio de la química mineral del apatito, a pesar de que este mineral es clave para entender el rol del fósforo (P), halógenos (F, Cl) y otros volátiles (H_2O, S) en la formación y evolución de los depósitos IOA, así y refinar los modelos genéticos propuestos hasta la fecha.

El apatito [$Ca_{10}(PO_4)_6$(F, Cl, OH)] se considera un monitor del comportamiento de los volátiles de los sistemas magmáticos-hidrotermales, dado a la sustitución de los halógenos (Pan and Fleet, 2002; Schettler et al., 2011), y a la incorporación de otros volátiles, por ejemplo, el S (Peng et al., 1997; Perseil et al., 2000; Kim et al., 2017), en su estructura cristalina. Por consiguiente, la composición de los halógenos en el apatito se utiliza para obtener información sobre la partición de elementos entre apatito, fluidos y fundidos (Webster and Piccoli, 2015). Asimismo, la estructura cristalina del apatito es capaz de incorporar y concentrar una gran cantidad de elementos traza como Sr, U, Th, tierras raras, Y, S, y As, con coeficientes de partición apatito/fundido que superan la unidad para la mayoría de estos elementos (Watson and Green 1981; Sawka, 1988; Prowatke and Klemme, 2006; Konecke et al., 2017; Kim et al., 2017). Por lo que el apatito es susceptible a la variación de las concentraciones de dichos elementos traza al momento de la cristalización en los sistemas magmáticos (Bea et al., 1994; Toplis and Dingwell, 1996; Sha and Chappel, 1999; Belousova, 2000; Belousova et al., 2001). Adicionalmente, las concentraciones de F, Cl y OH, así como la presencia de inclusiones de monacita, xenotima y/o torita en apatito, permiten constreñir los procesos metasomáticos que han afectado a los depósitos IOA. Esto último, ha sido demostrado mediante una serie de estudios en apatitos naturales (e.g., Hansen and Harlov., 2007), experimentales (e.g., Harlov and Förster, 2003; Harlov et al., 2005; Betkowski et al., 2016), y también ha sido reportado en una serie de depósitos IOA de la región de Bafq, Iran (e.g., Daliran et al., 2010), Kiirunavaara; Suecia (e.g., Harlov et al. 2002a) y Gräsgesberg, Suecia (e.g., Jonsson et al., 2010). Finalmente, el apatito se puede utilizar como un indicador petrogenético sobre la base de sus composiciones isotópicas de Sr y Nd (Zaitsev and Bell, 1995; Rakovan et al., 1997). La razón de $^{87}Sr/^{86}Sr$ se aproxima al valor del isótopo de Sr inicial debido a las extremadamente bajas razones de Rb/Sr en la mayoría de los apatitos. En definitiva, la razón de $^{87}Sr/^{86}Sr$ inicial se puede utilizar de manera efectiva para obtener antecedentes de la fuente de los magmas y como trazador de la evolución de los fluidos hidrotermales (e.g., Li and Zhou, 2015; Zhao et al., 2015; Zeng et al., 2016).

Este trabajo de tesis consta de cuatro capítulos principales: el Capítulo 1 que corresponde a una introducción general; los Capítulos 2 y 3, en inglés, consisten en dos artículos científicos titulados "*Halogens, trace element concentrations, and Sr-Nd isotopes in apatite from iron oxide-apatite (IOA) deposits in the Chilean iron belt: Evidence for magmatic and hydrothermal stages of mineralization",* publicado el año 2019 en Geochimica et Cosmochimica Acta*; y "A review of magnetite geochemistry of Chilean Iron Oxide-Apatite (IOA) deposits and its implications for ore-forming processes"* en proceso de revisión en Ore Geology Reviews. En estos capítulos se presentan el marco geológico, las metodologías empleadas, los resultados y las principales discusiones de cada estudio. Finalmente, el Capítulo 4 de esta tesis resume las conclusiones generales del trabajo realizado.

Con base a lo anteriormente mencionado, el artículo científico del Capítulo 2 se centra en el estudio de la química mineral de los apatitos de los depósitos Carmen, Fresia y Mariela de la Franja Ferrífera Chilena de la Cordillera de la Costa. Estos cuerpos de magnetita presentan abundante apatito (~20-40 % modal), de centímetros a metros de largo, y presentan texturas pegmatíticas. Con el fin de determinar el rol de los volátiles (F, Cl, OH) y proporcionar antecedentes sobre la naturaleza de los magmas y fluidos relacionados con los procesos de formación en estos depósitos, en este estudio se integran datos microtexturales, micro-analíticos (EMPA y LA-ICP-MS) y de isotópos de Sr y Nd en apatito.

Los depósitos Carmen y Fresia presentan características mineralógicas, texturales y estructurales similares. Los cuerpos de magnetita se caracterizan por presentar abundantes cristales alargados de apatito y actinolita de hasta ~50 cm de largo, con texturas pegmatítitcas del tipo *comb.* Adicionalmente, evidencian alteración hidrotermal, donde la interacción fluido-roca fue de mayor intensidad en Fresia que en Carmen; además de múltiples eventos de crecimiento de cristales de apatito y actinolita, y brechización. Por el contrario, el depósito Mariela corresponde a una pipa de brecha, compuesta de una matriz de apatito, actinolita y menor magnetita con agregados de apatitos que alcanzan hasta 3 m de largo, y fragmentos de intrusivo de la roca de caja, fuertemente alterado a clorita y menor epidota.

En el artículo científico del Capítulo 3, se presentan nuevos datos microtexturales y micro-analíticos (EMPA y LA-ICP-MS) de las magnetitas de los depósitos IOA El Romeral, Carmen, Fresia y Mariela. Se presenta un resumen y una discusión crítica de los datos de química de las magnetitas de depósitos IOA e IOCG recopilados durante estos últimos años. Los elementos traza en magnetita y una serie de diagramas de discriminación (e.g., Dupuis and Beaudoin, 2011; Nadoll et al., 2014) se utilizan para identificar y caracterizar los distintos tipos texturales de magnetita observadas en cada depósito, y constreñir sobre la formación y evolución de los depósitos IOA Andinos. La composición química de la magnetitas de Cerro Negro Norte, El Romeral y El Laco reflejan sus condiciones de formación y revelan sistemas que evolucionan desde condiciones de alta-temperatura, puramente ígneas/magmáticas en profundidad, a condiciones de baja-temperatura, magmáticas-hidrotermales a hidrotermales, hacia los niveles más someros (Ovalle et al., 2018; Rojas et al., 2018b; Salazar et al., 2019; La Cruz et al., en revisión). Dichos estudios han sido descritos como consistentes con el *modelo de flotación* para explicar el origen de los depósitos IOA Andinos. Adicionalmente, se propone un mecanismo de formación para los depósitos IOA pegmatíticos, Carmen, Fresia y Mariela de la Franja Ferrífera Chilena.

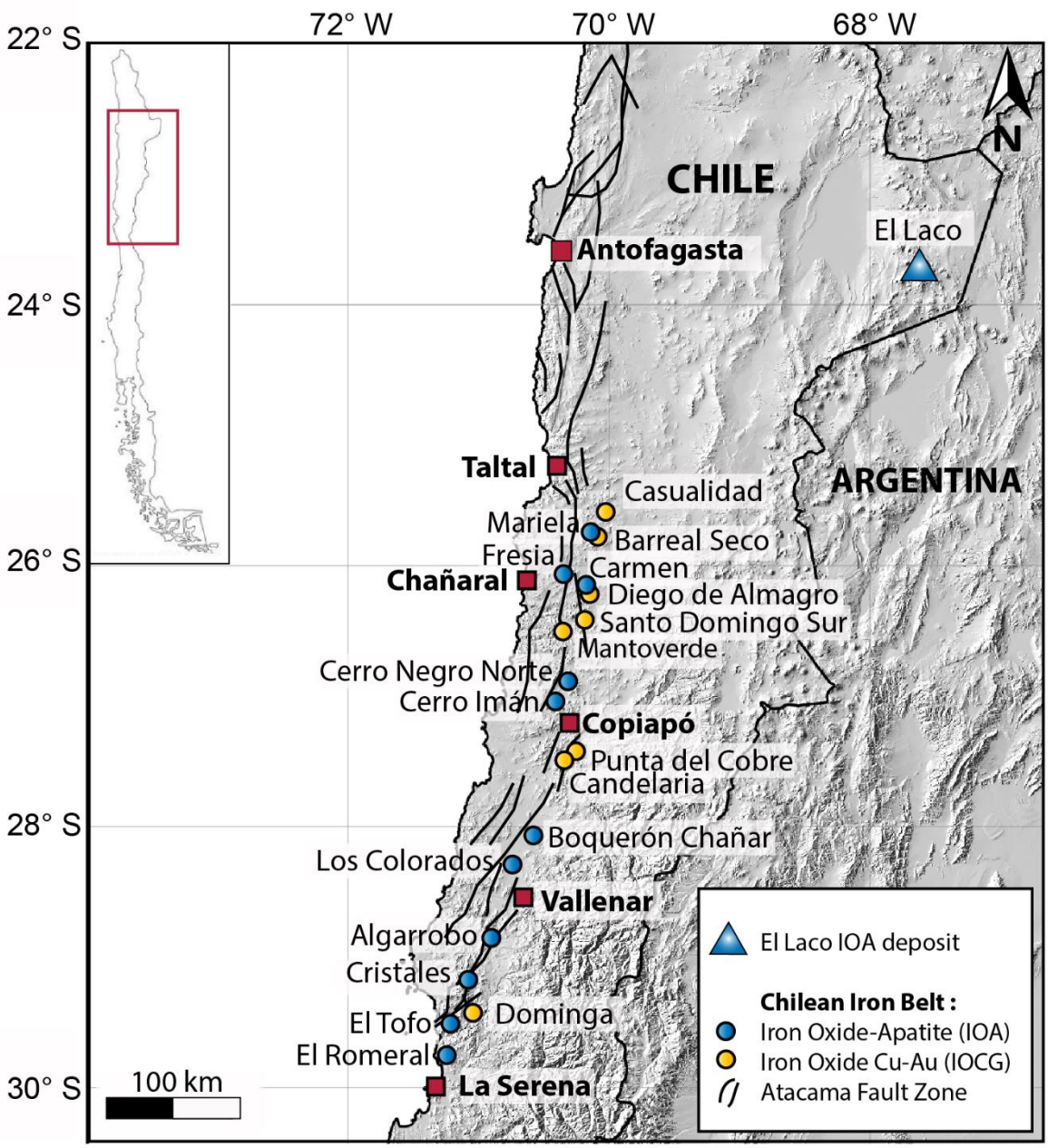

Figura 1. Mapa en donde se presentan los principales depósitos IOCG e IOA en la Provincia IOCG delos Andes Centrales del Jurásico-Cretácico Temprano (25-31°S9 y el depósito IOA El Laco (23° 48´ S) en el Altiplano del norte de Chile. Modificado de Barra et al. (2017).

Este trabajo fue financiado por el proyecto FONDECYT: Metallogenesis of the mesozoic magmatic arc of northern Chile: Testing the IOCG connection using a multyproxy geochemical approach con el Dr. Fernando Barra como investigador principal y profesor guía de este trabajo de tesis, y se enmarca dentro del Núcleo Milenio Trazadores de Metales (NMTM), núcleo financiado por la Iniciativa Científica Milenio (ICM) del Ministerio de Economía, Fomento y Turismo, con el Dr. Martin Reich como director y el Dr. Fernando Barra como director alterno,

1.2. OBJETIVOS

1.2.1. Objetivo general

El objetivo principal de este trabajo es determinar el rol de los volátiles (F, Cl, OH) y aportar con nuevos antecedentes al modelo genético y evolución de los depósitos IOA Andinos, a partir del estudio de la química mineral del apatito y la magnetita.

1.2.2. Objetivos específicos

1- Caracterizar las microtexturas del apatito y de la magnetita de los depósitos IOA pegmatíticos Carmen, Fresia y Mariela.

2- Caracterizar la composición de elementos mayores, menores y traza en los apatitos y las magnetitas de los depósitos Carmen, Fresia y Mariela, incluyendo la posible detección de zonaciones texturales y composicionales en estos minerales.

3- Examinar el vínculo entre las características composiciones y microtexturales en los apatitos y las magnetitas de Carmen, Fresia y Mariela, identificar los procesos geológicos/geoquímicos involucrados en su formación y evolución, y establecer un mecanismo de formación.

4- Caracterizar las concentraciones de elementos traza en las magnetitas de El Romeral, en las porciones más profundas y más someras del depósito.

5- Resumir y comparar las microtexturas y geoquímica de las magnetitas de los depósitos IOA de la Franja Ferrífera Chilena de la Cordillera de la Costa (Los Colorados, El Romeral, Cerro Negro Norte, Carmen, Fresia y Mariela) y el El Laco.

6- Establecer un modelo genético y de evolución que integre las características microtexturales y geoquímicas de las magnetitas y apatitos, y los principales factores que controlan la formación de los depósitos IOA Andinos.

1.3. HIPÓTESIS DE TRABAJO

Los depósitos IOA Andinos tienen un origen complejo, donde la mineralización de hierro se forma en un continuo desde un ambiente netamente magmático a un ambiente transicional magmático-hidrotermal, genéticamente ligados a magmas intermedios-máficos y bajo un fuerte control estructural. Esta transición se refleja en las texturas y la composición química de la magnetita (Fe_3O_4).

El apatito [$Ca_{10}(PO_4)_6$(F, Cl, OH)] es un monitor del comportamiento de los volátiles en sistemas magmáticos-hidrotermales. Las concentraciones de los halógenos (F y Cl) en el apatito son susceptibles a los cambios de composición de un magma o un fluido acuoso. Las variaciones texturales y composicionales del apatito reflejan un origen magmático para zonas de fluorapatito y un origen hidrotermal para zonas de cloroapatito.

Las texturas y química mineral de la magnetita y el apatito en los depósitos IOA Andinos son un reflejo de los factores que controlan la formación y evolución de estos depósitos.

CAPÍTULO 2

Halogens, trace element concentrations, and Sr-Nd isotopes in apatite from Iron Oxide-Apatite (IOA) deposits in the Chilean iron belt: Evidence for magmatic and hydrothermal stages of mineralization

Gisella Palma[1*], Fernando Barra[1, 2], Martin Reich[1, 2], Victor Valencia[3], Adam C. Simon[4]
Jeff Vervoort[3], Mathieu Leisen[2], Rurik Romero[2]

[1]Department of Geology, FCFM, Universidad de Chile, Santiago, Plaza Ercilla 803, Chile
[2]Andean Geothermal Center of Excellence (CEGA), FCFM, Universidad de Chile, Santiago, Plaza Ercilla 803, Chile
[3]School of Earth and Environmental Sciences, Washington State University, Pullman, Washington 99164, USA
[4]Department of Earth Sciences, University of Michigan, 1100 North University Ave, Ann Arbor, Michigan, USA

Published in:
Geochimica et Cosmochimica Acta

Corresponding author: Gisella Palma
gipalma@ing.uchile.cl

ABSTRACT

The ratio of the halogens F and Cl in apatite is highly sensitive to changes in the composition of an evolving silicate melt or aqueous fluid. For this reason apatite chemistry is widely used as a monitor of halogen behavior in magmatic-hydrothermal systems. Apatite is an ubiquitous mineral in iron oxide - apatite (IOA) mineral deposits, where P and volatiles such as F, Cl, H_2O and S play a major role in ore genesis. In this study, we present a combination of textural, micro-analytical and isotopic data for apatite from three Andean IOA deposits (Carmen, Fresia and Mariela) of Early Cretaceous age from the Coastal Cordillera of northern Chile.

Apatite textures and compositions show evidence of post-crystallization alteration. Apatite is predominantly zoned with respect to Cl and F, showing a decoupled geochemical behavior between these two elements. Overall, four types of apatite or domains were identified in the analyzed grains based on the $X_{Cl\text{-}apatite}/X_{F\text{-}apatite}$ and $X_{Cl\text{-}apatite}/X_{OH\text{-}apatite}$ ratios determined using the atomic proportions of F, Cl and OH. F-apatite is characterized by a $X_{Cl\text{-}apatite}/X_{F\text{-}apatite}$ <0.1 and a $X_{Cl\text{-}apatite}/X_{OH\text{-}apatite}$ = 0.03-2; Cl-apatite displays a $X_{Cl\text{-}apatite}/X_{F\text{-}apatite}$ >25 and a $X_{Cl\text{-}apatite}/X_{OH\text{-}apatite}$ >4.5 and up to 3000; Cl-OH-F-apatite has a $X_{Cl\text{-}apatite}/X_{F\text{-}apatite}$ = 0.15-8 and a $X_{Cl\text{-}apatite}/X_{OH\text{-}apatite}$ = 0.25-5.45; and Cl-OH-apatite shows a $X_{Cl\text{-}apatite}/X_{F\text{-}apatite}$ = 8-75 and a $X_{Cl\text{-}apatite}/X_{OH\text{-}apatite}$ = 0.5-3.

Carmen apatite is mostly F-apatite, but shows Cl-OH compositions restricted to rims and fractures, whereas apatite from Mariela is dominantly Cl-apatite and Cl-OH-apatite. Apatite from Fresia have variable compositions between Cl-OH-F, Cl-OH- and Cl-apatite, where Cl- and Cl-OH-apatites are characterized by an enrichment of S, Na, Sr and Fe relative to F-apatite. Most notably, S and Na correlate with Cl. In Carmen and Fresia, Cl-OH-apatite is slightly depleted in LREEs, Th and U, a finding consistent with micro-textural evidence of metasomatic processes including coupled dissolution-reprecipitation and formation of secondary monazite and xenotime inclusions. In contrast, apatite from Mariela exhibits no depletion in LREEs and displays a homogeneous distribution of Th and U between the different apatite types, with no monazite and xenotime inclusions. The textural types of apatite identified in this study, coupled with the halogen and trace element composition of apatite, are consistent with modification of primary, F-apatite by interaction with hydrothermal fluids, which led to the formation of Cl-OH-apatite and Cl-apatite. In addition, the initial $^{87}Sr/^{86}Sr$ ratios and ε_{Nd} values of apatite (0.7038 to 0.7050 and -0.3 to +6.5, respectively), calculated considering a 130 Ma age, are consistent with a magmatic origin for the primary F-apatite with minimal or no crustal contribution. Thus, textural, geochemical, and isotopic results of apatite support a magmatic-hydrothermal origin for these Andean IOA deposits with variable degrees of metasomatic overprint as evidenced by the formation of Cl-OH and Cl-apatite.

Keywords: Apatite, halogens, trace elements, Sr-Nd isotopes, iron oxide-apatite deposits, Chile

2.1. INTRODUCTION

Apatite [$Ca_{10}(PO_4)_6(F, Cl, OH)$] is a common accessory mineral in igneous rocks, with usually less than 1% modal abundance (Patiño Douce and Roden, 2006; Piccoli and Candela, 2002; Spear and Pyle, 2002), but can constitute a major phase in iron oxide-apatite (IOA) or "Kiruna-type" deposits. These mineral deposits comprise massive magnetite ore bodies with variable amounts (1-50% modal) of apatite, actinolite and/or pyroxene, and are considered as the copper-poor end-member of the iron oxide-copper-gold (IOCG) clan (Sillitoe, 2003; Williams et al., 2005; Barton, 2014). Iron oxide-apatite deposits have been described in Kiruna and Grängesberg, Sweden (Harlov et al., 2002a; Jonsson et al., 2010, 2016); Mineville and Pea Ridge, USA (Sidder et al., 1993; Lupulescu and Pyle, 2008; Childress et al., 2016; Harlov et al., 2016); in the Bafq region, Iran (Daliran et al., 2010; Taghipour et al., 2015), and in northern Chile (Treloar and Colley, 1996; Broman et al., 1999; Gelcich et al., 2005; Knipping et al., 2015a, b; Barra et al., 2017; Rojas et al., 2018a, b). The ages of these deposits range from Proterozoic (e.g. Kiruna district, Sweden; Westhues et al., 2017) to Pleistocene (El Laco, Chile; Maksaev et al., 1988, Naranjo et al., 2010).

The origin of IOA deposits continues to be a controversial topic and several models have been presented. Some researchers have proposed a magmatic liquid immiscibility model, where an oxidized Fe-P-rich melt and a conjugate Si-rich melt are formed with the subsequent intrusion and crystallization of the Fe-P-rich melt at upper crustal levels (e.g., Nyström and Henríquez, 1994; Naslund et al., 2002; Chen et al., 2010; Velasco et al., 2016; Hou et al., 2018). Other researchers have suggested a hydrothermal model for IOA deposits, in which Fe-rich fluids of magmatic origin replace the volcanic host rocks (e.g., Rhodes and Oreskes, 1995; Barton and Johnson, 1996, 2004; Rhodes et al., 1999; Sillitoe and Burrows, 2002; Dare et al., 2015). A more recent genetic model

reconciles these two opposed views and proposes that IOA deposits formed by a combination of magmatic and hydrothermal processes (Knipping et al., 2015a, b; Simon et al., 2018). In this new model, i.e., the flotation model, microlites of magmatic magnetite crystallize from a silicate melt and later ascend by coupling with bubbles of fluids exsolved from the magma. As these magmatic magnetite suspensions ascend, they coalesce and the modal abundance of magnetite increases by further precipitation of hydrothermal magnetite as rims over primary magnetite and filling interstitial space at the level of neutral buoyancy, reflecting a continuous process from magmatic to hydrothermal conditions.

Although these models attempt to explain the origin of the iron ore, the role of phosphorus and of halogens including F and Cl in the formation of IOA deposits is still poorly understood. This information is critical for the development and refinement of genetic models so far proposed. In this respect, apatite plays a fundamental role because it is the major P-bearing phase and its structure has an affinity to incorporate and concentrate trace elements such as Sr, U, Th, REEs, Y, S, and As, with apatite/melt partition coefficients typically above 1 for many of these elements (Watson and Green 1981; Sawka, 1988; Prowatke and Klemme, 2006; Konecke et al., 2017; Kim et al., 2017). Apatite is a phase that is sensitive to geochemical changes in magmatic systems, and is considered a trace element recorder of magmatic processes at the time of crystallization (Bea et al., 1994; Toplis and Dingwell, 1996; Sha and Chappel, 1999; Belousova, 2000; Belousova et al., 2001). In addition, apatite acts as a monitor of volatiles in magmatic-hydrothermal processes because of the substitution of F, Cl and OH in the halogen site of its structure (Pan and Fleet, 2002; Schettler et al., 2011), and the incorporation of other volatile elements such as sulfur (Peng et al., 1997; Perseil et al., 2000; Kim et al., 2017). Hence, the halogen composition of apatite can provide important information on elemental partitioning among apatite, fluids and melts (Webster and Piccoli, 2015). Moreover, studies of natural occurrences (e.g., Hansen and Harlov., 2007) and experimental studies (e.g., Harlov and Förster, 2003; Harlov et al., 2005; Betkowski et al., 2016) show that the F, Cl and OH concentration and the presence of monazite, xenotime and/or thorite inclusions in apatite can be used to constrain metasomatic processes that have affected IOA deposits, as has been reported for IOAs in the Bafq region, Iran (e.g., Daliran et al., 2010), Kiirunavaara, Sweden (e.g., Harlov et al. 2002a) and Gräsgesberg, Sweden (e.g., Jonsson et al., 2010).

Furthermore, apatite can be used as a petrogenetic indicator by means of its Sr and Nd isotope compositions (Zaitsev and Bell, 1995; Rakovan et al., 1997). The measured $^{87}Sr/^{86}Sr$ ratio in apatite can approximate the initial Sr isotope value because of the extremely low Rb/Sr ratio in most apatite grains. Hence, the $^{87}Sr/^{86}Sr$ ratio can effectively be used to obtain information regarding the source of the magmas, and as a tracer of the evolving hydrothermal fluids (e.g., Li and Zhou, 2015; Zhao et al., 2015; Zeng et al., 2016).

In this contribution, we present results from electron probe microanalyzer (EPMA), laser ablation inductively coupled mass spectroscopy (LA-ICP-MS), and Sr and Nd isotopes (MC-ICP-MS and TIMS) of apatite from the Carmen, Fresia and Mariela IOA deposits located in the Cretaceous Iron Belt, northern Chile. We relate textures with major (Ca, PO_4^{3-}, F, Cl, OH) and trace elements (S, Na, Mg, Fe, V, Ni, Cu, Zn, As, Rb, Sr, Y, Zr, Ba, REEs, Hf, Pb, Th and U). Our aim is to constrain the geochemical processes involved in the formation and subsequent alteration of apatite, in order to determine the role of volatiles (F, Cl, OH) in the formation of IOA deposits and thus, provide insights on the nature of the magma and fluids related to the mineralization processes. The Carmen, Fresia and Mariela IOA deposits represent the apical sections of IOA systems, and are characterized by pegmatitic and breccia-like textures with abundant magnetite-

actinolite and ~30-50% modal apatite, reflecting high volatile/melt conditions during their formation. Therefore, these relatively young, undeformed deposits and their large cm-sized apatite crystals provide a unique opportunity for the study of the source and mechanism of concentration of phosphorus and volatiles in IOA deposits.

2.1.1. IOA deposits of northern Chile

Chilean iron ore deposits include iron-oxide apatite deposits (IOA), also known as Kiruna-type deposits, such as El Romeral, El Algarrobo, Cerro Negro Norte and Los Colorados; and iron-oxide copper gold deposits (IOCG) like Mantoverde and Candelaria (e.g., Nyström and Henríquez, 1994; Sillitoe, 2003; Barra et al., 2017) (**Figure 2**). Most of the IOA deposits occur within the Chilean Iron Belt (CIB) in the Coastal Cordillera of northern Chile (Ruiz et al., 1965; Park, 1972; Espinoza, 1984a, 1990; Oyarzún and Frutos, 1984; Ménard, 1986; Ruiz and Peebles, 1988). The CIB is a N-S-trending belt approximately 600 km long and 25 km wide which extends between 25° and 31°S. It consists of seven large (>100 million tons of high-grade ore) and about 50 small- and medium-sized IOA deposits (Nyström and Henríquez, 1994). The ore deposits have a general N-S orientation, related to the main trace of the Atacama Fault System, or an ENE-WSW orientation related to a set of transfer faults, which correlate with lineaments formed during the arc-backarc development, or at the intersection of these two fault sets, where transtensional displacements created dilatational zones that focused the flow of the mineralizing fluids (Bonson et al., 1996).

In this study we focus on three IOA deposits (Carmen, Fresia and Mariela) located at ~26º S in the northern section of the Chilean Iron Belt (**Figure 2**), and which are characterized by having abundant apatite (20-40% modal; **Figure A1**). A brief description of the geology of each deposit is presented in **Annex A**.

2.2. ANALYTICAL METHODS

Nine representative apatite-bearing samples from Carmen (samples Ca-1 to Ca-6, Ca-8, Ca-10 and Ca-T), 15 from Fresia (samples Fre-1 to Fre-10, Fre-18, Fre-19, Fre-20, Fre-T-I and Fre-T-II), and 9 from Mariela (samples Ma-1 to Ma-6, Ma-0, Ma-11 and Ma-T) were selected for this study. Because these deposits are abandoned mines, samples were collected from stockpiles (Carmen and Fresia) and underground tunnels (Mariela), so the exact location within the ore deposit is unknown.

2.2.1. Scanning electron microscope (SEM)

Electron microscopy analyses were performed using a FEI Quanta 250 SEM equipped with secondary electron (SE), backscattered electron (BSE), cathodoluminescence (CL), and energy-dispersive X-ray spectrometry (EDS) detectors, at the Andean Geothermal Center of Excellence (CEGA) in the Department of Geology, Universidad de Chile. Carbon coated polished sections were prepared to characterize the different micro-textures, to evaluate chemical zonation (F, Cl) and to determine the composition of mineral inclusions in apatite using the EDS detector. BSE

images were obtained by using a filament current of 80 μA, accelerating voltage of 15 kV, a beam intensity of 1 nA, a spot size of 1-3 μm, and a working distance of 10 mm.

2.2.2. Electron probe microanalysis (EPMA)

Major and minor element concentrations in apatite from Carmen (samples Ca-1 to Ca-6, Ca-T), Fresia (samples Fre-1 to Fre-6, Fre-T-I, Fre-T-II), and Mariela (samples Ma-1 to Ma-6, and Ma-T) were quantified by using electron microprobe techniques at Washington State University (WSU) and at the University of Arizona (UA), using a JEOL JXA-8500F field emission electron microprobe and a CAMECA SX100 electron microprobe, respectively. Quantitative spot analyses along core to rim traverses (WSU and UA) and wavelength dispersive X-ray maps (UA) were obtained for apatite from Carmen, Fresia and Mariela.

Operating conditions at Washington State University were 15 kV, a beam current of 20 nA, and a beam size of 8 μm, considering a counting time of 15 s for P and Ca; 20 s for Na; 30 s for Si and As; 40 s for Mg and Cl; 50 s for La, Ce, Fe, Mn and Sr; 80 s for F; and 100 s for Y and S. Diopside (Si), YAG synthetic garnet (Y), $LaPO_4$ (La), pyrite (Fe), spessartine (Mn), MgF_2 (Mg), wollastonite (Ca), $SrTiO_3$ (Sr), albite (Na), Durango fluorapatite (P), anhydrite (S), $RbTiOAsO_4$ (As), KCL (Cl), and MgF_2 (F) were used as standards for EMPA analyses at WSU.

Single-spot microanalyses were performed at the University of Arizona under the following analytical conditions: (i) an accelerating voltage of 15 kV, a beam current of 20 nA, a beam size of 8μm considering a peak time of 10 s for F, Cl, P, Ca, Mn, Fe, S, Na; and (ii) 15 kV, a beam current of 40 nA, and a beam size of 8 μm; considering a peak time of 20 s for Y, La and Ce. In addition to quantitative spot analysis, qualitative WDS X-ray maps of F, Cl, P, Ca, Na, S and Ce were obtained by using an accelerating voltage of 15 kV, a beam current of 50 nA and a counting time of 80 s/element. Synthetic apatite (F, P, Ca), scapolite (Cl), rhodochrosite (Mn), fayalite (Fe), barite (S), albite (Na), YAG synthetic garnet (Y) REE3 (La, Ce) were used as standards.

2.2.3. LA-ICP-MS trace element analysis

Trace elements in apatite from samples Ca-T, Fre-T-I, Fre-T-II and Ma-T were analyzed by using a Photon Machines Analyte G2 ArF excimer nanosecond laser (193 nm) coupled to a Thermo Fisher Scientific ICAP-Q quadrupole ICP-MS at the Andean Geothermal Center of Excellence (CEGA) in the Department of Geology, Universidad de Chile. Apatite thick sections (200 μm) were first examined by using the SEM, followed by analysis using EPMA. Each spot analysis involved 60 s ablation time and 20 s background measurement using a laser repetition rate of 10 Hz, measured fluence of 7.8 J/cm² and a 30 μm laser spot diameter. The dwell time was 0.01 s for all trace elements (Mg, V, Mn, Fe, Ni, Cu, Zn, As, Rb, Sr, Y, Zr, Ba, REEs, Hf, Pb, Th and U).

The concentration of Ca, determined by EPMA, was used as the internal standard for calibration. The NIST-610 glass reference material was used as the external calibration standard. Durango fluorapatite (Chew et al., 2016) was used as an unknown to constrain potential matrix effects and to determine analytical accuracy and precision. Twenty analyses were carried out on the Durango fluorapatite (**Table A0**) and the trace element concentrations obtained are within the concentration ranges reported by Chew et al. (2016). The analytical precision determined using the Durango fluorapatite is within 2 to 5%. LA-ICP-MS analyses were carried out by using the bracketing method with measurement of the NIST-610 glass (n=2), Durango fluorapatite (n=2), and then 15 to 20 unknowns, followed by measurements of NIST 610 (n=2) and Durango (n=2). Data reduction was performed by using the Iolite software (Paton et al., 2011), in which heterogeneities in signal profiles were discarded due to the possible presence of mineral inclusions.

2.2.4. Nd and Sr isotopes

The Nd and Sr isotopic composition for 4 apatite samples from each deposit was determined at the Radiogenic Isotopic and Geochronology Laboratory at Washington State University, Pullman, USA. Representative apatite crystals were selected and pulverized with a Dremel drill to obtain apatite powders. Approximately 0.02 g of sample was weighed into 15 ml Savillex beakers and 2 ml of 6 M HCl was added for apatite digestion. The beakers were then heated on a hotplate at 100 °C for 12 hours. After dissolution, samples were transferred to microcentrifuge tubes (1.5 ml) and centrifuged at 3500 rpm for 15 minutes to separate dissolved apatite from its insoluble silicate inclusions. The clear solution was transferred to clean beakers and a mixed ^{150}Nd-^{149}Sm spike was added to accurately determine the ^{147}Sm/^{144}Nd ratios. REE (including Sm and Nd) and Sr were initially separated on single cation exchange columns loaded with AG 50W-X8 resin (200-400 mesh). Strontium was eluted in 2.5 M HCl followed by the elution of Sm-Nd in 6 M HCl (Patchett and Tatsumoto, 1981). A second column loaded with 1.7 ml of LN Spec resin was used for the separation of Sm and Nd. Neodymium was eluted in 0.14 M HCl followed by the elution of Sm in 0.4 M HCl (Gaschnig et al., 2011). The Sr eluted from cation exchange columns was subsequently purified twice by using 0.2 ml Sr-spec resin and eluted in 0.5M HNO_3 (Gaschnig et al., 2011). Aliquots of Nd were redissolved in 2% HNO_3 for isotopic measurements using a Thermo-Finnigan Neptune multiple collector ICP-MS at Washington State University. Neodymium analyses were corrected for mass fractionation using ^{146}Nd/^{144}Nd=0.7219 and normalized by using JNdi Nd reference material (^{143}Nd/^{144}Nd=0.512115; Tanaka et al., 2000).

Strontium aliquots were loaded on Re filaments as nitrate with a Ta_2O_5 activator. Strontium isotope ratios were measured on an Isotopx Phoenix using thermal ionization mass spectrometer (TIMS) at Washington State University. The ^{87}Sr/^{86}Sr and ^{84}Sr/^{86}Sr ratios were corrected for mass fractionation by using an exponential law and a value for the ^{86}Sr/^{88}Sr ratio of 0.1194.

2.3. RESULTS

2.3.1. Apatite textures

Apatite from the Carmen (**Figure 3**), Fresia (**Figure 4**) and Mariela (**Figure 5**) IOA deposits has different textures and numerous mineral inclusions and pores. Chemical zoning related to the variation of F and Cl is observed in BSE images. In general, light areas in the BSE images correspond to Cl-rich apatite, whereas dark domains are F-rich apatite. In Carmen, the transition between the two types of apatite is sharp (**Figures 3a-d**). Dark zones (i.e., F-rich apatite) are mostly observed in apatite cores while light areas (i.e., Cl-rich apatite) occur in grain rims (**Figure 3b**), and in fractures, veinlets and/or sealed fractures (**Figure 2d**). Locally, apatite shows an inverse zonation, with light cores and dark rims (**Figure 2c**). In Fresia, apatite exhibits a concentric zonation with dark cores and rims, and light intermediate zones (**Figure 4a**). Some grains display a rim composed of fine-grained Cl-rich apatite (**Figure 4b**), whereas others are replaced by Cl-rich acicular (**Figure 4c**) or elongated (**Figure 4d**) apatite crystals. Mineral inclusions such as monazite (**Figures 3a, b, d; 4a, b**), magnetite, quartz, actinolite and minor xenotime (**Figure 3c**) are found in Carmen and Fresia. Carmen apatite contains numerous monazite inclusions up to hundreds of microns in size, whereas mineral inclusions in apatite from Fresia are considerably less abundant and smaller (<15 μm). Monazite is mainly observed along grain boundaries in Cl-rich apatite, apatite overgrowths, or near the interface between Cl-rich and F-rich apatite.

Apatite from Mariela is porous and zoned with respect to halogens (F and Cl). Most apatite displays an irregular, patchy zonation dominated by Cl-rich domains (**Figures 5a, b**). Some grains show different pore sizes within halogen domains, where larger pores are present in Cl-rich and smaller ones in Cl±F domains (**Figure 5b**). Locally, some euhedral apatite crystals show a sharp boundary between F-rich porous cores and Cl-rich pore-free rims (**Figures 5c, d**). In some cases, a thin layer of F-rich apatite forms over these euhedral apatite crystals. In addition, Cl-rich apatite with acicular, radial habits can crystallize over this thin F-rich layer (**Figures 5c, d**). In contrast to Carmen and Fresia, no monazite inclusions were observed in apatite from Mariela, although inclusions of magnetite, actinolite, titanite and a Cu-Cl mineral, possibly atacamite, are present. Atacamite is also identified filling fine fractures in apatite (**Figure 5b**).

2.3.2. WDS X-ray elemental maps

The elemental distribution of P, Ca, F, Cl, S, Na, and Ce within apatite from Carmen, Fresia and Mariela was determined by collecting X-ray maps and evaluating the distribution of elements. These maps were used to identify chemical zonation and to determine the correspondence of these elements with specific domains (F and Cl).

Apatite from Carmen shows a strong zonation between Cl-rich and F-rich apatite, with F-rich compositions predominating over Cl-rich ones (**Figure 6**). Fluorine and Cl are geochemically decoupled, with Cl-rich domains slightly depleted in P and Ca relative to F-rich domains (**Figure 6a**) and restricted to crystals rims (**Figures 6a, b**) and/or microfractures in F-rich grains (**Figures**

6a, c). Moreover, the X-ray maps reveal a coupled behavior between S, Na and Cl (**Figure 6b**). The Ce map shows numerous monazite inclusions, which are spatially related to the Cl-rich domains (**Figure 6c**).

The X-ray maps of apatite from Fresia (**Figure 7**) and Mariela (**Figure 8**) show an increasing Cl concentration towards grain rims (**Figures 7a, 8a**). In some cases an increase in Cl is observed in the core of heavily fractured grains from Fresia and Mariela (**Figures. 7b, 8b**). As in apatite from Carmen, F and Cl are geochemically decoupled, but the F concentration in apatite from Fresia and Mariela is lower than in Carmen. Chlorine-rich domains are also depleted in P and Ca (**Figs. 6a, 7b**). In Carmen high S and Na concentrations are associated with Cl-rich domains, whereas in Fresia and Mariela high S and Na are not always related to high Cl-rich apatite (**Figure 7b**).

A summary of the observed textures and general characteristics of each domain is presented in **Table A1**.

2.3.3. EPMA analysis

Major and minor elements including Ca, P, F, Cl, S, Na, Fe, Sr, Mn, Si, Y, La, Ce were measured in apatite from Carmen, Fresia, and Mariela by EPMA. Spot analyses and core to rim EPMA traverses in apatite from Carmen, Fresia, and Mariela were performed to characterize chemical zonation of F, Cl, OH, Ca, P, S, Na, Fe, and Sr in each apatite type or domain.

Major and minor elements

Apatite from Carmen, Fresia and Mariela contains variable concentrations of F and Cl. The OH concentration in apatite is calculated based on the measured concentration of F and Cl, and assuming that the halogen site is fully occupied ($X_{F\text{-}ap} + X_{Cl\text{-}ap} + X_{OH\text{-}ap} = 1$; Piccoli and Candela, 2002; **Table A2**). Carbonate (CO_3^{2-}), which could also enter the anion column of the apatite structure, is mainly restricted to narrow and late-stage calcite veins in the studied IOA deposits. Therefore, the carbonate-apatite end-member is not considered here as an apatite component.

Based on the atomic proportions of F, Cl and OH, four types of apatite or domains were identified: F-apatite, Cl-apatite, Cl-OH- and Cl-OH-F-apatite. F-apatite is characterized by a $X_{Cl\text{-}apatite}/X_{F\text{-}apatite} < 0.1$ and a $X_{Cl\text{-}apatite}/X_{OH\text{-}apatite} = 0.03\text{-}2$; Cl-apatite displays a $X_{Cl\text{-}apatite}/X_{F\text{-}apatite} > 25$ and a $X_{Cl\text{-}apatite}/X_{OH\text{-}apatite} > 4.5$ and up to 3000; Cl-OH-F apatite has a $X_{Cl\text{-}apatite}/X_{F\text{-}apatite} = 0.15\text{-}8$ and a $X_{Cl\text{-}apatite}/X_{OH\text{-}apatite} = 0.25\text{-}5.45$; and Cl-OH apatite shows a $X_{Cl\text{-}apatite}/X_{F\text{-}apatite} = 8\text{-}75$ and a $X_{Cl\text{-}apatite}/X_{OH\text{-}apatite} = 0.5\text{-}3$ (**Figure 9; Tables A3, A4**). **Table 1** shows a summary of the entire dataset of all EPMA analyses (Ca, P, F, Cl, S, Na, Fe, Sr, Mn, Si, Y, La, Ce) for each apatite type or domain, and all data are reported in **Table A4**.

Apatite from Carmen is mainly F-apatite and Cl-OH-apatite, with a small group of points showing a Cl-OH-F composition. Mariela apatite is dominated by Cl-apatite with minor Cl-OH- and Cl-OH-F-apatite. Apatite from Fresia exhibits a wide compositional range with fluorapatite-chlorapatite-hydroxyapatite present in solid solution (**Figure 9a**). The F-Cl plot in **Figure 9b** shows a negative correspondence between F and Cl (e.g., F-poor apatite has a higher Cl concentration and vice versa) as shown by the F and Cl WDS maps (**Figures 6-8**).

Major apatite components, i.e., CaO and P_2O_5, display a broadly positive correspondence with the highest concentrations of CaO and P_2O_5 found in F-apatite from the Carmen, whereas lower concentrations are seen in Cl-OH- and Cl-apatite from Fresia and Mariela (**Table 1**; **Figure A2**).

EPMA traverses and zonations

EPMA traverses were performed across representative zoned apatite from Carmen (sample Ca-T), Fresia (sample Fre-T-I) and Mariela (sample Ma-T); and from an unzoned apatite from Fresia (Fre-T-II) (**Table A3**). Each transect comprised 8 to 9 core-to-rim points across individual grains (Carmen and Fresia) or distinct compositional domains (Mariela). Major (P, Ca, F, Cl) and trace (S, Na, Fe, Sr, Mn, Si, Ce, La and Y) elements were measured.

For the Carmen deposit, a grain with a strong zonation and a sharp interface between F-apatite and Cl-OH-apatite is shown in **Figure 10**. Carmen apatite has the highest average F concentration of all apatites studied (**Figure 10c; Tables 1 and A4**). The apatite cores have F concentrations ≥2.9 wt% corresponding to F-apatite (2.9 wt% F represents 75% of the F-apatite end-member). The Cl/F ratio increases from core to rim from ca. 0.02 to ~132. The abrupt change of halogen composition from core to rim is consistent with the sharp contact between dark and light domains observed in the BSE images (**Figure 2**).

Because apatite from Fresia shows the strongest variability in halogen composition, two grains (Apatite type I and II) with different textures were chosen for EPMA traverse analysis in order to relate the apatite composition with their textures (**Figure 11**). Apatite type I has a Cl-OH-F composition and shows a fine-grained, porous rim of Cl-OH-apatite; Apatite type II corresponds to an unzoned apatite interpreted to be completely replaced by fine-grained Cl-OH-apatite (**Figure 11**). Apatite type I and II from Fresia have similar Cl concentrations and have a lower F concentration than Carmen apatites (**Table A3**). Apatite type I is dominated by a Cl-OH-F composition with sparse Cl-apatite found as irregular patches, sometimes related to fractures, and Cl-OH-apatite observed as a highly porous rim of fine-grained apatite. Apatite type II (**Figure 11c**) is compositionally homogeneous with a Cl-OH composition. Notably, Cl-OH apatite in both Apatite type I and II have similar F, Cl and also SO_3, Na_2O, SrO and FeO concentration (**Figures 11c, d**).

The analyzed sample from Mariela is a fractured Cl-apatite grain with a patchy halogen zonation (**Figure 12**). The Cl-OH-apatite has a higher $X_{OH\text{-}apatite}$ than $X_{Cl\text{-}apatite}$ (**Figure 12b**) and also a lower Cl concentration than the Cl-OH-F-apatite (**Table 1**).

Of the three deposits under study, apatite from the Carmen deposit shows the largest range of SO_3, Na_2O, and FeO concentrations between F-apatite and Cl-apatite (**Table A4; Figure 10d**). The Cl- and Cl-OH apatite from Fresia Apatite type is more enriched in SO_3, Na_2O, FeO and SrO in comparison with Cl-OH-F-apatite. Similar SO_3, Na_2O, FeO and SrO concentrations were determined in Fresia Apatite type II (**Figure 11d**). In Mariela, similar concentrations of SO_3, Na_2O, FeO and SrO are observed in Cl-OH-F- and Cl-OH-apatite (**Figure 12d**).

2.3.4. LA-ICP-MS analysis

The abundances of trace elements, including REE, were carried out by LA-ICP-MS in the four apatite types previously defined by the EPMA traverses for each deposit. A total of 226 points were measured for 31 elements (Mg, V, Fe, Mn, Ni, Cu, Zn, As, Rb, Sr, Y, Zr, Ba, REEs, Hf, Pb, Th, and U). A statistical summary is presented in **Table 3**, whereas all data are provided in **Table A5**.

Trace elements

Box plot diagrams show that the trace element concentrations are very similar and overlap among different apatite types (**Figure 13**); however, it is possible to distinguish some trends when comparing the average, median and maximum values (**Table 2; Figure 13**). Cl-OH-apatite from Carmen is slightly enriched in Mg, V, Cu, As, Ba and Pb, but depleted in Th and U, compared to F-apatite. Trace element trends observed in apatite from Carmen are very similar to those from Fresia. The Cl-apatite from Fresia is enriched in Mg, Mn and Ba compared to the Cl-OH- and Cl-OH-F-apatite. Manganese and Ba are also slightly enriched in Cl-OH-apatite relative to Cl-OH-F-apatite. On the other hand, Cl-OH-apatite from Fresia displays the highest average and reaches the highest concentration for V, Cu, As and Pb, but are depleted in Th and U compared to Cl-OH-F- and Cl-apatite. Cl-apatite from Mariela has higher concentrations of Mg, Mn, Ba, and Pb than Cl-OH- and Cl-OH-F-apatite. Magnesium and Mn are also slightly enriched in Cl-OH-apatite relative to Cl-OH-F-apatite. The V, Th and U concentration is relatively homogeneous within the three domains identified in apatite from the Mariela deposit. Arsenic also shows a similar behavior to V, Th, and U; however, Cl-apatite is slightly more depleted with respect to Cl-OH- and Cl-OH-F-apatite.

REE patterns and distribution

REE concentrations for apatite from the three deposits are reported in **Table A5** and summarized in **Table 2**. Cl-OH-apatite from Carmen has total LREE concentrations of ca. 1900 μg/g with (La/Yb)cn= 0.46-3.8, lower than in F-apatite (ca. 2600 μg/g LREEs and (La/Yb)cn= 1.5-10.8), but their HREE concentrations are in the same range (ca. 680 and 710 μg/g, respectively). The REE pattern clearly shows lower La, Ce and Pr values in Cl-OH-apatite relative to F-apatite (**Figure 14**). Apatite from Fresia has higher LREEs, HREEs and (La/Yb)cn ratios in Cl-apatite (6400 μg/g; 700 μg/g; 12.7-17.4, respectively), followed by Cl-OH-F apatite (5600 μg/g; 660 μg/g;

3.7-17.4, respectively) and Cl-OH-apatite (930 μg/g; 320 μg/g; 1.2-2.0 respectively). It should be noted that there is a slight difference in the REE pattern in Cl-OH-apatite in Apatite I and II. Cl-OH-apatite in Apatite I shows a decrease in the La concentration. On the other hand, Cl-OH apatite in Apatite II is depleted in all LREEs. Apatite from Mariela has very similar LREEs concentrations for the three domains, i.e., Cl-, Cl-OH- and Cl-OH-F-apatite (ca. 1260 μg/g), whereas HREEs are ~55 μg/g for Cl- and Cl-OH-F-apatite, and about 100 μg/g for Cl-OH apatite. The LREE/HREE fractionation and size of the Eu anomaly are also very similar for all apatite types with average values of (La/Yb)cn= 46 and Eu/Eu* =0.42. Moreover, apatite from Mariela does not show LREE depletion in any of the domains. Regardless of the difference in REE concentration observed for each apatite type (**Table A5**), all chondrite-normalized analyses display the typical LREE enrichment relative to HREE, and negative Eu anomaly (**Figure 14**).

2.3.4. Strontium and Nd isotopes

Apatite from Carmen, Fresia and Mariela contain negligible Rb (~0.1 μg/g Rb), and low Rb/Sr ratios; hence, only the $^{87}Sr/^{86}Sr$ ratio was measured. The Sm, Nd, and Sr concentrations and isotope ratios are reported in **Table 3**. The analyzed apatite grains have a $^{147}Sm/^{144}Nd$ ratio ranging from 0.1164 to 0.1339 for Carmen, 0.1187 to 0.1533 for Fresia, and lower values between 0.0857 and 0.0950 for the Mariela deposit. In addition, apatite from the Carmen deposit has $^{143}Nd/^{144}Nd$ and $^{87}Sr/^{86}Sr$ ratios ranging from 0.51289 to 0.51291 and 0.7038 to 0.7047, respectively, whereas Fresia and Mariela apatites have a $^{143}Nd/^{144}Nd$= 0.51226-0.51278 and $^{87}Sr/^{86}Sr$=0.7041-0.7059, and $^{143}Nd/^{144}Nd$=0.51283-0.51285 and $^{87}Sr/^{86}Sr$= 0.7039-0.7041, respectively (**Table 3**). The ε_{Nd} values for apatite from the three deposits were calculated using a 130 Ma age. Only the Carmen deposit has a reported U-Pb apatite age of 131.0 ± 1.0 Ma (Gelcich et al., 2005). Apatite from Carmen yielded the highest ε_{Nd} values, which vary between +5.9 and +6.5, followed by Mariela (ε_{Nd}=+5.5 to +6.0). In Fresia the ε_{Nd} values are lower and range from negative to positive values (ε_{Nd}= -0.3 to +4.1).

2.4. DISCUSSION

2.4.1. Magmatic compositions and hydrothermal alteration processes

It is widely documented that the partitioning behavior of F, Cl and OH into apatite is controlled by parameters such as melt and/or fluid composition, temperature, pressure, fO_2, and the occurrence of other F^-- and Cl^--bearing phases (Zhu and Sverjensky, 1991). Primary apatite composition is dominated by fluorapatite (Webster and Piccoli, 2015) becoming one of the main F-bearing phases, in addition to biotite and amphibole, in quartz-bearing igneous rocks and metamorphic rocks (Zhu and Sverjensky, 1991). In magmatic systems, F is preferentially partitioned into the silicate melt during differentiation, ascent and degassing of fluid-saturated magmas (Carrol and Webster, 1994; Kiprianov, 2006; Kiprianov and Karpkhina, 2006; Dolejš and Baker, 2007a; Auippa et al., 2009). In felsic-intermediate igneous rocks apatite shows a restricted

F-Cl-OH compositional range with $X_{F\text{-apatite}}$ 50-100%, $X_{OH\text{-apatite}}$ 0-50% and $X_{Cl\text{-apatite}}$ <20% (Piccoli and Candela, 2002). On the other hand, apatite in mafic systems is a minor phase that occurs as inclusions in cumulus minerals and as a cumulate or interstitial mineral, and has a more variable composition between the three end-members (Piccoli and Candela, 2002). Cl-apatite has been documented in layered mafic intrusions such as the Bushveld Complex in South Africa and Stillwater in Montana (Boudreau et al., 1986; Boudreau and Kruger, 1990; Boudreau and McCallum, 1989, 1999). However, Cl-apatite (>3.5 wt% Cl) is more common in hydrothermal systems (Webster and Piccoli, 2015). Chlorine solubility is strongly dependent on the melt composition, but in general it is very soluble. Furthermore, Cl is preferentially partitioned into the fluid phase rather than the melt as magmas evolve from mafic to more silicic compositions, becoming one of the main ligands in metal-bearing hydrothermal systems (Metric and Rutherford, 1992; Chevychelov, 1999; Webster and DeVivo, 2002, Chevychelov et al., 2003; Williams-Jones and Heinrich, 2005; Kiprianov, 2006; Kiprianov and Karpukhina, 2006).

The textural and compositional data from Carmen, Fresia and Mariela record the modification of primary (magmatic) apatite compositions by interaction with metasomatic fluids. The BSE images, elemental maps and compositional traverses show that the cores of primary apatite in Carmen correspond to F-apatite (>3.0 wt% F). The occurrence of Cl-OH-apatite as pore-free rims of apatite crystals and as fracture fillings in Carmen suggests formation of Cl-OH-apatite by metasomatic processes. These processes are also evidenced by the occurrence of fine-grained Cl-OH-apatite in Carmen and Fresia.

In Fresia and Mariela, the apatite cores incorporated Cl and OH (Cl-OH-F-domains: F <1 wt%) through interaction with metasomatic fluids, reflecting a modification/replacement of their primary F-rich composition. Further evidence of interaction with aqueous fluids is the presence of apatite with an acicular texture in Fresia and Mariela (**Figures 5 and 5**). The presence of acicular apatite in granitic rocks has been interpreted as evidence of a rapid cooling and/or the presence of a fluid (Bargossi et al., 1999; Piccoli and Candela, 2002). Nonetheless, the main evidence that apatite from Carmen and Fresia has been metasomatized is the occurrence of reaction zones and the presence of monazite and xenotime inclusions. Experimental studies have demonstrated that the formation of these inclusions in apatite is a fluid-induced process that results from a coupled dissolution-reprecipitation process (Harlov and Förster, 2003; Harlov et al., 2005; Putnis, 2009; Betkowski et al., 2016). Several studies have reported the presence of monazite and/or xenotime inclusions in altered apatite domains from Kiruna-type IOA deposits (e.g., Sidder et al., 1993; Harlov et al., 2002a; Jonsson et al., 2010; Daliran et al., 2010). The LREEs depletion in Cl-OH-apatite, in addition to the relative Th and U depletion compared to other domains from the Carmen and Fresia deposits (**Figures 13 and 14**), indicate that part of the primary F-apatite was altered and dissolved, leading to the fluid-aided coupled dissolution of LREEs, Th, U, P, and later precipitation of monazite inclusions. The difference between hydrothermal and igneous monazite can be recognized chemically by ThO_2 concentration, which is commonly <1 wt% for hydrothermal monazite and 3 to >5 wt% for igneous monazite (Schandl and Gorton, 2004). Monazite inclusions of altered domains in apatite from Carmen contain values of 0.07 wt% ThO_2, <300 μg/g U, and <189 μg/g Pb (Gelcich et al., 2005), compatible with a hydrothermal origin. The preservation of shape and orientation of primary apatite crystals, the sharp compositional boundary between F-apatite and replaced apatite, and micro-porosity within the altered zones, are also evidence of coupled dissolution-reprecipitation processes. On the other hand, apatite from Mariela shows a relatively homogeneous Th and U concentration in all domains, does not display the LREE depletion pattern **(Figures 13 and 14)**, and lacks monazite inclusions; however, textural evidence

indicates that the apatite was affected by fluid-aided, coupled dissolution-reprecipitation processes. The most important textural evidence corresponds to secondary porosity produced by the dissolution of primary apatite developed at the rims of these grains, such that the areas with higher Cl concentrations are characterized by larger pores. A recent experimental study shows how synthetic Cl-apatite can be replaced by the formation of porous Cl-OH apatite or a solid solution between Cl-OH-F-apatite during the interaction with aqueous solutions (KOH, NaCl and NaF) at crustal conditions (400-700 °C and 0.2 GPa) (Kusebauch et al., 2015).

Formation of apatite with porous cores and pristine, porosity-free rims at Mariela can also be explained by interaction with saline aqueous fluids. Experiments performed at 500 °C in the presence of a NaCl-bearing fluid produced a porosity-free apatite formed as an epitaxial overgrowth on primary apatite, which formed when major components of apatite (Ca^{2+} and PO_4^{3-}) were dissolved at the replacement front, and then transported outside of the primary grain. This allowed re-precipitation of apatite as an epitaxial overgrowth, which also indicates an effective interconnectivity between the replacement front and the fluid (Kusebauch et al., 2015).

Field evidence supports the involvement of metasomatic fluids in the evolution of the Carmen, Fresia and Mariela IOA deposits. Iron oxide-apatite deposits are characterized by a pervasive and extensive Ca-Na alteration with abundant actinolite, epidote, minor albite and occasionally scapolite. In the Carmen and Fresia deposits, several magnetite veinlets crosscut apatite and primary magnetite, evidencing remobilization and later precipitation of magnetite. Moreover, Treloar and Colley (1996) suggested that the presence of mm-thick magnetite and epidote veinlets, and the large size of apatite and actinolite crystals in these deposits are indicative of a low viscosity or pegmatite-derived fluids. In Mariela, copper oxides (chrysocolla and atacamite) formed by oxidation of scarce primary copper sulfides, indicating a late sulfide hydrothermal event followed by a supergene/oxidation event that in addition to Cu oxides precipitated gypsum.

2.4.2. Mechanisms of fluid-apatite alteration

The processes of metasomatic alteration of primary, F-apatite are shown schematically in **Figure 15**. The degree of alteration is strongly related to the fluid/mineral (apatite) ratio and the composition of the metasomatic fluid. In apatite from Carmen, alteration was restricted to the formation of Cl-OH-apatite in rims and fractures, with grain cores mostly unaltered, suggesting a low fluid/apatite ratio. In apatite from Fresia, alteration was dominated by the formation of Cl-OH-apatite, whereas in apatite from Mariela alteration was pervasive and dominated by Cl-apatite indicating a higher fluid/mineral ratio in Mariela. The metasomatic alteration of apatite also resulted in enrichment in S, Na, Sr, Fe and to a lesser extend in Mg, V, Mn, Cu, As, Ba, and Pb in Cl-apatite and Cl-OH-apatite.

Fluid-mineral interaction caused by the infiltration of a metasomatic fluid of a specific composition that is in disequilibrium with apatite, or by a change of temperature and/or pressure, can trigger the dissolution of the parent F-apatite, such that the resulting fluid could become supersaturated in certain components (e.g., U, Th, REEs; Putnis 2002; 2009), causing the

precipitation of monazite (and lesser xenotime) as seen in apatite from Carmen and Fresia (**Figure 15**). As the fluid reacts with the mineral surface, it generates porosity and permeability allowing the fluid to further infiltrate into the apatite structure. The pseudomorphic replacement of F-apatite by Cl-bearing apatite results in the formation of porosity within the replaced phase due to changes in molar volume of the different apatite types (Yanagisawa et al., 1999) and the differences in solubility between the primary and the replacing phases (Putnis 2002, 2009). The occurrence of epitaxial apatite, as in the case of Mariela, also indicates an efficient interconnectivity of the replacement front with the bulk fluid (Kusebauch et al., 2015). Fluid-assisted transport of cations and anions through the pore network into apatite promotes nucleation and growth of monazite grains and resulting in the transport of dissolved P^{5+}, Y^{3+}, $LREE^{3+}$, U^{+}, and Th^{+} towards the newly formed monazite grains, while $Ca^{2+}$and some P^{5+} (and probably other components as Na^{+} and Si^{4+}) are transported by the fluid out of the surrounding apatite.

The formation of monazite and xenotime inclusions depends strongly on the reactivity of primary apatite with the fluid and the abundance of (Y + REE) in primary apatite. In addition to high pH fluids such as HCl or H_2SO_4, pure H_2O, H_2O+CO_2 and KCl brines have been shown experimentally to facilitate the formation of monazite and xenotime inclusions over a wide range of P-T conditions (<900 °C and <1000 MPa) (Harlov et al., 2002b, 2005; Harlov and Förster, 2003). In contrast, NaCl and $CaCl_2$ brines have been reported to inhibit the formation of inclusions. Some studies have suggested that aqueous Na may prevent Na from leaving the apatite structure such that charge balance is maintained, inhibiting REE remobilization and formation of monazite inclusions (Harlov and Förster, 2003; Harlov et al., 2005, Hansen and Harlov, 2007). However, Antignano and Manning (2008) reported that monazite inclusions in apatite can form in the presence of a NaCl-enriched brine, and Betkowski et al. (2016) demonstrated experimentally that coupled dissolution-reprecipitation in the presence of a Na-rich aqueous fluid results in the exsolution of $[REE]PO_4$ from the apatite structure during metasomatism at temperatures from 300 to 600 °C.
Monazite and xenotime formation from apatite involves REE^{3+} remobilization through coupled substitutions ($REE^{3+} + Si^{4+} \leftrightarrow Ca^{2+} + P^{5+}$, or $REE^{3+} + Na^{+} \leftrightarrow 2Ca^{2+}$) leading to the REE^{3+} leaching from primary apatite and mass transfer into the fluid, whereas Ca^{2+} and P^{5+} are incorporated into the replaced apatite (Harlov, 2015). Moreover, studies have demonstrated that REEs are readily concentrated by hydrothermal processes, but where LREEs are more readily mobilized by metasomatic fluids than HREEs (Reed et al., 2000), and where Cl ions can form stable complexes with REE, especially at high temperatures and low pH fluids (Williams-Jones et al., 2012). Thus, LREE could have been effectively leached from F-apatite by Cl-rich fluids that allowed monazite nucleation and growth, and also replacement of primary apatite by Cl- and Cl-OH apatite. Furthermore, the fluid-mediated reaction of monazite and xenotime with the surrounding silicate minerals can produce allanite [$Ca\,(Ce, La, Y)Fe^{2+}Al_2(Si_2O_7)(SiO_4)O(OH)$] as seen in some areas close to apatite grains from Fresia.

The lack of monazite inclusions in Mariela apatite could be related to a lower initial Y+REEs concentration (>0.2 - 0.3 wt%) of primary apatite, or more likely the composition of the metasomatic fluid; i.e., Cl-bearing brines (NaCl or $CaCl_2$) which may inhibit substitution, REE remobilization and monazite nucleation (Harlov et al., 2002a, 2005; Harlov and Förster, 2003). Apatite from Mariela contains <0.2 wt% total REE for all domains.

2.4.3. The role of volatiles on apatite alteration

The Cl- and Cl-OH-apatite compositions of replaced apatite (i.e., apatite that grows during coupled dissolution-reprecipitation) from Carmen, Fresia and Mariela highlight the significant control of the fluid composition on the alteration product. **Figure 16** shows the halogen (F, Cl) and OH concentration of several Kiruna-type deposits, e.g., El Romeral, Chile (Early Cretaceous; Rojas et al., 2018b), Chadormalu, Chogart and Esfordi in the Bafq region, Central Iran (early Cambrian; Taguipour et al., 2015), deposits of the Kiruna district, northern, Sweden (early Proterozoic; Harlov et al., 2002), Taocun, Eastern China (Early Cretaceous; Zeng et al., 2016) and the Yinachang IOCG deposit, Southwest China (early Proterozoic; Li and Zhou, 2015). All these deposits, except for the El Romeral IOA deposit (Chile), report the presence of monazite and xenotime inclusions produced by fluid-aided dissolution-reprecipitation processes. Also shown in **Figure 16** are the compositional fields for apatite from the Carmen, Fresia and Mariela deposits as determined in this study, as well as data for Carmen and Fresia reported by Treloar and Colley (1996).

Comparatively, magmatic apatite from all the cited IOA deposits is dominantly F-apatite whereas hydrothermal apatite (metasomatized areas) has significant variability in composition. For example, at the El Romeral deposit the composition of magmatic apatite (sampled at ~300 m depth) is F-apatite, whereas hydrothermal apatite found at shallow levels (~50 m) is OH-apatite rather than Cl-apatite (Rojas et al., 2018b). In contrast, the compositions of hydrothermal apatite from Yinachang, Taocun, Bafq and Kiruna deposits are mainly F-apatite and not very different from magmatic apatite.

The involvement of highly saline fluids (e.g., late-stage magmatic fluids) in the formation of Kiruna-type IOA deposits is, although limited, supported by fluid inclusion data in apatite (e.g., Broman, 1999; Broman and Martinsson, 2000; Knipping et al., 2015b). For the particular case of Carmen, aqueous-gas rich fluid inclusions with homogenization temperatures >360 °C, restricted to the rims and fractures in F-apatite, indicate the presence of highly saline $CaCl_2$-$MgCl_2$ fluids (>30 wt% NaCl eq; Velasco and Tornos, 2009). Lower homogenization temperatures and salinities measured in later-stage fluid inclusion assemblages in apatite point to cooler fluids that circulated throughout the system and were probably responsible for the formation of the late Cu-bearing sulfides and hematite formation at shallow depths (Velasco and Tornos, 2009).

In addition to the composition of the metasomatic fluids, other factors should be considered to explain the high Cl concentration in hydrothermal apatite (>3.5 wt% Cl) from the Carmen, Fresia and Mariela deposits. According to Doherty et al. (2014), Cl partitioning between apatite-melt-fluids depends, among other factors, on pressure. These authors demonstrated experimentally that Cl incorporation into apatite increases considerably, relative to felsic melt or vapor ± saline fluid, as the pressure decreases from 200 to 50 MPa. Considering the strong structural control of the studied deposits, decompression may have played an important role in the incorporation of high Cl concentrations in apatite, as previously demonstrated for Fe precipitation at the El Romeral IOA deposit (Rojas et al., 2018b). This also is compatible with thermodynamic calculations in the apatite-HCl-H_2O system that shows an increasing stability of OH-apatite with increasing temperature and pressure at fixed HCl activity (Zhu and Svenjensky, 1991).

In addition to F and Cl, S is a significant volatile in magmatic and magmatic-hydrothermal systems, including IOA deposits. The positive correspondence between S and Na (**Figure A3**)

suggests that Na charge-balances the incorporation of S into the apatite structure through the substitutional mechanism $SO_4^{2-} + Na^+ = PO_4^{3-} + Ca^{2+}$, however, many studies on S-bearing apatite have pointed to S present as the S^{6+} ion only (Rouse and Dunn, 1982; Liu and Comodi, 1993; Tepper and Kuehner, 1999; Parat et al., 2011). More recently, Konecke et al. (2017) show that apatite can incorporate three S oxidation states into different locations within the apatite structure. These authors show qualitatively that variable abundances of S^{6+}, S^{4+} and S^{2-} are incorporated into apatite as crystallized from a mafic silicate melt under varying oxygen fugacity conditions: as the fO_2 increases from FQM to FMQ+1.2 to FMQ+3 the oxidation state of S in igneous apatite changes from S^{2-} dominant to $S^{6+}>S^{4+}$ to $S^{6+}>>S^{4+}$. Konecke et al. (2017) show that XANES and EPMA transects across apatite from the Carmen IOA deposit reveal a ~2 orders of magnitude increase in the S concentration from F-apatite non-metasomatized area to Cl-apatite metasomatized area near a volatile-bearing cavity rim, which correlates inversely with the evolution of the $S^{6+}/\sum S$ total peak area ratios, due to the enrichment in S^{4+} relative to S^{6+}. This feature was interpreted by those authors to indicate metasomatic overprinting via reaction with a S-bearing (e.g., SO_2) fluid or vapor phase (cf. Harlov, 2015). Recently, Kim et al. (2017) suggested that S^{4+} and S^{6+} replace the PO_4^{3-} group, while S^{2-} is positioned in the anionic column (F-Cl-OH). In addition, the incorporation of S^{4+} is controlled through the reduction of S^{6+} to S^{4+} ($SO_4^{2-}{}_{melt} \leftrightarrow SO_3^{2-}{}_{apatite} + 1/2O_{2\ melt}$). These recent findings of variable oxidation states of S in apatite from the Carmen IOA deposit are consistent with our EPMA results that document that hydrothermal Cl-OH-apatite displays a higher S concentration (S^{6+} and S^{4+}) than magmatic F-apatite, which probably contains a larger proportion of reduced S (S^{2-}).

2.4.4. Magmatic source of volatiles and environment of IOA formation

Apatite from the Carmen, Fresia and Mariela IOA deposits have high ε_{Nd} and low initial $^{87}Sr/^{86}Sr$ isotopic values (**Table 3; Fig. A4**), which is compatible with a mantle source with minimal crustal contribution. The high ε_{Nd} (+5.9 to +6.5) and low initial $^{87}Sr/^{86}Sr$ values (0.70382 to 0.70474) of apatite from Carmen are consistent with the textural and geochemical magmatic signature of unaltered F-apatite. On the other hand, Cl- and Cl-OH-apatite from Fresia have more negative and scattered ε_{Nd} values (-0.3 to +4.1) and higher $^{87}Sr/^{86}Sr$ (up to 0.70590), probably as a result of fluid-rock interaction. However, it is important to note that the isotopic composition of apatite was determined by digesting bulk samples that include several domains; i.e., F-apatite (unaltered) to Cl-OH or Cl-apatite (metasomatized) domains. Isotopic studies of apatite from the Taocun IOA deposit (Zeng et al., 2016) and Yinachang Fe-Cu-REE deposit (Zhao et al., 2015), both in China, reported an increase in the initial $^{87}Sr/^{86}Sr$ ratio measured with LA-MC-ICP-MS from unaltered to altered domains, indicating that metasomatic fluids were more enriched in radiogenic Sr and were more likely to have a greater contribution from sedimentary rocks due to fluid circulation. The apatite from Mariela exhibits high and narrow ε_{Nd} values (+5.5 to +6.0), and the lowest initial $^{87}Sr/^{86}Sr$ values of the three deposits (0.70390-0.70407), despite the fact that this apatite has the highest Cl concentration. These signatures are difficult to interpret owing to the limited data and the lack of spatially resolved Sr analyses, but a possible explanation is that Mariela apatite was formed from a high temperature and high salinity magmatic-hydrothermal fluid exsolved from a primitive magmatic source.

North of Taltal (24°58´- 25°22´S, 70°23´´W, not shown in **Figure 2**), plutonic rocks of ca. 160 Ma have initial $^{87}Sr/^{86}Sr$ ratios of 0.70120 to 0.70624, $^{143}Nd/^{144}Nd$ ratios of 0.512628 to 0.512869 and ε_{Nd} values of +0.4 to +6.1 (Lucassen et al., 2006; **Fig. A4**). A few analyses,

considered atypical by those authors, showed higher initial $^{87}Sr/^{86}Sr$ ratios (0.71050-0.71324) and lower ε_{Nd} values (-8.4 to -8.5). South of Taltal (25°28´S, 70°30´´W), Early Cretaceous (~140 Ma) dikes corresponding to the latest documented magmatic activity in the area, have reported initial $^{87}Sr/^{86}Sr$ ratios ranging between 0.70363 and 0.70497, $^{143}Nd/^{144}Nd$ ratios of 0.512725 to 0.512905, and ε_{Nd} values between +2.7 and +6.0 (Lucassen et al., 2006). South of Copiapó, at the Candelaria-Punta del Cobre district (27°31´35´´ S 70°17´40´´W), Early Cretaceous plutonic rocks (110-115 Ma) that form part of the Coastal Batholith of northern Chile, have initial $^{87}Sr/^{86}Sr$ ratios of 0.70307-0.70323, $^{143}Nd/^{144}Nd$ ratios of 0.512841-0.512881 and ε_{Nd} values between +4.6 and +5.6 (Marschik et al., 2003). These Sr and Nd isotopic data of plutonic rocks are very similar to the isotopic signal of apatite measured in the studied deposits, point to a dominantly primitive, mantle source. However, and considering recent studies that genetically link IOA deposits to intrusive bodies in the districts (e.g. Rojas et al., 2018a), the available isotopic data are very limited and further studies are required to link the formation of the IOA deposits in the Carmen, Fresia and Mariela districts to particular pulses of magmatism (i.e., plutonism) in the region.

2.5. CONCLUSIONS

Apatite from the Carmen, Mariela and Fresia IOA deposits in the Chilean iron belt records both magmatic and hydrothermal stages of mineralization associated with fluid-aided coupled dissolution-reprecipitation processes. Apatite characterized by a high F concentration is indicative of a magmatic origin, whereas high Cl concentrations are indicative of a metasomatic overprint for apatite from Carmen, Fresia and Mariela.

Apatite from the Carmen deposit has a higher F concentration than those from Fresia and Mariela, suggesting a low fluid/apatite interaction that resulted in a restricted alteration/replacement by Cl-OH apatite in fractures and grain rims, and preservation of the primary F-apatite composition in grain cores. In Fresia and Mariela, metasomatic alteration was more pervasive; i.e., higher fluid/apatite interaction where the primary F-apatite was partially to completely replaced by Cl-OH and Cl-apatite as evidenced by chemical and textural observations; e.g., replacement by fine-grained Cl-OH-apatite, monazite and to a lesser extent xenotime inclusions in Fresia, and high porosity with large pore sizes in Cl-apatite domains. The Cl-OH-apatite altered domains from Carmen and Fresia are slightly depleted in LREE, Th, and U, compatible with fluid-aided REE remobilization and subsequent nucleation and growth of monazite and lesser xenotime inclusions, and enriched in S, Na, Sr, Fe Mg, V, Mn, Cu, As, Ba, and Pb. In Mariela, the REE pattern shows no LREE depletion and very similar Th and U concentrations for the different domains, observations that are consistent with the absence of formation of monazite inclusions.

The halogen composition of altered apatite suggests that aqueous Cl-bearing fluids were responsible for the metasomatic alteration and that the Cl and OH apatite compositions depend on the pH of the metasomatic fluid, which controls the availability of OH in the fluid and, therefore, controls the incorporation of OH and Cl in the apatite structure. Moreover, in the Carmen deposit, the presence of S in hydrothermal apatite responds to oxidizing SO_2-bearing fluids and sulfate-sulfite coupled substitution during the metasomatic overprint, leading apatite to incorporate both S^{4+} and S^{6+} via local redox reactions that reduced S^{6+} to S^{4+}.

The isotopic data support the geochemical and textural results, which indicate a primitive magmatic origin with little or no crustal contamination for these Andean IOA deposits. This study shows that textural studies coupled with halogen concentrations, trace element composition, and isotopic composition of apatite can be used to characterize the magmatic and metasomatic processes involved in the formation and evolution of IOA deposits. These findings are consistent with the flotation model that explains the formation of IOA deposits by both magmatic and hydrothermal processes.

2.6. ACKNOWLEDGEMENTS

This research was funded by Project FONDECYT 1140780 "Metallogenesis of the Mesozoic magmatic arc of northern Chile: Testing the IOCG connection using multiproxy geochemical approach", and by the Millenium Nucleus for Metal Tracing along Subduction (NC130065). The LA-ICP-MS analytical work was funded by Conicyt-Fondequip instrumentation grant EQM120098. G. Palma thanks financial support provided by CONICYT-PFCHA/Doctorado Nacional/2016-2116003, through a PhD scholarship. We thank Chao Zhang and Diane Wilford for assistance with apatite isotope analysis at Washington State University in Pullman. ACS acknowledges funding from the U.S. National Science Foundation (EAR 1250239 and 1524394). We thank Daniel E. Harlov, two anonymous referees, and Associate Editor Edward M. Ripley for detailed reviews that improved the manuscript.

2.7. References

Aiuppa A. (2009) Degassing of halogens from basaltic volcanism: insights from volcanic gas observations. *Chem. Geol*.,**263**, 99–109

Antignano A. and Manning C. E. (2008) Fluorapatite solubility in H2O and H2O–NaCl at 700 to 900 C and 0.7 to 2.0 GPa. *Chem. Geol*. **251**, 112-9.

Bargossi G.M., Del Moro A., Ferrari M., Gasparotto G., Mordenti A., Rottura A. and Tateo F. (1999) Caratterizzazione petrografico-geochimica e significato dell'associazione monzogranito-inclusi femici microgranulari della Vetta di Cima d'Asta (Alpi Meridionali). *Mineral. Petrog. Acta* **42**, 155-179.

Barra F., Reich M., Selby D., Rojas P., Simon A., Salazar E. and Palma G. (2017) Unraveling the origin of the Andean IOCG clan: a Re-Os isotope approach. *Ore Geol Rev*. **81**, 62–78.

Barton M. D. and Johnson D.A. (1996) Evaporitic-source model for igneous-related Fe oxide–(REE-Cu-Au-U) mineralization. *Geol.* **24**, 259-262.

Barton M. D. and Johnson D. A. (2004) Footprints of Fe-oxide (-Cu-Au) systems. University of Western Australia Special Publication, **33**, 112-116.

Barton M. D. (2014) Iron oxide (–Cu–Au–REE–P–Ag–U–Co) systems. In *Scott, S.D., ed., Treatise on Geochemistry* (second edition, volume 13): Amsterdam, Elsevier, 515–541.

Bea F., Pereira M. D. and Stroh A. (1994) Mineral/leucosome trace-element partitioning in a peraluminous migmatite (a laser ablation-ICPMS study). *Chem. Geol*. **117**, 291-312.

Betkowski V., Harlov D. and Rakovan J. (2016) Hydrothermal mineral replacement reactions for an apatite-monazite assemblage in alkali-rich fluids at 300 - 600 °C and 100 MPa. *Am. Mineral.* **101**, 2620–2637.

Belousova E. A. (2000) Trace elements in zircon and apatite: application to petrogenesis and mineral exploration. PhD thesis. Macquare University, Australia.

Belousova E. A., Walters S., Griffin W. L. and O´Reilly S. Y. (2001) Trace element signatures of apatites from granitoids of Mount Isa Inlier, north-west Queensland, Australia. *Aust. J. Earth Sci.* **48**, 603-619.

Bonson C. G., Grocott J. and Rankin A. H. (1996) A structural model for the development of Fe-Cu mineralization within the Atacama fault system (25°00´ S-27° 15´ S), northern Chile. Third ISAG, St Malo (France), 17-19/9/1996.

Boudreau A. E., Mathez E. A. and McCallum I. S. (1986) Halogen geochemistry of the Stillwater and Bushveld Complexes: evidence for transport of the platinum-group elements by Cl-rich fluids. *J. Petrol.* **27**, 967-986.

Boudreau A. E. and McCallum I. S. (1989) Investigations of the Stillwater Complex: Part V. Apatites as indicators of evolving fluid composition. *Contrib. Mineral. Petrol*. **102**, 138-153.

Boudreau A. E. and Kruger F. J. (1990) Variation in the composition of apatite through the Merensky cyclic unit in the western Bushveld Complex. *Econ. Geol*. **85**, 737-745.

Boudreau A. E. and Meurer W. P. (1999) Chromatographic separation of the platinum-group elements, gold, base metals and sulfur during degassing of a compacting and solidifying igneous crystal pile. *Contrib. Mineral. Petrol.* **134**, 174-185.

Broman C., Nyström J. O., Henríquez F. and Elfman M. (1999) Fluid inclusions in magnetite-apatite ore from a cooling magmatic system at El Laco, Chile. *Gff*. **121**, 253-267.

Broman C. and Martinsson O. (2000) Fluid inclusions in epigenetic Fe-Cu-Au ores in Northern
Carroll, M.R., Webster, J.D., 1994. Solubilities of sulfur, noble gases, nitrogen, chlorine, and fluorine in magmas. In: Carroll, M.R., Holloway, J.R. (Eds.), Volatiles in Magmas. *Rev. Mineral. Geochem.* **30**, 231–279.

Chen H., Clark A. H. and Kyser T. K. (2010) The Marcona magnetite deposit, Ica, south-central Peru: a product of hydrous, iron oxide-rich melts?. *Econ. Geol.* **105**, 1441-1456.

Chevychelov V. Y. (1999) Chlorine dissolution in fluid-rich granitic melts: the effect of calcium addition. *Geochem. Internat.* **37**, 456–467.

Chevychelov V. Y., Simakin A. G. and Bondarenko G. V. (2003) Mechanism of chlorine dissolution in water-saturated model granodiorite melt: applications of IR spectroscopic methods. *Geochim. Internat.* **41**, 395–409.

Chew D. M., Babechuk M. G., Cogné N., Mark C., O'Sullivan G. J., Henrichs I. A., Doepke D. and McKenna C. A. (2016) (LA, Q)-ICPMS trace-element analyses of Durango and McClure Mountain apatite and implications for making natural LA-ICPMS mineral standards", *Chem. Geol.* **435**, 35-48.

Childress T. M., Simon A. C., Day W. C., Lundstrom C. C. and Bindeman I. N. (2016) Iron and oxygen isotope signatures of the Pea Ridge and Pilot Knob magnetite–apatite deposits, southeast Missouri, USA. *Econ. Geol.* **111**, 2033-2044.

Daliran F., Stosch H. G., Williams P., Jamli H. and Dorri M. B. (2010) Early Cambrian Iron Oxide-Apatite-REE (U) Deposits of the Bafq District, East-Central Iran. In Exploring for Iron oxide copper-gold deposits: Canada and Global analogues (L. Corriveau & H. Mumin, eds.). Geological Association of Canada Short Course Notes. **20**, 143–155.

Dare S., Barnes S. J. and Beaudoin. G. (2015) Did the massive magnetite "lava flows" of El Laco (Chile) form by magmatic or hydrothermal processes? New constraints from magnetite composition LA-ICP-MS. *Miner Deposita*. **50**, 607.

Doherty A. L., Webster J. D., Goldoff B. A., Piccoli P. M. (2014) Partitioning behavior of chlorine and fluorine in felsic melt–fluid(s)–apatite systems at 50 MPa and 850–950 °C. *Chem. Geol.* **384**, 94-109.

Dolejš D. and Baker D. R. (2007b) Liquidus equilibria in the system K_2O–Na_2O– Al_2O_3-SiO_2-F_2O_{-1}–H_2O to 100 MPa: II. Differentiation paths of fluorosilicic magmas in hydrous systems. *J. Petrol.* **48**, 807–828.

Espinoza S. (1984a) Le rôledu volcanisme du Crétecé inférieur dans la métallogénèse de la ceinture ferrifère d´ Atacama-Coquimbo, Chili. Unpublished doctoral thesis, Paris, l´ Université Pierre et Marie Curie, Paris, 153 p.

Espinoza S. (1990) The Atacama-Coquimbo ferriferous belt, northern Chile. In Fontboth, L., Amstutz, G.C., Cardozo, M., Cedillo, E., and Frutos, J., eds., Stratabound ore deposits in the Andes :Berlin, Springer-Verlag. p, 353-364.

Gaschnig R. M., Vervoort J. D., Lewis R. S. and Tikoff B. (2011) Isotopic evolution of the Idaho batholith and Challis intrusive province, northern US Cordillera. *J. Petrol.* **52**, 2397–2429.

Gelcich S., Davis D. W. and Spooner E. T. (2005) Testing the apatite-magnetite geochronometer: U-Pb and $^{40}Ar/^{39}Ar$ geochronology of plutonic rocks, massive magnetite-apatite tabular bodies, and IOCG mineralization in Northern Chile. *Geochim. Cosmochim. Acta*, **69**, 3367-3384.

Hansen E. C. and Harlov D. E. (2007) Whole-rock, phosphate, and silicate compositional trends across an amphibolite-to granulite-facies transition, Tamil Nadu, India. *J. Petrol*. **48**, 1641-1680.

Harlov D. E., Förster H. J. and Nijland T. G. (2002a) Fluid-induced nucleation of REE-phosphate minerals in apatite: nature and experiment. Part I. Chlorapatite. *Am. Mineral.* **87**, 245-261.

Harlov D. E. and Förster H. J. (2003) Fluid-induced nucleation of (Y+REE)-phosphate minerals within apatite: Nature and experiment. Part II. Fluorapatite. *Amer. Min*. **88**, 1209–1229.

Harlov D. E., Wirth R. and Förster H. J. (2005) An experimental study of dissolution–reprecipitation in fluorapatite: fluid infiltration and the formation of monazite. *Contrib. Mineral. Petrol*. **150**, 268-286.

Harlov D. E. (2015) Apatite: A Fingerprint for Metasomatic Processes. *Elements* **11**, 171-176.

Harlov D. E., Corey J. M., Ian D. K. and Lain M. S. (2016) Mineralogy, Chemistry, and Fluid-Aided Evolution of the Pea Ridge Fe Oxide-(Y + REE) Deposit, Southeast Missouri, USA. *Econ. Geol.* **111**, 1963-1984.

Hou T., Charlier B., Holtz F., Veksler I., Zhang Z., Thomas R. and Namur O. (2018) Immiscible hydrous Fe–Ca–P melt and the origin of iron oxide-apatite ore deposits. *Nature Comm*. **9**, 1415.

Hughes J. M., Cameron M. and Crowley K. D. (1989) Structural variations in natural F, OH, and Cl apatites. *Amer. Min.* **74**, 870-876.

Jonsson E., Persson-Nilsson K., Högdahl K., Troll V. and Hallberg A. (2010) REE distribution and mineralogy in a Palaeoproterozoic apatite-iron oxide deposit: Grängesberg, Bergslagen, Sweden. In IMA 2010 Vol. 6, p. 234.

Jonsson E., Harlov D. E., Majka J., Högdahl K. and Persson-Nilsson K. (2016) Fluorapatite-monazite-allanite relations in the Grängesberg apatite-iron oxide ore district, Bergslagen, Sweden. *Amer. Min.* **101**, 1769-1782.

Kim Y., Koecke B., Fiege B., Simon A. and Becker U. (2017) An ab-initio study of the energetics and geometry of sulfide, sulfite and sulfate incorporation in apatite; The thermodinamic basis for using this system as an oxybarometer. *Amer. Min*. 102, 1646-1656.

Knipping J. L., Bilenker L.D., Simon A.C., Reich M., Barra F., Deditius A. P., Lundstrom C., Bindeman I. and Munizaga R. (2015a) Giant Kiruna-type deposits form by efficient flotation of magmatic magnetite suspensions. *Geol.* **43**, 591-594.

Knipping J. L., Bilenker L. D., Simon A. C., Reich M., Barra F., Deditius A. P., Wälle M., Heinrich C. A., Holtz F. and Munizaga R. (2015b) Trace elements in magnetite from massive iron oxide-apatite deposits indicate a combined formation by igneous and magmatic-hydrothermal processes. *Geochim. Cosmochim. Acta* **171**, 15-38.

Kiprianov A. A. (2006) Regular trends in uptake of halogens by alkali silicate glasses containing two glass-forming components. *Russ. J. App. Chem*. **79**, 20–28.

Kiprianov A. A. and Karpukhina N. G. (2006) Oxyhalide silicate glasses. *Glass Phys. Chem*. **32**, 1–27.

Konecke B., Fiege A., Simon A., Parat F. and Stechern A. (2017) Co-variability of S^{6+}, S^{4+}, and S^{2-} in apatite as a function of oxidation state: Implications for a new oxybarometer. *Amer. Min.* **102**, 548–557.

Kusebauch C., John T., Whitehouse M. J., Klemme S. and Putnis A. (2015) Distribution of halogens between fluid and apatite during fluid-mediated replacement processes. *Geochim. Cosmochim. Acta* **170**, 225-246.

Li X. and Zhou M-F. (2015) Multiple stages of hydrothermal REE remobilization recorded in fluorapatite in the Paleoproterozoic Yinachang Fe-Cu-(REE) deposit, Southwest China. *Geochim. Cosmochim. Acta* **166**, 53-73.

Liu Y. and Comodi P. (1993) Some aspects of the crystal-chemistry of apatites. *Mineral. Mag.* **57**, 709-719.

Lucassen F., Kramer W., Bartsh V., Wilke H., Franz G., Romer R. and Dulski P. (2006) Nd, Pb, Sr isotope composition of juvenile magmatism in the Mesozoic large magmatic province of northern Chile (18-27°S): indications for a uniform subarc mantle. *Contrib. Mineral. Petrol.* **152**, 571-589.

Lupulescu M. and Pyle J. (2008) Mining history, mineralogy and origin of the gneiss (granite)-hosted Fe-P-REE and Fe oxide and gabbro-hosted Ti-Fe oxide deposits from the Mineville-Port Henry region, Essex Country, NY. In: Selleck BW (ed) Fieldtrip Guidebook for the 80th Annual Meeting of the New York State Geological Association, pp 117-129.

Maksaev V., Gardeweg M., Ramírez C. F. and Zentilli M. (1988). Aplicación del método trazas de fisión (fission track) a la datación de cuerpos de magnetita de El Laco e Incahuasi en el altiplano de la Región de Antofagasta. In Congreso Geológico Chileno, No. 5, v. 1: B1-B23.

Marschik R., Fontignie D., Chiaradia M. and Voldet P. (2003) Geochemical and Sr-Nd-Pb-O isotope composition of granitoids of the Early Creaceous Copiapó plutonic Complex (27° 30"), Chile. J. S. *Amer. Earth Sci.* **16**, 381-398.

Ménard J-J. (1986) Un modèle métasomatique pour les gisements de la Ceinture de fer du Chili. Académie des Sciences [Paris] Comptes Rendus des Séances, ser. II, **302**, 775-778.

Metrich N., Rutherford M. J. (1992) Experimental study of chlorine behavior in hydrous silicic melts. *Geochim. Cosmochim. Acta* **56**, 607–616.

Naslund H. R., Henríquez F., Nyström J. O., Vivallo W., Dobbs F. M. (2002) Magmatic iron ores and associated mineralisation: examples from the Chilean high Andes and coastal Cordillera. In: hydrothermal Iron Oxide-Copper-Gold A Global Perspective, 2 (ed. T. M. Porter. PGC Publishing, Adelaide, Australia, pp. 207-226.

Nyström J. O. and Henríquez F. (1994) Magmatic features of iron ores of the Kiruna-type in Chile and Sweden: ore textures and magnetite geochemistry. *Econ. Geol.* **89**, 820-839.

Oyarzún J. and Frutos J. (1984) Tectonic and petrological frame of the Cretaceous iron deposits of north Chile. *Min. Geol.* **34**, 21-31.

Pan Y. and Fleet M. (2002) Compositions of the apatite-group minerals: substitution mechanisms and controlling factors. *Rev. Mineral. Geochem.* **48**, 13-50.

Parat F., Holtz F. and Streck M. (2011) Sulfur-bearing Magmatic Accessory Minerals. *Rev. Mineral. Geochem.* **73**, 285-314.

Park C. F. (1972) The iron ore deposits of the Pacific basin. *Econ. Geol*. **67**, 339-349.

Patiño Douce, A.E., Roden, M.F., 2006. Apatite as a probe of halogen and water fugacities in the terrestrial planets. *Geochim. Cosmochim. Acta* **70**, 3173–3196.

Paton C., Hellstrom J., Paul B., Woodhead J. and Hergt J. (2011) Iolite: Freeware for the visualization and processing of mass spectrometric data. *J. Anal. At. Spectrom.* **26**, 2508-2518.

Peng G., Luhr J. F. and McGee J. J. (1997) Factors controlling sulfur concentrations in volcanic apatite. *Amer. Min.* **82**, 1210-1224.

Patchett P. J. and Tatsumoto M. (1981) A routine high-precision method for Lu- Hf isotope geochemistry and chronology. *Contrib. Mineral. Petrol.* **75**, 263–267.

Perseil E. A., Blanc P. and Ohnenstetter D. (2000) As-bearing fluorapatite in manganiferous deposits from St. Marcel–Praborna, Val d'Aosta, Italy. *Can. Mineral.* **38**, 101-117.

Piccoli P. M. and Candela P. A. (2002) Apatite in Igneous Systems. In: Kohn, M.J., Rakovan., Hughes, J.M. (eds.), Phosphates: geochemical, geobiological, and materials importance. : *Rev. Mineral. Geochem.* **48,** 255-292.

Prowatke S. and Klemme S. (2006) Trace element partitioning between apatite and silicate melts. *Geochim. Cosmochim. Acta* **70**, 4513-4527.

Putnis A. (2002) Mineral replacement reactions: from macroscopic observations to microscopic mechanisms. *Mineral. Mag.* **66**, 689-708.

Putnis A. (2009) Mineral replacement reactions. *Rev. Mineral. Geochem.* **70**, 87-124.

Rakovan J., McDaniel D. K. and Reeder R. J. (1997) Use of surface-controlled REE sectoral zoning in apatite from Llallagua, Bolivia, to determine a single-crystal Sm-Nd age. *Earth Planet. Sci. Lett.* **146**, 329-336.

Reed M. J., Candela P. A. and Piccoli P. M. (2000) The distribution of rare earth elements between monzogranitic melt and the aqueous volatile phase in experimental investigations at 200 MPa and 800 °C. *Contrib. Mineral. Petrol.* **140**, 251-262.

Rhodes A. L. and Oreskes N. (1995) Magnetite deposition at El Laco, Chile: implications for Fe-oxide formation in magmatic-hydrothermal systems. Giant ore deposits-II: Controls on the scale of orogenic magmatic-hydrothermal mineralization Clark, AH, 582-622.

Rhodes A. L. and Oreskes N. (1999) Oxygen isotope composition of magnetite deposits at El Laco, Chile: Evidence of formation from isotopically heavy fluids. Geology and Ore Deposits of the

Central Andes, Brian J. Skinner, ed., Society of Economic Geologists Special Publication **7**, 333-351.

Rojas P., Barra F., Reich M., Deditius A., Simon A., Uribe F., Romero R. and Rojo M. (2018a) A genetic link between magnetite mineralization and diorite intrusión at the El Romeral iron oxide-apatite deposit, northern Chile. *Miner. Deposita* 1-20.

Rojas P., Barra F., Deditius A., Reich M., Simon A., Roberts M. and Rojo M. (2018b) New contributions to the understanding of Kiruna-type iron oxide-apatite deposits revealed by magnetite ore and gangue mineral geochemistry at the El Romeral deposit, Chile. *Ore Geolog. Rev.* **93** 413-435.

Rouse R. C. and Dunn P. J. (1982) A contribution to the crystal chemistry of ellestadite and the silicate sulfate apatites. *Amer. Min.* **67**, 90-96.

Ruiz C., Aguirre L., Corvalan J., Klohn C., Klohn E. and Levi B. (1965) Geología y yacimientos metalíferos de Chile: Instituto de Investigaciones Geológicas [Chile], 386 p.

Ruiz C.and Peebles F. (1988) Geología, distribución y Génesis de los yacimientos metalíferos chilenos, Santiago, Editorial Universitaria, 334 p.

Sawka M. N. and Wenger C. B. (1988) Physiological responses to acute exercise-heat stress (No. USARIEM-M-14/88). Army research inst of environmental medicine natick ma.

Schandl E. S. and Gorton M. P. (2004) A textural and geochemical guide to the identification of hydrothermal monazite: criteria for selection of samples for dating epigenetic hydrothermal ore deposits. *Econom. Geol.* **99**, 1027-1035.

Schettler G., Gottschalk M. and Harlov, D. E. (2011) A new semi-micro wet chemical method for apatite analysis and its application to the crystal chemistry of fluorapatite-chlorapatite solid solutions. *Am. Mineral.* **96**, 138-152.

Sha L. K. and Chappell B. W. (1999) Apatite chemical composition, determined by electron microprobe and laser-ablation inductively coupled plasma mass spectrometry, as a probe into granite petrogenesis. *Geochim. Cosmochim. Acta* **63**, 3861-3881.

Sidder G. B., Day W. C., Nuelle L. M., Seeger C. M. and Kisvarsanyi E. B. (1993) Mineralogic and fluid-inclusion studies of the Pea Ridge depositiron-rare-earth-element deposit, Southeast Missouri. **2039**, 205-216.

Sillitoe R. H. and Burrows D. R. (2002) New field evidence bearing on the origin of the El Laco magnetite deposit, northern Chile. *Econ. Geol.* **97**, 1101-1109.

Sillitoe R. H. (2003) Iron oxide–copper–gold deposits: An Andean view. *Miner. Deposita* **38**, 787–812.

Simon A. C., Kniping J., Reich M., Barra F., Deditius A. P., Bilenker L. and Childress T. (2018) Kiruna-Type Iron Oxide-Apatite (IOA) and Iron Oxide Copper-Gold (IOCG) Deposits form by a

combination of ignous and magmatic-hydrothermal processes:evidence from the Chilean Iron Belt. *SEG Special Publications*, **21**, 89-114.

Spear F. S. and Pyle J. M. (2002) Apatite, monazite, and xenotime in metamorphic rocks. *Rev. Mineral. Geochem.* **48**, 293-335.

Taghipour S., Kananian A., Harlov D. and Oberhänsli R. (2015) Kiruna-type iron oxide-apatite deposits, Bafq district, Central Iran: fluid-aided genesis of fluorapatite-monazite-xenotime assemblages. *Can. Mineral.* **00**, 1-17.

Tanaka T., Togashi S., Kamioka H., Amakawa H., Kagami H., Hamamoto T., Yuhara M., Orihashi Y., Yoneda S., Shimizu H., Kunimaru T., Takahashi K., Yanagi T., Nakano T., Fujimaki H., Shinjo R., Asahara,Y., Tanimizu M. and Dragusanu C. (2000) JNdi-1: a neodymium isotopic reference in consistency with LaJolla neodymium. *Chem Geol.* **168**,279–281.

Tepper J. and Kuehner S. (1999) Complex zoning in apatite from the Idaho Batholith; a record of magma mixing and intracrystalline trace element diffusion. *Amer. Min*. **4**, 581-595.

Toplis M. J. and Dingwell D. B. (1996) The variable influence of P_2O_5 on the viscosity of melts of differing alkali/aluminium ratio: Implications for the structural role of phosphorus in silicate melts. *Geochim. Cosmochim. Acta* **60**, 4107-4121.

Treloar P. J. and Colley H. (1996) Variations in F and Cl concentrations in apatites from magnetite-apatite ores in northern Chile, and their ore-genetic implications. *Mineral. Mag.* **60**, 285-301.

Velasco F. and Tornos F. (2009) Origen de las Pegmatitas de Magnetita-Apatito de la Mina Carmen del Fierro (Atacama, Chile). Macla n°11 septiembre 2009, revista de la sociedad española de mineralogía.

Velasco F., Tornos F. and Hanchar J. M. (2016) Immiscible iron-and silica-rich melts and magnetite geochemistry at the El Laco volcano (northern Chile): Evidence for a magmatic origin for the magnetite deposits. *Ore Geolg. Rev*. **79**, 346-366.

Watson E. B. and Green T. H. (1981) Apatite/liquid partition coefficients for the rare earth elements and strontium. *Earth Planet. Sci. Lett.* **56**, 405-421.

Webster J. D. and DeVivo B. (2002) Experimental and modeled solubilities of chlorine in aluminosilicate melts, consequences of magma evolution, and implications for exsolution of hydrous chloride melt at Mt. Somma-Vesuvius. *Amer. Mineral.* **87**-1046-1061.

Webster J. D. and Piccoli P. M. (2015) Magmatic apatite: A powerful, yet deceptive, mineral. *Elements* **11**, 177-182.

Williams P. J., Barton M. D., Fontbote L., de Haller A., Johnson D. A., Mark G., Marschik R. and Oliver N. H. S. (2005) Iron oxide-copper-gold deposits: Geology, space-time distribution, and possible modes of origin. Economic Geology 100^{Th} Anniversary Volume, 371–406.

Westhues A., Hanchar J., Le Messurier M. and Whitehouse M. (2017) Evidence for hydrothermal alteration and source regions for the Kiruna iron oxide-apatite ore (northern Sweden) from zircon Hf and O isotopes. *Geol.* **45**, 571–574.

Williams-Jones A. E. and Heinrich C. A. (2005) Vapor transport of metals and the formation of magmatic-hydrothermal ore deposits. Economic Geology 100Th Anniversary Volume, 1287-1312.

Williams-Jones A. E., Migdisov A. A. and Samson I. M. (2012) Hydrothermal mobilisation of the rare earth elements–a tale of "ceria" and "yttria". *Elements* **8**, 355-360.

Woodcock N. H. (1986) The role of strike-slip fault systems at plate boundaries. Royal Soc. (London) Philos. Trans. **A317**, 13-29.

Yanagisawa K., Rendon-Angeles J. C., Ishizawa N. and Oishi S. (1999) Topotaxial replacement of chlorapatite by hydroxyapatite during hydrothermal ion exchange. *Am. Mineral*. **84**, 1861-1869.

Zaitsev A. and Bell K. (1995) Sr and Nd isotope data of apatite, calcite and dolomite as indicators of source, and the relationships of phoscorites and carbonatites from the Kovdor massif, Kola peninsula, Russia. *Contrib. Mineral. Petrol*. **121**, 324-335.

Zeng L., Zhao X., Li X., Hu H., and McFarlane C. (2016) In situ elemental and isotopic analysis of fluorapatite from the Taocun magnetite-apatite deposit, Eastern China: Constraints on fluid metasomatism. *Amer. Min.***101**, 2468-2483.

Zhao X., Zhou M. and Gao J. (2015) In situ Sr isotope analysis of apatite by La-MC-ICPMS: constraints on the evolution of ore fluids of the Yinachang Fe-Cu-REE deposit, Southwest China. *Miner. Deposita* **50**, 871-884.

Zhu C. and Sverjensky D. A. (1991) Partitioning of F-Cl-OH between minerals and hydrothermal fluids. *Geochim. Cosmochim. Acta* **55**, 1837-1858.

2.8. TABLES

Table 1. Summary of EPMA analyses for apatite types in each deposit

	Carmen								Fresia								Mariela							
	n	*F-apatite*	n	*Cl-OH-F-apatite*	n	*Cl-OH-apatite*	n	*Cl-apatite*	n	*Cl-OH-F-apatite*	n	*Cl-OH-apatite*	n	*Cl-apatite*			n	*Cl-OH-F-apatite*	n	*Cl-OH-apatite*	n	*Cl-apatite*		
P_2O_5	28	36.1-42.9 *41.6*	5	39.5-40.6 *40.1*	14	35.8-40.1 *39.3*	3	39.4-40.2 *39.7*	64	38.8-42.3 *40.6*	21	37.4-40.8 *39.7*	6	39.7-40.1 39.8			12	40.1-41.2 *40.7*	11	41.0-41.4 *41.3*	30	39.2-41.3 *40.3*		
SiO_2	5	BDL-0.27 *0.12*	1	0.18 *0.18*	10	0.02-0.27 *0.08*	0		22	0.05-0.92 *0.28*	21	BDL-0.29 *0.16*	6	BDL-0.22 *0.09*			12	BDL-0.16 *0.05*	11	0.02-0.09 *0.06*	30	0.04-0.13 *0.08*		
Y_2O_3	28	BDL-0.19 *0.11*	5	0.08-0.11 *0.09*	14	BDL-0.14 0.09	3	0.07-0.10 *0.08*	64	BDL-0.15 *0.09*	21	0.04-0.13 *0.08*	6	BDL-0.14 *0.07*			12	BDL-0.04 *0.03*	11	BDL-0.04 *0.03*	30	BDL-0.04 *0.03*		
La_2O_3	28	BDL-0.14 *0.03*	5	BDL-0.018 *0.006*	14	BDL-0.06 *0.04*	3	BDL-0.03 *0.03*	64	BDL-0.18 *0.08*	21	BDL-0.15 *0.05*	6	BDL-0.16 *0.11*			12	BDL-0.07 *0.06*	11	BDL-0.07 *0.04*	30	BDL-0.07 *0.05*		
Ce_2O_3	28	0.035-0.36 *0.10*	5	BDL-0.08 *0.04*	14	0.03-0.11 *0.06*	3	BDL-0.09 *0.08*	64	BDL-0.41 *0.20*	21	BDL-0.33 *0.08*	6	BDL-0.34 *0.15*			12	0.04-0.16 *0.09*	11	0.07-0.14 *0.10*	30	0.06-0.15 *0.10*		
CaO	28	50.8-55.6 *54.6*	5	51.2-53.7 *52.9*	14	51.7-54.2 *53.4*	3	53.4-53.8 *53.6*	64	50.6-55.2 *53.8*	21	51.7-54.6 *52.7*	6	51.3-53.5 *52.3*			12	54.1-55.6 *54.6*	11	54.3-55.4 *54.8*	30	53.0-54.6 *53.6*		
MnO	28	BDL-0.07 *0.02*	5	BDL-0.03 *0.02*	14	BDL-0.03 *0.02*	3	BDL-0.02 *0.02*	64	BDL-0.04 *0.01*	21	BDL-0.03 *0.02*	6	BDL-0.04 *0.04*			12	BDL-0.03 *0.02*	11	BDL-0.02 *0.02*	30	0.01-0.04 *0.02*		
FeO	28	BDL-0.67 *0.05*	5	0.16-0.30 *0.19*	14	0.05-0.58 *0.30*	3	0.07-0.08 *0.07*	64	BDL-2.14 *0.48*	21	BDL-1.51 *1.16*	6	0.05-0.75 *0.34*			12	BDL-0.02 *0.02*	11	BDL-0.01 *0.01*	30	0.02-0.04 *0.03*		
SrO	10	0.03-0.06 *0.05*	1	0.24 *0.24*	10	0.06-0.12 *0.08*	0		22	0.03-0.09 *0.05*	21	0.03-0.16 *0.09*	6	0.14-0.31 *0.22*			12	0.03-0.10 *0.07*	11	0.03-0.07 *0.04*	30	0.03-0.18 *0.15*		
Na_2O	28	BDL-0.17 *0.04*	5	0.10-0.55 *0.35*	14	0.09-1.71 *0.34*	3	0.10-0.14 *0.11*	64	BDL-0.25 *0.08*	21	0.03-0.47 *0.19*	6	0.13-0.28 *0.20*			12	0.02-0.04 *0.03*	11	BDL-0.03 *0.03*	30	0.02-0.11 *0.09*		
SO_3	28	BDL-0.53 *0.06*	5	0.24-1.60 *1.11*	14	0.30-2.93 *0.84*	3	0.28-0.42 *0.34*	64	BDL-1.03 *0.18*	21	0.01-0.89 *0.14*	6	0.02-0.20 *0.07*			12	0.04-0.19 *0.07*	11	0.02-0.07 *0.05*	30	0.10-0.18 *0.14*		
F	28	2.99-3.73 *3.32*	5	0.03-0.60 *0.42*	14	BDL-0.22 0.10	3	0.03-0.04 *0.04*	64	0.11-2.62 *0.98*	21	0.03-1.28 *0.14*	6	0.03-0.25 *0.07*			12	0.40-1.25 *0.57*	11	0.03-0.15 *0.07*	30	BDL-0.14 *0.06*		
Cl	28	0.02-0.41 *0.13*	5	2.37-4.89 *3.58*	14	3.58-4.96 *4.16*	3	6.31-6.50 *6.40*	64	0.74-4.36 *2.41*	21	1.97-4.65 *3.56*	6	5.36-6.45 *6.11*			12	1.18-4.62 *3.87*	11	2.41-3.94 *2.94*	30	6.31-6.70 *6.46*		
O=F, Cl	28	1.29-1.58 *1.43*	5	0.79-1.33 *0.98*	14	0.87-1.14 0.98	3	1.44-1.48 *1.46*	64	0.74-1.40 *0.96*	21	0.78-1.06 *0.86*	6	1.22-1.52 *1.41*			12	0.79-1.21 *1.11*	11	0.57-0.92 *0.69*	30	1.44-1.53 *1.48*		
Total	28	89.9-100	5	96.6-99.3	14	95.4-98.7	3	98.8-99.1	64	95.4-99.8	21	95.1-98.8	6	97.2-99.5			12	98.4-99.6	11	98.0-99.3	30	98.4-101		

	98.8	*97.9*	*97.7*	*98.9*	*98.0*	*97.4*	*98.04*	*99.0*	*98.7*	*100*

Note: All concentrations are reported in wt%. The range indicates the minimum and maximum concentration and the average is shown in italics.
BDL=below detection limit; n= number of analyses.

Table 2. Summary of trace element concentrations for apatite types in each deposit determined by using LA-ICPMS.

	Carmen		Fresia			Mariela		
Apatite type	*F-apatite*	*Cl-OH-apatite*	*Cl-OH-F-apatite*	*Cl-OH-apatite*	*Cl-apatite*	*Cl-OH-F-apatite*	*Cl-OH-apatite*	*Cl-apatite*
Number of analysis	49	23	17	42	9	20	14	26
Mg	5.22-110	3.38-266	2.27-603	5.33-194	63.1-161	2.67-880	9.00-801	38.2-2690
	30.7	*69*	*36.9*	*35.3*	*118*	*152*	*284*	*504*
V	8.12-20.9	9.99-66.3	13.5-60.2	39.3-262	13.9-17.1	91.0-120	101-114	101-117
	13.3	*32.6*	*32.0*	*105.9*	*15.4*	*107.7*	*107.5*	*109.8*
Fe	505-1201	1840-9800	569-6510	4210-12450	889-1649	439-707	613-830	464-828
	687	*3353*	*1212*	*10014*	*1036*	*569*	*682*	*668*
Mn	55.7-310	86.5-278	37.9-168	130-300	243-341	36.1-97.2	57.7-161	104-190
	135	*127*	*76.2*	*194*	*292*	*70.5*	*93.4*	*171*
Ni	0.73-2.95	0.48-3.37	1.09-4.23	0.59-2.42	1.33-2.81	0.74-2.32	1.14-2.26	0.58-3.12
	1.88	*2.03*	*1.87*	*1.64*	*1.92*	*1.61*	*1.75*	*1.79*
Cu	BDL-2.39	BDL-24.7	0.38-13.9	0.98-11.9	0.67-1.35	0.41-6.81	0.12-6.30	0.12-20.2
	1.16	*5.14*	*1.92*	*2.29*	*0.98*	*2.06*	*2.99*	*3.51*
Zn	BDL-2.50	BDL-8.8	1.81-4.76	BDL-5.85	BDL-1.72	BDL-3.22	BDL	BDL-2.51
	1.46	*2.53*	*2.89*	*2.47*	*1.01*	*1.70*	*BDL*	*1.46*
As	43.7-168	54-387	103-232	201-299	63.7-107	117-319	119-332	78.9-240
	94.6	*199*	*177*	*239*	*81.2*	*189*	*240*	*123*
Rb	BDL-0.38	BDL-0.4	BDL-0.27	BDL-0.36	BDL-0.16	BDL-0.21	BDL-0.51	BDL-0.22
	0.14	*0.18*	*0.15*	*0.17*	*0.12*	*0.16*	*0.32*	*0.16*
Sr	61.1-236	410-1190	131-423	359-945	688-1182	96.7-640	122-950	396-1378
	120	*684*	*208*	*704*	*955*	*232*	*419*	*1173*
Y	480-1362	541-1570	692-1027	308-674	974-1030	69.9-91.6	82.6-94.1	75.5-89.0
	1005	*857*	*939*	*514*	*1003*	*83.9*	*87.8*	*82.9*
Zr	BDL-0.14	BDL-0.4	BDL-0.94	BDL-0.5	BDL-0.45	BDL-0.09	BDL-0.22	BDL-0.07
	0.06	*0.18*	*0.22*	*0.10*	*0.11*	*0.04*	*0.07*	*0.03*
Ba	BDL-3.27	1.36-13.8	BDL-7.55	1.55-3.23	2.32-4.55	0.23-1.78	0.12-2.15	1.54-2.83
	0.75	*5.03*	*1.02*	*2.43*	*3.39*	*0.64*	*0.91*	*1.95*
La	105-426	49.7-180	206-1429	29.1-109	1080-1460	301-391	339-381	347-398
	228	*89.6*	*1145*	*67.1*	*1361*	*353*	*364*	*371*
Ce	484-1685	350-843	768-2947	90.4-670	2528-3125	531-704	573-675	574-678
	991	*540*	*2558*	*320*	*2952*	*643*	*637*	*638*
Pr	88.4-284	87.2-229	118-373	24.4-76.2	310-371	45.5-59.5	50.1-59.4	50.8-57.3
	174	*133*	*322*	*54.6*	*355*	*54.9*	*54.9*	*54.3*
Nd	515-1494	595-1529	573-1536	143-421	1327-1547	155-201	171-195	168-188
	966	*858*	*1349*	*294*	*1476*	*182*	*183*	*179*

Sm	147-349	212-508	151-298	46.6-120	265-293	20.9-25.6	23.2-25.9	22.6-26.3
	245	*289*	*265*	*89.2*	*281*	*24.5*	*24.5*	*24.3*
Eu	5.48-16.5	10.9-33.7	3.25-14.4	0.47-1.84	12.4-14.83	2.44-3.99	2.88-3.57	2.99-3.69
	12.01	*20.4*	*9.81*	*1.27*	*13.9*	*3.29*	*3.28*	*3.40*
Gd	152-377	211-478	156-294	62.4-144	266-289	19.5-26.2	22.3-25.7	20.6-26.3
	264	*297*	*264*	*108*	*281*	*23.5*	*23.9*	*23.7*
Tb	16.2-50.4	27.1-58.6	23.4-37.6	9.16-20.8	34.5-36.7	2.30-2.97	2.54-3.00	2.31-2.86
	34.5	*39.5*	*33.6*	*15.8*	*35.5*	*2.68*	*2.74*	*2.63*
Dy	82.7-271	139-328	129-197	54.4-119	179-192	11-15.4	12.4-16.2	12.6-14.9
	188	*202*	*179*	*90.4*	*186*	*14.1*	*14.1*	*13.8*
Ho	14.9-53.5	22.3-63	25.0-37.8	10.8-23.02	35.6-38.6	2.41-3.19	2.56-3.16	2.38-3.10
	36.6	*35.6*	*34.5*	*17.7*	*37.4*	*2.88*	*3.00*	*2.79*
Er	35.2-130	46.4-150	59.8-91.2	2..4-57.5	88.3-93.4	5.87-8.01	7.24-8.34	6.27-8.11
	87.8	*78.3*	*82.4*	*43.1*	*90.0*	*7.35*	*7.79*	*7.25*
Tm	3.5-15.4	4.31-17.5	6.96-10.5	2.77-6.67	9.95-10.8	0.69-1.04	0.75-1.03	0.74-0.97
	10.3	*8.67*	*9.53*	*4.93*	*10.5*	*0.87*	*0.90*	*0.85*
Yb	18.3-85.6	17.6-99.1	37.3-58.8	12.4-33.1	55.2-60.4	4.04-6.31	5.00-5.96	4.41-6.26
	57.1	*43.9*	*52.6*	*25.4*	*57.6*	*5.43*	*5.58*	*5.22*
Lu	2.15-11.1	1.47-11.2	4.1-7.58	1.31-3.67	7.09-8.02	0.63-1	0.71-0.98	0.66-0.94
	7.42	*4.65*	*6.81*	*2.85*	*7.53*	*0.83*	*0.86*	*0.84*
Total REE	1772-5055	1851-4234	2259-7322	512-1565	6205-7468	1122-2416	1216-1384	1219-1408
	3301	*2640*	*6311*	*1133*	*7176*	*1365*	*1322*	*1327*
Pb	BDL-0.92	0.82-4.74	0.28-10.4	9.09-15.8	0.58-4.31	BDL-0.64	BDL-0.54	0.23-1.07
	0.29	*2.23*	*1.99*	*12.8*	*1.74*	*0.32*	*0.27*	*0.61*
Th	0.89-40.3	0.44-56	34.3-53.4	2.57-90	34.8-42.2	10.8-14.6	12.1-15.3	12.3-14.3
	22.0	*8.02*	*39.7*	*23.7*	*39.5*	*13.3*	*13.6*	*13.4*
U	0.06-7.41	0.02-5.51	0.41-1.99	0.11-1.4	1.25-1.58	0.44-0.83	0.51-0.81	0.50-0.75
	1.24	*0.90*	*1.10*	*0.32*	*1.40*	*0.64*	*0.65*	*0.61*
Hf	0.01-0.29	BDL-0.39	0.07-0.25	BDL-0.11	0.08-0.16	BDL-0.03	BDL-0.04	BDL-0.01
	0.16	*0.20*	*0.14*	*0.05*	*0.14*	*0.01*	*0.04*	*0.02*

Note: All the concentrations are reported in µg/g. The range indicates the minimum and maximum concentration and the average is shown in italics.
BDL=below detection limit.

Table 3. Apatite isotopic data for the Carmen, Fresia and Mariela deposits.

Deposit	Samples	Sm (ppm)	Nd (ppm)	$^{147}Sm/^{144}Nd$	± (abs stderr)	$^{143}Nd/^{144}Nd$	± (abs stderr)	Sr (ppm)	$^{87}Sr/^{86}Sr$	2SE	U-Pb age (Ma)*	ε_{Nd}	± (abs stderr)
Carmen	Ca-10	586	2645	0.1339	0.0006696	0.512888	0.000008	185	0.704633	0.000009	130.6 ±0.3	+5.9	0.15
	Ca-8	392	1942	0.1220	0.0006102	0.512906	0.000009	174	0.704736	0.000008	130.6 ±0.3	+6.5	0.18
	Ca-2	429	2211	0.1174	0.0005872	0.512900	0.000011	332	0.703817	0.000007	130.6 ±0.3	+6.4	0.22
	Ca-1	404	2100	0.1164	0.0005821	0.512893	0.000010	154	0.704170	0.000006	130.6 ±0.3	+6.3	0.20
Fresia	Fre-18	199	1266	NR		NR		196	NR				
	Fre-20	86	360	0.1447	0.0007236	0.512258	0.002561	753	0.705896	0.000005	130	-0.3	0.24
	Fre-5	200	1019	0.1187	0.0005937	0.512780	0.002564	291	0.704643	0.000009	130	+4.1	0.11
	Fre-19	101	400	0.1533	0.0007665	0.512635	0.002563	689	0.704107	0.000005	130	+0.7	0.20
Mariela	Ma-3	34	214	0.0950	0.0004749	0.512833	0.002564	356	0.704069	0.000005	130	+5.5	0.24
	Ma-11	35	224	0.0933	0.0004666	0.512849	0.002564	595	0.703983	0.000004	130	+5.9	0.14
	Ma-1	36	241	0.0900	0.0004501	0.512842	0.002564	243	0.703932	0.000005	130	+5.7	0.16
	Ma-0	27	193	0.0857	0.0004283	0.512850	0.002564	32	0.703895	0.000005	130	+6.0	0.25

Note: NR=not run

The U-Pb age for apatite grains from Carmen correspond to Gelcich et al. (2015)

$\varepsilon_{Nd}(t)= [((^{143}Nd/^{144}Nd)sample(t))/((^{143}Nd/^{144}Nd)CHUR(t)) -1]x10000$

2.9. FIGURES

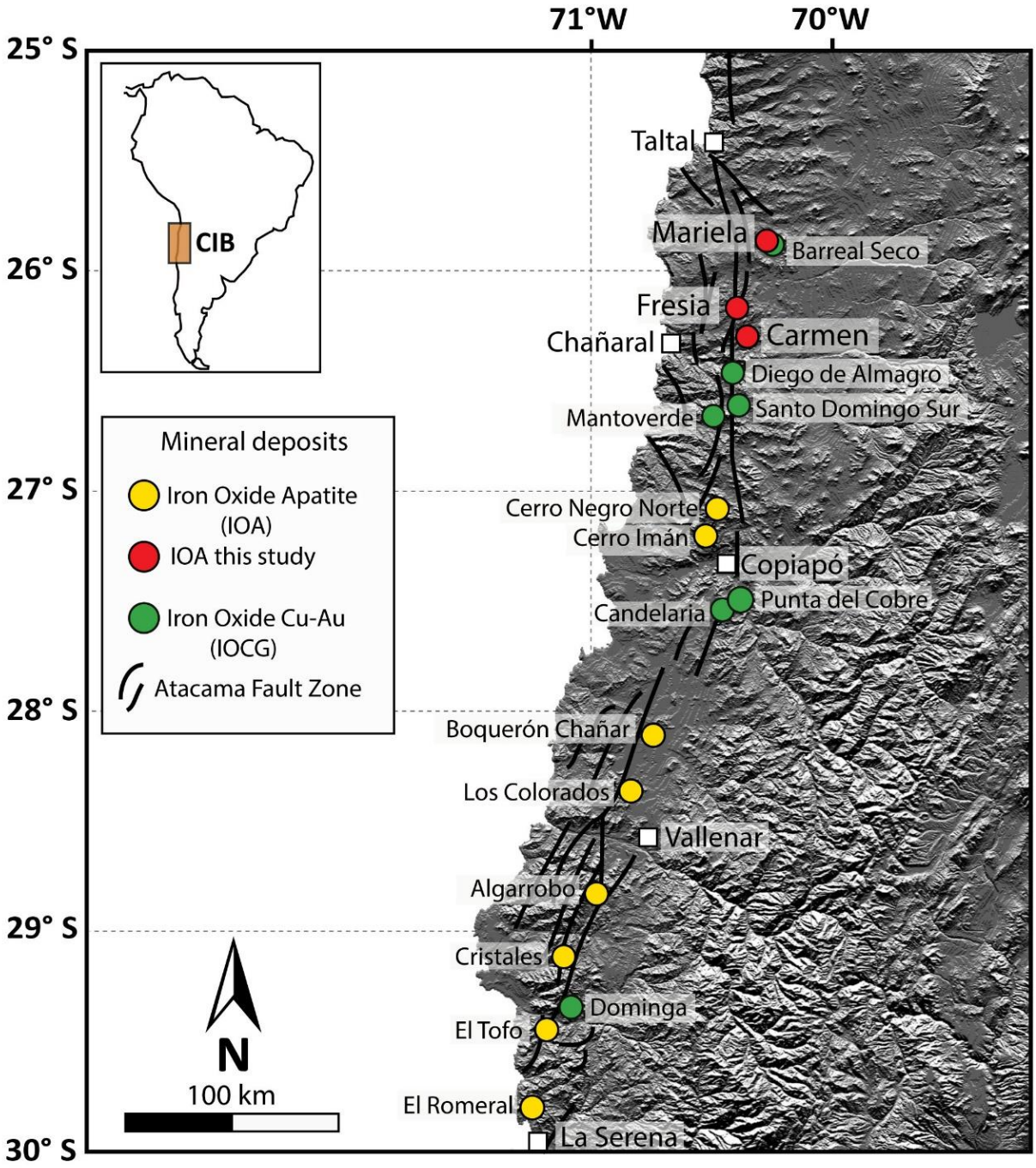

Figure 2. Map showing the location of IOCG and IOA deposits, including Carmen, Fresia and Mariela, within the Chilean Iron Belt and related to the Atacama Fault System. Modified from Barra et al. (2017).

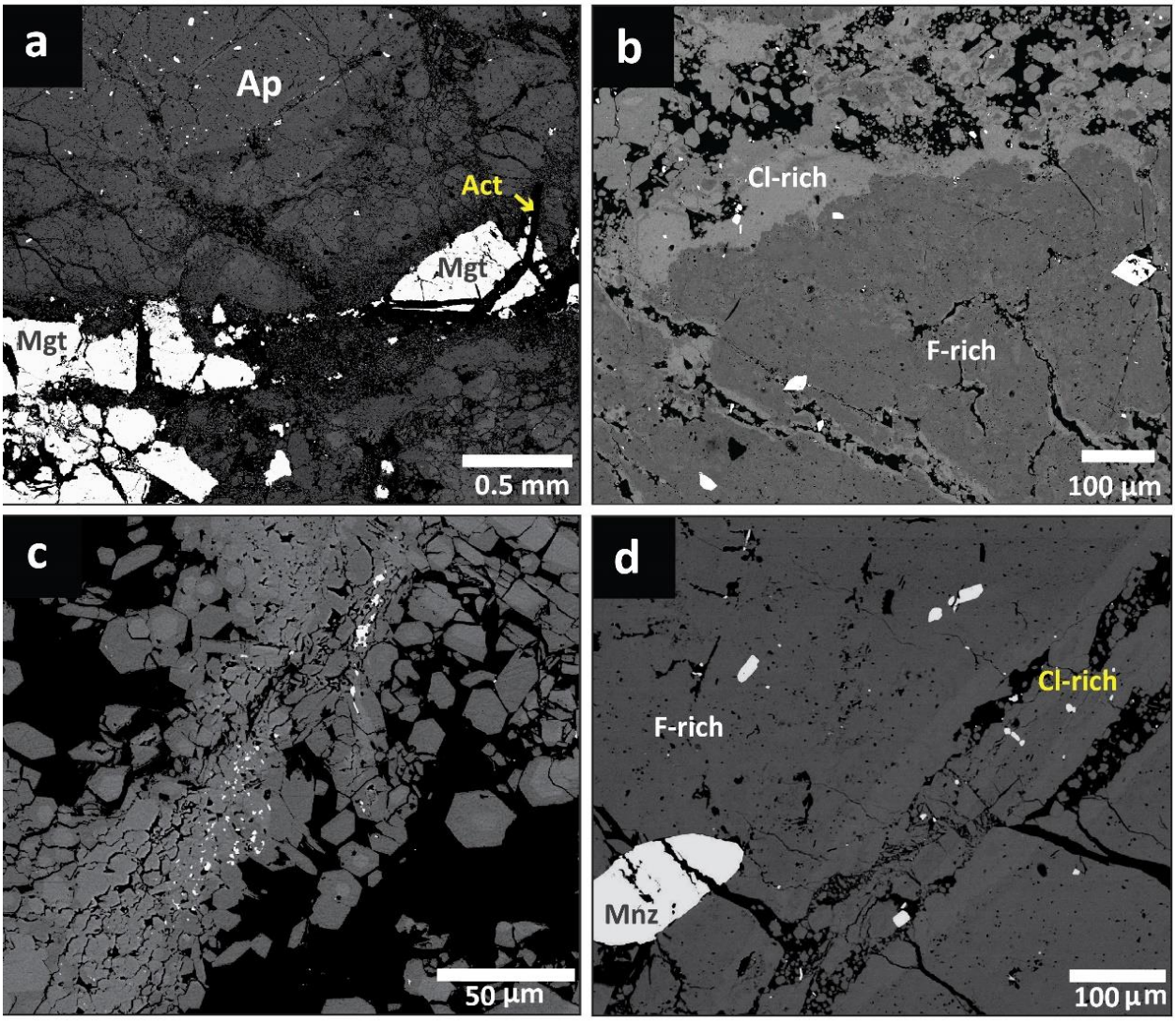

Figure 3. Back-scattered electron images of apatite textures from the Carmen deposit. (a) Apatite (Ap) with dark and light domains in contact with magnetite (Mgt) and actinolite (Act); (b) Zoned apatite with dark F-rich core and light Cl-rich rim. Note the sharp boundary between dark core and light rim. White mineral inclusions are monazite in (a) and (b); (c) Aggregate of euhedral apatite grains. Note the inverse zonation of some grains with light cores and dark rims. Most of the white mineral inclusions correspond to xenotime; (d) Light Cl-rich apatite filling a sealed fracture in F-rich apatite. White mineral inclusions are monazite (Mnz).

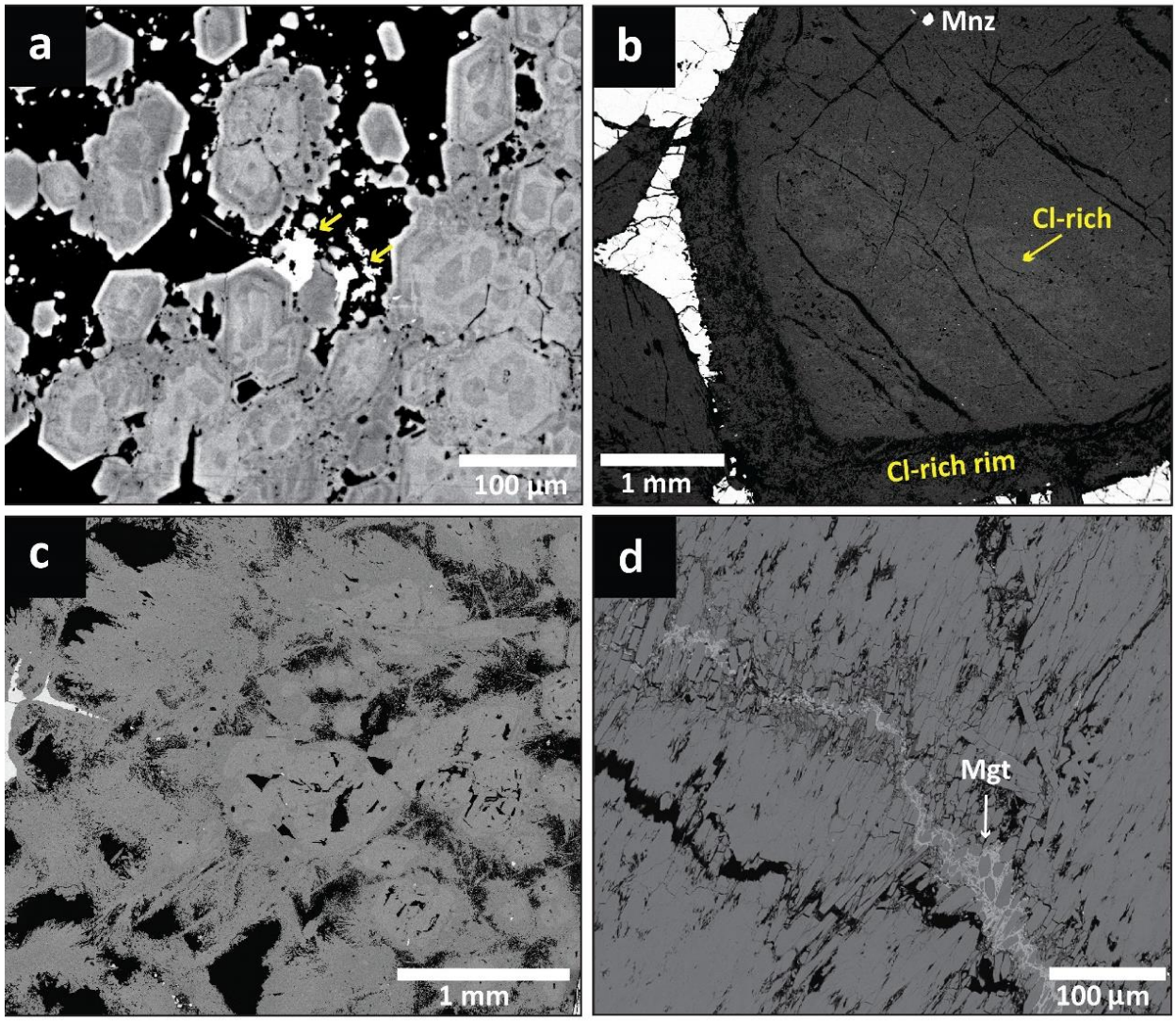

Figure 4.. Back-scattered electron images of apatite textures from the Fresia deposit. (a) Concentric zonation in apatite with a variable F-Cl-apatite composition. Yellow arrows indicate monazite grains; (b) Apatite grain core with Cl-rich domains and replaced in the rim by fine-grained Cl-rich apatite. Also shown is a monazite (Mnz) inclusion; (c) Complete replacement of primary(?) apatite by Cl-rich apatite. Note lighter prismatic cores grading to Cl-rich acicular and radial apatite; (d) Completely replaced apatite by-fine grained elongated Cl-rich apatite. The sample is crosscut by a thin magnetite (Mgt) veinlet.

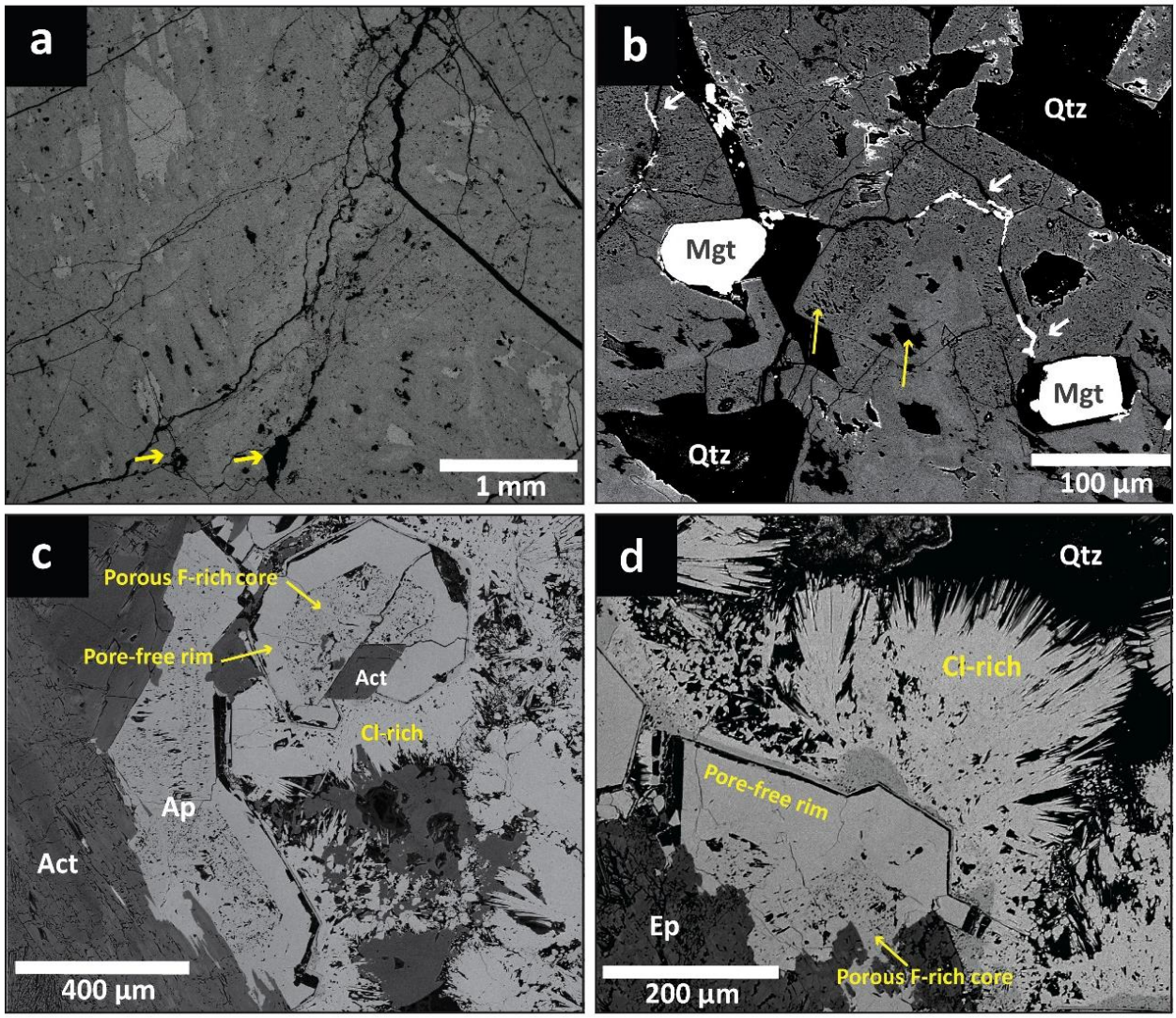

Figure 5. Back-scattered electron images of apatite textures from the Mariela deposit. (a, b) Coarse and porous grains from the apatite breccia matrix. Apatite displays a patchy zonation of light-dark domains of Cl-rich apatite. Yellow arrows in (a) and (b) indicate pores developed in apatite. In (b) note the largest pore-size in the light Cl-rich domain compared to the darker Cl-F domain. White arrows in (b) point to Cu-Cl minerals in fractures; (c, d) Euhedral apatite developed in cavities with porous cores and pore-free, pristine rims. A sharp contact between porous and pristine apatite also delimits different halogen compositions with F-rich cores compared to pristine rims of Cl-F composition that develop an external zone of Cl-rich apatite with acicular, radial habit.

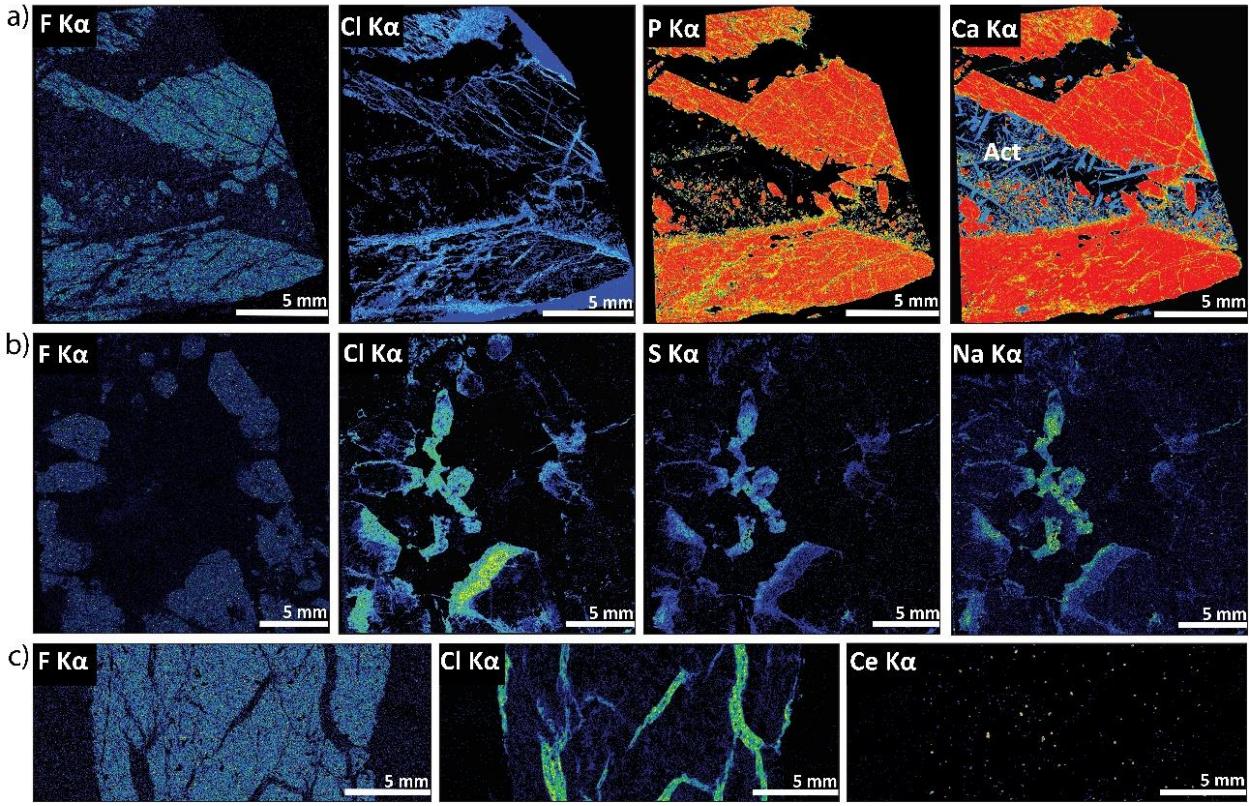

Figure 6. WDS maps for selected elements in apatite from the Carmen deposit. Abbreviations: Act= actinolite.

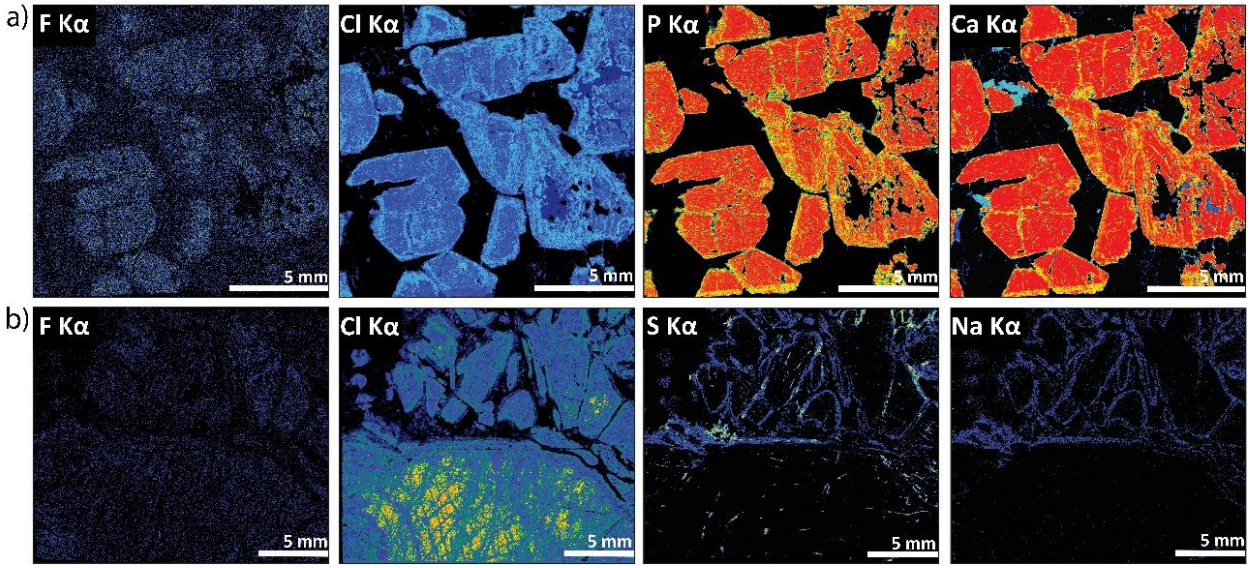

Figure 7. WDS maps for selected elements in apatite from the Fresia deposit.

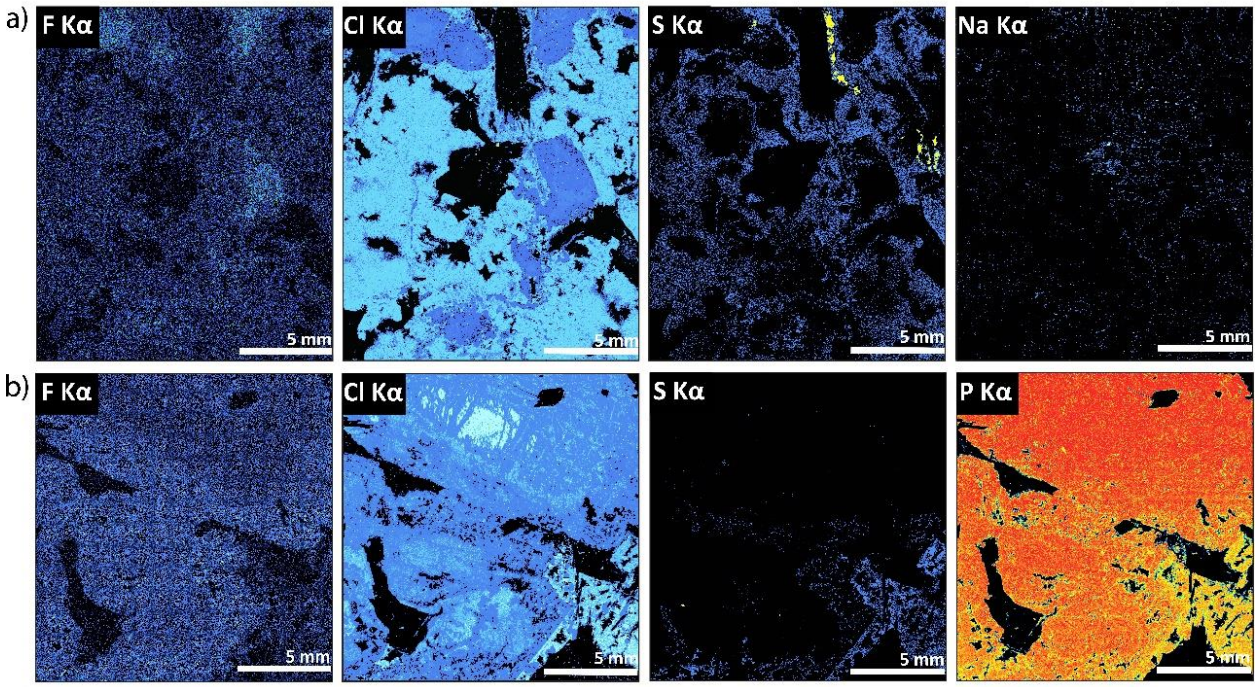

Figure 8. WDS maps for selected elements in apatite from the Mariela deposit.

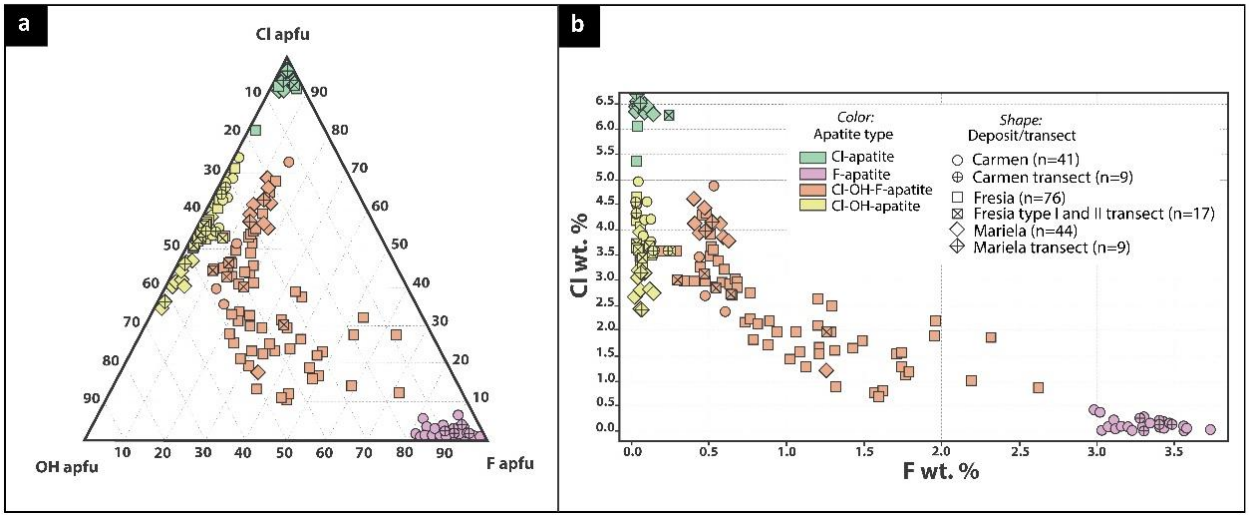

Figure 9. Halogen concentration determined by EPMA. Apatite type or domain based on XCl-apatite/XF-apatite and XCl-apatite/XOH-apatite ratios. (a) Ternary plot in terms of F-Cl-OH atomic proportions, calculated using the method by Piccoli and Candela (2002); (b) Divariant plot of F and Cl concentrations (wt%). The plot shows a negative correspondence between F and Cl.

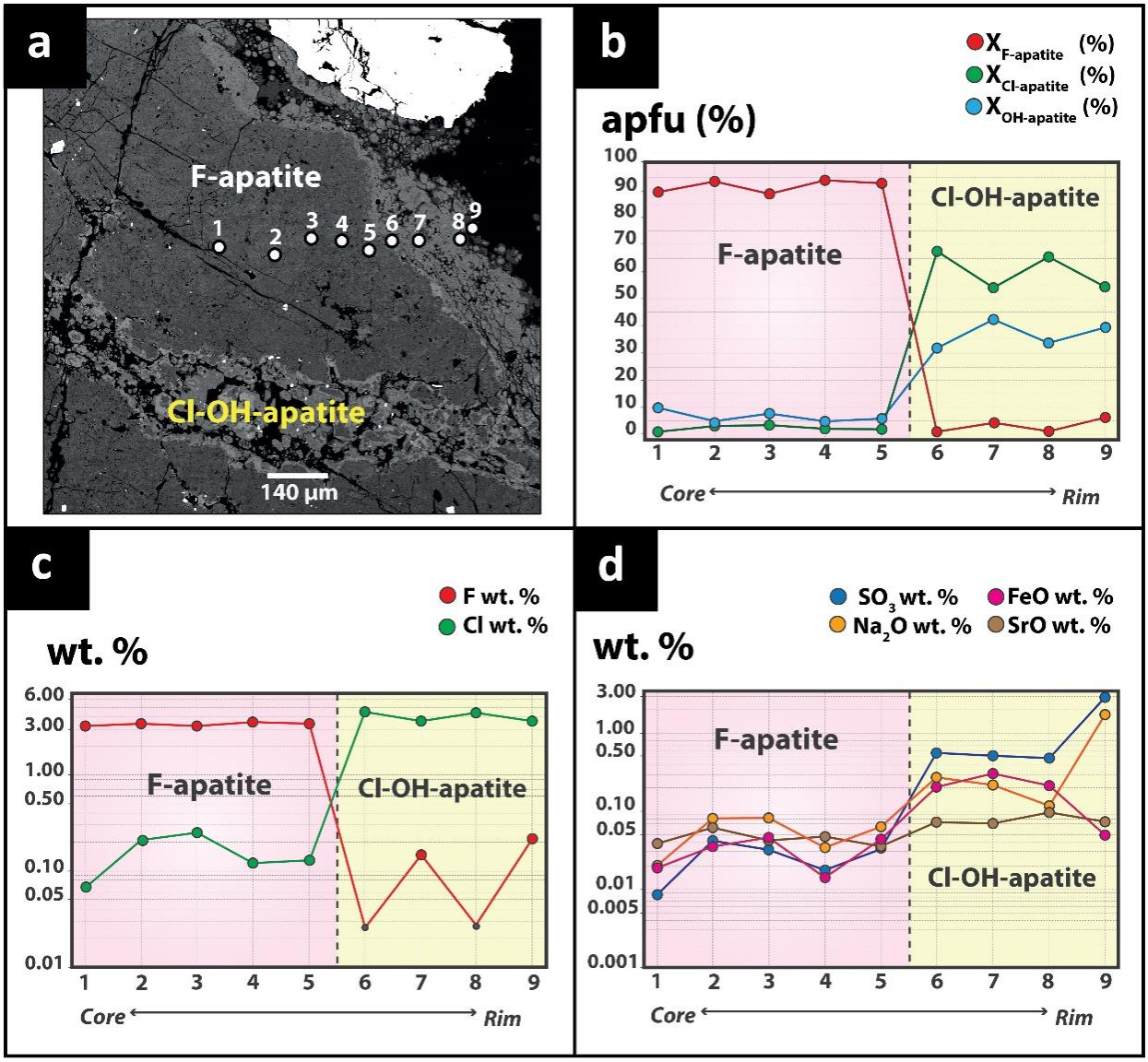

Figure 10. EPMA compositional traverses across zoned apatite from Carmen. (a) BSE-image showing the location of the analyzed points; (b) Traverse showing the F, Cl and OH atomic proportions represented as percentages (%). OH concentration was calculated based on Piccoli and Candela (2002). Two apatite types were defined based on the XCl-apatite/XF-apatite and XCl-apatite/XOH-apatite ratios: F- and Cl-OH apatite; (c) Traverse displaying the F and Cl concentrations (wt%). Black dots in the F concentration traverse indicate below detection limit values; (d) Traverse showing the SO3, Na2O, SrO and FeO concentrations (wt%).

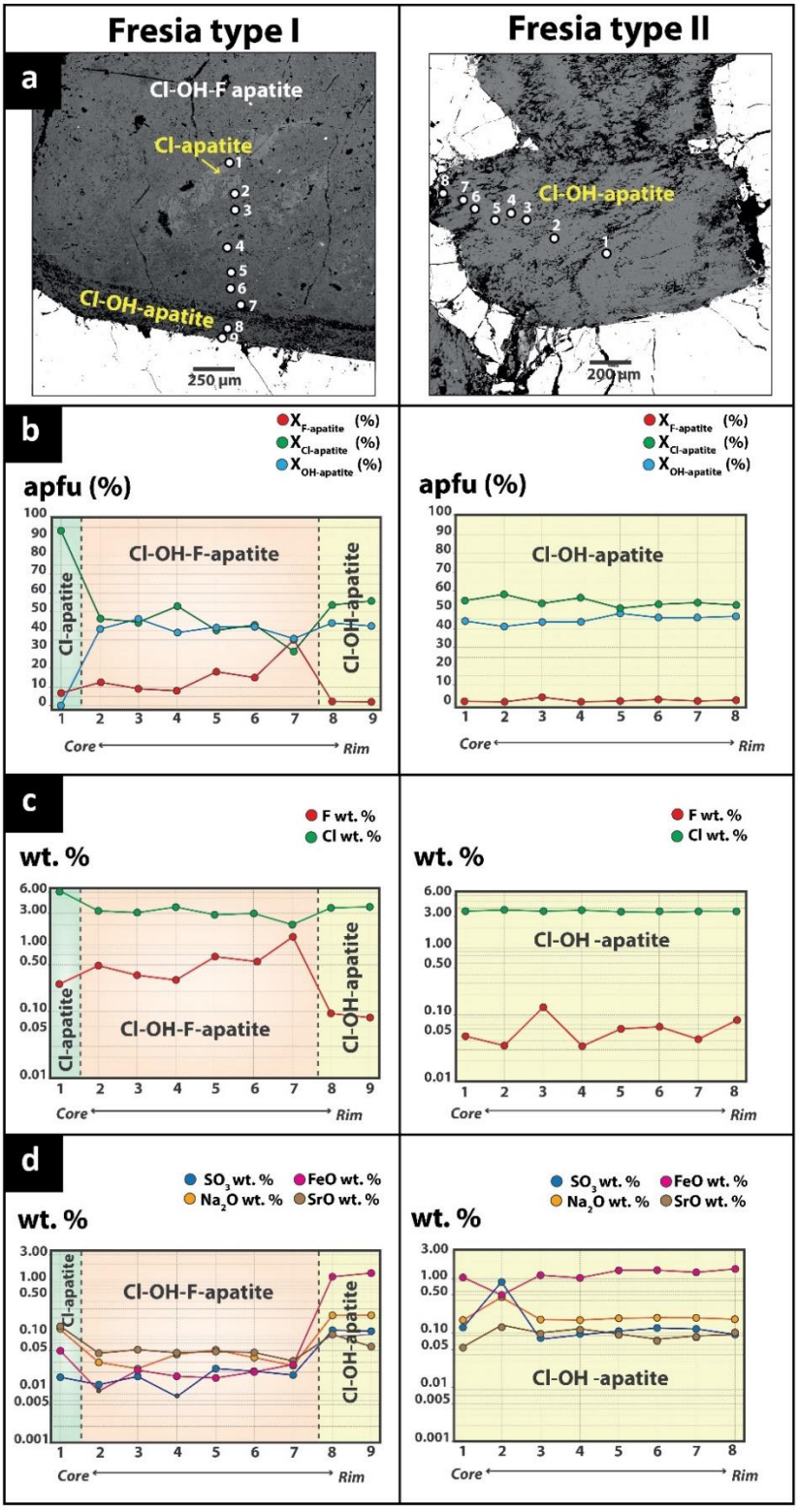

Figure 11. EPMA compositional traverses across zoned (Apatite type I) and unzoned apatite (Apatite type II) from Fresia. (a) BSE-image showing the location of the analyzed points; (b) Traverse showing the F, Cl and OH atomic proportions represented as percentages (%). Three apatite types are recognized: Cl-, Cl-OH-F- and Cl-OH-apatite; (c) Traverse illustrating the F and Cl concentrations (wt%); (d) Traverse showing the variation in the SO3, Na2O, SrO and FeO concentration (wt%). Black dots in the SO3 and FeO concentration traverse indicate below detection limit values.

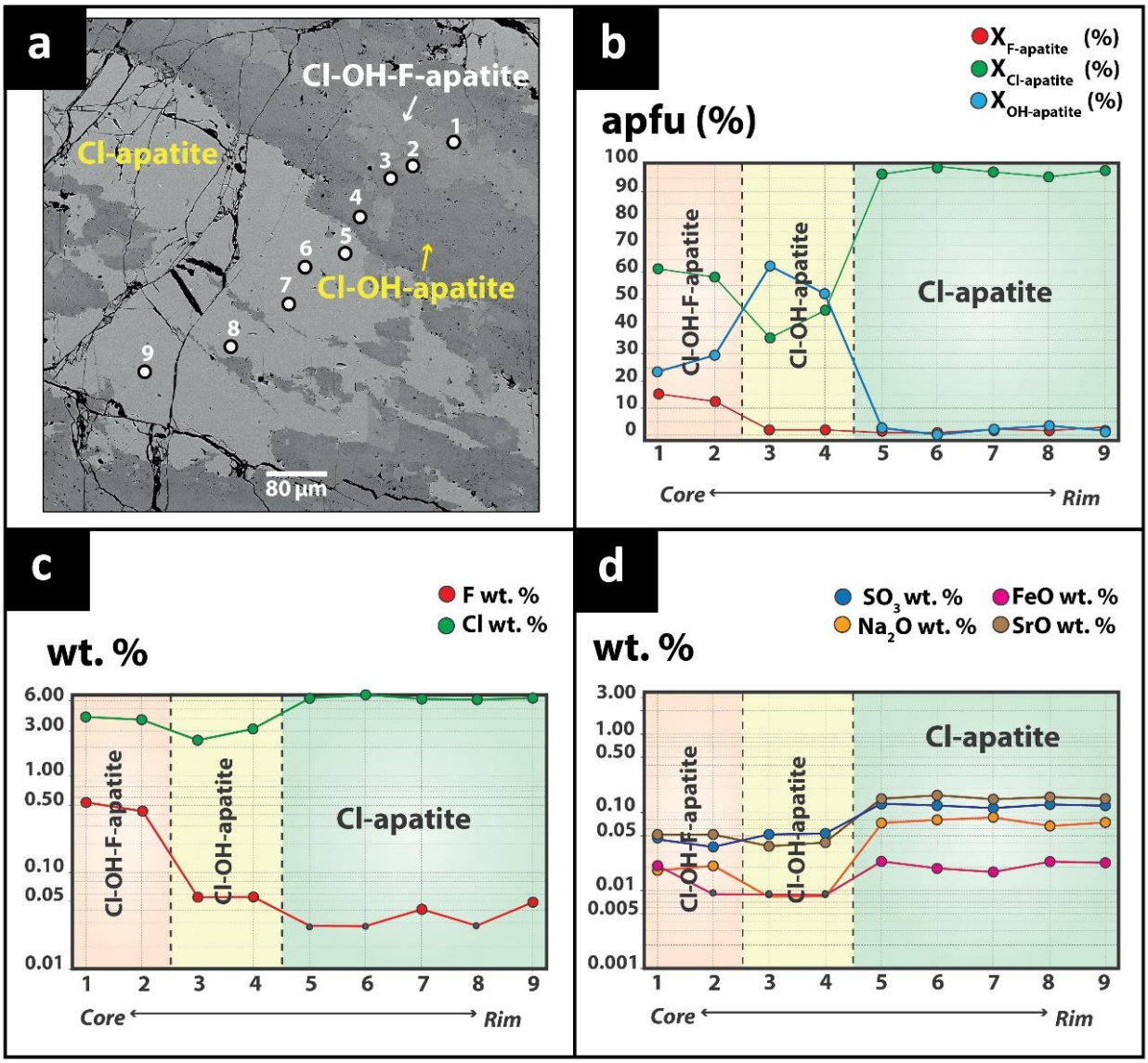

Figure 12. EPMA compositional traverses across zoned apatite from Mariela. (a) BSE-image showing the location of the analyzed points; (b) F, Cl and OH atomic proportions represented as percentages (%). The three apatite types or domains were defined: Cl-, Cl-OH-F- and Cl-OH apatite; (c) F and Cl concentrations (wt%) along the transect. Black dots in the F concentration traverse indicate below detection limit values; (d) Variation of the SO3, Na2O, SrO and FeO concentrations (wt%) along the transect. Black dots in the FeO and Na2O concentration traverse are below detection limit values.

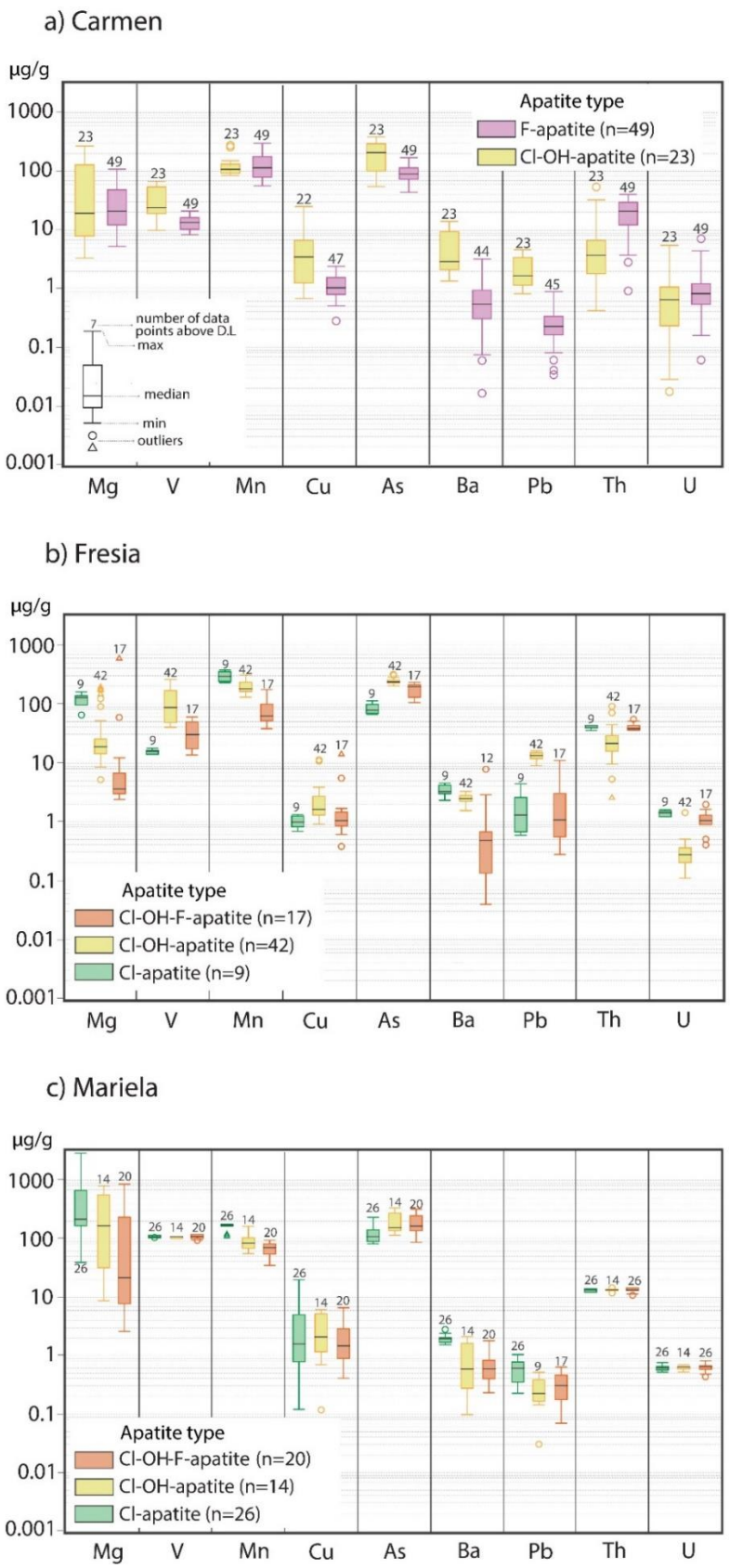

Figure 13. Trace element concentrations determined for apatite types from (a) Carmen, (b) Fresia and (c) Mariela.

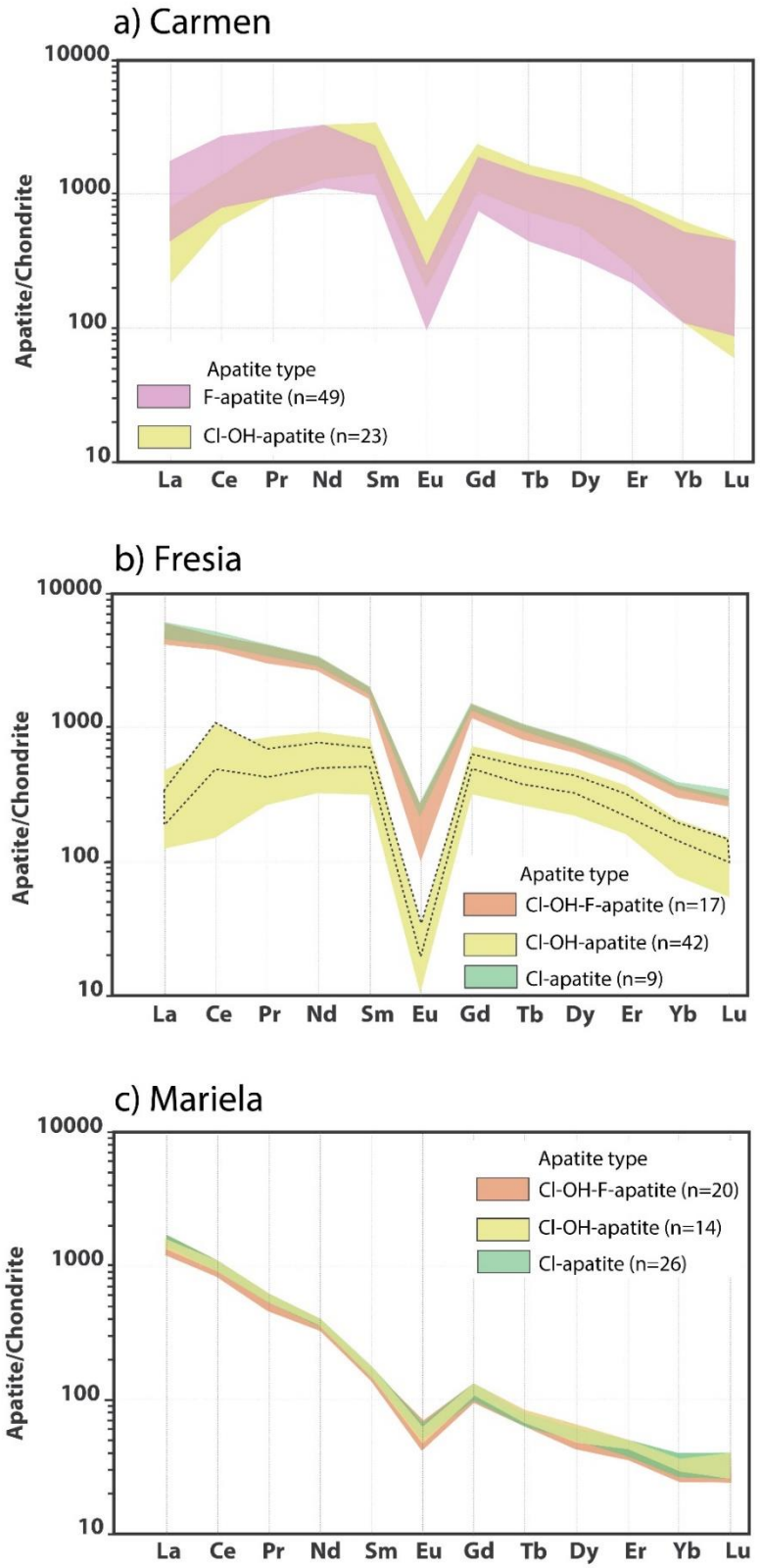

Figure 14. REE patterns for each apatite type or domain from (a) Carmen, (b) Fresia and (c) Mariela. In Fresia, Cl-OH-apatite from Apatite type I (area enclosed within dotted line) shows a decrease in the La concentration, while Cl-OH-apatite in Apatite type II (yellow area) is depleted in all LREE.

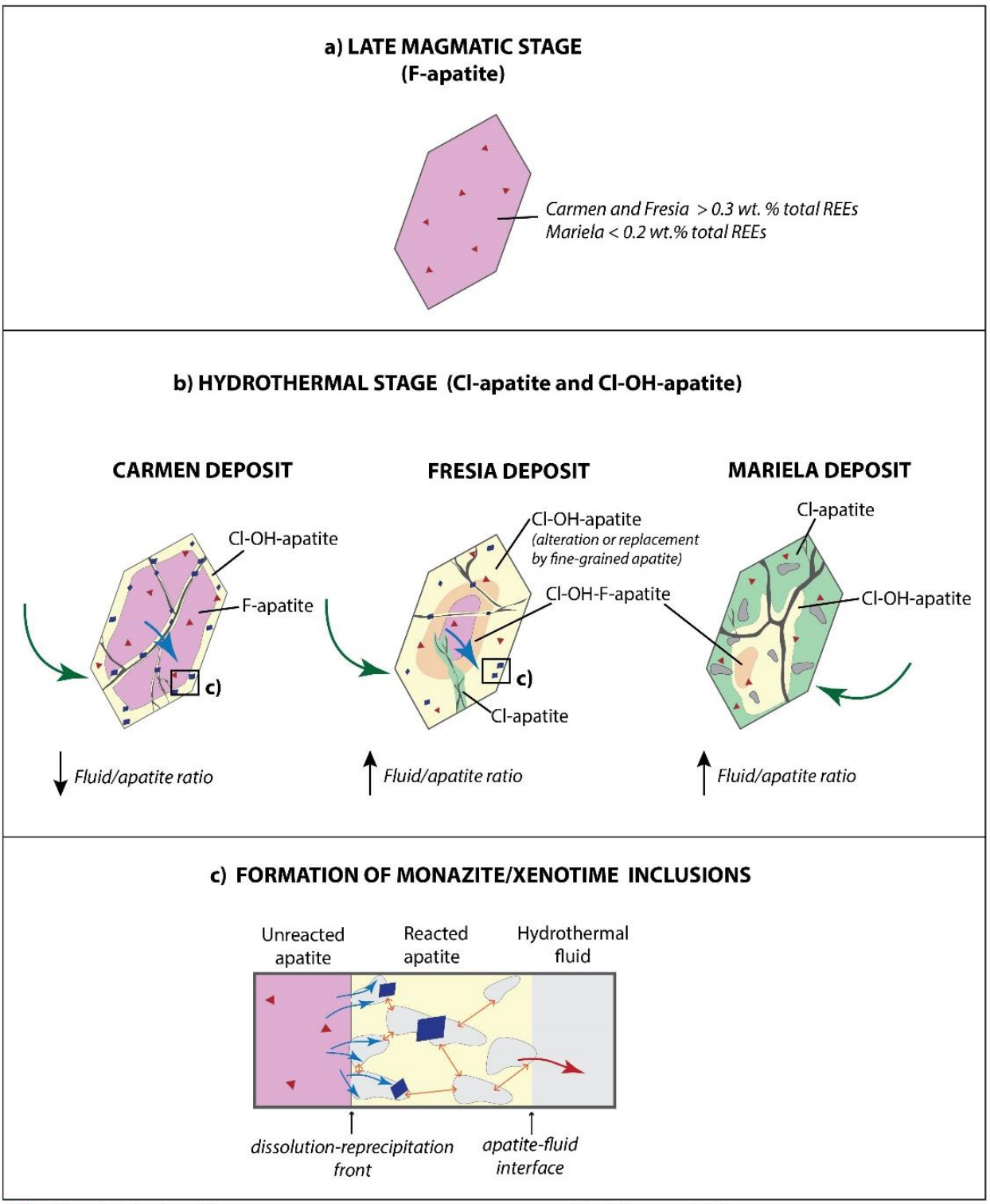
a) LATE MAGMATIC STAGE
(F-apatite)
Carmen and Fresia > 0.3 wt. % total REEs
Mariela < 0.2 wt.% total REEs
b) HYDROTHERMAL STAGE (Cl-apatite and Cl-OH-apatite)
CARMEN DEPOSIT
FRESIA DEPOSIT
MARIELA DEPOSIT
Cl-OH-apatite
F-apatite
c)
Fluid/apatite ratio
Cl-OH-apatite
(alteration or replacement
by fine-grained apatite)
Cl-OH-F-apatite
c)
Cl-apatite
Fluid/apatite ratio
Cl-apatite
Cl-OH-apatite
Fluid/apatite ratio
c) FORMATION OF MONAZITE/XENOTIME INCLUSIONS
Unreacted
apatite
Reacted
apatite
Hydrothermal
fluid
dissolution-reprecipitation
front
apatite-fluid
interface
Primary inclusions in apatite
Monazite/xenotime inclusions
Pores
Fractures
Hydrothermal fluid
Incorporation of Cl, OH, S, Na, Sr, Fe, Cu, Mg, Ba, Mn, V, Pb within apatite structure (As
and V only in Carmen and Fresia deposits)
Dissolution-reprecipitation process:
Dissolution of primary apatite and reprecipitation of [LREEs + Y + Th + U + PO4] as
monazite inclusions
Interconnected porosity :
Transport of LREE+Y+Th+U through pores
Loss of the primary apatite component (Ca, PO4) to the fluid

Figure 15. Schematic figure illustrating the magmatic and hydrothermal stages of apatite formation in the Carmen, Fresia and Mariela IOA deposits. (a) Magmatic stage with formation of F-apatite in Carmen and Fresia, and possibly in Mariela. Primary apatite is also enriched in LREEs. (b) Metasomatic stage (overprint), characterized by the replacement of F-apatite by Cl-apatite and/or Cl-OH-apatite. The extent of the alteration/replacement is related to the fluid/apatite ratio. Metasomatism also produces the enrichment of S, Na, Sr, Fe and to a lesser extent of some trace elements such as Mg, V, Mn, Cu, As, Ba and Pb in Cl-apatite. (c) Formation of monazite (and xenotime) inclusions by dissolution-reprecipitation processes. As the fluid percolated in F-apatite, generates porosity creating permeability (dissolution-reprecipitation front). The fluid-assisted transport of cations and anions through the pore network into apatite, promotes the nucleation and growth of monazite with P^{5+},Y^{3+}, $LREE^{3+}$, U^{+} and Th^{+}, whereas Ca^{2+} and some P^{5+} (and probably other components such as Na^{+} and Si^{4+}) are removed from apatite.

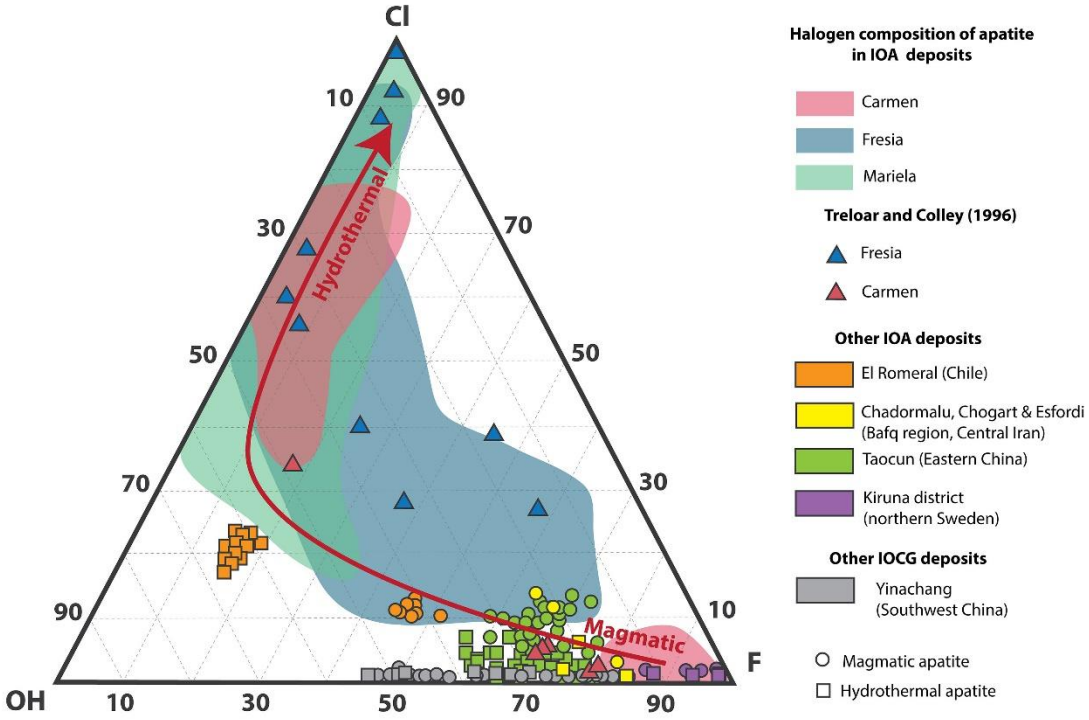

Figure 16. Ternary plot of the halogen content in apatite in terms of the F-Cl-OH atomic proportions. Fields are based on the Carmen, Fresia and Mariela EPMA data from this study (Fig. 8), in which F-rich compositions represent a magmatic, primary apatite and Cl- and OH-apatite hydrothermal/metasomatic apatite. Apatite analyses (magmatic: circles; hydrothermal: squares) from other IOA deposits are also shown. Data include: El Romeral, Chile (Rojas et al., 2018b); deposits of the Bafq region, Central Iran (Taguipour et al, 2015); Kiruna district, northern Sweden (Harlov et al., 2002); Yinachang, Southern China (Li and Zhou, 2015), Taocun (Zeng et al., 2016) and data from Carmen and Fresia (triangles) reported by Treloar and Colley (1996). See text for discussion.

CAPÍTULO 3

A review of magnetite geochemistry of Chilean Iron Oxide-Apatite (IOA) deposits and its implications for ore-forming processes

Gisella Palma[1*], Fernando Barra[1, 2], Martin Reich[1, 2], Adam C. Simon[3], Rurik Romero[2]

[1]Department of Geology and Millennium Nucleus for Metal Tracing Along Subduction, FCFM, Universidad de Chile, Santiago, Plaza Ercilla 803, Chile

[2]Andean Geothermal Center of Excellence (CEGA), FCFM, Universidad de Chile, Santiago, Plaza Ercilla 803, Chile

[3]Department of Earth Sciences, University of Michigan, 1100 North University Ave, Ann Arbor, Michigan, USA

Invited review
Ore Geology Reviews

Corresponding author: Gisella Palma
gipalma@ing.uchile.cl

ABSTRACT

Magnetite is the most important iron ore in iron oxide-apatite (IOA) deposits which represent the Cu-poor end-member of the iron oxide-copper-gold (IOCG) clan. Magnetite chemistry has been used as a petrogenetic indicator to identify the geological environment of ore formation and as a fingerprint of the source reservoir of iron. In this study, we present new textural and microanalytical EPMA and LA-ICP-MS data of magnetite from the El Romeral, Carmen, Fresia and Mariela IOA deposits located in the Cretaceous Coastal Cordillera of northern Chile. We also provide a comprehensive summary and discussion of magnetite geochemistry from Andean IOAs including Los Colorados, Cerro Negro Norte, El Romeral (Chilean Iron Belt) and the Pliocene El Laco IOA deposit located in the Central Volcanic Zone of the Chilean Andes. Microtextures coupled with geochemical data were used to define and characterize the occurrence of different magnetite types. Magnetite exhibits a variety of textural features including oscillatory zoning, colloform banding, re-equilibration textures, exsolution lamellae and symplectites. The magmatic vs. hydrothermal origin of the different magnetite types and the evolution of IOA deposits can be assessed using diagrams based on compatible trace elements. However, magnetite is very susceptible to hydrothermal alteration and to both textural and compositional re-equilibration during magmatic and superimposed hydrothermal events. Based on the data presented here, we conclude that V and Ga are possibly the most reliable compatible elements in magnetite to trace ore-forming processes in the Andean IOA deposits. Magnetite chemistry reveals different

conditions/events of formation for each IOA deposit ranging from high-temperature, low-oxygen fugacity (fO_2), purely magmatic (>600 °C) conditions; to lower temperature and higher fO_2 magmatic-hydrothermal (300-600 °C) to low-temperature hydrothermal (< 200-300 °C) conditions. Specifically, a continuous transition from high-temperature, low-fO_2 conditions in the deepest portions of the deposits to low-temperature, relatively higher fO_2 conditions towards surface are described for magnetite from El Laco. The new and compiled magnetite data from IOA deposits from the Chilean Iron Belt and El Laco are consistent with a transition from magmatic to hydrothermal conditions. The *flotation model* plausibly explains such features, which result from the crystallization of magnetite microlites from a silicate melt, nucleation and coalescence of aqueous fluid bubbles on magnetite surfaces, followed by ascent of a fluid-magnetite suspension along reactivated transtensional faults or through fissures formed during the collapse of the volcanic structure (El Laco). The decompression of the coalesced fluid-magnetite aggregates during ascent promotes the continued growth of magnetite microlites from the Fe-rich magmatic-hydrothermal fluid. As with any general genetic model, the *flotation model* allows variation and the definition of different styles or subtypes of IOA mineralization. The deeper, intrusive-like Los Colorados deposit shows contrasting features when compared with the Cerro Negro Norte hydrothermal type, the pegmatitic apatite-rich deposits of Carmen, Fresia and Mariela, and the shallow, subaerial deposits of El Laco. These apparent differences depend fundamentally on the depth of formation, the presence of structures and faults that trigger decompression, the composition of the host rocks, and the source and flux rate of hydrothermal fluids.

Keywords: magnetite textures, magnetite geochemistry, iron oxide-apatite deposits, IOA genetic models, Chile.

3.1. INTRODUCTION

Magnetite (Fe_3O_4) is a common accessory mineral in igneous, metamorphic and sedimentary rocks and can form under a wide range of temperature and pressure conditions. It can also become concentrated in large quantities to form ore deposits such as banded iron formations (e.g., Angerer et al., 2012), magmatic Fe-Ti-V oxide (e.g., Zhou et al., 2005), iron skarns (e.g., Nadoll et al., 2014, 2015), iron oxide-copper-gold (IOCG) and Kiruna-type iron oxide-apatite (IOA) deposits (e.g., Williams et al., 2005).

Iron oxide-apatite deposits represent the Cu-poor end-member of the IOCG clan (Sillitoe, 2003) and are an important source of Fe. Iron oxide-apatite mineralization is dominated by low-Ti magnetite, which can be accompanied by variable amounts (1-50% modal) of apatite, actinolite, pyroxene, epidote and sulfides (Williams et al., 2005). On the other hand, IOCG deposits are mined for their Cu content, but in some cases Au, U, REE, P, Co, Bi and Nb are relevant by-products (Hitzman et al., 1992; Sillitoe, 2003; Williams et al., 2005; Groves et al., 2010; Barton, 2014). IOCG mineralization is characterized by Cu-Fe sulfides (chalcopyrite and minor bornite), Cu oxides and abundant iron oxides (magnetite and/or specular hematite). Hydrothermal alteration is represented by sodic-calcic (albite, actinolite, epidote) and potassic (biotite, orthoclase) assemblages with minor chlorite, sericite and late calcite. Regardless of the high concentration of iron oxides in IOCGs, they are rarely mined for Fe.

Both IOCG and IOA deposits occur globally with reported ages ranging from Archean (e.g., Carajás Province, Brazil; de Melo et al., 2017), early Proterozoic (e.g., Kiruna district, Sweden and Olympic Dam district, Australia; Westhues et al 2017a,b; Apukhtina et al., 2017), middle Proterozoic (e.g., Pea Ridge and Pilot Knob deposits, USA, and Cloncurry district, Australia; Rusk et al., 2010, Day et al., 2016; Childress et al., 2016), Cretaceous (e.g., Los Colorados, El Romeral, Candelaria and Mantoverde, Chile; Benavides et al., 2007; Rieger et al., 2010; 2012; Knipping et al., 2015a,b; Rojas et al., 2018a) and Pliocene (e.g., El Laco, Chile; Maksaev et al., 1988; Nyström and Henriquez, 1994; Naranjo et al., 2010).

In Chile, most of the IOCG and IOA deposits occur spatially and temporally associated with one another in the Jurassic−Early Cretaceous Chilean Iron Belt (CIB) within the Coastal Cordillera of northern Chile between latitudes 25° and 31°S (**Figure 17**). These deposits occur closely associated with coeval Mesozoic intrusions and are structurally controlled by the arc-parallel Atacama Fault System (AFS) (Sillitoe, 2003; Williams et al., 2005). As the youngest-known IOCG−IOA province in the world, mostly unaffected by metamorphism and deformation (Sillitoe, 2003), the CIB is an ideal area to study the processes involved in the formation of IOA and IOCG deposits and to refine the current genetic model. Noteworthy, the Pliocene El Laco volcanic complex (ELVC), located further north (23°48´S) in the high Andes, hosts the youngest, least altered, and best preserved IOA deposit discovered to date (Naranjo et al., 2010; **Figure 17**). Within an area of ~35 km^2, six magnetite ore bodies have been described at El Laco (i.e., Laco Norte, Laco Sur, San Vicente Alto, Rodados Negros, Cristales Grandes and San Vicente Bajo). These ore bodies display remarkable volcanic and subvolcanic features that have fueled the controversy regarding a magmatic (immiscibility model) or metasomatic origin for IOA deposits (Frutos and Oyarzún, 1975; Nyström and Henriquez 1994; Sillitoe and Burrows, 2002; Naranjo et al., 2010; Tornos et al., 2016; Velasco et al., 2016; Ovalle et al., 2018).

It is well known that IOCG deposits are mostly formed by hydrothermal processes (Sillitoe, 2003; Williams et al., 2005; Mumin et al 2007; Groves et al., 2010; Barton, 2014). However, the origin of IOA deposits remains controversial and, historically, two contrasting "classic" hypotheses have been proposed. The first hypothesis comprises a purely magmatic origin involving the separation of an immiscible Fe-P-rich melt from a silicate melt with the subsequent intrusion and crystallization of an Fe-rich ore body at upper crustal levels (e.g., Nyström and Henriquez, 1994; Naslund et al., 2002; Chen et al., 2010; Velasco et al., 2016). The second hypothesis involves a purely hydrothermal origin where the magnetite ore is formed by metasomatic replacement of host rocks by Fe-rich fluids sourced from magmatic or non-magmatic sources (e.g., Rhodes and Oreskes, 1995, 1999; Sillitoe and Burrows, 2002; Barton and Johnson 1996, 2004; Pollard, 2006; Dare et al, 2015; Westhues et al., 2016, 2017a,b). Most of the current debate regarding the origin of IOA deposits has been centered on El Laco, where some researchers have argued that the magnetite ore bodies preserve purely igneous/volcanic features, such as *pahoehoe*- and *aa*-like lava flows, different degrees of vesicularity, contorted flow layering, spherulitic and dentritic magnetite, and vertical structures interpreted as gas escape tubes (Nyström and Henríquez, 1994; Naslund, et al., 2002). However, others have interpreted these textures as relicts of the andesite lava flows that have been replaced by hydrothermal iron oxides, based on magnetite veins and breccias, and hydrothermal alteration assemblages observed around the magnetite bodies (Rhodes et al., 1999; Sillitoe and Burrows, 2002).

Over the past few years, and in light of a renewed interest in magnetite geochemistry studies, a novel genetic model was proposed by Knipping et al. (2015a,b) to explain the formation of IOA deposits. By using a combination of field observations, trace element geochemistry and Fe and O stable isotopes composition in magnetite grains from Los Colorados, those authors propose that IOA deposits formed by a combination of igneous and magmatic-hydrothermal processes. In their *flotation model,* microlites of magnetite crystallized from a silicate melt triggering bubble nucleation, forming a magnetite-fluid suspension that transported magnetite to shallow depths through pre-existing fault structures that are reactivated by crustal extension. This new model not only reconciles the two opposing genetic hypotheses (liquid immiscibility vs. metasomatic replacement), but also provides a plausible explanation for the formation of spatially associated IOCG deposits as part of the same evolving system (Reich et al., 2016; Barra et al., 2017; Simon et al., 2018). A genetic connection between IOA and IOCG deposits of the Coastal Cordillera of northern Chile has been previously proposed, where IOA (sulfide-poor) deposits may represent the roots or deep portion of IOCG (sulfide-rich) systems (Espinoza et al., 1996; Sillitoe, 2003).

The current discussion about the genesis of IOA deposits is based on, among other proxies, the major and trace element geochemistry of magnetite, which is the modally dominant mineral in all IOA deposits. Both electron microprobe analysis (EMPA) and laser ablation inductively coupled plasma mass spectrometry (LA-ICP-MS) have been used to measure the chemical composition of major and trace elements in magnetite, respectively. While EMPA allows for a low-micron size beam (<5 μm) to analyze a limited number of elements, e.g., Mg, Al, Ca, Ti, V, Cr and Mn at detection limits of tens to hundreds of ppm (e.g., Dupuis and Beaudoin, 2011), LA-ICP-MS allows *in-situ* measurements on 20-50 μm spots of a large number of trace elements (>40) at ppm to sub-ppm levels. These analytical advances have resulted in a growing interest in the study of magnetite as a petrogenetic indicator and as tool to identify past geological environments of ore formation or as a fingerprint of mineral deposit types (Dupuis and Beaudoin, 2011; Dare et al., 2012, 2014; Nadoll et al., 2012, 2014; Huang et al., 2018, 2019; Huang and Beaudoin, 2019). In particular, Knipping et al. (2015a,b) documented distinct chemical zoning in magnetite grains from Los Colorados IOA deposit, where cores are enriched in Ti, Al, Mn and Mg indicating crystallization from a silicate melt. In contrast, magnetite rims show a pronounced depletion in these elements, consistent with magnetite grown from a Fe-rich magmatic-hydrothermal aqueous fluid (Knipping et al., 2015b).

After Knipping et al. (2015a,b), several geochemical and textural studies have been carried out on magnetite and other mineral phases (pyrite, actinolite, apatite) in the Andean IOCG and IOA deposits including: El Romeral (Rojas et al., 2018a,b); Los Colorados (Bilenker et al., 2016; Reich et al., 2016; Deditius et al., 2018; La Cruz et al., 2019; Knipping et al., 2019a); El Laco (Ovalle et al., 2018; La Cruz et al., 2019; La Cruz et al., under review); Cerro Negro Norte (Salazar et al., 2019); Carmen, Fresia and Mariela (Palma et al., 2019); Candelaria (Rodriguez et al., under review); Mantoverde (Childress et al., accepted). The chemical composition of magnetite grains from Cerro Negro Norte, El Romeral and El Laco deposits reflect their formation conditions, revealing systems that evolved from high-temperature purely igneous/magmatic conditions at depth to lower temperature magmatic-hydrothermal conditions at shallow depths (Ovalle et al., 2018; Rojas et al., 2018b; Salazar et al., 2019; La Cruz et al., under review). The data presented in such studies have been described as consistent with the *flotation model* to explain the origin of Andean IOA deposits.

In this contribution we present a review of the extensive magnetite chemical data gathered during these last few years on Andean IOA and IOCG deposits. In addition, we present and discuss new micro-textural, EPMA and LA-ICP-MS data for magnetite from the El Romeral, Carmen, Fresia and Mariela IOA deposits. The trace element composition of magnetite and several discrimination diagrams (e.g., Dupuis and Beaudoin, 2011; Nadoll et al., 2014) are used here to fingerprint the texturally different magnetite types observed in each deposit and provide new constraints on the formation of these deposits. We also demonstrate how magnetite compositional data should be closely inspected and complemented with micro-textural observations to avoid misinterpretations. Finally, we propose a mechanism of formation for the apatite-rich (~20-50 % modal), pegmatitic IOA subtype of Carmen, Fresia and Mariela.

3.2. GEOLOGICAL SETTING

3.2.1. The Chilean Iron Belt, Coastal Cordillera of northern Chile (25-31°S)

In the Chilean Iron Belt (CIB), IOCG and IOA deposits formed during the Late Jurassic to Early Cretaceous under an extensional tectonic regime (Mariana-type subduction) in response to subduction rollback at the retreating convergent margin (Mpodozis and Ramos 1989; Grocott and Taylor, 2002). The extensional conditions during this period resulted in the formation of a subsiding trench-parallel magmatic arc and a sedimentary marine back-arc basin (Mpodozis and Ramos, 1989; Scheuber et al., 1994; Brown, 1995; Charrier et al., 2007; Ramos, 2010). The magmatic arc was dominated by tholeiitic basaltic magmas, gabbros and mafic dikes associated with calc-alkaline andesites and basaltic andesite flows (Mpodozis and Ramos, 1989; Scheuber et al. 1994; Oliveros et al., 2006). The plutonic complexes, emplaced into broadly contemporaneous arc and intra arc-volcanic products, comprise hornblende-biotite gabbros, diorites, tonalites, granodiorites and minor granites (Dallmeyer et al., 1996).

The dominant structural feature of the CIB is the Atacama Fault System (AFS), a >1,000 km long, trench-parallel, strike-slip fault zone (**Figure 17**) that resulted from the synchronous opening of the South Atlantic Ocean basin and oblique subduction beneath western South America (Uyeda and Kanamori, 1979; Scheuber and Andriessen, 1990; Brown, 1993; Scheuber and González, 1999). This fault system consists of a set of branches marked by prior ductile shear zones and later brittle faults with NNW-, N- and NNE-orientations (Brown, 1995; Dallmeyer et al., 1996; Scheuber and González, 1999; Grocott and Taylor, 2002). The AFS was characterized by a sinistral movement during the Jurassic to Early Cretaceous, followed by dextral shearing during the Late Cretaceous and final vertical displacements as a result of changes in the plate configuration and in the convergence vector of the subducting plate (Scheuber and Andriessen, 1990; Scheuber and González, 1999).

The Central Andean IOCG-IOA province of northern Chile and southern Peru formed over a period of ca. 65 Ma (Chen et al., 2013). The IOCG and IOA ore systems are apparently diachronous and both appear to have accompanied the eastward migration of arc magmatism (Sillitoe, 2003). Although IOCG mineralization began to develop during the Middle Jurassic (165-155 Ma), it was during the mid-Cretaceous (ca. 130-100 Ma) that most IOA deposits were formed (Oyarzún et al., 2003; Chen et al., 2013; Barra et al., 2017). Iron oxide-apatite deposits are usually hosted by mafic-to-intermediate sub-aerial volcanic units (e.g., La Negra Formation: Middle to

Late Jurassic or Punta del Cobre Formation: Late Jurassic to Early Cretaceous) or broadly contemporaneous gabbro to granodiorite intrusions (Sillitoe, 2003). Most of the IOCG and IOA deposits of the Coastal Cordillera of northern Chile occur in the vicinity of the AFS usually related to second order faults (Sillitoe, 2003; Cembrano et al., 2005).

The Andean IOA deposits are characterized by the occurrence of massive magnetite ore bodies, veins, lens-like bodies, mantos and breccias with actinolite, minor apatite (usually <1% modal) and traces of sulfides such as pyrite and chalcopyrite. About 50 IOA deposits, including seven large deposits (>100 Mt high grade Fe-ore) occur within the Coastal Cordillera between 25 and 31°S (Nyström and Henríquez, 1994). Some deposits were mined in the past for iron (e.g., El Algarrobo, El Tofo, Carmen) or phosphates (Mariela) and only a few are currently under production (Los Colorados and Cerro Negro Norte). Some small IOA deposits including Carmen, Fresia and Mariela display pegmatitic, comb-like and breccia-like textures with ~20-40% modal apatite, pointing to high volatile/melt conditions in the apical parts of IOA deposits (Treloar and Colley, 1996; Palma et al., 2019). In some areas of the Carmen and Fresia deposit, large apatite crystals (up to 50 cm long) have crystallized perpendicular to the magnetite vein walls (Treloar and Colley, 1993, 1996; Palma et al., 2019). In the Mariela IOA deposit, apatite with minor actinolite and magnetite occurs as a breccia matrix around chlorite-epidote altered intrusive fragments (Palma et al., 2019). In the central and eastern part of Mariela, pegmatitic apatite and actinolite crystals can reach up to 3 m long (Río Tinto internal report, 2001).

Iron oxide-copper-gold (IOCG) mineralization comprises specular hematite or magnetite massive ore bodies, veins, mantos, stockworks and breccia, with abundant chalcopyrite, pyrite and lesser bornite. Iron mineralization occurs accompanied by hydrothermal albite, K-feldspar, chlorite, sericite, epidote, carbonates, quartz, actinolite and minor scapolite (Hitzman et al., 1992; Sillitoe, 2003; Williams et al., 2005; Groves et al., 2010). The largest IOCG deposits in Chile are the Mantoverde (hematite rich-type) and Candelaria (magnetite rich-type) deposits, both with over 400 Mt of Cu with a 1% ore grade (Marschik et al., 2000; Marschick and Fontboté, 2001; Benavides et al., 2007; Rieger et al., 2010, 2012; del Real et al., 2018) (**Figure 17**; **Table 4**). The main geological features of the IOA deposits discussed in this study including Los Colorados, Cerro Negro Norte, El Romeral, Carmen, Fresia, Mariela and El Laco, and both Candelaria and Mantoverde IOCG deposits, are summarized in **Table 4**.

3.2.2 El Laco IOA deposit, Chilean Altiplano

The El Laco Volcanic Complex (ELVC) is located at elevations of 4,600-5,200 m a.s.l. in the Plio-Pleistocene volcanic arc of the Central Volcanic Zone of the Andes, northern Chile (**Figure 1**7). This volcanic complex comprises a cluster of andesitic to dacitic volcanic structures with NW-trending fissural emission centers and secondary craters associated with ring-shaped structures around Pico Laco (Naranjo et al., 2010). Within the ELVC the magnetite ore bodies occur interbedded between lava flows and pyroclastic rocks, spatially associated with the pre-existing subvertical annular collapse structures and with secondary craters (Frutos and Oyarzún, 1975; Naranjo et al., 2010). The El Laco IOA deposit is composed of six massive magnetite ore bodies including the lava-like flows of Laco Norte, Laco Sur and San Vicente Alto; the N-W-trending tabular bodies of Rodados Negros and Cristales Grandes; and the dome-shaped bodies of San Vicente Bajo (Nyström and Henríquez, 1994; Naranjo et al., 2010; Ovalle et al., 2018; **Table 4**). The magnetite ore bodies are mainly composed of magnetite (~98 % modal)—with minor

hematite-goethite formed by the supergene alteration of magnetite outcrops—apatite, diopside, scapolite, apatite, REE-rich and iron phosphates (Naranjo et al., 2010; Ovalle et al., 2018). Total estimated resources are 733.9 Mt with an average ore grade of 49.2 % Fe (CAP Minería 2016 Annual Report), making it one of the largest Chilean iron deposits. Many textures and morphologies have been described for the massive magnetite ore bodies including vesicular textures mainly at shallow levels, breccia bodies with fragments of andesite and magnetite matrix, vertical chimney-like cavities lined with euhedral magnetite crystals and intergrown with diopside and apatite, and lava-like flows dominated by a *pahoehoe* and locally *aa* texture (Nyström and Henríquez, 1994; Naslund et al., 2002; Sillitoe and Burrows, 2002; Ovalle et al., 2018).

Recently, Ovalle et al. (2018) studied drill core samples from the Laco Norte, Laco Sur and Extension Laco Sur ore bodies, and reported a similar structure and clear relationship among ore bodies, breccias and hydrothermal alteration. The main part of the massive magnetite bodies correspond to the shallower zone (~0-65 m) zone characterized by magnetite with lava-like textures (> 90% modal), minor diopside and scarce apatite. The surface part of this zone contains magnetite with vesicular textures and a high degree of hematite and goethite alteration, while the deepest part of this zone is dominated by the weakly to moderate magnetite replacement by hematite and late gypsum veinlets that crosscut and fill open spaces in massive magnetite. A transition zone (65-145 m) between shallow magnetite and magnetite breccias is characterized by massive magnetite with abundant coarse-grained diopside grains that vary in size from few tens of micrometers to a few millimeters. The deepest zone (150-200 m) comprises magnetite breccia bodies with andesite fragments replaced by fine-grained diopside within a magnetite-diopside matrix. In the Pasos Blancos area, high-temperature diopside-magnetite-quartz–rich contact metamorphic aureoles associated with the emplacement of the tabular magnetite ore bodies were reported by Vivallo et al. (1994) and, at depth, an alkali-calcic alteration assemblage is particularly well-developed. This alteration has been interpreted as the result of subvolcanic contact metasomatism (Rhodes et al., 1999; Naranjo et al., 2010) and comprises intense scapolitization and diopside formation that partially to pervasively replaced andesitic fragments immersed in a magnetite-diopside-scapolite matrix. The most visible expression of the hydrothermal alteration in the complex corresponds to steam-heated zones marked by a penetrative leaching of the andesite rocks and an alteration assemblage dominated by tridymite, cristobalite, alunite and jarosite, forming silicic vein-like structures and irregular hydrothermal breccia bodies (Vivallo et al., 1994; Sillitoe and Burrows, 2002; **Table 4**). Large exhalative deposits represented by gypsum-rich mounds, which appear to be fossil fumaroles, are located at discrete centers of emission spatially associated with NW-trending collapse structures that controlled the late hot-spring-like geothermal activity at ELVC (Vivallo et al., 1994).

3.3. SAMPLES AND METHODS

3.3.1. Sources of data and samples

This study is based on micro-textural and geochemistry data of magnetite previously published from different deposits of the Chilean Iron Belt and El Laco, and new data from the Carmen, Fresia, Mariela and El Romeral deposits. The magnetite chemical data compiled from the literature correspond only to EPMA in some cases, such as El Romeral (Rojas et al., 2018b), Mantoverde (Simon et al., 2018), Candelaria (Rodriguez et al., under review); and both EMPA and

LA-ICP-MS in other cases, such as Los Colorados (Knipping et al., 2015a,b; Deditious et al., 2018), Cerro Negro Norte (Salazar et al., 2019) and El Laco (Ovalle et al., 2018; La Cruz et al., under review).

Regarding the new microtextural and magnetite chemical data, a total of twelve magnetite-bearing samples from Carmen (Ca-2, Ca-7, Ca-8 and Ca-9), Fresia (F-2, F-5, Fre-4 and Fre-10) and Mariela (Ma-1, Ma-10, Ma-11 and Ma-21) were selected for SEM, EPMA and LA-ICP-MS analysis. Samples from Carmen and Fresia were collected from stockpiles, whereas those from Mariela were collected from inside the abandoned underground mine. The selected samples are representative of the main styles of mineralization observed in the magnetite ore bodies. A brief description of the main magnetite mineralization styles in each deposit is presented in the SM file and shown in **Figures B1-3**. In addition, two samples from El Romeral (Rom-094 and Rom-149), collected from drill cores, were also analyzed in this study. Sample Rom-094 represents the main magnetite ore body (Cerro Principal) at depth of ~347 m, whereas sample Rom-149 was collected from a contact zone between the magnetite ore body and the host andesite at shallow levels (~10 m). Both samples contain the main and most abundant textural magnetite types (Type-I and -II) identified in the deposit (Rojas et al., 2018b). These samples were studied to determine possible variations in the magnetite trace element composition with depth.

3.3.2. SEM and EPMA

Carbon coated polished sections were studied by using a FEI Quanta 250 SEM at the Andean Geothermal Center of Excellence (CEGA) in the Department of Geology, Universidad de Chile. The SEM was used to characterize different microtextures, mineral inclusions and exsolutions in magnetite, and to select sites for both EPMA and LA-ICP-MS analyses. Backscattered-electron (BSE) images were obtained using a filament current of 80 µA, an accelerating voltage of 15 and 20 kV, a beam intensity of ~1 nA, a spot size of 5 µm, and a working distance of 10 mm.

Major and minor element concentrations in magnetite from Carmen, Fresia, Mariela and El Romeral were determined by using a JEOL JXA-8230 Superprobe at the LAMARX Laboratory of the Universidad Nacional de Cordoba, Argentina. EPMA data for El Romeral sample Rom-094 was previously reported in Rojas et al. (2018b). Magnesium, Al, Si, Ca Sc, Ti, V, Cr, Fe, Mn, Co, Zn and Nb concentrations were quantified in the magnetite grains. Operation conditions included an accelerating voltage of 15 kV, a beam current of 20 nA and a counting time of 20 s for each element. A focused beam of ~1 µm was used to avoid hitting any mineral inclusion or exsolution lamellae within magnetite grains. X-ray lines, crystals and standards used for the analyses are summarized in **Table B0**. In addition to quantitative spot analyses, qualitative wavelength dispersive X-ray maps (WDS) of Mg, Al, Si, Ca, Ti, V, Fe and Mn were obtained for magnetite grains from Carmen, Fresia and Mariela by using an accelerating voltage of 15 kV, a beam current of 150 nA and a counting time of 30-40 ms/point. Interference corrections were carried out for V concentrations since Ti Kβ affects the V Kα signal.

Single-spot microanalyses were also undertaken in some Fe-Ti oxides intergrown with magnetite from Mariela, in order to properly identify these mineral phases. Analysis was performed

using the same analytical conditions and standards as for magnetite, with the only exception of Ti for which a titanite standard was used (**Table B0**).

3.3.3. LA-ICP-MS

LA-ICP-MS measurements were carried out on selected magnetite grains from Carmen, Fresia, Mariela and El Romeral by using a Teledyne-Photon Machines Analyte G2 193-nm ArF excimer laser ablation coupled to a Thermo Fisher Scientific iCAP-Q quadrupole mass spectrometer at the CEGA Mass Spectrometry Laboratory, Department of Geology, Universidad de Chile. Thick sections (200 µm) were first examined by using SEM, followed by EPMA of major elements. The mass spectrometer was tuned for maximum sensitivity, low-oxide formation rate (ThO/Th<0.005) and low double-charged ion formation ($^{22}M/^{44}Ca<0.0005$). Considering that He gas was used as a carrier and Ar as a plasma gas, interferences with these elements were evaluated when choosing representative isotopes for each element. Thus, although ^{56}Fe is more abundant than ^{57}Fe, the latter was measured to determine the iron content because ^{56}Fe has an isobaric interference with ArO.

Each spot involved a 60 s ablation time and 20 s background measurement using a laser repetition rate of 8 Hz, a fluence of 4.0−6.0 J/cm^2 and a 30–40 µm spot diameter. The dwell time was 0.01 s for all the monitored isotopes: ^{23}Na, ^{24}Mg, ^{27}Al, ^{29}Si, ^{31}P, ^{39}K, ^{44}Ca, ^{45}Sc, ^{52}Cr, ^{55}Mn, ^{59}Co, ^{60}Ni, ^{63}Cu, ^{66}Zn, ^{73}Ge, ^{85}Rb, ^{88}Sr, ^{51}Y, ^{90}Zr, ^{93}Nb, ^{95}Mo, ^{107}Ag, ^{111}Cd, ^{120}Sn, ^{121}Sb, ^{138}Ba, ^{139}La, ^{140}Ce, ^{208}Pb, ^{232}Th and ^{238}U with the exception of ^{51}V, ^{49}Ti and ^{69}Ga that was 0.02 s.

The concentration of Fe in magnetite grains, determined by EPMA, was used as the internal standard for calibration. The USGS GSE-1G reference material was used for magnetite analysis and the USGS GSD-1G as a secondary standard. The USGS GSD-1G standard (Jochum et al., 2005) was used as a unknown to determine analytical accuracy and precision. Thirty-seven analyses were performed on the GSD standard (**Table B1**) in which the trace element concentrations obtained present a small relative difference (up to 15.9%) with those reported by Jochum et al. (2005). The analytical precision determined using the GSD standard is within 2 to 5% for most analytes. LA-ICP-MS analyses were carried out using the sample-standard bracketing method with measurements of the NIST-610 glass (x 1), GSE-1G (x 2), GSD-1G (x 1), and then 20-25 unknowns, followed by measurements of GSD-1G (x 1), GSE-1G (x 2) and NIST-610 glass (x 1). Data reduction was performed by using the Iolite software (Paton et al., 2011), which calculates detection limits after Longerich et al. (1996). Heterogeneities in signal profiles due to the possible presence of micro- to nanometer-sized mineral inclusions within magnetite zones were avoided.

3.4. RESULTS

3.4.1 Magnetite microtextures

Several types of magnetite in Andean IOA deposits have been identified based on microtextural observations, as reported in previous studies. A brief description of the main

magnetite types at Los Colorados (Knipping et al., 2015a,b; Deditius et al., 2018), El Romeral (Rojas et al., 2018b), Cerro Negro Norte (Salazar et al., 2019) and El Laco (Ovalle et al., 2018) are summarized below. In addition, SEM observations of magnetite from the El Romeral, Carmen, Fresia and Mariela deposits are also described here and shown in **Figures 18-21**. Microtextural descriptions are shown in **Table 5**.

Los Colorados

Knipping et al. (2015a,b) defined three main textural types of magnetite (Types 1, 2 and 3) from the western massive magnetite tabular ore body at Los Colorados. These magnetite types correspond to three different domains observed within single magnetite grains and include an inclusion-rich core (Type-1), a transition zone (Type-2) and inclusion-poor rims (Type-3). Type-1 magnetite is Ti-rich with abundant polycrystalline microinclusions randomly distributed within grain cores (Knipping et al., 2015a,b; **Figure B4-A**). The most abundant inclusions (≥10 μm) correspond to actinolite, clinopyroxene, titanite and an unspecified Mg-Al-Si phase. Noteworthy is the presence of halite-saturated fluid inclusions (<10 μm), which were interpreted as evidence of a saline fluid involved in the formation of magnetite in Los Colorados (Knipping et al., 2015b). Magnetites Type-2 and 3 show decreasing Ti concentrations, when compared to Type-1 cores. Furthemore, Deditius et al. (2018) studied late-stage magnetite veinlets in the diorite intrusion that are texturally more diverse than magnetite grains from the western magnetite ore body, and represent growth of magnetite under purely hydrothermal conditions (Knipping et al., 2015a,b). Deditius et al. (2018) defined three different types of hydrothermal magnetite (Type-X, -Y and -Z; **Figure B4**). Magnetite-Z is the most abundant of these three types and is characterized by oscillatory zoning (**Figure B4-D**). Magnetite-X also shows sector zoning in euhedral grains with trace element-rich BSE-dark grey areas and trace element-poor BSE-light zones (**Figure B4-B**). In addition, Magnetite-Y is characterized by a zonal, "tooth-like" texture and sector zoning (Deditius et al., 2018; **Figure B4-C**). Transmission electron microscopy (TEM) analyses of magnetite-Z revealed six types of nano- to micron-sized particles including diopside, enstatite, amphibole (tremolite-actinolite), mica (phlogopite), ulvöspinel and Ti-rich magnetite (Deditius et al., 2018).

Cerro Negro Norte and El Romeral

At Cerro Negro Norte (Salazar et al., 2019) and El Romeral (Rojas et al., 2018b), four types of magnetite (Type-I to -IV) were identified (**Table 5**). In both deposits, Type-I and -II dominate over the other types of magnetite with 35 and 60 modal% abundance, respectively, at El Romeral (Rojas et al., 2018b) and >90 modal% abundance of magnetite Type-I and Type-II in Cerro Negro Norte (Salazar et al., 2019). These magnetite types are similar to Type-1 and -2 from Los Colorados (Knipping et al., 2015a,b) with inclusion-rich cores (Type-I) surrounded by inclusion-poor rims (Type-II) (**Figure 18**; **Figure B5-A**). Several polycrystalline and one-phase inclusions 50 um to a few nm in size occur oriented or randomly distributed in Type-I magnetite from El Romeral and Cerro Negro Norte. The compositions of these inclusions were determined by using SEM-EDS and micro-Raman spectroscopy. In magnetite samples from El Romeral, inclusions >10 μm were identified as actinolite, ilmenite and rutile, whereas smaller inclusions correspond to rutile, ilmenite, titanite, chlinoclore, calcite, phlogopite, tremolite, NaCl and pargasite (Rojas et al., 2018b). At shallow depths (<100 m), Si-rich inclusions occur aligned along magnetite

crystallographic planes. At Cerro Negro Norte, actinolite, quartz and an unspecified Mg-Al-Si-phase are present as major inclusions. The El Romeral samples studied here (samples Rom-094, ~347 m; Rom-149, ~10 m) are texturally different. In sample Rom-094, magnetite Type-I predominates over Type-II, whereas at shallow depths (sample Rom-149) Type II predominates over Type-I (**Figure 18**) and can occur associated with pyrite and chalcopyrite filling fractures in the magnetite. In Cerro Negro Norte, Type-III magnetite is characterized by an inclusion-poor core with a cryptic zonation towards the rim (**Figure B5-B**), whereas in El Romeral Type-III magnetite is represented by an inclusion-poor chemically-zoned magnetite. A late magnetite vein event (Type-IV) was identified in both deposits and crosscuts all previous magnetite types. In Cerro Negro Norte some of these magnetite grains display several submicron- to micron-sized inclusions arranged in a sinuous oscillatory zoning (Salazar et al., 2019; **Figure B5-C**; **Table 5**).

Carmen

There are four types of magnetite in the massive magnetite ore bodies from Carmen, identified here as Type-I to -IV. Type-I magnetite is volumetrically dominant (~50 modal%), followed by Type-III magnetite (~30 modal%) (**Table 5**). Type-I magnetite contains abundant mineral inclusions ranging in size from ~30 μm to <1 μm and aligned along magnetite crystallographic planes or randomly distributed (**Figure 19A**). Some grains exhibit oscillatory zoning (**Figure 19B,C**), in which inclusions are more concentrated in darker bands (**Figure 19C**). The individual bands vary in width between 5 and 70 μm. Some larger inclusions are composed of Mg, Al, Fe-bearing silicates and Fe-Ti oxides such as ilmenite and rutile. Quartz, Ca-Mg-carbonates, apatite, monazite and titanite occur filling fractures and open spaces. Type-I magnetite is crosscut by pristine, inclusion-free Type-II magnetite veinlets of variable thickness (*Figure 19A,B*). Type-III magnetite is defined as large magnetite grains intergrown with coarse actinolite and apatite crystals. Large apatite and actinolite crystals grew with a non-uniform distribution or perpendicular to vein walls of magnetite Type-III (**Figure 19D**). Type-III magnetite is texturally diverse and is characterized by the occurrence of nano-inclusions/exsolution lamellae either oriented, randomly distributed or clustered in the grain cores (**Figure 19D**). Some grains exhibit porosity or show recrystallization textures characterized by fine-grained aggregates of magnetite grains exhibiting a mosaic texture with 120° triple junctions (**Figure 19D**). Type-IV magnetite is recognized as a late event and occur as inclusion-poor magnetite forming veinlets that range from a few cm to tens of cm in thickness. Some of these magnetite veinlets crosscut Type-III magnetite and are associated with Cl-rich apatite, monazite and enstatite (Type-IVa; **Figure 19E**), or exhibit porosity (Type-IVb; **Figure 19F**).

Fresia

Four textural types of magnetite were identified at Fresia, including Type-A (~40 modal%), -B (~30 modal%), -C (~25 modal%) and -D (~5 modal%) (**Table 5**). In general, these magnetite types are partially to completely recrystallized to subhedral aggregates of porous magnetite (**Figure 20A**) or display well-developed zonation, oscillatory zoning or a mosaic texture. Hematite (dark grey in BSE images) occurs as irregular patches replacing magnetite along rims and fractures (**Figure 20A**). Type-A magnetite exhibits well-developed oscillatory zoning, and scarce mineral inclusions (**Figure 20B**). Type-B magnetite occurs as the matrix of aggregates in which apatite and

minor actinolite are intergrown. Notably, some grains of Type-B magnetite contain exsolution lamellae of a Ti-bearing mineral phase and several submicrometer-sized inclusions, mainly oriented along magnetite crystallographic planes (**Figure 20C**). Type-C magnetite corresponds to a texturally crustiform-colloform banded magnetite. Successive bands of magnetite, minor quartz and fine-grained Cl-rich apatite display a rhythmic colloform texture. The width of the magnetite bands is variable, and some are altered to hematite (**Figure 20D**). Recrystallization to fine grained-magnetite, porosity and/or oscillatory zoning are recognized in individual grains of the magnetite bands (**Figure 20E**). Finally, Type-D magnetite forms part of cm-sized magnetite veinlets that crosscut the altered host rock at the margin of the deposit. In this type, the porous and recrystallized magnetite grains are characterized by a well-developed mosaic texture (**Figure 20F**) and are intergrown with actinolite crystals that are oriented and distributed perpendicular to the walls of the veinlets.

Mariela

The magnetite microtextures of Mariela (Type-α, -β, -γ, -δ and -ε) are distinctly different from those described for the other deposits studied here, and reported in the cited literature (**Table 5**). In general, magnetite occurs in close association with ilmenite, rutile, titanite and ulvöspinel. Type-α magnetite is the most abundant textural type (~40 modal%) and is characterized by a symplectite texture composed of interstitial magnetite and rutile-titanite±ilmenite of vermicular morphology (**Figure 21A-C**). Rutile is the most abundant phase in the symplectite, whereas ilmenite is less abundant. Both rutile and ilmenite are replaced by titanite. Type-β magnetite (~5 modal%) occurs in sharp contact with Type-α magnetite (**Figure 21A,B**), displays ulvöspinel/ilmenite exsolution lamellae and is replaced by hematite along grain boundaries and crystallographic planes (**Figure 21D**). A late generation of pristine magnetite (Type-γ; ~30 modal%) occurs as an overgrowth (**Figure 21A**) and as veinlets that crosscut Type-α magnetite (**Figure 21E**). In some areas, Type-γ magnetite presents actinolite inclusions (**Figure 21A**). Type-δ magnetite (~10 modal%) is subhedral and occurs forming veinlets with minor apatite that crosscut the altered host rock. This magnetite type is characterized by a well-defined cubic cleavage (**Figure 21F)** and exsolution lamellae (**Figure 21G**) consisting of an unspecific Fe-Mg-Al-O-bearing mineral. Titanite, rutile and an unspecified Mn-silicate occur along the magnetite crystallographic planes. Locally, early magnetite types can be replaced by a Si-rich magnetite (Type-ε; ~10 modal%) with a colloform-banding texture sometimes surrounding small (<10 μm) pyrite grains (**Figure 21H**). Bladed specular hematite (**Figure 21I**) is also observed as a late phase intergrown with quartz and magnetite.

El Laco

Ovalle et al. (2018) showed that magnetite from surface and drill core samples from Laco Norte, Laco Sur and Extension Sur (samples LCN-0944, LCO-0721A and LCO-0715) are significantly different, both chemically and texturally (Magnetite-S, -Z, -X, -Y, -γ, -β and -α; **Table 5**; **Figure B6**). The upper zone (0-65 m depth) comprises >90% modal magnetite with minor diopside and scarce apatite with a vesicular texture. Magnetite-S (**Figure B6-A**) corresponds to surface outcrop samples, whereas Magnetite-Z (**Figure B6-B**) is representative of the shallow drill core samples. Both types are dominated by replacement of magnetite by hematite and goethite. In

the intermediate zone (~65-145 m depth), diopside appears immersed in a texturally diverse magnetite matrix. In this zone, pristine microcrystalline cores of Magnetite-X are replaced by Magnetite-Y overgrowths, evidencing dissolution-reprecipitation processes (**Figure B6-C**). The lowest section of the intermediate zone (~144 m) consists of Magnetite-γ veinlets with pyrite and gypsum, and where Magnetite-γ was formed as an overgrowth on inclusion-rich relict cores of Magnetite-β (**Figure B6-D**). The deep zone (150-200 m depth) corresponds to breccias with andesite fragments replaced by fine-grained diopside within a magnetite-diopside matrix. In this zone, Magnetite-β is characterized by euhedral inclusion-rich cores surrounded by inclusion-free rims (**Figure B6-E**), while Magnetite-α comprises aggregates of titano-magnetite crystals with well-developed ilmenite exsolutions (**Figure B6-F**).

3.4.2 Magnetite chemistry

The concentrations of Mg, Al, Si, Ca, Sc, Ti, V, Cr, Fe, Mn, Co, Zn and Nb in magnetite types from El Romeral (sample Rom-149), Carmen, Fresia and Mariela were analyzed by electron probe microanalyzer (EPMA). The new EPMA data are reported in **Tables B2 and B3**. A statistical summary of EPMA analyses (Mg, Al, Si, Ca, Ti, V, Mn, Fe and O) for each magnetite type identified in Los Colorados (Knipping et al., 2015a,b; Deditius et al., 2018); Cerro Negro Norte (Salazar et al., 2019); El Romeral (Rojas et al., 2018b and this study); Carmen, Fresia, Mariela (this study) and El Laco (Ovalle et al., 2018) is reported in **Table 6**.

The concentrations of trace elements were determined by using LA-ICP-MS in the most abundant magnetite types from El Romeral (Type-I and -II; samples Rom-094 and Rom-149), Carmen (Type-I, -II and -III), Fresia (Type-A, -B and -C), and Mariela (Magnetite-α, -β, -γ and -δ). A total of 430 analyses for 34 elements, e.g., Na, Mg, Al, Si, P, K, Ca, Sc, Ti, V, Cr, Mn, Co, Ni, Cu, Zn, Ga, Ge, Rb, Sr, Y, Zr, Nb, Mo, Ag, Cd, Sn, Sb, Ba, La, Ce, Pb, Th and U were carried out. All LA-ICP-MS data are reported in **Tables B6 and B7**. A summary of all analyzed trace elements from Los Colorados (Knipping et al., 2015b), Cerro Negro Norte (Salazar et al., 2019), and El Laco (Broughm et al., 2017, La Cruz et al., under review) are reported in **Table B4**. It should be noted that the LA-ICP-MS data correspond to spot analyses with the exception of Los Colorados in which transects or profiles in magnetite were performed (Knipping et al., 2015b). Minimum, maximum and average concentrations for each of these elements found in the most relevant magnetite types are reported in **Table 7**.

The main features of the magnetite chemical compositional dataset from Andean IOA deposits are outlined below.

Los Colorados

EPMA and LA-ICP-MS analyses reported by Knipping et al. (2015a,b) reveal that magnetite cores (Type-1) are enriched in Ti, V, Al, Mn, Ni, Ga and Zn in comparison with magnetite rims (Type-2 and -3) (**Table 6**). Notably, X-ray maps of magnetite from the massive magnetite ore body display a clear Ti zonation with a Ti-rich, inclusion-rich core (Type-1), a Ti-poor transition zone (Type-2), and an inclusion-free rim depleted in Ti (Type-3) (**Figure B7-A**). LA-ICP-MS traverses and elemental X-ray maps also reveal that magnetite cores (Type-1) are enriched in Si-, Al-, Mn- and Mg-bearing inclusions (Knipping et al., 2015a,b). On the other hand,

late-stage hydrothermal magnetite veinlets, i.e., Type-X, -Y and -Z, have a similar chemical composition and lower concentrations of Mg, Mn, Si, Al , Ti and V (Deditius et al., 2018; **Table 6**) than the massive magnetite dike (All data, Type-1 and -2; **Table 6**). Trace element concentrations in magnetite Type-3 are slightly lower than concentrations in Magnetite-X and -Z (**Table 6**). The major difference between Magnetite-X, -Y and -Z is the Ti concentration, with Magnetite-Y having the highest contents (average 0.27 wt.% Ti; **Table 6**). Elemental (Al, Si, Ca, Ti, Mn and Mg) X-ray maps for Magnetite-Z reveal an oscillatory zoning with alternating element-rich and depleted bands. In particular, Ti is present as Ti-rich particles in element-depleted bands but is homogeneously distributed in some enriched bands (Deditius et al., 2018; **Figure B7-B**).

Cerro Negro Norte and El Romeral

In general, magnetite grains from Cerro Negro Norte (Types I to IV; Salazar et al., 2019) and El Romeral (Type-I and -II; Rojas et al., 2018b and this study) contain lower concentrations of trace elements than magnetite from Los Colorados (Knipping et al., 2015a,b) (**Table 6**). Most of the EPMA magnetite analyses from Cerro Negro Norte were below the detection limit with the exception of Fe, V, Si and Al (**Table 6**). Notably, both Type-I and -II magnetite have similar and higher concentrations of V (average 0.21 wt.%), but lower Si (average 0.09 wt.%), when compared to Type-III and -IV magnetite (0.13 wt.% V and 0.20 wt.% Si on average). The WDS X-ray maps revealed that Type-I magnetite (inclusion-rich cores) is enriched in Mg, Al, Ca, Mn and Ti relative to Type-II magnetite (rims) (Salazar et al., 2019; **Figure B7-C**). LA-ICP-MS analyses showed that Type-I magnetite displays the highest concentrations of Na, Mg, K, Ca, Mn, Zn and Ga (**Table 7** and **Table B5**); Type-I and -II magnetite contain similar concentrations of Ni and Co; Type-III magnetite has the highest concentration of Cu, whereas Type-IV magnetite has the lowest concentrations of Ti, V, Al, Mn, Zn and Ga, but the highest in P, Ni, Co and Ba. It should be noted that the average concentrations of Ti are similar in Type-I, -II and -III magnetite (~330 ppm Ti), but Type-I has the highest Ti concentration (up to ~1,990 ppm; **Table 7**).

EPMA analyses of magnetite from El Romeral (**Table 6**) reveal that Type-I has higher concentrations of Si and Ca than Type-II in the deep sample (~347 m; Rojas et al., 2018b), whereas the concentrations of Mg, Al, Si, Ca, Ti, V and Mn are very similar in both types in the shallow sample (~10 m; this study). Notably, the V concentration is similar in Type I and Type II magnetite, both in the shallow (average 0.15 wt.%) and depth sample (average 0.26 wt.%). On the other hand, LA-ICP-MS analyses show that Mg, Al, V, Co and Ga concentrations are higher at depth than at shallow levels, whereas Mn, Ni and Zn are higher in the shallow sample (**Table 7**). Overall, both at depth and at shallow levels, Mg, Al and Ti average concentrations are higher in Type-I than in Type-II magnetite; Zn and Mn average concentrations are similar, but slightly higher in Type-I than in Type-II; Ni concentrations are slightly higher in Type-II, and Co and V concentrations are similar in Type-I and -II.

Carmen, Fresia and Mariela

WDS X-ray maps

Elemental (Fe, Mg, Ca Si, Al, Ti, Mn and V) WDS X-ray maps for magnetite grains of Carmen, Fresia and Mariela are shown in **Figures 22, 23** and **24**, respectively. These maps correspond to representative magnetite textures identified and illustrated in **Figures 19, 20** and **21**, i.e., Type-I magnetite from Carmen; Type-A and -C magnetite from Fresia; Type-α and -γ magnetite from Mariela).

Type-I magnetite from Carmen (**Figure 22**) exhibits a distinct oscillatory zoning of Mg, Si and Al, which is less pronounced for Fe. Magnesium, Si and Al form particles in the dark bands of Type-I magnetite. Both Ca and Ti are homogeneously distributed, with no oscillatory zoning and only a few, micro-particles with Ca and Ti. A thin magnetite veinlet (Type-II) crosscuts Type-I magnetite, and is more depleted in Mg, Si and Al and slightly more enriched in Fe than Type-I magnetite.

In magnetite grains from Fresia, a distinct oscillatory zoning for Mg, Ca, Si and Al but less pronounced for Fe and Ti is observed in Type-A magnetite (**Figure 23A**). Magnesium, Al, Si and Fe also occur forming abundant particles, whereas Ca-Ti-bearing particles are scarce. On the other hand, a pronounced oscillatory zoning of Mg, Ca and Si, and a less distinct for Fe is observed in Type-C magnetite (**Figure 23B**). Both Al and Ti WDS X-ray elemental maps are consistent with low Al and Ti concentrations (0.01-0.02 wt.%), which are close to the detection limit (**Table 6**). Aluminum appears slightly enriched in some fractures in Type-C magnetite.

WDS maps of magnetite grains from Mariela reveal the elemental distribution related to the symplectite texture observed in these samples (**Figure 24**). In particular, Types-α and -γ magnetite show similar concentrations of Fe, but Type-α is more enriched in Ca, Al, Si, Ti and V than Type-γ. High concentrations of Ca, Mg, Si and Al in Type-γ magnetite are related to silicate particles and microfracture fillings. It should be noted that the vermicular Fe and Ti oxide minerals (rutile, titanite and ilmenite) that are intergrown with Type-α magnetite forming the symplectite, are depleted in Fe, Mg, Si and V, and slightly enriched in Ca, Al, Ti and Mn. Specifically, the Ca-rich domains and the Mn-rich particles within the vermicular Fe-Ti oxide mineral phases are related to titanite and ilmenite, respectively.

EPMA and LA-ICP-MS spot analyses

EPMA data for magnetite from Carmen, Fresia and Mariela are presented in **Table 6** and a statistical summary of trace element concentrations (Mg, Al, Ti, V, Cr, Mn, Co, Ni, Cu, Zn, Ga and Sn) determined by LA-ICP-MS for each deposit is presented in **Figure 25**.

Overall, EPMA analyses reveal a similar magnetite chemical composition for the different types of magnetite in each deposit (**Table 6**; **Table B2**). The major compositional variations occur for Mg, Al, Si, Ca, Ti, V, Fe and Mn, whereas Sc, Cr, Zn and Nb concentrations are below or close to the detection limit. For some magnetite types (Fresia: Type-A and -D; Mariela: Type-α,- β, -γ and -δ), totals are relatively low (~95% on average) probably related to the presence of numerous micropores related with dissolution-reprecipitation processes (Fresia) and the occurrence of Ti-Fe oxides exsolution lamellae from titano-magnetite (Mariela). For magnetite types characterized by

oscillatory zoning (Carmen: Type-I; Fresia: Type-A and -C) analyses were carried out on both light and dark BSE bands (**Table 6**).

For the Carmen deposit, EPMA analyses reveal that magnetite Type-I has the highest average concentration of Mg and Ca of all magnetite types in this deposit (**Table 6**). The maximum and average concentrations of Mg, Al, Si and Ca are higher in the dark BSE bands than in light BSE bands. The higher concentrations of Ca detected in the dark BSE bands (average 0.07 wt.%) compared to light BSE bands (average 0.04 wt.%) are probably due to the presence of some Ca-bearing particles. Titanium, Fe and Mn concentrations are similar between dark and light BSE bands. The Ti concentration is low (average 0.07 wt.%; **Table 6**). On the other hand, Type-III and -IV magnetite have a higher Ti concentration (average 0.08-0.14 wt.%) than both Type-I and-II (average 0.07 wt.%). It should be noted that V is homogeneously distributed throughout all magnetite types (average 0.23-0.25 wt.%). LA-ICP-MS analyses reveal that Type-I magnetite has the highest average Mg and Al concentration, i.e., 3,842 and 1,036 ppm, respectively, followed by Type-II magnetite (average 2,811 ppm Mg; 744 ppm Al) and Type-III (average 965 ppm Mg; 560 ppm Al) (**Table 7**). Gallium displays the same distribution between the different magnetite types (Type-I > Type-II > Type-III), but variations in concentration are not significant (averages between 33.4 to 38.5 ppm). Titanium, V, Co and Ni show similar concentrations in Type-I and -II magnetite, whereas Type-III has a wide range of concentrations of Ti, V and Co than Type-I and -II. Manganese concentrations are higher in Type-III magnetite (average 1,077 ppm).

In Fresia, Type-A and -C magnetite are characterized by oscillatory zoning (**Figure 20A,B,D,E**) in which dark BSE bands are more enriched in Mg, Al, Si and Ca than light bands (**Table 6**). In addition, Ti concentrations are detectable in dark BSE bands of Type-A magnetite (average 0.22 wt.%), whereas for Type-C magnetite, Ti is below the detection limit (<0.06 wt.%). LA-ICP-MS analyses of Type-A magnetite show high concentrations of Mg and Ga, i.e., 2,214 and 35 ppm on average, respectively, whereas the Type-C variety contains the lowest concentrations of Al, Ti, V, Ni and Ga, but the highest concentrations of Co and Cu in comparison with all other magnetite types from Fresia. Finally, Type-B magnetite grains display the highest concentrations of Al, Ti, V, Mn and Ni in Fresia (**Table 7**).

Magnetite from Mariela is characterized by a high concentration of V (up to 2.28 wt.%; Table 3) and Ti (up to 0.98 wt.%, T**able 6**). The V concentrations reported for Mariela magnetite grains are the highest reported for any Andean IOA deposit, whereas Ti concentrations are the second highest after some magnetite types from El Laco (Magnetite-α and Magnetite-β, -β1, -β2; Ovalle et al., 2018) (**Tables 6** and **8**; **Figure 25**). LA-ICP-MS and EPMA analyses yielded contrasting results for Ti and V (**Tables 6** and **7)**. The highest Ti and V concentrations determined by EPMA were found in Type-α magnetite (**Table 6),** whereas LA-ICP-MS data showed the highest concentrations in Type-β magnetite (**Table 7**). These differences are probably due to the presence of Fe-Ti oxides exsolution lamellae (**Figure 21D**) and nano-inclusions in Type-β magnetite that were most likely affected by the large spot size of the laser (~40 µm spot diameter). In addition, LA-ICP-MS analyses revealed that Type-α magnetite has the highest concentration of Cr and Mn (51.2 ppm Cr and 8,400 ppm Mn; **Table 7**) reported so far for Andean magnetites. It should be noted that together with El Laco, Mariela is the only IOA deposit studied here that shows detectable concentrations of Cr in magnetite (**Table 7**). Type-γ magnetite has the lowest average concentration of Ti, V and Al, but the highest content of Co and Cu. Copper concentrations in magnetite are much higher than in any other deposit studied here, reaching concentrations up to

~1,620 ppm in this magnetite type (**Table 7**). Gallium contents are similar between the different magnetite types (~40 ppm on average), but Type-δ magnetite contains slightly higher concentrations (average 48.5 ppm). EPMA analyses of Fe-Ti oxides including rutile, titanite and minor ilmenite, which are intergrown with magnetite Type-α of the symplectite are presented in **Table B4**.

El Laco

The EPMA data in surface and drill core samples from El Laco Norte (**Table 6**) reported by Ovalle et al. (2018) reveal that Ti, V and Al concentrations increase with depth (Magnetite-S < -Z < -X < -Y < -γ < -α < -β, -β1, -β2; **Figure B6**). Manganese concentrations are low, close to the detection limit (average 0.01-0.04 wt.%), and decrease slightly with depth (Ovalle et al., 2018). It should be noted that Ti concentrations in Magnetite-α (average 0.76 wt.%) and Magnetite-β, -β1, -β2 (average 0.57 wt.%) are among the highest reported so far in Andean IOA deposits (**Table 6**).

La Cruz et al. (under review) performed LA-ICP-MS in magnetite samples from the different magnetite ore bodies from El Laco including Cristales Grandes, Rodados Negros, San Vicente Alto, Laco Norte and Laco Sur. In addition to the magnetite types defined by Ovalle et al. (2018), i.e., types -Z, -X, -Y, -α, and -β, La Cruz et al. (under review) identified three new types of magnetite (Magnetite-A, -S1 and -S2) in surficial and shallow level samples. Magnetite-A is defined as a Si-rich magnetite, whereas Magnetite-S1 (inclusion-rich) and -S2 (inclusion-poor) are defined based on their abundance of mineral inclusions. In order to simplify the data analysis, we report all surface samples including Type-A, -S1 and -S2 magnetite as Type-S in **Table 8**. However, the trace element concentrations for each type are reported separately in **Table B5**.

LA-ICP-MS analyses from Laco Norte reveal that Ti, V and Cr concentrations increase with depth and where the highest concentrations are found in Type-α and -β magnetite (**Table 7**). Manganese is highest in Type-β magnetite, and is higher in the Types-X and -Y varieties than in Type-α magnetite (**Table 8**). The highest Al concentration was found in Type-X and -Y, followed by Type-α, -β and -Z magnetite. The highest Ga concentration was determined in Type-X, -Y and -β, followed by -α and -Z. The Co concentration is consistent in all magnetite types ranging from 105 to 160 ppm on average. At Laco Sur, LA-ICP-MS analyses were performed on samples from different depths (surface, shallow level, intermediate depth, and deep; **Table 8**). The results show that Ti, Cr, Mn and Zn increase progressively with depth, while the highest Al and V concentrations occur at intermediate depths. Magnesium increases towards the surface and the average Ga concentration is similar between the intermediate and deep levels. However, the highest Ga concentration was measured in magnetite from the deepest samples (27 ppm on average).

3.5. DISCUSSION

3.5.1. Magnetite microtextures and their link to physico-chemical processes

Previously published data and new analyses from Andean Kiruna-type IOA deposits show a wide variety of magnetite textures (**Figures 18**, **19**, **20**, **B4, B5**, **B6**; **Table 5**). The observed

microtextures, chemical zoning and distribution of various mineral inclusion types (**Table 5**) provide evidence of the geological processes involved in the formation and evolution of these deposits. We stress that a detailed textural characterization of magnetite grains must be undertaken in order to avoid misinterpretations of the geochemical dataset. Key aspects include a precise determination of the magnetite paragenesis in each deposit, and a careful evaluation of chemical zoning features and the presence of micro- to nano-sized metered mineral inclusions. Furthermore, the effects of hydrothermal overprinting are critical to evaluate the impact of re-equilibration processes on the composition of primary magnetite. A brief description and interpretation of the observed microtextures is presented below.

Mineral inclusions

Different types of mineral inclusions, both oriented and randomly distributed, single or polycrystalline, were identified in the studied IOA deposits (**Table 5**). The massive magnetite ore in Los Colorados, Cerro Negro Norte and El Romeral is characterized by magnetite grains with inclusion-rich cores surrounded by pristine, inclusion-poor or inclusion-free rims (**Figures 18**; **B4-A**; **B5-A,B**). The magnetite cores, usually interpreted as magmatic in origin and labeled as Type-1, contain numerous polycrystalline mineral inclusions. In Los Colorados, Type-1 magnetite inclusions include Mg-rich clinopyroxene, magnetite, titanite and an unknown Mg-Al-Si-phase, all of them interpreted as formed at high-temperatures based on the temperature at which some inclusions re-homogenize to silicate melt (>950 °C) (Knipping et al., 2015b; 2019b). At El Romeral, on the other hand, mineral inclusions of Ti-pargasite were identified in the magnetite inner cores, while titanite, rutile, ilmenite and clinochlore were identified as inclusions in the outer portions of the magnetite cores (Rojas et al., 2018b). Both pargasite and clinochlore breakdown at ~200 MPa, suggest formation temperatures between 800-1020 °C for the magnetite inner cores and <780 °C for the outer cores (Jenkins, 1983; Staudigel and Schreyer, 1977).

It is likely that the presence of high-temperature mineral inclusions indicates a high formation temperature for the magnetite host if both were formed at the same time. However, Rojas et al. (2018b) interpreted that the Si-rich (α-quartz) inclusions, aligned along magnetite crystallographic planes in shallow samples at El Romeral may indicate exsolution processes related to slow cooling rates. The presence of Si-rich inclusions may be relevant because most Si-rich domains in magnetite have been attributed to the presence of Si in solid-solution and/or small silicate inclusions (Newberry et al., 1982; Huberty et al., 2012). However, those authors did not rule out the hydrothermal crystallization of quartz along microfractures and/or as inclusions during cooling. More recently, Huang and Beaudoin (2019) studied a few deep magnetite samples from El Romeral and described inclusion-rich cores with abundant quartz, chlorite, albite, titanite and chalcopyrite mineral inclusions, mainly of hydrothermal origin, that formed after magnetite crystallization. They suggest that a fluid-assisted alteration mechanism could explain the incorporation of cations with a small ionic radius (e.g., Si^{4+}) within magnetite (Hu et al., 2014). It follows that a part of the pristine, inclusion-free magnetite rims could be formed by dissolution and reprecipitation of inclusion-rich magnetite (Huang and Beaudoin, 2019). In addition, inclusion-rich magnetite cores from Cerro Negro Norte are dominated by actinolite, an unspecified Mg-Al-Si phase, rutile, ilmenite, clinopyroxene, orthopyroxene, titanite and chlinoclore (Salazar et al., 2019). Many of these mineral inclusions were also observed in magnetite from the El Romeral deposit (Rojas et al., 2018b). However, inferring the temperature of formation of the magnetite host based

on the presence of mineral inclusions must be performed with caution because some of these inclusions could have been incorporated (or exsolved) at a lower temperature and hence, not necessarily represent the temperature conditions at which magnetite crystallized.

Oscillatory zoning and colloform banding

Oscillatory zoning textures, characterized by alternating trace element-rich and trace element-poor bands separated by sharp compositional boundaries were observed in magnetite grains from Los Colorados (magnetite from the diorite intrusion and Magnetite-Z; Knipping et al., 2015a,b; Deditius et al., 2018; **Figure B4-D**), Carmen (Type-I; **Figures 19B,C**), Fresia (Type-A and -C; **Figures 20B,E**) and El Laco (Dare et al., 2015). Oscillatory textures have been also described in Si-rich magnetite from hydrothermal Fe skarns (Shimazaki 1998; Dare et al., 2014; Hu et al., 2014) and in many other mineral phases such as sulfides, oxides, halides, carbonates and phosphates in various ore-forming environments (e.g., Shore and Fowler, 1996; Deditius et al., 2009; Reich et al., 2013; Tardani et al., 2017). In the particular case of sulfide minerals, oscillatory textures are interpreted to reflect crystallization from fluids of fluctuating elemental composition, for instance, related to periodic influxes of magmatic vapor (e.g., Reich et al., 2013) and/or compositional changes in the fluid driven by tectonically induced decompression and boiling (e.g., Peterson and Mavrogenes, 2014; Sanchez-Alfaro et al., 2016; Roman et al., 2019).

Locally, Type-C magnetite from Fresia exhibits crustiform-colloform banding (**Figures 20D**), whereas Si-rich Type-ε magnetite from Mariela displays colloform banding textures (**Figure 21I**). These textures have been interpreted in the literature as related to open fissures or fluid-filled voids and formation at relatively low temperatures, possibly less than 250 °C (Morrison et al., 1990; Moncada et al., 2012). Thus, the occurrence of oscillatory zoning is consistent with magnetite growth during fluctuating fluid compositions or under a changing physico-chemical regime (Craig and Vaughan, 1981; Shimazaki 1998; Holten et al., 2000), whereas colloform textures are possibly related to formation under low temperature and more steady physico-chemical conditions.

Re-equilibration textures

Several magnetite grains from Carmen (Type-III and -IV), Fresia (Type-C and -D) and El Laco (Magnetite-X) show microtextural evidence of re-equilibration, most likely due to dissolution-reprecipitation processes (DRP) (**Table 5**). Re-equilibration processes in magnetite have been reported in skarns (Hu et al., 2014, 2015; Yin et al., 2017), IOA deposits (Heidarian et al., 2016) and in hydrothermally altered igneous magnetite from granitic plutons (Wen et al., 2017). It has been widely reported that textures and the trace element composition of primary and hydrothermal magnetite could be significantly modified by various stages of re-equilibration (Hu et al. 2014, 2015; Heidarian et al., 2016; Wen et al., 2017; Yin et al., 2017; Huang et al., 2018; Huang and Beaudoin, 2019). Both the porosity of magnetite grains from Carmen and Fresia (**Figures 19F**; **20A,F**), and the sinuous and reabsorbed edges in Magnetite-X from El Laco (**Figure B6-C**) are key features of DRP (Putnis, 2009). Textural and geochemical evidences of DRP are also recorded in apatite grains from Carmen and Fresia including high porosity, a sharp replacement front between F-rich (magmatic) and Cl-rich (hydrothermal) apatite domains, and the

formation of secondary monazite inclusions (Palma et al., 2019). The infiltration of mixed basinal brines and meteoric waters that already dissolved evaporites could trigger dissolution-reprecipitation reactions in magnetite from skarns (Hu et al., 2014, 2015; Huang et al., 2018) and IOA deposits (Heidarian et al., 2016) deposits. Accordingly, these externally derived fluids could contribute to an increase in salinity and Cl^- contents of late fluids, enhancing Fe solubility and consequently leading to disequilibrium between the precipitated magnetite and evolving fluids (Chou and Eugster, 1977; Ilton and Eugster, 1989). Some magnetite grains from Carmen and Fresia also display a mosaic texture characterized by well-defined 120° triple junctions (**Figures 19D**; **20F**). A mosaic texture is also evidence of textural re-equilibration, resulting from the annealing and recrystallization of magnetite (Ciobanu and Cook, 2004; Nold et al., 2013; Huang and Beaudoin, 2019). It has been proposed that the mosaic texture could be formed by fluid-assisted recrystallization process in an open system in skarns (Hu et al., 2015) or by the simultaneous recrystallization and annealing of inclusion-rich magnetite in IOCG and IOA deposits (Huang and Beaudoin, 2019).

Exsolution lamellae and symplectite textures

Both exsolution lamellae and symplectites of Fe-Ti oxides are common textures in Ti-rich magnetite from magmatic Fe-Ti,V deposits and mafic-ultramafic igneous rocks (Buddington and Lindsley, 1964; Frost and Lindsley,1991; Pang et al., 2008, 2010; Wang et al., 2008; Song et al., 2013; Liu et al., 2015; Tan et al., 2015; Tan and Liu, 2016.)

Well-developed exsolution lamellae are observed in Type-B magnetite (Fresia; **Figure 20C**), Type-β and -δ (Mariela; **Figure 21D,G**) and Magnetite-α (El Laco; **Figure B6F**). The composition of these lamellae was only determined in Type-β magnetite (ilmenite-ulvöspinel) and Magnetite-α (ilmenite) by using SEM and LA-ICP-MS analyses due to the small size (<10 μm) of these exsolution lamellae. The exsolution of different Fe-Ti oxides are indicative of the physico-chemical conditions of the host Ti-rich magnetite and of the different mechanisms of formation (Buddington and Lindsley, 1964; Lattard, 1995; Mücke, 2003; Tan and Liu, 2016). The composite ilmenite-ulvöspinel exsolution lamellae observed in Type-β magnetite (**Figure B8**) suggest that the exsolution was probably controlled by oxidation of an original magnetite-ulvöspinel solid solution during cooling. At relatively oxidizing conditions, the ulvöspinel component in the ulvöspinel-magnetite solid solution (SS) series could be oxidized at a temperature <600 °C (SS solvus) and exsolved directly as ilmenite (Buddington and Lindsley, 1964). The ilmenite lamellae are also possibly formed by the direct exsolution from cation-deficient $spinel_{SS}$ through the substitution of Fe^{2+} by Ti^{4+} at low oxygen fugacity and high-temperature conditions or the subsolidus re-equilibration of coexisting Fe-Ti oxides (Tan and Liu, 2016).

Hu et al. (2015) reported that during the main stage of mineralization in iron skarn deposits, Ti-bearing magnetite (up to 1.27 wt.% Ti) originally formed at high-temperatures under relatively reducing conditions was subsequently re-equilibrated through exsolution lamellae of Fe-Ti-Al-oxides in response to increasing fO_2 and decreasing temperatures. We interpret the exsolution lamellae in magnetite grains from Mariela, and probably from El Laco, to have formed by oxy-exsolution processes, whereas it is more likely that the exsolution lamellae observed in magnetite from Fresia (Type-B) formed by re-equilibration processes based on the hydrothermal chemical signature of magnetite (**Figures 26**, **27**, **29**).

The symplectite texture forms by the breakdown of unstable minerals (2 or more) that are intergrown as straight, curved or vermicular lamellae as a result of changing chemical and/or physical factors (e.g., Mongkoltip and Ashwoth, 1983; Claeson, 1998). This texture is well-documented in the literature and various mechanisms of formation including rapid cooling, decompression, oxidation, infiltration of aqueous fluids have been proposed (Moseley, 1984; Claeson, 1998; Hippertt and Valarelli, 1998; Field, 2008; Dégi et al., 2010; Elardo et al., 2012; Tan et al., 2015; Regan et al., 2019). Indeed, symplectite intergrowth of magnetite-rutile±ilmenite as seen in Mariela (**Figures 21A**,**B**,**C**,**E**, **24**) are reported in certain mafic-ultramafic layered intrusions (e.g., Von Gruenewaldt, 1985; Claeson, 1998; Tan et al., 2015). According to Tan et al. (2015), the magnetite-rutile symplectite hosted by ilmenite from the Xinjie Fe-Ti oxide-bearing mafic-ultramafic layered intrusion (SW China) was formed by the subsolidus oxidation of the ilmenite-hematite SS, under relatively oxidizing conditions, controlled by the composition and proportion of interstitial fluids (Buddington and Lindsley, 1964). Although the mineralogical assemblage of both symplectites is similar, in Mariela the host or precursor mineral is a Ti-rich magnetite and it is more likely formed by decompression as evidenced by the breccia-pipe structure observed in Mariela.

3.5.2. Magnetite chemistry and temperature trends: [Ti + V] vs. [Al + Mn] plots

Discrimination diagrams based on minor and trace elements concentrations in magnetite have been proposed by several authors to constrain ore-forming environments (e.g., Dare et al., 2014, Dupuis and Beaudon,2011; Knipping et al., 2015b; Nadoll et al., 2012, 2014). **Figure 26** shows the widely used [Al + Mn] versus [Ti + V] discrimination diagram (Dupuis and Beaudoin, 2011; Nadoll et al., 2014) for all magnetite types from the Andean IOA and IOCG deposits discussed here. The plots illustrate the geochemical signature of the different magnetite types recognized in Los Colorados, Cerro Negro Norte, El Romeral, Carmen, Fresia and Mariela from the Chilean Iron Belt (**Figure 26A,B**), El Laco (**Figure 26C**) and the Candelaria and Mantoverde IOCG deposits (**Figure 26D**). The EPMA dataset was used for these plots except for Cerro Negro Norte in which the LA-ICP-MS data were used, because of their very low Ti concentration that could not be measured by EPMA (**Table 6**). Overall, the magnetite data for the studied deposits configure consistent cooling trends from high-temperature, magmatic-hydrothermal conditions (>600 ºC) to lower temperature hydrothermal conditions (<600 ºC) (Nadoll et al., 2014). In the next paragraphs, we discuss and compare the chemical composition of major elements in magnetite (Ti, V, Al, Mn) for the studied deposits, in relation with its inferred temperature of formation. It is important to highlight that the temperature trends discussed here, as noted by Nadoll et al. (2014), should be interpreted with care and correspond to broad and qualitative estimations based on magnetite chemistry, coupled to mineralogical observations of the different mineralization styles.

At Los Colorados, and as described by Knipping et al. (2015a,b), most of the data from the magnetite (western) dike from Los Colorados plot in the *Porphyry field* with a few data points in the *Fe-Ti,V* and *Kiruna fields* (**Figure 26A**). Type-1, -2 and -3 (**Table 6**) are also shown in **Figure 26A**. The cores of magnetite grains (Type-1) have the highest trace element concentration and overlap with magnetite formed in magmatic Fe-Ti,V deposits (*Fe-Ti,V)*, followed by Type-2 magnetite that plot mostly in the *Porphyry field*. Type-3 magnetite, which correspond to the rims of magnetite grains, plot in the *Kiruna* and *IOCG fields*. Based on Nadoll et al. (2014), Knipping et al. (2015a,b) interpreted the above described trend as a result of cooling from dominantly high-

temperature, magmatic-hydrothermal conditions (>600 ºC) to lower temperature hydrothermal conditions (<500 ºC). A similar trend is observed for magnetite compositions in samples from Cerro Negro Norte and El Romeral (**Figure 26A**). At Cerro Negro Norte, both Type-I (magnetite cores) and Type-II (magnetite rims) have similar [Ti + V] concentrations, but Type-I has slightly higher [Al + Mn] concentrations than Type-II (Salazar et al., 2019). Both magnetite types plot mostly within (and below) the *Kiruna field*. Type-III magnetite plots in the *IOCG* and *Kiruna fields*, whereas Type-IV magnetite (late magnetite vein event) plots within (and below) the *BIF field* (**Figure 26A**). Even though no magmatic magnetite was identified in Cerro Negro Norte (e.g., plotting in the *Fe-Ti,V field*), a cooling trend similar to the one described for Los Colorados was recognized (**Figure 26A**). Similarly, both Type-I and -II from El Romeral plot mostly within and below *the Kiruna field* (**Figure 26A**). Only a few points plot in the low part of the *Porphyry field* and near the boundary between the *IOCG* and *Kiruna fields*. It should be noted that the data corresponding to the deepest drill core sample at El Romeral (Type-I and -II; ~347 m) present slightly higher [Ti + V] and [Al + Mn] concentrations than magnetite from shallow levels (Type-I and -II; ~10 m), reflecting a higher formation temperature of magnetite at depth (**Figure 26A**). At the deepest section of the deposit, Type-I magnetite shows a more dispersed distribution of data points and slightly higher [Ti + V] and [Al + Mn] concentrations than Type-II magnetite, whereas at shallow depths Type-I and -II data are equally dispersed (**Figure 26A**). Therefore, based on the chemistry of magnetite types, we infer that the Cerro Negro Norte and El Romeral deposits were formed under relatively lower temperature conditions than Los Colorados (~300-500 °C; within and below the *Kiruna field*), with slightly lower temperatures recognized in Cerro Negro Norte when compared to El Romeral. At Cerro Negro Norte, a late low-temperature magnetite formation event (<300 °C; *BIF field*) was also recognized.

All magnetite types from the Carmen deposit (i.e., Type-I to -IV) show a very similar range of [Ti + V] and [Al + Mn] concentrations (**Figure 26B**). At Fresia, magnetite types A, B and D display similar [Ti + V] concentrations as Carmen (**Figure 26B**). Type-A magnetite from Fresia has a higher [Al + Mn] concentration plotting mostly in the upper part of the *Porphyry field* and in the *IOCG field*. On the other hand, Type-C magnetite plots mostly within the *IOCG field* (~200-300 °C). The occurrence of re-equilibration textures in these magnetites (**Figures 19D**,**F**, **20A**,**F**) indicate that the original trace element geochemistry of primary magnetite was significantly modified. Therefore, we conclude that the magnetite ores from Carmen and Fresia were formed by re-equilibration of previously formed magnetite via dissolution-reprecipitation processes. These processes could have been triggered by the infiltration of externally derived hydrothermal fluids of moderate (300-500 °C) to low (200-300 °C) temperatures, similar to those related to magnetite formation in porphyries and IOCG deposits, respectively.

In contrast to all the deposits mentioned above, most magnetite data points from Mariela plot in the magmatic *Fe-Ti,V field* or at the boundary between the *Fe-Ti,V* and *Porphyry fields* (**Figure 26B**). The igneous affinity of magnetite from Mariela (*Fe-Ti,V field*) is confirmed by both the formation of symplectite and the well-developed ilmenite±ulvöspinel exsolution lamellae (see Section 5.1, **Figure 21D**). We highlight that the Ti concentrations measured in the magnetite from Mariela are lower than in primary magmatic magnetite due to the formation of exsolution lamellae and symplectite, which resulted in the loss of Ti from magnetite into exsolved ilmenite, ulvöspinel and rutile.

Figure 26C, modified from Ovalle et al. (2018), depicts the chemical variation of drill core and surface outcrop data in magnetite from the El Laco Norte deposit. In general, a distinctive trend is recognized from magmatic (*Fe-Ti,V field*) at depth to moderate-, low-temperature hydrothermal conditions (200-300 °C) towards the surface (Magnetite-Z to Magnetite-α; **Figure 26C**). It should be pointed out that Magnetite-α, which plots mostly in the *Fe-Ti,V field*, displays well-developed ilmenite exsolution lamellae further confirming its magmatic origin (**Figure B6-F**). Furthermore, surface samples display lower [Ti + V] concentrations than drill core samples, plotting in all fields, even below the *IOCG field* and *BIF field*, but not in the *Fe-Ti,V field*. This points to magnetite growing from moderate- to low-temperature hydrothermal fluids or that magnetite was chemically re-equilibrated by lower temperature fluids after mineralization as evidenced by dissolution-reprecipitation textures observed in Magnetite-X (**Figure B6-C**).

Finally, the data from the Candelaria and Mantoverde IOCG deposits display a wide range of [Ti + V] and [Al + Mn] values that plot in all fields, but only a few scattered analyses plot in the *Fe-Ti,V field* (**Figure 26D**). The average of all data from Candelaria and Mantoverde plot in the *IOCG field*. The large amount of data that plot in the *BIF field* and below the *Kiruna field* reflect the comparatively low trace element concentration in hydrothermal magnetite from IOCG deposits. This can be interpreted as magnetite in IOCG systems being formed from cooling hydrothermal fluids of lower temperature than those involved in IOA formation.

3.5.3. Igneous and hydrothermal magnetite: V-Ti and V/Ti -Fe plots

Discrimination diagrams based on trace elements have been proposed to distinguish between igneous and hydrothermal magnetite, e.g., Sn versus Ga (Nadoll et al., 2014), Ti versus Ni/Cr (Dare et al., 2014), Ti versus V (Nadoll et al., 2015), and V/Ti versus Fe (wt.%) (Wen et al., 2017). Experimental studies have demonstrated that the incorporation of trace elements in igneous magnetite depends mostly on temperature, host rock/melt composition, elemental availability, and oxygen (fO_2) and sulfur (fS_2) fugacity (Toplis and Corgne 2002; Sievwright et al., 2017; Sossi et al., 2018). Magnetite/melt partition coefficients for trace elements vary by several orders of magnitude for igneous magnetite (Dare et al., 2012; Nadoll et al., 2014), whereas there are no available experimental data that constrain the partitioning of trace elements between magnetite and hydrothermal fluid. Acknowledging the lack of partitioning data for hydrothermal magnetite, Nadoll et al. (2014) point out that the chemical composition of hydrothermal magnetite would be controlled by the composition of the aqueous fluids, temperature, fO_2, fS_2 and host rock buffering. A discussion about the trace element data in magnetite in Chilean IOA deposits is presented below.

Tin is below or close to the detection limit of the LA-ICP-MS technique in the studied IOA deposits (**Tables B5**, **B6**), therefore, the Sn versus Ga plot was not used here. The Ti versus V and V/Ti versus Fe (wt.%) diagrams in **Figures 27** and **28**, respectively, present new and previously published magnetite analyses from Andean IOAs. In addition, geochemical analyses of magnetite from layered mafic-ultramafic, anorthosite and granitic complexes (Liu et al., 2014; He et al., 2016; Polivchuk, 2017; Wen et al., 2017), and magnetite data from the Candelaria IOCG deposit (Huang and Beaudoin, 2019), are presented as a reference.

Figures 27A and **27B** show the Ti and V concentrations in magnetite for each deposit from the Chilean Iron Belt (CIB) and El Laco, respectively. Titanium vs. V diagrams for each magnetite

type are shown in **Figure B10**. Most of the data from Los Colorados plot in the overlapping area between igneous and hydrothermal magnetite and in the *igneous field*. Data for El Romeral and Carmen plot mostly in the overlapping area between both fields (**Figure 27A**). Notably, three data clusters are observed for El Romeral. The deep and the shallow samples from El Romeral (this study) have similar V concentrations (average ~2,586 ppm and 1,269 ppm for Type-I and Type-II, respectively), but the deep sample has higher Ti concentrations than the shallow magnetites (average ~573 and 397 ppm Ti, respectively) (**Figure 27A**). The data from Huang and Beaudoin (2019) contain slightly higher concentrations of Ti and V and plot mostly at the top of the *igneous field*. Data from Fresia are scattered within this plot with a cluster (Type-C) showing a V concentrations consistent with a hydrothermal composition, but with lower Ti concentrations. Magnetite from Cerro Negro Norte plot mostly in the overlapping area between igneous and hydrothermal magnetite (Type-I, -II and -III), whereas Type-IV magnetite plot mostly outside of the *hydrothermal field*, similarly to Fresia´s Type-C (**Figure 27A**). Magnetite from Mariela plot above the *igneous field* and have similar V concentrations but lower concentrations of Ti compared to magmatic magnetite. The few data points from the Candelaria IOCG deposit plot in the overlap area and in the *hydrothermal field* (**Figure 27A**).

The chemistry of El Laco magnetites reveal a trend from magmatic (high Ti and V concentrations; drill core data) to hydrothermal signatures (low Ti and V concentrations; surface data) (**Figure 27B**). Most of the drill core data plot in the *igneous field* with only a few data points in the overlapping area. Moreover, Magnetite-β and -α plot above the *igneous field* showing high Ti and V concentrations. On the other hand, most of the data from surface (outcrop) samples (Magnetite-S) plot in the overlapping area with some points plotting outside of this area with lower Ti concentrations (**Figure 27B**).

Figure 28 shows the Fe concentration (wt.%) versus the V/Ti ratio discrimination diagram proposed by Wen et al. (2017). This plot was constructed based on the observation that igneous and hydrothermal magnetite have different V/Ti ratios, and variable Fe concentrations (Wen et al., 2017). **Figures 28A** and **28B** show the data from IOA deposits from the CIB and El Laco, respectively. All data from the Andean IOA deposits (CIB and El Laco) plot in the *hydrothermal field* (**Figure 28A, B**), and a re-equilibration trend is only observed for magnetite from Los Colorados (Deditius et al., 2018). Based on our analysis, we conclude that the V/Ti ratio should be used with caution because of re-equilibration or post-crystallization processes that can modify the original Ti concentration in magnetite. On the other hand, V appears to be a better discriminant element in magnetite because it is less susceptible to chemical re-equilibration or remobilization and it is more homogeneously distributed in magnetite grains (Rojas et al., 2018b; this study). Mariela and Los Colorados data show slightly lower Fe concentrations that other IOA deposits from the CIB, pointing to a more magmatic character (**Figure 28A**). Most of the magnetite drill core data from El Laco present lower V/Ti ratio (V/Ti<1 on average) than the surface data (V/Ti>1 on average), however, there is some overlap between drill core and surface data (**Figure 28B**).

3.5.4. Temperature and fO_2 trends: Ga vs. V plots

Recently, the Ga versus V plot was used to trace the chemical evolution of magnetite from the Cerro Negro Norte deposit (Salazar et al., 2019). This diagram was proposed after observations that Ga concentrations, as well as V, are consistently higher in magmatic magnetite than in

hydrothermal occurrences (Nadoll et al., 2014). Vanadium is preferentially incorporated into magnetite at high temperature and more reducing (low fO_2) conditions (Toplis and Corgne, 2002; Nadoll et al., 2014). The data plotted in **Figure 29** show the Ga and V signature of magnetite from the studied deposits. A more detailed figure for all types of magnetites for each deposit is reported in **Figure B10**. **Figure 29A** shows that IOA deposits from the Chilean Iron Belt are characterized by variable Ga and V concentrations in magnetite. Data for Los Colorados and Mariela, for instance, show a distinctive high-temperature magmatic character and highly reduced formation conditions, with relatively high Ga (50-73 ppm and 21.7-68.3 ppm, respectively) and very high V (1,368-6,435 ppm and 4,760-16,800 ppm, respectively) concentrations in magnetite (**Table 7** and **Table B**5). Data from El Romeral obtained in this study indicate a decreasing temperature trend from high-temperature magmatic-hydrothermal conditions (intermediate area between high-temperature magmatic and high-temperature hydrothermal; **Figure 29A**) to relative low-temperature hydrothermal conditions from bottom to top of the deposit (Rojas et al., 2018b; this study; **Figure 29A**).

Magnetite from Cerro Negro Norte reflect a continuous decreasing temperature trend from high-temperature hydrothermal conditions and relatively low fO_2 (Type-I and -II; **Figure B10**), to low-temperature conditions (Figure 29A) probably related to changes in the composition of the fluid as it ascended and cooled (Type-III; **Figure B10**; Salazar et al., 2019). The precipitation of magnetite veinlets (Type-IV, **Figure B10**) at even lower temperatures (~200-300 °C) would be related to a late metasomatic event and more oxidized hydrothermal fluids (**Figure 29A**; Salazar et al., 2019). Magnetite from Carmen and Fresia reflect similar conditions of magnetite formation, but at Fresia temperatures would reach lower values (**Figure 29A**) probably related to the infiltration of late oxidized fluids. For El Laco, a transition from high-temperature magmatic hydrothermal and relative low fO_2 conditions observed in drill core magnetites (Magnetite-α and -β), to high-temperature hydrothermal and relative intermediate fO_2 conditions (Magnetite-Z), to low-temperature and relative high fO_2 conditions is observed in surface samples (Magnetite-S) (**Figure 29B**).

3.5.5. Other discrimination diagrams: the Ni-V and Cr-V plots

Figure 30 and **31** show the V versus Cr (Knipping et al., 2015b) and Ni versus V (Loberg and Horndahl, 1983) plots, respectively, for magnetite from the Chilean Iron Belt and El Laco. The V versus Cr plot is used to discriminate Kiruna-type IOA deposits from other high-temperature deposits including porphyry, IOCG and Fe-Ti,V deposits (Nyström and Henríquez, 1994). Chromium (Cr^{3+}) is highly compatible in magmatic magnetite; however, it may be depleted in magnetite from IOA deposits either due to the preferred incorporation of Cr into augite or more probably to the high mobility of Cr^{6+} in fluids (James, 2003). Chromium is below detection limits in Cerro Negro Norte, Carmen and Fresia (**Table 7**). Data from Los Colorados, El Romeral, Mariela and El Laco plot in the *Kiruna field* (<100 ppm Cr and >500 ppm V; Knipping et al., 2015b). It should be noted that the V concentration in magnetite from Mariela (average 9,547 ppm) is similar to values reported for magmatic magnetite **(Figure 30**); however, they show a lower Cr concentration (~15 ppm). Kiruna-type deposits present higher V concentrations than IOCG and iron skarn deposits, but lower Cr concentrations than porphyry deposits (**Figure 30**).

Previous studies have shown that the transition metals including Co and Ni are strongly compatible (Ni>Co) in igneous magnetite (D_{Co}=7.5 and D_{Ni}=30; Dare et al., 2012), but are incompatible relative to co-precipitating hydrothermal sulfides such as pyrite and chalcopyrite. Hence, hydrothermal magnetite in porphyry systems, IOCG and IOA deposits is commonly depleted in Co and Ni. **Figure 31** shows a trend from high to low Ni and V concentrations. For the CIB, the high Ni (9,547 ppm) and V (250 ppm) concentrations in magnetite from Mariela are similar to those reported for igneous magnetite (**Figure 31A**). Relatively similar Ni concentrations in magnetite from Carmen and Fresia (Carmen: 299 ppm; Fresia: 189 ppm on average) are consistent with the presence of scarce sulfides. In addition, the low Ni concentration in hydrothermal magnetite from Cerro Negro Norte (average 83 ppm; Type-III and -IV) and Candelaria are consistent with the abundant presence of sulfides in these deposits.

In the El Laco deposit, the highest Ni concentrations are found at depth (Magnetite-α and -β; average 440 and 392 ppm, respectively), whereas superficial magnetite (Magnetite-S) has a lower Ni (<300 ppm) concentration, probably related to pyrite mineralization found in the Pasos Blancos area (Naranjo et al., 2010).

3.5.6. A genetic model for Andean IOA deposits

The data presented here provide new insights on the evolution of Cretaceous IOA deposits from the Chilean Iron Belt and the Pliocene El Laco deposit in Chilean Altiplano of northern Chile. These deposits were formed and later modified by different processes under varied conditions, which are recorded in microtextures and the geochemistry of magnetite.

Based on our observations and data from the CIB and El Laco, different styles or subtypes of IOA mineralization were identified (**Figure 32**). These IOA subtypes reflect formation at different crustal depths, e.g., deep, intrusive-like (e.g., Los Colorados); transitional (e.g., El Romeral); intermediate, hydrothermal (e.g., Cerro Negro Norte); pegmatitic, apatite-rich (Carmen, Fresia and Mariela); and shallow, subvolcanic/aerial (e.g., El Laco) deposits. In addition to the depth of formation, Andean IOA deposits are fundamentally controlled by: (i) cooling, reflected in magnetite trace element geochemistry and microtextures, which also depend of the source and flux rate of hydrothermal fluids and even the infiltration of meteoric waters or basinal brines; and (ii) decompression, related to the presence of structures and faults, which entails classifying IOA deposits based on subtypes.

Knipping et al. (2015a,b) explained the presence of a distinct textural and chemical variation between cores (Type-1) and rims (Type-2 and -3) in the intrusive-like Los Colorados by a transition from magmatic to magmatic-hydrothermal conditions. In this novel genetic model, i.e., the *flotation model*, microlites of magmatic magnetite (Type-1) crystallize from an intermediate to mafic silicate melt and later ascend by coupling with bubbles of fluids exsolved from the magma. As the magmatic magnetite suspensions ascend, they coalesce and the modal abundance of magnetite increases by further precipitation of hydrothermal magnetite as overgrowths (Type-2 and -3) on primary magnetite filling interstitial spaces at the level of neutral buoyancy. The rapid ascent of the bubble-magnetite suspensions through structures or faults resulted in the formation of these magnetite-rich ore bodies (**Figure 32**). The transtensional, strike-slip, crustal scale Atacama Fault System (AFS) provides and optimum, structurally-controlled, permeable conduit

that allowed the magnetite-rich suspensions to ascend from the source magma (Knipping et al., 2015a,b; Simon et al., 2018).

Considering that most IOA deposit in the Chilean Iron Belt are genetically related to major transtensional fault systems, the effect of pressure on magnetite solubility is likely a crucial control on magnetite mineralization (Simon et al., 2004; Rojas et al., 2018b). Iron solubility modeling, as a function of pressure and temperature, was performed by Rojas et al. (2018b) considering for $FeCl_2$ solubility and magnetite precipitation a fluid salinity of 35 wt.% $NaCl_{eq}$ and a temperature and pressure range of 380°-620 °C and 60-200 MPa, respectively. The model supports that structures favor the emplacement of ore bodies and that the consequent pressure drop decreases the solubility of $FeCl_2$ in aqueous fluids and triggers magnetite precipitation. Moreover, the rate of decompression affects the efficiency of magnetite precipitation such that rapid decompression favors formation of large magnetite ore bodies. Thus, a $FeCl_2$ bearing hydrothermal fluid at 600 °C will precipitate 50% more magnetite at 100 MPa compare with the mass of magnetite at 120 MPa (Rojas et al., 2018b).

The mineralogical, microtextural and geochemical data from Los Colorados (Knipping et al., 2015a,b; Bilenker et al., 2016; Deditius et al., 2018), El Romeral (Rojas et al., 2018b; this study) and Cerro Negro Norte (Salazar et al., 2019) deposits are consistent with a combined igneous/magmatic-hydrothermal model, in agreement with deposits from the Kiruna district in Sweden (Jonsson et al., 2013; Weis et al., 2013; Westhues et al., 2016, 2017a,b). However, in both the transitional El Romeral and the hydrothermal-like Cerro Negro Norte (**Figure 32**), high-temperature, magmatic magnetite (>600 °C) was not identified (**Figures 26**, **27**, **29**). This suggests that the magnetite ore bodies in both deposits could extend to deeper levels.

The Carmen, Fresia and Mariela pegmatitic, apatite-rich IOA deposits may be genetically and spatially related to extensional strike-slip duplexes in which IOA mineralization is located at or close to intersecting faults (Treloar and Colley 1993; 1996; Bonson et al 1997; Río Tinto Report, 2001; **Table 4**). These fault configurations coupled with transtensional displacement created localized dilational zones that act as tectonic traps for the formation of IOA with abundant F-rich apatite in comb textures (Carmen and Fresia) or Cl-rich apatite in dilational breccias (Mariela) (Palma et al., 2019). In here, the crystallization of apatite was controlled by the fracture opening velocity, crystal growth rate and fluid saturation (Chauvet, 2019). These vein systems characterized by comb textures and relatively large crystals reported at the Caleta Coloso strike-slip duplex (~24°S) developed along the Atacama Fault System (AFS) during the Early Cretaceous (Herrera et al., 2005; Olivares et al., 2010). These fluid-filled open fractures formed under sub-hydrostatic pressures suggesting that mineral precipitation was triggered by a pressure drop at shallow crustal levels (<4 km) through suction-pump mechanism (Olivares et al., 2010). In this fluid-fracture relationship, the migration of fluids would be triggered by fracturing of the rock associated with the activity of the fault and not by fluid overpressure (Herrera et al., 2005). The abrupt pressure drop within the fracture triggers fluid injection into dilatation zones (Sibson et al., 1975; Sibson, 2001; Cox et al., 2001) causing the immediate filling of the fracture by fluids coming from areas of higher pressure (pressure gradient), and the consequent precipitation of ore minerals (Olivares et al., 2010). The suction-pump mechanism could explain the formation of pegmatite-like IOA deposits such as Carmen and Fresia, and of comb textures where the rate of crystallization is lower that the fracture opening rate (Chauvet, 2019). Thus, crystallization only covers the fracture/vein wall and crystals grow larger during multiple stages of growth, sometimes associated with a change

in the fluid composition (Dowling and Morrison 1990). The fracture is sealed by mineral precipitation until a new seismic rupture can cause brecciation, as observed in Carmen and Fresia. On the other side, the Cl-rich apatite dilational breccias from Mariela formed by cracking due to fluid overpressure or hydraulic fracturing (Chauvet., 2019). The space created by fragmentation of the intrusive host rock affected by the strike-slip duplex formation, and the dilational breccias texture could have formed at the initiation of the process when rates of aperture are weak (Chauvet., 2019). Therefore, fragments derived from a much greater depth, evidenced by the purely magmatic magnetite signature from Mariela, were emplaced at shallow levels. This could suggest the occurrence of a much larger massive magnetite body at depth and is consistent with the high and restricted ε_{Nd} values (+5.5 to +6.0) and low $^{87}Sr/^{86}Sr$ initial ratios of Cl-rich apatite from Mariela (0.70390-0.70407) that support crystallization from a high-temperature, saline magmatic-hydrothermal fluid exsolved from a primitive magmatic source (Palma et al., 2019).

Importantly, post-mineralization hydrothermal alteration and re-equilibrating processes (e.g., dissolution-reprecipitation) may modify the primary signature of magnetite and apatite microlites. Titanium, originally dissolved in magnetite, can form secondary titanite or rutile as observed in Andean (this study) and in other (Nold et al., 2014) Kiruna-type and porphyry (Berger et al., 2008) deposits or alternatively, partition into other Fe-Ti oxides by exsolution processes (exsolution lamellae and symplectite textures). Wen et al (2017) reported that the pervasive replacement of ilmenite exsolution lamellae by titanite in hydrothermally altered igneous magnetite tend to deform the host magnetite, creating accommodation, such as fractures or disconnected domains, for the newly formed titanite. As described in previous sections, abundant titanite fractures are recognized in magnetite grains from Carmen, Fresia and Mariela, in which these fractures provide conduits for hydrothermal fluids and could accelerate the dissolution-reprecipitation processes in magnetite. Rapp et al. (2010) performed experiments to test the effect of Cl- and F-rich hydrous fluids on the rutile solubility at 0.5 GPa and high-temperatures. The experiments indicate that rutile solubility in saline fluids is strongly dependent on the predominant anion in the fluid and that the solubility is much higher in Cl^- (2-4 times) and F^- brines (20-100 times) than in pure H_2O fluids. A decrease in the F concentration in the fluid suppresses rutile solubility and triggers its precipitation. Fluoride has been shown to effectively mobilize Ti in a fluid and consequently, Ti should not always be regarded as immobile in geological fluids (e.g., Audétat and Keppler, 2005; Tanis et al., 2016). The coexistence of apatite and hydrothermal titanite in veins and fractures is observed in several deposits such as Carmen, Fresia and Mariela. Other experimental studies have demonstrated that magnetite can be dissolved by Cl-rich hydrothermal fluids (Chou and Eugster, 1977; Ilton and Eugster, 1989) and a significant amount of Fe can also be transported by low-density aqueous vapor in the magmatic-hydrothermal environment (Simon et al., 2004). Conversely, at the Carmen and Fresia deposits, the Cl-rich apatite domains are consistent with the modification of primary magmatic F-rich apatite by a later hydrothermal overprint evidenced by post-alteration replacement and re-equilibration textures and the formation of secondary monazite inclusions formed by coupled dissolution-reprecipitation processes (Palma et al., 2019). The presence of relatively homogeneous aqueous inclusions, restricted to rims and fractures in apatite grains from Carmen, record a later input of Na-, Ca- and Mg-rich brines, however, other fluid inclusion assemblages with lower homogenization temperatures and salinities point to the circulation of even cooler fluids probably related to the formation of Cu-bearing sulfides and hematite at shallow depths (Velasco and Tornos, 2009).

The occurrence of Cl-rich apatite seems to be a particular feature of IOA deposits from the Chilean Iron Belt. Hydrothermal apatite (metasomatized areas) in other IOA deposits worldwide,

e.g., Kiruna (northern Sweden), Bafq (central Iran), Taocun (Eastern China), Pea Ridge (USA) and Cerro Mercado (México) (Harlov et al., 2002; 2016; Torab and Lehman 2007; Taguipour et al., 2015; Zeng et al., 2016), are not compositionally very different from F-rich magmatic apatite (Palma et al., 2019). It follows that the Atacama Fault System not only exerts a first order control in the emplacement of the magnetite ore bodies but also plays a fundamental role on (hydrothermal) fluid dynamics. The formation of pegmatitic-IOA deposits by suction-pump mechanisms (Carmen and Fresia) or dilational breccias by the hydraulic injection of high-temperature hydrothermal fluids (Mariela) into strike-slip duplex configurations support this strong structural control. Doherty et al. (2014) demonstrated experimentally that Cl partitioning between apatite-melt-fluids depends strongly on pressure. Moreover, experiments show that the Cl concentration in apatite increases considerably, relative to the felsic melt or the vapor saline fluid, when pressure drops from 200 to 50 MPa. The magnetite from the different ore bodies from El Laco recorded both purely igneous and magmatic-hydrothermal signatures (Ovalle et al., 2018). Ovalle et al. (2018) proposed that El Laco formed as a result of an optimal convergence of common subaerial volcanic processes in arc volcanoes (**Figure 32**). In the early stages, Ti-rich igneous magnetite (Magnetite-α and -β) crystallized at near liquidus conditions within the andesitic magma chamber beneath the volcanic complex (**Figure 32**). The periodic injections of crystal-bearing, vapor-saturated mafic magma into the base of the magma chamber could lead to rapid decompression and volatile exsolution (i.e., bubbles of supercritical fluid), which increases the magnetite budget. The consequent ascent, growth, coalescence and accumulation of the magnetite-fluid-bubble pairs form a magnetite-rich, hypersaline suspension that continues ascending and becomes Fe-rich by scavenging Fe (Cl and other metals) from the magma. During the collapse of the El Laco volcanic edifice, the hydraulic injection of the magnetite-fluid suspension via collapse-related fissures, ring structures and secondary craters on the flanks of the El Laco volcano form the hydrothermal breccia bodies at depth observed in the drill core samples from deeper levels in the deposit. The Fe-rich magmatic-hydrothermal fluids continue ascending to shallow levels and crystallizes hydrothermal magnetite (Magnetite-X, -Y and -Z) during progressive cooling until it reached the surface where magnetite-S is subject to weathering. The surface venting of the hydrothermal magnetite suspension may formed the Fe-rich lava-like flows and dike-like bodies that outcrop around the Pico Laco resurgent dome (**Figure 32**).

Finally, the IOA deposits from the Chilean Iron Belt and El Laco deposit are consistent with a model wherein a magnetite-apatite fluid suspension evolves from an intermediate to mafic silicate magma and ascend towards the surface along preexisting crustal faults (Chilean Iron Belt), and alternative, fissures formed during the collapse of a volcanic structure (El Laco). However, where in the CIB volatile-rich fluids are exsolved directly from intermediate to mafic magmas in El Laco volatile-rich fluids are exsolved from a mafic magma underplating the andesitic magma body and then transferred to the overlaying magma chamber (**Figure 32**). It should be noted that there is abundant evidence that magnetite segregation is a common process in arc magmas (Edmonds et al., 2014). The *flotation model* allows a variation and the definition of different styles or subtypes of IOA mineralization and provides a new general framework to understand the formation of Andean IOA deposit. It is clear though, that as new data become available from other IOA deposits around the world, the model could be modified to accommodate these new observations and further variations of the general model are likely to be presented.

3.5.7. The IOA and IOCG connection

The oscillatory zoning, crustiform-colloform banding and re-equilibration textures observed in several magnetite types, as well as a low concentration of compatible (e.g., Ti, V, Ga, Cr) and a high concentration of incompatible and fluid mobile elements (e.g., Si, Ca, Pb, Cu), support formation at moderate to low-temperatures (<600 °C). On the other hand, the magnetite chemistry of the Candelaria and Mantoverde IOCGs reflects a continuum from high-temperature magmatic, to magmatic-hydrothermal magnetite, to shallow IOCG magnetite mineralization formed from cooling hydrothermal fluids (**Figure 26D**). The *genetic model* described above (**Figure 32**), allows for a vertical continuum or transition from a deep-seated IOA (e.g., Los Colorados, El Romeral and Cerro Negro Norte) to shallow IOCG mineralization.

Geochemical data and field observations in IOA deposits from the CIB are consistent with a continuum from deep IOA to shallow IOCG hydrothermal mineralization. This is evidenced by the change in magnetite chemistry and the ubiquitous presence of sulfides in IOA deposits (e.g., Cerro Negro Norte; **Figure 32**), some of which could be related to late superimposed hydrothermal events (Knipping et al., 2015a,b; Barra et al., 2017; Rojas et al., 2018b). According to Raab (2001) the minor Cu-Au mineralization at Cerro Negro Norte is predominantly associated with pyrite±chalcopyrite veinlets and to the tourmaline–quartz alteration. Previously, Vivallo et al. (1995) documented Au grades up to 1 ppm in pyrite and less than 100 ppb in magnetite. Those authors concluded that a late hydrothermal event characterized by a high fS_2 remobilized Au from the Fe ore (Vivallo et al., 1995; Raab, 2001). Evidence of pyrite and Cu oxide mineralization and significant concentrations of Cu in both apatite (Palma et al., 2019) and magnetite (**Table 8**, **Figure 25**) further support this transition of mineralization styles. In addition, the Mariela and Carmen deposits are spatially related to IOCG mineralization zones. Specifically, the Barreal Seco (Teresa de Colmo) IOCG hematite breccias (Correa and Hopper, 2000) is located ~3 km south of the Mariela. This spatial relation supports a possible genetic connection between IOA and IOCG mineralization.

According to Knipping et al. (2015a,b), during the formation of the IOA mineralization, the exsolved bubbles, i.e., the high-Cl magmatic-hydrothermal fluid, would efficiently scavenge metals (Fe, Cu, Au, S and others) from the silicate melt due to the high fluid/melt partition coefficients for these element (Chou and Eugster, 1977; Boctor et al., 1980; Simon et al., 2004; Williams-Jones and Heinrich, 2005; Simon and Ripley, 2011; Zajacz et al., 2012a,b). Thus, the hydrothermal fluids have the ability to transport these elements into more distal or shallow levels in the crust where they precipitate their chemical load as oxides±sulfides±phosphates, either through cooling (T<400 °C; Hezarkhani et al., 1999; Ulrich et al., 2001; Hurtig and Williams-Jones, 2014; Williams-Jones and Migdisov, 2014) or possibly by mixing with meteoric fluids (Barton, 2014; Monteiro et al., 2018a,b) forming IOCG mineralization. Experimental data reveal that the maximum solubility for Cu is reached at ~600 °C and drops abruptly as the fluid cools (Migdisov et al., 2014; Williams-Jones and Migdisov, 2014). The solubility of Cu in the cooling-magmatic hydrothermal fluid also increases with increasing fO_2 (Williams-Jones and Migdisov, 2014). On the other hand, the maximum solubility of Au in a cooling magmatic-hydrothermal fluid shifts to lower temperatures with decreasing the density of the fluid (Hurtig and Williams-Jones, 2014). Those authors determined experimentally that the Au solubility reaches a maximum at ~500 °C in an intermediate density fluid and at ~400 °C for a low density fluid. The fact that some Au-rich deposits are magnetite-rich suggests that high fO_2/fS_2 ratios favor the deposition of large

amount of magnetite under feldspar-stable conditions and important amounts of gold (Sillitoe, 1979; Simon et al., 2004). Thus, as the fluid ascends and migrates from the deep, IOA environment its chemical composition will change increasing its metal (e.g., Fe, Cu, Au) and salinity content. Later sulfide (chalcopyrite, pyrite and bornite) precipitation occurs at lateral or upper crustal levels upon cooling under ~400 °C (Simon et al., 2018).

3.6. CONCLUDING REMARKS

The new data presented here coupled to previous studies on the microtextures and chemistry of magnetite from Andean IOA deposits located in the Cretaceous Iron Belt (CIB), Coastal Cordillera (25-31°S), and the Pliocene El Laco volcanic complex (23° S), Central Volcanic Zone of the Chilean Altiplano, provide new constraints on the formation of this ore deposit type.

Textural observations (SEM) combined with microanalitycal techniques (EPMA and LA-ICP-MS analyses) reveal different magnetite types in Los Colorados, Cerro Negro Norte, El Romeral, Carmen, Fresia and Mariela. The different magnetite types display a broad spectrum of microtextures (e.g., oscillatory zoning, colloform banding, re-equilibration textures, exsolution lamellae and symplectite) and mineral inclusions randomly distributed in magnetite cores, arranged following crystallographic planes or in trace element-rich bands. Each of these textures provide information on the formation processes, i.e., igneous, magmatic-hydrothermal, metasomatic or re-equilibration processes. Overall, these microtextures coupled with the magnetite chemical composition reveal that IOA deposits formed by a combination of magmatic and hydrothermal processes, and that magnetite is susceptible to multiple textural and compositional re-equilibrium events during the formation and evolution of IOA deposits. The chemistry of magnetite reflects variable conditions/events of formation for each of the deposits under study. These conditions range from purely magmatic, high-temperature (>600 °C) and reduced (low-fO_2) conditions; to moderate, low-temperature magmatic-hydrothermal and intermediate-fO_2; to low-temperature (200-300 °C) and more oxidized (high-fO_2) hydrothermal conditions. A clear continuous transition from high-temperatures, low fO_2 conditions in the deepest portions of the deposits to low-temperature, high fO_2 conditions towards shallow levels are recognized in El Laco. Trace elements, such as Al, Ti, V, Cr, Mn, Ni, Cu and Ga are incorporated into both magmatic and hydrothermal magnetite. The concentration of these elements in magnetite are a function of element availability (source), oxygen and sulfur fugacity, co-precipitation of competing mineral phases, fluid-rock interaction, the occurrence of nano- to micron-scale inclusions and most importantly, temperature. Moreover, the observation of re-equilibration textures in magnetite suggest that the primary composition of magnetite can be modified, complicating the use and interpretation of different discrimination diagrams. In particular, the Ti concentration in magnetite has been used extensively as a tracer a magmatic origin, however, Ti appears to be mobile during hydrothermal alteration and/or re-equilibration processes. In addition, the presence of Fe-Ti oxides exsolution lamellae and symplectite formed by oxy-exsolution processes and decompression, respectively, requires complex recalculations to determine the original composition of magnetite. Therefore, both V and Ga are better discriminant elements to determine the temperature and fO_2 conditions of magnetite crystallization.

The microtextural and geochemical data in magnetite from IOA deposits from both the Chilean Iron Belt and El Laco, can be explained by the *flotation model*. In this model a magnetite-

apatite-fluid suspension evolves from an intermediate-mafic silicate magma and ascends towards the surface along preexisting crustal faults (Chilean Iron Belt) or alternatively, through fissures formed during the collapse of the volcanic structure (El Laco). As exemplified by El Laco (Ovalle et al., 2018) and Cerro Negro Norte (Salazar et al., 2019), the *flotation model* allows a variation within its general framework to accommodate different styles or subtypes of IOA mineralization within upper crustal levels. The variations observed in Andean IOA deposits suggest that these deposits comprise a group or clan of deposits with variable degrees of magmatic and hydrothermal signatures from deep, intrusive-like (e.g., Los Colorados); transitional (e.g., El Romeral); intermediate, hydrothermal-like (e.g., Cerro Negro Norte); pegmatite, apatite-rich (Carmen, Fresia and Mariela); and, shallow, subvolcanic/aerial (e.g., El Laco) deposits. These different IOA subtypes are controlled fundamentally on the depth of formation, the presence of structures/faults for decompression, the composition of the host rock, the source and flux rate of hydrothermal fluids, and even the infiltration of non-magmatic fluids such as meteoric waters and possible basinal brines. The proposed formation model also supports the observed genetic link between IOA and IOCG mineralization in which a continuum from deep, sulfide-free, magnetite-apatite (IOA) mineralization to shallow magnetite+sulfide-rich (IOCG) mineralization is supported by magnetite geochemical data and field observations in the Andean IOA-IOCG province.

In addition, pegmatite-like apatite-rich IOA deposits, characterized by macroscopic comb-like textures and breccias, support the fact that the structural configuration and decompression are first order control factors in the formation of Andean IOA deposits. These deposits would be formed by a drop in pressure caused by fracturing (suction pump mechanism; Carmen and Fresia) or by the hydraulic injection of high-temperature and high-salinity magmatic-hydrothermal fluids, respectively, that lead to the precipitation of pressure-dependent solubility mineral phases such as magnetite and apatite.

3.7. Acknowledgments

This research was funded by Fondecyt grants 1190105 and 1140780. The authors acknowledge the support of the Millennium Nucleus for Metal Tracing along Subduction. The LA-ICP-MS analytical work was funded by Conicyt-Fondequip instrumentation grant EQM120098. G.Palma thanks financial support provided by CONICYT-PFCHA/Doctorado Nacional/2016-2116003, through a PhD scholarship.

3.8. References

Angerer, T., Hagemann, S.G., Danyushevsky, L.V., 2012. Geochemical evolution of the banded iron formation-hosted high-grade iron ore system in the Koolyanobbing Greenstone Belt, Western Australia. Econ. Geol. 107, 599-644.

Apukhtina, O.B., Kamenetsky, V.S., Ehrig, K., Kamenetsky, M.B., Maas, R., Thompson, J., Cook, N.J., 2017. Early, deep magnetite-fluorapatite mineralization at the Olympic Dam Cu-U-Au-Ag deposit, South Australia. Econ. Geol. 112, 1531-1542.

Audétat, A., Keppler, H., 2005. Solubility of rutile in subduction zone fluids, as determined by experiments in the hydrothermal diamond anvil cell. Earth Planet. Sci. Lett. 232, 393-402.

Barra, F., Reich, M., Selby, D., Rojas, P., Simon, A., Salazar, E., Palma, G., 2017. Unraveling the origin of the Andean IOCG clan: a Re-Os isotope approach. Ore Geol. Rev. 81, 62–78.

Barton, M.D., Johnson, D.A., 1996. Evaporitic-source model for igneous-related Fe oxide–(REE-Cu-Au-U) mineralization. Geology 24, 259-262.

Barton, M.D., Johnson, D.A., 2004. Footprints of Fe-oxide (-Cu-Au) systems. University of Western Australia Sp. Pub. 33, 112-116.

Barton, M.D., 2014. Iron oxide (–Cu–Au–REE–P–Ag–U–Co) systems. Treatise on Geochemistry (second edition, volume 13): Amsterdam, Elsevier, 515–541.

Benavides, J., Kyser, T.K., Clark, A.H., Oates, C.J., Zamora, R., Tarnovschi, R., Castillo, B., 2007. The Mantoverde iron oxide-copper-gold district, III Región, Chile: the role of regionally derived, nonmagmatic fluids in chalcopyrite mineralization. Econ. Geol. 102, 415-440.

Berger, B.R., Ayuso, R.A., Wynn, J.C., Seal, R.R., 2008. Preliminary model of porphyry copper deposits. USGS Open-file Report, 1321, 55.

Bilenker, L.D., Simon, A.C., Reich, M., Lundstrom, C.C., Gajos, N., Bindeman, I., Munizaga, R., 2016. Fe–O stable isotope pairs elucidate a high-temperature origin of Chilean iron oxide-apatite deposits. Geochim. Cosmochim. Acta 177, 94-104.

Boctor, N.Z., Popp, R.K., Frantz, J.D., 1980. Mineral-solution equilibria—IV. Solubilities and the thermodynamic properties of FeCl20 in the system Fe2O3-H2-H2O-HCl. Geochim. Cosmochim. Acta 44, 1509-1518.

Bonson, C., Grocott, J., Rankin, A., 1997. A structural model for thedevelopment of Fe–Cu mineralisation Coastal Cordillera, Northern Chile (25815VS–27815VS). Congreso Geológico Chileno, vol. III. Universidad Católica del Norte, Antofagasta, Chile, 1608–1612.

Broughm, S.G., Hanchar, J.M., Tornos, F., Westhues, A., Attersley, S., 2017. Mineral chemistry of magnetite from magnetite-apatite mineralization and their host rocks: examples from Kiruna, Sweden, and El Laco, Chile. Miner. Deposita 52, 1223-1244.

Brown, M., 1995. P–T–t evolution of orogenic belts and the causes of regional metamorphism. J. Geol. Soc. London 150, 227-241.

Buddington, A.F., Lindsley, D.H., 1964. Iron-titanium oxide minerals and synthetic equivalents. J. Petrol. 5, 310-357.

CAP Minería Anuual Report 2016 http://www.capmineria.cl/wp-content/uploads/2017/03/cap_mineria_memoria_2016.pdf

Cembrano, J., González, G., Arancibia, G., Ahumada, I., Olivares, V., Herrera, V., 2005. Fault zone development and strain partitioning in an extensional strike-slip duplex: A case study from the Mesozoic Atacama fault system, Northern Chile. Tectonophysics 400, 105-125.

Charrier, R., Pinto, L., Rodríguez, M.P., 2007. Tectonostratigraphic evolution of the Andean Orogen in Chile. In: The Geology of Chile, pp. 21-114.

Chauvet, A., 2019. Structural Control of Ore Deposits: The Role of Pre-Existing Structures on the Formation of Mineralised Vein Systems. Minerals 9, 56.

Chen, H., Clark, A.H., Kyser, T.K., 2010. The Marcona magnetite deposit, Ica, south-central Peru: a product of hydrous, iron oxide-rich melts? Econ. Geol. 105, 1441-1456.

Chen, H., Cooke, D.R., Baker, M.J., 2013. Mesozoic iron oxide copper-gold mineralization in the Central Andes and the Gondwana supercontinent Breakup. Econ. Geol. 108, 37-44.

Childress, T., Simon, A., Day, W.C, Lundstrom, C.C., Bindeman, I., 2016. Iron and oxygen isotope signatures of the Pea Ridge and Pilot Knob magnetite-apatite deposits, southeast Missouri, USA. Econ. Geol. 111: 2033-2044.

Childress T., Simon, A.C., Reich, M., Barra, F., Arce, M., Lundstrom, C.C., Bindeman, I., (accepted) Formation of the Mantoverde iron oxide - copper - gold deposit, Chile: Insights from Fe and O stable isotopes and comparisons to iron oxide - apatite deposits. Miner. Deposita

Chou, I.M., Eugster, H.P., 1977. Solubility of magnetite in supercritical chloride solutions. Am. J. Sci. 277, 1296-1314.

Ciobanu, C.L., Cook, N.J., 2004. Skarn textures and a case study: the Ocna de Fier-Dognecea orefield, Banat, Romania. Ore Geol. Rev. 24, 315-370.

Claeson, D.T., 1998. Coronas, reaction rims, symplectites and emplacement depth of the Rymmen gabbro, Transscandinavian Igneous Belt, southern Sweden. Miner. Mag. 62, 743-757.

Core, D.P., 2004. Oxygen and sulfur fugacities of granitoids: Implications for ore-forming processes. Ph.D. thesis, Ann Arbor, University of Michigan, 245 p.

Correa, A., Hopper, D., 2000. The Panulcillo and Teresa de Colmo copper deposits: Two contrasting examples of Fe-ox Cu-Au mineralization from the Coastal Cordillera of Chile. In: Porter T M (Ed), 2000 Hydrothermal Iron Oxide Copper-Gold & Related Deposits: A Global Perspective PGC Publishing, Adelaide v.1 pp. 177-189.

Cox, S.F., Knackstedt, M.A., Braun, J., 2001. Principles of structural control on permeability and fluid flow in hydrothermal systems. SEG Rev. 14, 1-24.

Craig, J.R., Vaughan, D.J., 1981. Ore Microscopy and Ore Petrography. New York, Wiley, pp.434.

Dallmeyer, R.D., Brown, M., Grocott, J., Taylor, G.K., Treloar, P.J., 1996. Mesozoic magmatic and tectonic events within the Andean plate boundary zone, 26-27 30'S, north Chile: Constraints from 40Ar/39Ar mineral ages. J. Geol. 104, 19-40.

Dare, S.A., Barnes, S-J., Beaudoin, G., 2012. Variation in trace element content of magnetite crystallized from a fractioning sulfide liquid, Sudbury, Canada: Implications for provenance discrimination. Geochim. Cosmochim. Acta 88, 27-50.

Dare, S.A., Barnes, S-J., Beaudoin, G., Méric, J., Boutroy, E., Potvin-Doucet, C., 2014. Trace elements in magnetite as petrogenetic indicators. Miner. Deposita 49, 785-796.

Dare, S.A., Barnes, S-J., Beaudoin, G., 2015. Did the massive magnetite "lava flows" of El Laco (Chile) form by magmatic or hydrothermal processes? New constraints from magnetite composition by LA-ICP-MS. Miner. Deposita 50, 607-617.

Day, W.C., Slack, J.F., Ayuso, R.A., Seeger, C.M., 2016. Regional geologic and petrologic framework for iron oxide±apatite±rare earth element and iron oxide copper-gold deposits of the Mesoproterozoic St. Francois Mountains terrane, southeast Missouri, USA. Econ. Geol. 111, 1825-1858.

De Melo G.H.C, Monteiro, L.V.S, Xavier, R.P, Moreto, C.P.N, Santiago, E.S.B, Dufrane, S.A, Aires, B, Santos, A.F.F., 2017. Temporal evolution of the giant Salobo IOCG deposit, Carajás Province (Brazil): constraints from paragenesis of hydrothermal alteration and U-Pb geochronology. Miner. Deposita 52, 709-732.

Deditius, A.P., Utsunomiya, S., Ewing, R.C., Chryssoulis, S.L., Venter, D., Kesler, S.E., 2009. Decoupled geochemical behavior of As and Cu in hydrothermal systems. Geology 37, 707-710.

Deditius, A.P., Reich, M., Simon, A.C., Suvorova, A., Knipping, J., Roberts, M.P., Saunders, M., 2018. Nanogeochemistry of hydrothermal magnetite. Contrib. Mineral. Petrol. 173, 46.

Dégi, J., Abart, R., Török, K., Bali, E., Wirth, R., Rhede, D., 2010. Symplectite formation during decompression induced garnet breakdown in lower crustal mafic granulite xenoliths: mechanisms and rates. Contrib. Mineral. Petrol. 159, 293-314.

Del Real, I., Thompson, F.H., Carriedo, J., 2018. Lithological and structural controls on the genesis of the Candelaria-Punta del Cobre Iron Oxide Copper Gold district, Northern Chile. Ore Geol. Rev. 102, 106-153.

Doherty, A.L., Webster, J.D., Goldoff, B.A., Piccoli, P.M., 2014. Partitioning behavior of chlorine and fluorine in felsic melt–fluid (s)–apatite systems at 50 MPa and 850–950 C. Chem. Geol. 384, 94-111.

Dowling, K., Morrison, G., 1990 Application of quartz textures to the classification of gold deposits using North Queensland examples. Econ. Geol. Monogr. 6, 342-255.

Dupuis, C., Beaudoin, G., 2011. Discriminant diagrams for iron oxide trace element fingerprinting of mineral deposit types. Miner. Deposita 46, 319-335.

Edmonds, M., Brett, A., Herd, R.A., Humphreys, M.C.S., Woods, A., 2014, Magnetite-bubble aggregates at mixing interfaces in andesite magma bodies: Geol. Soc. London Sp. Pub. 410.

Elardo, S.M., McCubbin, F.M., Shearer Jr, C.K., 2012. Chromite symplectites in Mg-suite troctolite 76535 as evidence for infiltration metasomatism of a lunar layered intrusion. Geochim. Cosmochim. Acta 87, 154-177.

Espinoza, R.S., Véliz, G.H., Esquivel, L.J, Arias, F.J., Moraga, B.A., 1996. The cupriferous province of the Coastal Range, northern Chile. Andean copper deposits: New discoveries, mineralization, styles and metallogeny, SEG Sp. Pub. 5, 19-32.

Field, S., 2008. Diffusion, discontinuous precipitation, metamorphism, and metasomatism: The complex history of South African upper-mantle symplectites. Am. Mineral. 93, 618-631.

Frost, B.R., Lindsley, D., 1991. Oxide minerals: petrologic and magnetic significance. Rev. Mineral. Soc. Am. 25, 509.

Frutos, J., Oyarzún M, J., 1975. Tectonic and geochemical evidence concerning the genesis of El Laco magnetite lava flow deposits, Chile. Econ. Geol. 70, 988-990.

Grocott, J., Taylor, G.K., 2002. Magmatic arc fault systems, deformation partitioning and emplacement of granitic complexes in the Coastal Cordillera, north Chilean Andes (25 30′ S to 27 00′ S). J. Geol. Soc. London 159, 425-443.

Groves, D.I., Bierlein, F.P., Meinert, L.D., Hitzman, M.W., 2010. Iron oxide copper-gold (IOCG) deposits through Earth history: Implications for origin, lithospheric setting, and distinction from other epigenetic iron oxide deposits. Econ. Geol. 105, 641-654.

Harlov, D.E., Förster, H.J., Nijland, T.G., 2002. Fluid-induced nucleation of REE-phosphate minerals in apatite: nature and experiment Part I. Chlorapatite. Am. Mineral. 87, 245-261.

Harlov, D.E., Corey, J.M., Ian, D.K., Lain, M.S., 2016. Mineralogy, chemistry, and fluid-aided evolution of the Pea Ridge Fe oxide-(Y + REE) deposit, Southeast Missouri, USA.
Econ. Geol. 111, 1963–1984.

He, H.L., Song, Y.Y., Song, Y.X., Du, Z.S., Dai, Z.H., Zhou, T., Xie, W., 2016. Origin of nelsonite and Fe–Ti oxides ore of the Damiao anorthosite complex, NE China: Evidence from trace element geochemistry of apatite, plagioclase, magnetite and ilmenite. Ore Geol. Rev. 79, 367-381

Heidarian, H., Lentz, D., Alirezaei, S., Peighambari, S., Hall, D., 2016. Using the chemical analysis of magnetite to constrain various stages in the formation and genesis of the Kiruna-type chadormalu magnetite-apatite deposit, Bafq district, Central Iran. Miner. Petrol. 110, 927-942.

Herrera, V., Cembrano, J., Olivares, V., Kojima, S., Arancibia, G., 2005. Precipitación por despresurización y ebullición en vetas hospedadas en un dúplex de rumbo extensional: evidencias microestructurales y microtermométricas. Rev. Geol. de Chile 32, 207-228.

Hezarkhani, A., Williams-Jones, A.E., Gammons, C.H., 1999. Factors controlling copper solubility and chalcopyrite deposition in the Sungun porphyry copper deposit, Iran: Miner. Deposita 34, 770–783.

Hippertt, J.F., Valarelli, J.V., 1998. Myrmekite: constraints on the available models and a new hypothesis for its formation. Eur. J. Mineral. 317-332.

Hitzman, M.W., Oreskes, N., Einaudi, M.T., 1992. Geological characteristics and tectonic setting of proterozoic iron oxide (Cu□ U□ Au□ REE) deposits. Precambr. Res. 58, 241-287.

Holten, T., Jamtveit, B., Meakin, P., 2000. Noise and oscillatory zoning of minerals. Geochim. Cosmochim. Acta 64, 1893-1904.

Huberty, J.M., Konishi, H., Heck, P.R., Fournelle, J.H., Valley, J.W., Xu, H., 2012. Silician magnetite from the Dales Gorge Member of the Brockman Iron Formations, Hamersley Group, Western Australia. Am. Mineral. 97, 26–37.

Hu, H., Li, J.W., Lentz, D., Ren, Z., Zhao, X., Deng, X.D., Hall, D., 2014. Dissolution-reprecipitation process of magnetite from the Chengchao iron deposit: insights into ore genesis and implication for in-situ chemical analysis of magnetite. Ore Geol. Rev. 57, 393-405.

Hu, H., Lentz, D., Li, J.W., McCarron, T., Zhao, X.F., Hall, D., 2015. Reequilibration processes in magnetite from iron skarn deposits. Econ. Geol. 111, 1-8.

Huang, X.W., Zhou, M.F., Beaudoin, G., Gao, J.F., Qi, L., Lyu, C., 2018. Origin of the volcanic-hosted Yamansu Fe deposit, Eastern Tianshan, NW China: constraints from pyrite Re-Os isotopes, stable isotopes, and in situ magnetite trace elements. Miner. Deposita 53, 1039-1060.

Huang, X.W., Beaudoin, G., 2019. Textures and chemical compositions of magnetite from iron oxide copper-gold (IOCG) and Kiruna-type iron oxide-apatite (IOA) deposits and their implications for ore genesis and magnetite classification schemes. Econ. Geol. 114, 1-74.

Huang, W.W., Sappin, A.A., Boutroy, E., Beaudoin, G., Makvandi, S., 2019. Trace Element Composition of Igneous and Hydrothermal Magnetite from Porphyry Deposits: Relationship to Deposit Subtypes and Magmatic Affinity. Econ. Geol. 114, 917-952.

Hurtig, N.C., Williams-Jones, A.E., 2014. An experimental study of the transport of gold through hydration of AuCl in aqueous vapour and vapour-like fluids. Geochim. Cosmochim. Acta 127, 305-325.

Ilton, E.S., Eugster, H.P., 1989. Base metal exchange between magnetite and a chloride-rich hydrothermal fluid. Geochim. Cosmochim. Acta 53, 291-301.

James, B.R., 2003. Chromium. In Encyclopedia of Water Science. In: B.A. Stewart and T.A. Howell (Eds.). Marcel Dekker Inc, pp.77-82.

Jenkins, D.M., 1983. Stability and composition relations of calcic amphiboles in ultramafic rocks. Contrib. Mineral. Petrol. 83, 375–384.

Jochum, K.P., Willbold, M., Raczek, I., Stoll, B., Herwig, K., 2005. Chemical characterisa-tion of the USGS reference glasses GSA-1G, GSC-1G, GSD-1G, GSE-1G, BCR-2G,BHVO-2G and BIR-1G using EPMA, ID-TIMS, ID-ICP-MS and LA-ICP-MS. Geostand.Geoanal. Res. 29, 285–302.

Jonsson, E., Troll, V.R., Högdahl, K., Harris, C., Weis, F., Nilsson, K. P., Skelton, A., 2013. Magmatic origin of giant 'Kiruna-type'apatite-iron-oxide ores in Central Sweden. Sci. Rep. 3, 1644.

Knipping, J.L., Bilenker, L.D., Simon, A.C., Reich, M., Barra, F., Deditius, A.P., Munizaga, R., 2015a. Giant Kiruna-type deposits form by efficient flotation of magmatic magnetite suspensions. Geology 43, 591-594.

Knipping, J.L., Bilenker, L.D., Simon, A.C., Reich, M., Barra, F., Deditius, A.P., Munizaga, R., 2015b. Trace elements in magnetite from massive iron oxide-apatite deposits indicate a combined formation by igneous and magmatic-hydrothermal processes. Geochim. Cosmochim. Acta 171, 15-38.

Knipping, J., L., Fiege, A., Simon, A.C., Oeser-Rabe, M., Reich, M., Bilenker, L. 2019a. In-situ iron isotope analyses reveal igneous and magmatic-hydrothermal growth of magnetite at the Los Colorados Kiruna-type iron oxide-apatite deposit, Chile. Am. Mineral. 104, 471–484.

Knipping, J., Webster, J.D., Simon, A.C., Holtz, F. 2019b. Accumulation of magnetite by flotation on bubbles during decompression of silicate magma. Sci. Rep. 9, 3852.

La Cruz, N.L., Simon, A.C., Wolf, A.S., Reich, M., Barra, F., Gagnon, J.E., 2019. The geochemistry of apatite from the Los Colorados iron oxide–apatite deposit, Chile: implications for ore genesis. Miner. Deposita 54, 1143-1156.

Lattard, D., 1995. Experimental evidence for the exsolution of ilmenite from titaniferous spinel. Am. Mineral. 80, 968-981.

Liu, W., Zhang, J., Sun, T.,Wang, J., 2014. Application of apatite U–Pb and fission-track double dating to determine the preservation potential of magnetite–apatite deposits in the Luzong and Ningwu volcanic basins, eastern China. J. Geochem. Explor. 138, 22-32.

Liu, P.P, Zhou, M.F, Chen, W.T, Gao, J.F, Huang, X.W., 2015. In situ LA-ICP-MS trace elemental analyses of magnetite: Fe-Ti-(V) oxide-bearing mafic-ultramafic layered intrusions of the Emeishan Large Igneous Province, SW China. Ore Geol. Rev. 65, 853-871.

Loberg, B.E., Horndahl, A.K., 1983. Ferride geochemistry of Swedish Precambrian iron ores. Miner. Deposita 18, 487-504.

Longerich, H.P., Günther, D., Jackson, S.E., 1996. Elemental fractionation in laser ablation inductively coupled plasma mass spectrometry. Fresenius' J. Analyt. Chem 355, 538-542.

Maksaev, V., Gardeweg, M., Ramírez, C.F.,. Zentilli, M., 1988. Aplicación del método trazas de fisión (fission track) a la datación de cuerpos de magnetita de El Laco e Incahuasi en el altiplano de la Región de Antofagasta. In: Congreso Geológico Chileno, No. 5, v. 1: B1-B23.

Marschik, R., Leveille, R.A., Martin, W., 2000. La Candelaria and the Punta del Cobre district, Chile: Early Cretaceous iron-oxide Cu-Au (-Zn-Ag) mineralization. In: Porter, T.M. (Ed.), Hydrothermal Iron Oxide Copper-Gold & Related Deposits: A Global Perspective, vol. 1; PGC Publishing, Adelaide, pp. 163-175.

Marschik, R., Fontboté, L., 2001. The Candelaria-Punta del Cobre iron oxide Cu-Au (-Zn-Ag) deposits, Chile. Econ. Geol. 96, 1799-1826.

Migdisov, A.A., Bychkov, A.Y., Williams-Jones, A.E., van Hinsberg, V.J., 2014. A predictive model for the transport of copper by HCl-bearing water vapour in ore-forming magmatic-hydrothermal systems: Implications for copper porphyry ore formation. Geochim. Cosmochim. Acta 129, 33-53.

Moncada, D., Mutchler, S., Nieto, A., Reynolds, T.J., Rimstidt, J.D., Bodnar, R.J., 2012. Mineral textures and fluid inclusion petrography of the epithermal Ag–Au deposits at Guanajuato, Mexico: Application to exploration. J. Geochem. Explor. 114, 20-35.

Mongkoltip, P., Ashworth, J.R., 1983. Quantitative estimation of an open-system symplectite-forming reaction: restricted diffusion of Al and Si in coronas around olivine. J. Petrol. 24, 635-661.

Monteiro, L.V.S., Xavier, R.P., Carvalho, E.R., Hitzman, M.W., Johnson, C.A., Souza Filho, C.R., Torresi, I., 2008a. Spatial and temporal zoning of hydrothermal alteration and mineralization in the Sossego iron oxide-copper-gold deposit, Carajás Mineral Province, Brazil: Paragenesis and stable isotope constraints. Miner. Deposita 43, 129–159.

Monteiro L.V.S., Xavier, R.P., Hitzman, M.W., Juliani, C., Souza Filho, C.R., Carvalho, E.R., 2008b. Mineral chemistry of ore and hydrothermal alteration at the Sossego iron oxide–copper–gold deposit, Carajás Mineral Province, Brazil. Ore Geol. Rev. 34, 317-336.

Morrison, G.W., Teale, G.S., Hodkinson, I., 1990. Geology and gold mineralisation at Mount Leyshon, north Queensland. In: Gold update 89-90, course manual. Gold bearing breccias: Characteristics, genesis and exploration, pp. 71-74.

Moseley, D., 1984. Symplectic exsolution in olivine. Am. Mineral. 69, 139-153.

Mpodozis, C., Ramos, V., 1989. The Andes of Chile and Argentina. In: Geology of the Andes and its relation to hydrocarbon and mineral resources; Ericksen, G.E., Cañas M.T. and Reinemund, J.A. (Eds), Houston, Texas, Circum-Pacific Council for Energy and Mineral Resources, Earth Science Series, vol. 11, pp. 59-90.

Mücke, A., 2003. General and comparative considerations of whole-rock and mineral compositions of Precambrian iron-formations and their implications. Neues Jahrbuch für Mineralogie-Abhandlungen: J. Mineral. Geochem. 179, 175-219.

Mumin A.H., Corriveau L., Somarin A.K., Ootes L., 2007. Iron oxide copper-gold-type polymetallic mineralization in the Contact Lake belt, Great Bear magmatic zone, Northwest Territories, Canada: Explor. Min. Geol. 16, 187–208.

Nadoll, P., Mauk, J.L., Hayes, T.S., Koenig, A.E., Box, S.E., 2012. Geochemistry of magnetite from hydrothermal ore deposits and host rocks of the Mesoproterozoic Belt Supergroup, USA. Econ. Geol. 107, 1275-1292.

Nadoll, P., Angerer, T., Mauk, J. L., French, D., Walshe, J., 2014. The chemistry of hydrothermal magnetite: a review. Ore Geol. Rev. 61, 1-32.

Nadoll, P., Mauk, J.L., Leveille, R.A., Koenig, A.E., 2015. Geochemistry of magnetite from porphyry Cu and skarn deposits in the southwestern United States. Miner. Deposita 50, 493-515.

Naranjo, J.A., Henríquez, F., Nyström, J.O., 2010. Subvolcanic contact metasomatism at El Laco volcanic complex, central Andes. Andean Geology, 37, 110-120.

Naslund, H.R., Henríquez, F., Nyström, J.O., Vivallo, W., Dobbs, F.M., 2002. Magmatic iron ores and associated mineralisation: examples from the Chilean high Andes and coastal Cordillera. In: Hydrothermal Iron Oxide-Copper-Gold: A Global Perspective. T.M. Porter (Ed.), PGC Publishing, Adelaide, Australia, vol. 2, pp. 207-226.

Newberry, N.G., Peacor, D.R., Essene, E.J., Geissman, J.W., 1982. Silicon in magnetite: high resolution microanalysis of magnetite-ilmenite intergrowths. Contrib. Mineral. Petrol. 80, 334–340

Nold, J.L., Davidson, P., Dudley, M.A., 2013. The Pilot Knob magnetite deposit in the Proterozoic St. Francois Mountains terrane, southeast Missouri, USA: A magmatic and hydrothermal replacement iron deposit. Ore Geol. Rev. 53, 446-469.

Nold, J.L., Dudley, M.A., Davidson, P., 2014. The Southeast Missouri (USA) Proterozoic iron metallogenic province—Types of deposits and genetic relationships to magnetite–apatite and iron oxide–copper–gold deposits. Ore Geol.Rev. 57, 154-171.

Nyström, J.O., Henríquez, F., 1994. Magmatic features of iron ores of the Kiruna-type in Chile and Sweden: ore textures and magnetite geochemistry. Econ. Geol. 89, 820-839.

Olivares, V., Cembrano, J., Arancibia, G., Reyes, N., Herrera, V., Faulkner, D., 2010. Significado tectónico y migración de fluidos hidrotermales en una red de fallas y vetas de un Dúplex de rumbo: un ejemplo del Sistema de Falla de Atacama. Andean Geology 37, 473-497.

Oliveros, V., Féraud, G., Aguirre, L., Fornari, M., Morata, D., 2006. The Early Andean Magmatic Province (EAMP): 40Ar/39Ar dating on Mesozoic volcanic and plutonic rocks from the Coastal Cordillera, northern Chile. J. Volcanol. Geotherm. Res. 157, 311-330.

Ovalle, J.T., La Cruz, N.L., Reich, M., Barra, F., Simon, A.C., Konecke, B.A., Morata, D., 2018. Formation of massive iron deposits linked to explosive volcanic eruptions. Sci. Rep. 8, 14855.

Oyarzún, J., Frutos, J., 1984. Tectonic and petrological frame of the Cretaceous iron deposits of north Chile. Min. Geol. 34, 21-31.

Oyarzún, R., Oyarzún, J., Ménard, J.J., Lillo, J., 2003. The Cretaceous iron belt of northern Chile: role of oceanic plates, a superplume event, and a major shear zone. Miner. Deposita 38, 640-646.

Palma, G., Barra, F., Reich, M., Valencia, V., Simon, A.C., Vervoort, J., Romero, R., 2019. Halogens, trace element concentrations, and Sr-Nd isotopes in apatite from iron oxide-apatite (IOA) deposits in the Chilean iron belt: Evidence for magmatic and hydrothermal stages of mineralization. Geochim. Cosmochim. Acta 246, 515-540.

Pang, K.N., Li, C., Zhou, M.F., Ripley, E.M., 2008. Abundant Fe–Ti oxide inclusions in olivine from the Panzhihua and Hongge layered intrusions, SW China: evidence for early saturation of Fe–Ti oxides in ferrobasaltic magma. Contrib. Mineral. Petrol. 156, 307-321.

Pang, K.N., Zhou, M.F., Qi, L., Shellnutt, G., Wang, C.Y., Zhao, D., 2010. Flood basalt-related Fe–Ti oxide deposits in the Emeishan large igneous province, SW China. Lithos 119, 123-136.

Paton, C., Hellstrom, J., Paul B., Woodhead, J., Hergt, J., 2011. Iolite: Freeware for the visualization and processing of mass spectrometric data. J. Anal. At. Spectrom. 26, 2508-2518.

Peterson, E.C., Mavrogenes, J.A., 2014. Linking high-grade gold mineralization to earthquake-induced fault-valve processes in the Porgera gold deposit, Papua New Guinea. Geology 42, 383–386.

Polivchuk, M., 2017. The Formation of Vanadium Deposits in the Archean Rivière Bell Complex, Quebec: Insights from Fe-Ti Oxide Chemistry. PhD thesis, Univ. of Ottawa.

Pollard, P.J., 2006. An intrusion-related origin for Cu–Au mineralization in iron oxide–copper–gold (IOCG) provinces. Miner. Deposita 41, 179.

Putnis, A., 2009. Mineral replacement reactions. Rev. Mineral. Geochem.70, 87-124.

Raab, A., 2001. Geology of the Cerro Negro Norte Fe-oxide (Cu-Au) District, Coastal Cordillera, northern Chile. MSc thesis, Oregon State Univ. 273 p.

Ramos, V.A., 2010. The tectonic regime along the Andes: Present day and Mesozoic regimes. Geol. J. 45, 2-25.

Rapp, J.F., Klemme, S., Butler, I.B., Harley, S.L. 2010. Extremely high solubility of rutile in chloride and fluoride-bearing metamorphic fluids: An experimental investigation. Geology 38, 323-326.

Regan, S., Lupulescu, M., Jercinovic, M., Chiarenzelli, J., Williams, M., Singer, J., Bailey, D., 2019. Age and Origin of Monazite Symplectite in an Iron Oxide-Apatite Deposit in the Adirondack Mountains, New York, USA: Implications for Tracking Fluid Conditions. Minerals 9, 65.

Reich, M., Deditius, A., Chryssoulis, S., Li, J.W., Ma, C.Q., Parada, M.A., Mittermayr, F., 2013. Pyrite as a record of hydrothermal fluid evolution in a porphyry copper system: A SIMS/EMPA trace element study. Geochim. Cosmochim. Acta 104, 42-62.

Reich, M., Simon, A.C., Deditius, A., Barra, F., Chryssoulis, S., Lagas, G., Roberts, M.P., 2016. Trace element signature of pyrite from the Los Colorados iron oxide-apatite (IOA) deposit, Chile:

A missing link between Andean IOA and iron oxide copper-gold systems? Econ. Geol. 111, 743-761.

Rhodes, A.L., Oreskes, N., 1995. Magnetite deposition at El Laco, Chile: implications for Fe-oxide formation in magmatic-hydrothermal systems. In: Giant ore deposits-II: Controls on the scale of orogenic magmatic-hydrothermal mineralization. Clark, A.H. (Ed.), Proceedings of the Second Giant Ore Deposits Workshop, Queen's University: 582-622. Kingston, Ontario, Canada.

Rhodes, A.L., Oreskes N., 1999. Oxygen isotope composition of magnetite deposits at El Laco, Chile: Evidence of formation from isotopically heavy fluids. In: Geology and Ore Deposits of the Central Andes, B.J. Skinner (Ed.) SEG Sp. Pub. 7, 333-351.

Rieger, A.A., Marschik, R., Díaz, M., Hölzl, S., Chiaradia, M., Akker, B., Spangenberg, J.E., 2010. The hypogene iron oxide copper-gold mineralization in the Mantoverde district, northern Chile. Econ. Geol. 105, 1271-1299.

Rieger, A.A., Marschik, R., Díaz, M., 2012. The evolution of the hydrothermal IOCG system in the Mantoverde district, northern Chile: new evidence from microthermometry and stable isotope geochemistry. Miner. Deposita 47, 359-369.

Río Tinto internal report., 2001. Sofía Prospect Final Report , Region II, Antofagasta, Chile.

Rojas, P., Barra, F., Reich, M., Deditius, A., Simon, A., Uribe, F., Romero, R., Rojo, M., 2018a. A genetic link between magnetite mineralization and diorite intrusion at the El Romeral iron oxide-apatite deposit, northern Chile. Miner. Deposita 53, 947-966.

Rojas, P., Barra, F., Deditius, A., Reich, M., Simon ,A., Roberts, M., Rojo, M., 2018b. New contributions to the understanding of Kiruna-type iron oxide-apatite deposits revealed by magnetite ore and gangue mineral geochemistry at the El Romeral deposit, Chile. Ore Geol. Rev. 93 413-435.

Roman, N., Reich, M., Leisen, M., Morata, D., Barra, F., 2019. Geochemical and micro-textural fingerprints of boiling in pyrite. Geochim. Cosmochim. Acta 246, 60–85.

Rusk, B., Oliver, N., Cleverley, J., Blenkinsop, T., Zhang, D., Williams, P., Habermann, P., 2010. Physical and chemical characteristics of the Ernest Henry iron oxide copper gold deposit, Australia; implications for IOGC genesis. In Implications for IOGC Genesis; PGC Publishing: Adelaide, Australia.

Sanchez-Alfaro, P., Reich, M., Arancibia, G., Driesner, T., Pérez-Flores, P., Cembrano, J., Heinrich, C., Rowland, J., Tardani, D., Campos, E., 2016. The optimal windows for seismically-enhanced gold precipitation in the epithermal environment. Ore Geol. Rev. 79, 463–473.

Salazar, E., Barra, F., Reich, M., Simon, A., Leisen, M., Palma, G., Rojo, M., 2019. Trace element geochemistry of magnetite from the Cerro Negro Norte iron oxide− apatite deposit, northern Chile. Miner. Deposita 1-20.

Scheuber, E., Andriessen, P.A., 1990. The kinematic and geodynamic significance of the Atacama fault zone, northern Chile. J. Struct. Geol. 12, 243-257.

Scheuber, E., Bogdanic, T., Jensen, A., Reutter, K. J., 1994. Tectonic development of the north Chilean Andes in relation to plate convergence and magmatism since the Jurassic. In: Tectonics of the southern central Andes. Springer, Berlin, Heidelberg, 121-139.

Scheuber, E., González, G., 1999.Tectonics of the Jurassic-Early Cretaceous magmatic arc of the north Chilean Coastal Cordillera (22°-26° S): a story of crustal deformation along a convergent plate boundary. Tectonics 18, 859-910.

Shimazaki, H., 1998. On the occurrence of silician magnetites. Resour. Geol. 48, 23-29.

Shore, M., Fowler, A.D., 1996. Oscillatory zoning in minerals; a common phenomenon. Can. Mineral. 34, 1111-1126.

Sibson, R.H., Moore, J.M.M., Rankin, A.H., 1975. Seismic pumping—a hydrothermal fluid transport mechanism. J. Geol. Soc. London 1316, 653-659.

Sibson, R.H., 2001. Seismogenic framework for hydrothermal transport and ore deposition. Rev. Econ. Geol. 14, 25-50.

Sievwright, R.H., Wilkinson, J.J., O'Neill, H.S.C., Berry, A.J., 2017. Thermodynamic controls on element partitioning between titanomagnetite and andesitic–dacitic silicate melts. Contrib. Mineral. Petrol. 172, 62.

Sillitoe, R., 1979. Some thoughts on gold-rich porphyry copper deposits. Miner. Deposita 14, 161-174.

Sillitoe, R. Burrows, D., 2002. New field evidence bearing on the origin of the El Laco magnetite deposit, northern Chile. Econ. Geol. 97, 1101-1109.

Sillitoe, R., 2003. Iron oxide–copper–gold deposits: An Andean view. Miner. Deposita 38, 787–812.

Simon, A.C., Pettke, T., Candela, P.A., Piccoli, P.M., Heinrich, C.A., 2004. Magnetite solubility and iron transport in magmatic-hydrothermal environments. Geochim. Cosmochim. Acta 68, 4905-4914.

Simon, A.C., Ripley, E.M., 2011. The role of magmatic sulfur in the formation of ore deposits. Rev. Mineral. Geochem. 73, 513-578.

Simon, A.C., Kniping, J., Reich, M., Barra, F., Deditius, A.P., Bilenker, L., Childress, T., 2018. Kiruna-Type Iron Oxide-Apatite (IOA) and Iron Oxide Copper-Gold (IOCG) Deposits form by a combination of ignous and magmatic-hydrothermal processes: evidence from the Chilean Iron Belt. SEG Sp. Pub. 21, 89-114.

Song, X.Y, Qi, H.W, Hu, R.Z, Chen, L.M, Yu, S.Y, Zhang, J.F., 2013. Formation of thick stratiform Fe-Ti oxide layers in layered intrusion and frequent replenishment of fractionated mafic magma: Evidence from the Panzhihua intrusion, SW China. Geochem Geophys. 14, 712-732.

Sossi, P.A., Prytulak, J., O'Neill, H.S.C., 2018. Experimental calibration of vanadium partitioning and stable isotope fractionation between hydrous granitic melt and magnetite at 800 C and 0.5 GPa. Contrib. Mineral. Petrol. 173, 27.

Staudigel, H., Schreyer, W., 1977. The upper thermal stability of clinochlore, Mg5Al [AlSi3O10](OH) 8, at 10–35 kb PH2O. Contrib. Mineral. Petrol. 61, 187-198.

Taghipour, S., Kananian, A., Harlov, D., Oberhänsli, R., 2015. Kiruna-type iron oxide-apatite deposits, Bafq district, Central Iran: fluid-aided genesis of fluorapatite-monazite-xenotime assemblages. Can. Mineral. 00, 1-17.

Tan, W., Wang C,Y., He, H., Xing, C., Liang, X.L., Dong, H. 2015. Magnetite-rutile symplectite derived from ilmenite-hematite solid solution in the Xinjie Fe-Ti oxide-bearing, mafic-ultramafic layered intrusion (SW China) Am. Mineral., 100, 2348–2351.

Tan, W., Liu, P., 2016. Mineralogy and origin of exsolution in ti-rich magnetite from different magmatic fe-ti oxide-bearing intrusions. Can. Mineral. 54, 539-553.

Tanis, E.A., Simon, A.C., Zhang, Y., Chow, P., Xiao, Y., Hanchar, J.M., Tschauner, O., Shen, G., 2016. Rutile solubility in NaF-NaCl-KCl-bearing aqueous fluids at 0.5-2.79 GPa and 250-650°C. Geochim. Cosmochim. Acta 177, 170-181.

Tardani, D., Reich, M., Deditius, A.P., Chryssoulis, S., Sánchez-Alfaro, P., Wrage, J., Roberts, M.P., 2017. Copper–arsenic decoupling in an active geothermal system: A link between pyrite and fluid composition. Geochim. Cosmochim. Acta 204, 179-204.

Toplis, M.J., Corgne, A., 2002. An experimental study of element partitioning between magnetite, clinopyroxene and iron-bearing silicate liquids with particular emphasis on vanadium. Contrib. Mineral. Petrol. 144, 22-37.

Torab, F.M., Lehmann, B., 2007. Magnetite-apatite deposits of the Bafq district, Central Iran: apatite geochemistry and monazite geochronology. Mineral. Mag. 71, 347-363.
Tornos, F., Velasco, F., Hanchar, J.M., 2016. Iron-rich melts, magmatic magnetite, and superheated hydrothermal systems: The El Laco deposit, Chile. Geology 44, 427–430.

Treloar P.J., Colley, H., 1993. Magnetite-apatite ores in the Atacama Fault Zone, El Salvador Region, northern Chile. Second ISAG, Oxford (UK), 21-23/9/1993.

Treloar, P.J., Colley, H., 1996. Variations in F and Cl contents in apatites from magnetite—apatite ores in northern chile, and their ore-genetic implications. Mineral. Mag. 60, 285-301.

Ulrich, T., Gunther, D., Heinrich, C.A., 2001. The evolution of a porphyry Cu-Au deposit, based on LA-ICP-MS analysis of fluid inclusions: Bajo de la Alumbrera, Argentina: Econ. Geol. 96, 1743–1774.

Uyeda, S., Kanamori, H., 1979. Back-arc opening and the mode of subduction. J. Geophys. Res. 84, 1049-1061.

Velasco, F., Tornos, F., 2009. Origen de las Pegmatitas de Magnetita-Apatito de la Mina Carmen del Fierro (Atacama, Chile). Macla n°11 septiembre 2009, Revista de la Sociedad Española de Mineralogía.

Velasco, F., Tornos, F., Hanchar, J.M., 2016. Immiscible iron-and silica-rich melts and magnetite geochemistry at the El Laco volcano (northern Chile): Evidence for a magmatic origin for the magnetite deposits. Ore Geol. Rev. 79, 346-366.

Vivallo, W., Henríquez, F., Espinoza, S., 1994. Oxygen and sulfur isotopes in hydrothermally altered rocks and gypsum deposits at El Laco mining district, northern Chile: Comunicaciones [Departamento de Geología, Universidad de Chile], n 45, 93-100.

Vivallo, W., Espinoza, S., Henriquez, F., 1995. Metasomatismo y alteración hidrotermal en el distrito ferrífero Cerro Negro Norte, Copiapó, Chile. Andean Geology 22, 75-88.

Von Gruenewaldt, G., Sharpe, M.R., Hatton, C.J., 1985. The Bushveld Complex; introduction and review. Econ. Geol. 80, 803-812.

Wang, C.Y., Zhou, M.F., Zhao, D.G., 2008. Fe-Ti-Cr oxides from the Permian Xinjie mafic-ultramafic layered intrusion in the Emeishan large igneous province, SW China: crystallization from Fe- and Ti-rich basaltic magmas. Lithos 102, 198-217.

Weis, F., Troll, V., Jonsson, E., Högdahl, K., Barker, A., Harris, C., Nilsson, K.P., 2013. Iron and oxygen isotope characteristics of apatite-iron-oxide ores from central Sweden. In: Mineral deposit research for a high-tech world, pp. 1675-1678.

Wen, G., Li, J.W., Hofstra, A.H., Koenig, A.E., Lowers, H.A., Adams, D., 2017. Hydrothermal reequilibration of igneous magnetite in altered granitic plutons and its implications for magnetite classification schemes: Insights from the Handan-Xingtai iron district, North China Craton. Geochim. Cosmochim. Acta 213, 255-270.

Westhues, A., Hanchar, J.M., Whitehouse, M.J., Martinsson, O., 2016. New constraints on the timing of host-rock emplacement, hydrothermal alteration, and iron oxide-apatite mineralization in the Kiruna district, Norrbotten, Sweden. Econ. Geol. 111, 1595-1618.

Westhues, A., Hanchar, J.M., LeMessurier, M.J., Whitehouse, M. J., 2017a. Evidence for hydrothermal alteration and source regions for the Kiruna iron oxide–apatite ore (northern Sweden) from zircon Hf and O isotopes. Geology 45, 571-574.

Westhues, A., Hanchar, J.M., Voisey, C.R., Whitehouse, M.J., Rossman, G.R., Wirth, R., 2017b. Tracing the fluid evolution of the Kiruna iron oxide apatite deposits using zircon, monazite, and whole rock trace elements and isotopic studies. Chem. Geol. 466, 303-322.

Williams, P.J., Barton, M.D., Fontbote, L., de Haller, A., Johnson, D.A., Mark, G., Marschik, R., Oliver, N.H. S., 2005. Iron oxide-copper-gold deposits: Geology, space-time distribution, and possible modes of origin. Econ. Geol. 100th Anniv. Vol. pp. 371–406.

Williams-Jones, A.E., Heinrich, C.A., 2005. Vapor transport of metals and the formation of magmatic-hydrothermal ore deposits. Econ. Geol. 100th Anniv.Vol. pp. 1287-1312

Williams-Jones, A.E., Migdisov, A.A., 2014. Experimental constraints on the transport and deposition of metals in ore-forming hydrothermal systems: SEG Sp. Pub. 18, 77–95.

Yin, S., Ma,. C, Robinson, P.T., 2017. Textures and high field strength elements in hydrothermal magnetite from a skarn system: Implications for coupled dissolution-reprecipitation reactions. Am. Mineral. 102, 1045–1056.

Zajacz, Z., Candela, P.A., Piccoli, P.M., Sanchez-Valle, C., 2012a. The partitioning of sulfur and chlorine between andesite melts and magmatic volatiles and the exchange coefficients of major cations. Geochim. Cosmochim. Acta 89, 81-101.

Zajacz, Z., Candela, P.A., Piccoli, P.M., Wälle, M., Sanchez-Valle, C., 2012b. Gold and copper in volatile saturated mafic to intermediate magmas: Solubilities, partitioning, and implications for ore deposit formation. Geochim. Cosmochim. Acta 91, 140-159.

Zeng, L., Zhao, X., Li, X., Hu, H., McFarlane, C., 2016. In situ elemental and isotopic analysis of fluorapatite from the Taocun magnetite-apatite deposit, Eastern China: Constraints on fluid metasomatism. Am. Mineral. 101, 2468-2483.

Zhou, M.F., Robinson, P.T., Lesher, C.M., Keays, R.R., Zhang, C.J., Malpas, J., 2005. Geochemistry, petrogenesis and metallogenesis of the Panzhihua gabbroic layered intrusion and associated Fe–Ti–V oxide deposits, Sichuan Province, SW China. J. Petrol. 46, 2253-2280.

3.9. Tables

Table 4. Main geological features of studied IOA deposits and most important IOCG deposits.

Deposit	Tonnage	Host rock (Formation)	Related intrusive rocks	Main structures	Age (technique)	Mineralization style	Alteration	Mineralization	Data source
Iron oxide-apatite (IOA) deposits of the Chilean Iron Belt (25-31°S)									
Los Colorados	491 Mt @36.5% Fe	Basaltic andesite, andesite lava flows and volcanoclastic rocks (Punta del Cobre Formation)	Diorite-microdiorite pluton	N10-15E; NS-N10 W faults	110-115 Ma (radiometric K-Ar)	Massive, tabular, dikes, breccias	Act, Ap, Chl, K-feld, Turm, Ser,clays	Mgt±Hmt; Py-Cpy	Pichon (1981), Oyarzún and Frutos (1984), Knipping et al. (2015a, 2015b), Reich et al (2016), Pincheira et al., (1990)
El Romeral	451 Mt@28.3% Fe	Andesite porphyry, metasedimentary rocks (La Liga Formation)	Diorite body, granodiorite pluton	Romeral fault (NS); NNE fault	129.0 ± 0.9 Ma (U-Pb on zircon)	Massive, veins, disseminated	Act, Ap, Bio, Chl	Mgt; Py-Cpy	Bookstrom (1977); Emparan and Pineda (2005), Rojas et al. (2018a, b)
Cerro Negro Norte	657.3 Mt@29.7% Fe	Volcanic breccias and andesite lavas (Bandurrias Formation)	Diorite and quartz-diorite stocks; monzodiorite to granodiorite dikes	NNE and EW fault	130.5 ± 0.7 Ma (U-Pb on zircon)	Massive, tabular to lobular; breccias, stockworks, disseminated	Act, Scap, Ap, Alb, Qz, Ttn, Ep, Bio, Carb, Tourm, Ser, Jar, Goe	Mgt±Hem; Py-Cpy±Bn; minor Cu-ox	Vivallo et al. (1995); Raab (2001); CAP Minería Annual Report (2016); Salazar et al. (2019)
Carmen	NR	Andesitic lava (La Negra Formation)	Diorite dike and quartz diorite pluton	EW, NE faults*	131.0 ±1.0 Ma (U-Pb on apatite); of 130.0±1.7 Ma (Lu-Hf on apatite)	Massive, dikes, veins, breccia	Act, Cl-ap, Chl, Qz, Ser, clays, Gyp	Mgt±Hmt; Py-Cpy	Treloar and Colley (1996); Gelcich et al. (2005), Zhang et al. (2017); Palma et al. (2019)
Fresia	NR	Andesitic lava (Los Cerros Florida Formation)	Microgabbro to microdiorite dikes	Two sets of faults trending at 80° and 65° *	132.8±5.3 Ma (Lu-Hf apatite)	Massive, dikes, veins, breccia	Ep, Chl, Carb, Qz, Cl-ap, clays	Mgt±Hmt	Treloar and Colley (1996); Zhang et al. (2017); Palma et al. (2019)
Mariela	NR	Granodiorite (Aeropuerto Formation)	Diorite	NNE-orientation (related to breccia pipe) ; N-S faults*	117.3±0.4 Ma (Lu-Hf apatite)	Breccia pipe, tabular	Chl, Ep, Ttn, Gyp, Qz, Goe	Mgt±Hmt; Py-Cpy; Chry±At	Río Tinto internal report (2001); Zhang et al. (2017); Palma et al. (2019)

El Laco IOA deposit (23° S)									
El Laco	733.9 Mt@49.2% Fe	Andesitic to dacitic lava flows and pyroclastic rocks (El Laco Volcanic Complex))	NR	NW and EW faults	Between 5.3 ± 1.9 and 1.6 ± 0.5 Ma (whole-rock K-Ar); 2.1 ±0.1 Ma (fission track apatite)	Lava-like flows (Laco Norte, Laco Sur and San Vicente Alto), tabular (Rodados Negros and Cristales Grandes) and dome-shaped bodies (San Vicente Bajo)	At depth: Scap, Di; steam-heated zones: Trd,Crs, Alu, Jar	Mgt±Hmt	Maksaev et al. (1988); Nyström and Henríquez. (1994), Naranjo et al. (2010); CAP Minería Annual report (2016)
Iron oxide Cu-Au (IOCG) deposits of the Chilean Iron Belt (25-31°S)									
Candelaria	470 Mt @0.95% Cu, 0.22 g/t Au, 3.1 g/t Ag	Volcanic, volcanoclastic and sedimentary units (Punta del Cobre Formation)	Diorite to quartz monzonite bodies, dikes and sills	NE-trending antiform (Tierra Amarilla anticlinorium); El Bronce SE-verging fold-thrust system; N-NW to NW sinistral transcurrent faults; N-, E-NE to NE- faults	115.2 ± 0.6 Ma (Re-Os molybdenite)	Veins, breccias, stratabound bodies (replacement-type), disseminated	Mgt, Act, Bio, K-feld, Qz	Cpy-Py-Po±Sp-Mo; Mgt±Mush; poorly developed Cu oxides, supergene enrichment zone	Marschik et al. (2000); Marschik and Fontboté (2001); Mathur et al. (2002); del Real et al. (2018)
Mantoverde	42.7 Mt @0.58% Cu (oxides); 440 Mt @0.56% Cu (sulfides), 0.12 g/t Au	Basaltic andesite, andesite flows and volcanoclastic rocks (La Negra Formation)	Granodiorite, diorite	Mantoverde fault: N15-20W/40-50E	128.9 ± 0.3 Ma (U-Pb zircon)	Veins, stockworks, breccias	K-feld, Bio, Tourm, Qz, Chl, Ser, Scap, Ep, Carb	Py-Cpy±gold; ; Cu ox; Mgt-Hmt	Gelcich et al. (2002), Benavides et al. (2007), Rieger et al. (2010, 2012)

Abbreviations: NR= not reported; Act= actinolite; Alb=albite;Alu=alunite; Ap= apatite; At=atacamite; Bio=biotite; Bn=bornite; Carb=carbonate; Chry=chrysocolla; Cpy=chalcopyrite; Chl=chlorite; Crs=cristobalite; Di=diopside; Ep=epidote; Goe=goethite; Gyp=gypsum; Hmt=hematite;Jar=jarosite; K-feld=K-feldspar; Mgt=magnetite ; Mo=molybdenite; Mush=mushketovite; Po=pyrrhotite; Py=pyrite Qz=quartz; Scap=scapolite; Sp=sphalerite; Ser=sericite; Tourm=tourmaline; Ttn=titanite; Trd=trydimite.
* Related to extensional strike-slip duplexes configuration.

Table 5. Summary of the main magnetite types and observed microtextures in the Andean IOA deposits under study.

Sector/ classification	Magnetite type	Main features/textures	Mineral inclusions	Geochemical analyses
Los Colorados				
Massive magnetite Western dike	Type-1	Inclusion-rich magnetite cores.	Polycrystalline large inclusions (≥ 10 um): Act, Cpx, Ttn, and an unspecified Mg-Al-Si-phase. Smaller inclusions often contain NaCl and KCl crystals.	EPMA and LA-ICP-MS
	Type-2	Pristine to inclusion-poor transition zone.		EPMA and LA-ICP-MS
	Type-3	Inclusion-free rims.		EPMA and LA-ICP-MS
Late-stage magnetite veinlets in the diorite intrusion	Magnetite-X	Euhedral magnetite with oscillatory and sector zoning. Some magnetite is partly recrystallized to porous fine-grained (~5 um) microcrystalline aggregates of Magnetite-X and silicates (e.g., amphibole).		EPMA
	Magnetite-Y	Magnetite with "tooth-like" texture and sector zoning (~ 500 um size).	Di, Cen, Am, Mca, Usp and Ti-mgt.	EPMA
	Magnetite-Z	Coarsed-grained magnetite with oscillatory zoning. Volumetrically, the most abundant of the three types of the late-stage magnetite veinlets.	Si and Al form particles in trace element-rich bands of magnetite (zones enriched in Al, Mg, Si and Ca); Ti and Mn form particles in trace element-poor bands (zones depleted in Al, Mg, Si and Ca).	EPMA
El Romeral				
Magnetite ore body (central and deep parts of the system)	Type-I	Early, inclusion-rich magnetite cores (~35 modal %).	Oriented or randomly distributed high-temperature polycrystalline and one-phase inclusions (50 um-few nanometers). Large inclusions: Act, Ilm and Rt. Small inclusions: Rt, Ilm, Ttn, Chl, Phl, NaCl, Prg, Clc, Cal and Tr. At shallow depths (< 100 m), Si-rich inclusions occur aligned along magnetite crystallographic planes.	EPMA and LA-ICP-MS
	Type-II	Pristine, inclusion-free magnetite rim. It occurs as an overgrowth on magnetite Type I (~60 modal %).		EPMA and LA-ICP-MS
Magnetite ore body (margin and shallow portions of the system)	Type-III	Inclusion-poor, chemically-zoned magnetite (~5 modal %).		NA

Magnetite ore body (central and deep parts of the system)	Type-IV	Inclusion-poor magnetite veinlets that crosscut the massive magnetite (late event).		NA
Cerro Negro Norte				
Massive magnetite	Type-I	Inclusion-rich magnetite cores.	Single or polycrystalline inclusions randomly distributed and/or arranged following crystallographic planes in magnetite (nano-meter size to a few tens of um): Act, Qz, Mg-Al-Si-phase, Rt, Ilm, Aug, Hy-En.	EPMA and LA-ICP-MS
	Type-II	Pristine, inclusion-free magnetite rims. It occurs as an overgrowth on Type I.		EPMA and LA-ICP-MS
	Type-III	Sub-to idiomorphic octahedral grains with an inclusion-poor core displaying a cryptic zonation towards the rim of the crystal.		EPMA and LA-ICP-MS
	Type-IV	Late magnetite vein event that crosscuts all the other magnetite types.	Randomly distributed inclusions and/or organized in repetitive sinous arrangements (micron-to sub-micron sized): Act, Qz, Aeg, Hy-En.	EPMA and LA-ICP-MS
Carmen				
Massive magnetite ore body	Type-I	Inclusion-rich magnetite. Some magnetite exhibit oscillatory zoning (bands of 5-70 μm wide). Ca-Mg-carbonates, apatite, monazite and titanite veinlets crosscut and fill open spaces (~50 modal %).	Abundant mineral inclusions (~30 μm to <1 μm) aligned along magnetite crystallographic planes or randomly distributed. In grains with oscillatory zoning, inclusions are concentrated in darker bands: Mg, Al, Fe-bearig silicates, Ilm and Rt.	EPMA and LA-ICP-MS
	Type-II	Inclusion-free, pristine magnetite veinlets that crosscut magnetite Type-I.		EPMA and LA-ICP-MS
	Type-III	Large magnetite grains intergrown with coarse actinolite and apatite crystals. Some grains exhibit porosity or show recrystallization textures (fine-grained aggregates of magnetite exhibiting a mosaic texture) (~30 modal %).	Nano-inclusions/exsolution lamellae either oriented, randomly distributed or clustered in the grain cores.	EPMA and LA-ICP-MS
	Type-IV	Late generation of inclusion-poor magnetite veinlets (few cm-tens cm) that crosscut magnetite Type-III. Type-IVa is associated with Cl-rich apatite, monazite and enstatite, whereas Type-IVb exhibits porosity.		EPMA and LA-ICP-MS
Fresia				
Massive magnetite ore body	Type-A	Massive magnetite that exhibits a well-developed and clear oscillatory zoning. Some grains are recrystallized to subhedral porous aggregates of magnetite (foam-like triple junctions) (~40 modal %).	Scarce mineral inclusions.	EPMA and LA-ICP-MS
	Type-B	Matrix of magnetite aggregates in which apatite and minor actinolite are intergrown. Some grains exhibit exsolution lamellae (~30 modal %).	Some grains exhibit submicrometer-sized inclusions mainly oriented along magnetite crystallographic planes.	EPMA and LA-ICP-MS
	Type-C	Crustiform-colloform banding magnetite with minor quartz and Cl-rich apatite. Recrystallization to fine-grained magnetite, porosity and/or oscillatory zoning are recognized in individual grains in the magnetite bands (~25 modal %).	Scarce mineral inclusions.	EPMA and LA-ICP-MS

	Type-D	Late magnetite veinlets (centimetric), intergrown with actinolite crystals, which crosscut the altered host rock. Recrystallized to porous aggregates of magnetite (mosaic texture) (~5 modal %).		EPMA and LA-ICP-MS
Mariela				
Breccia pipe	Type-α	Magnetite with symplectitic texture (interstitial magnetite and vermicular rutile, titanite and scarce ilmenite. Hematite replacement occurs along both grain boundaries and crystallographic planes (~40 modal %).		EPMA and LA-ICP-MS
	Type-β	Magnetite with ulvöspinel/ilmenite exsolution lamellae. It occurs in sharp contact with Type-α. Abundant fractures and open spaces are filled with titanite and minor ilmenite (~5 modal %).	Nano-inclusions of Fe-Ti-oxides.	EPMA and LA-ICP-MS
	Type-γ	Late generation of pristine magnetite. It occurs as an overgrown or veinlets that crosscut magnetite Type α (~30 modal %).	Act	EPMA and LA-ICP-MS
	Type-δ	Magnetite veinlets with euhedral to subhedral magnetite and minor apatite that crosscut the altered host rock. It is characterized by a well-defined cubic cleavage and exhibits an unspecified Fe-Mg-Al-O-bearing mineral exsolution lamellae (altered to titanite, rutile and an unspecified Mn-silicate) (~10 modal %).		EPMA and LA-ICP-MS
	Type-ε	Si-rich magnetite replacement with a colloform-banding texture. It hosts small grains of pyrite (< 10 um; < 1 modal %) (~10 modal %).		NA
El Laco-Laco Norte				
Massive magnetite ore body (shallow-surface zone/outcrop)	Magnetite-S	Magnetite (>500 μm size) with abundant microporosity and pervasive replacement by hematite and goethite (grain boundaries, fractures and pores).		EPMA and LA-ICP-MS
Massive magnetite ore body (shallow/surface zone) ~30-65 m depth	Magnetite-Z	Weakly to moderate oxidized magnetite with hematite formation along rims or through fractures. It forms aggregates of pristine, mostly euhedral crystals (~10-120 um). Late gypsum veinlets crosscut and fill open spaces in massive Magnetite-Z.		EPMA and LA-ICP-MS
Massive magnetite ore body (intermediate zone) ~65-145 m depth	Magnetite-X	Magnetite with pristine microcrystalline cores (~500 um). Replaced by Magnetite-Y.		EPMA and LA-ICP-MS
	Magnetite-Y	Magnetite with oscillatory texture (individual bands of ~4-100 um).		EPMA and LA-ICP-MS

	Magnetite-γ	It occurs as an overgrown on inclusion-rich relict cores of Magnetite-β.	It host inclusions from 10´s to 100´s nanometers to a few micrometers.	EPMA and LA-ICP-MS
Breccia body (deep zone) ~150-200 m	Magnetite-β	Coarse-grained euhedral crystals that contain inclusion-rich cores (Magnetite-β) surrounded by inclusion-free rims (Magnetite-β1). A third generation of smaller anhedral magnetite crystals associated with gypsum veinlets occurs at the outer rim of the inclusion-free magnetite (Magnetite-β2).		EPMA and LA-ICP-MS
	Magnetite-α	Aggregates of titano-magnetite crystals (~100-300 um size) with well-developed ilmenite exsolution lamellae and oxidation zones along grain rims and fractures.		EPMA and LA-ICP-MS

Notes: Data source: Knipping et al. (2015a, b), Deditius et al. (2018), Ovalle et al. (2018), Rojas et al. (2018b) and Salazar et al. (2019).
*Magnetite Type-3 defined by Knipping et al. (2015a, b) was later classified as Magnetite-X, -Y, and -Z by Dedidius et al. (2018).
Magnetite types from Carmen, Fresia and Mariela are defined in this study. See text for a more detailed description.
Abbreviations: NA= not analyzed, Act= actinolite, Aeg=aegirine, Am=amphinole, Aug=augite, Cal=calcite, Cen= clinoenstatite, Chl= chlorite, Clc= clinochlore, Cpx=clinopyroxene, Di=diopside, En= enstatite, Hy=hyperthene, Ilm=ilmenite, Mca= mica, Phl=phlogopite, Prg=pargasite, Qz=quartz, Rt=rutile, Tr=tremolite, Ti-mgt=Ti-rich magnetite, Ttn= titanite,Usp=ulvöspinel.

Table 6. Data summary of EPMA analyses for magnetite types from Los Colorados, El Romeral, Cerro Negro Norte, Carmen, Fresia, Mariela and El Laco.

Magnetite type	N	Mg	n	Al	n	Si	n	Ca	n	Ti	n	V	n	Mn	n	Fe	O	Total
Los Colorados																		
Type-1*	20	0.18-0.78 *0.49*	0	0.12-0.7 *0.48*	0	BDL-0.66 *0.36*	6	BDL-0.3 *0.15*	6	0.3-0.75 *0.44*	0	0.49-0.68 *0.62*	0	0.09-0.23 *0.14*	0	65.2-68.6 *67.2*	26.8-27.8 *27.4*	96.5-98.0 *97.2*
Type-2*	41	0.08-0.48 *0.19*	0	0.04-0.35 *0.17*	0	BDL-0.39 *0.05*	*7*	BDL-0.08 *0.03*	7	0.03-0.39 *0.12*	0	0.27-0.68 *0.36*	0	0.06-0.19 *0.12*	0	67.8-71.0 *70.1*	26.4-27.9 *27.4*	95.0-100 *98.5*
Type-3*	12	0.06-0.23 *0.13*	0	BDL-0.06 *0.03*	7	BDL-0.09 *0.05*	*8*	BDL-0.05 *0.02*	2	0.01-0.24 *0.03*	0	0.05-0.36 *0.21*	0	0.08-0.11 *0.1*	0	69.5-70.6 *69.9*	26.8-27.4 *26.9*	97-98.8 *97.4*
All Data**	551	BDL-6.96 *0.29*	4	BDL-1.82 *0.21*	8	BDL-4.18 *0.15*	42	BDL-3.64 *0.08*	61	BDL-9.0 *0.24*	21	0.05-0.68 *0.3*	0	0.02-2.23 *0.13*	0	43.8-72.5 *70.6*	25.2-31.4 *27.8*	86.2-103 *99.7*
Magnetite-X	49	0.05-0.81 *0.24*	0	0.19-1.10 *0.46*	0	0.04-1.34 *0.48*	0	0.01-0.37 *0.14*	0	0.07-0.85 *0.14*	0	0.26-0.27 *0.26*	0	0.03-0.27 *0.07*	0	66.4-71.6 *70*	25.3-27.3 *26.7*	96.3-99.8 *98.6*
Magnetite-Y	50	0.01-0.93 *0.23*	0	0.18-1.21 *0.5*	0	BDL-2.18 *0.43*	4	BDL-0.91 *0.19*	6	0.08-5.49 *0.27*	0	0.22-0.27 *0.26*	0	0.04-5.10 *0.2*	0	60.7-72.3 *70*	23.2-27.6 *26.7*	95-101 *99*
Magnetite-Z	94	0.01-2.06 *0.3*	0	0.13-1.18 *0.42*	0	0.009-1.83 *0.4*	0	0.01-0.59 *0.16*	0	0.06-1.27 *0.15*	0	0.21-0.24 *0.23*	0	0.02-0.23 *0.1*	0	65.2-72.2 *70*	24.9-27.5 *26.7*	96.4-100 *98.6*
El Romeral																		
Type-I (deep)	60	BDL-1.91 *0.19*	23	0.005-0.30 *0.04*	0	0.01-3.47 *0.26*	*0*	0.006-0.94 *0.1*	0	0.005-0.81 *0.1*	0	0.24-0.28 *0.26*	0	0.01-0.15 *0.04*	0	66.5-73.0 *71*	27.1-29.0 *27.8*	97.8-102 *99.7*
Type-II (deep)	51	BDL-0.59 *0.08*	41	0.005-0.46 *0.04*	0	BDL-1.19 *0.06*	*11*	BDL-0.10 *0.02*	22	0.005-1.14 *0.06*	0	0.23-0.33 *0.26*	0	0.01-0.04 *0.02*	0	69.3-73.0 *72.3*	27.4-28.5 *27.9*	99.1-102 *101*
Type-I (shallow)	21	BDL-0.02 *0.01*	14	BDL-0.06 *0.02*	2	BDL-0.31 *0.05*	9	BDL-0.24 *0.03*	3	BDL-0.23 *0.09*	17	0.09-0.21 *0.15*	0	BDL-0.14 *0.05*	2	71.7-74.0 *73.1*	27.2-28.2 *27.9*	100-103 *101*
Type-II (shallow)	20	BDL-0.02 *0.01*	13	BDL-0.03 *0.02*	4	BDL-0.07 *0.02*	8	BDL-0.05 *0.02*	13	BDL-0.14 *0.07*	18	0.04-0.20 *0.14*	0	BDL-0.08 *0.06*	4	72.4-74.3 *73.1*	27.6-28.3 *27.9*	101-103 *101*
Cerro Negro Norte																		
Type-I	41	BDL-0.11 *0.06*	2	BDL-0.43 *0.06*	17	BDL-0.50 *0.08*	22	BDL-0.19 *0.05*	20	BDL-0.36 *0.08*	29	0.17-0.30 *0.21*	0	BDL-0.06 *0.06*	39	68.9-71.4 *70.7*	26.5-27.7 *27.2*	96.0-99.2 *98.2*
Type-II	36	BDL-0.03 *0.03*	35	BDL-0.20 *0.66*	2	BDL-0.17 *0.09*	22	BDL-9.16 *0.05*	31	BDL-0.15 *0.1*	28	0.16-0.30 *0.21*	0	BDL *BDL*	36	68.9-71.4 *70.8*	26.5-27.4 *27.2*	95.7-99.2 *98.3*
Type-III	110	BDL-0.40	16	BDL-0.84	14	BDL-2.23	77	BDL-0.37	95	BDL-0.73	77	BDL-0.21	*34*	BDL-0.06	109	63.8-72.3	26.3-27.7	95.2-99.1

		0.12		*0.09*		*0.2*		*0.13*		*0.08*		*0.13*		*0.06*		*70.6*	*27.2*	*99.6*
Type-IV	62	BDL-0.82	52	BDL-0.30	34	BDL-2.82	*30*	BDL-1.76	35	BDL-0.04	61	BDL-0.14	*23*	BDL-0.06	61	62.6-72.0	26.7-27.6	95.8-99.8
		0.18		*0.1*		*0.22*		*0.15*		*0.04*		*0.09*		*0.06*		*70.6*	*27.1*	*98.1*
Carmen																		
Type-I	30	0.02-0.40	0	BDL-0.11	5	0.01-0.59	0	BDL-0.29	3	BDL-0.13	19	0.16-0.32	0	BDL-0.13	6	69.1-73.1	26.2-27.9	96.4-102
		0.18		*0.05*		*0.13*		*0.04*		*0.07*		*0.25*		*0.07*		*70.5*	*26.9*	*98.3*
		Oscillatory zoning: light BSE bands																
	10	0.12-0.24	0	0.03-0.09	0	0.01-0.11	0	0.01-0.05	0	BDL-0.13	7	0.16-0.29	0	BDL-0.11	4	69.6-73.1	26.5-27.9	97.2-102
		0.17		*0.05*		*0.11*		*0.04*		*0.07*		*0.24*		*0.07*		*70.6*	*26.9*	*98.4*
		Oscillatory zoning: dark BSE bands																
	8	0.12-0.40	0	BDL-0.11	1	0.02-0.59	0	0.02-0.29	*0*	BDL-0.08	*3*	0.17-0.31	0	BDL-0.09	1	69.3-71.3	26.4-27.2	96.4-99.4
		0.23		*0.07*		*0.16*		*0.07*		*0.07*		*0.26*		*0.06*		*70.5*	*26.8*	*98.4*
Type-II	18	0.02-0.21	0	BDL-0.10	6	BDL-0.03	4	BDL-0.03	11	BDL-0.07	16	0.18-0.37	0	BDL-0.15	2	69.8-72.07	26.6-27.5	97-100
		0.09		*0.05*		*0.02*		*0.02*		*0.06*		*0.25*		*0.07*		*71.06*	*27.1*	*98.8*
Type-III	28	BDL-0.27	1	0.01-0.08	0	0.01-0.56	0	BDL-0.09	1	BDL-0.11	21	0.18-0.35	0	0.02-0.18	0	66.6-72.0	25.3-27.4	93.1-100
		0.1		*0.04*		*0.2*		*0.04*		*0.08*		*0.26*		*0.1*		*69.1*	*26.3*	*96.3*
Type-IVa	23	BDL-0.22	2	BDL-0.22	4	BDL-9.25	2	BDL-0.06	8	BDL-0.29	16	0.11-0.35	0	0.03-0.19	0	67.7-71.0	25.7-27.1	94.3-98.9
		0.07		*0.07*		*0.06*		*0.02*		*0.14*		*0.25*		*0.1*		*69.3*	*26.4*	*96.5*
Fresia																		
Type-A		*Oscillatory zoning: light BSE bands*																
	10	0.11-0.43	0	0.09-0.25	0	0.49-0.93	0	0.13-0.29	0	BDL-0.1	1	BDL-0.16	1	BDL-0.09	3	67.6-70.1	25.5-26.5	95.2-98.0
		0.23		*0.16*		*0.73*		*0.2*		*0.1*		*0.09*		*0.05*		*68.7*	*26*	*96.4*
		Oscillatory zoning: dark BSE bands																
	10	0.15-0.52	0	0.3-0.46	0	1.09-1.29	0	0.35-0.51	0	0.15-0.28	0	0.04-0.13	0	0.03-0.1	0	66.4-67.8	24.8-25.3	94.0-95.6
		0.28		*0.39*		*1.22*		*0.39*		*0.22*		*0.1*		*0.06*		*66.9*	*25*	*94.8*
Type-B	10	BDL-0.16	4	0.1-0.21	0	BDL-0.26	2	BDL-0.11	4	BDL-0.15	3	0.13-0.3	0	BDL-0.13	3	69.1-70.4	26.3-26.8	96.0-97.9
		0.05		*0.12*		*0.06*		*0.04*		*0.1*		*0.22*		*0.06*		*69.8*	*26.5*	*97.1*
Type-C	24	0.03-0.56	0	BDL-0.24	5	0.19-1.4	0	BDL-0.5	1	BDL-0.07	22	BDL-0.13	15	BDL-0.13	12	67.7-72.2	25.4-27.4	95.1-100
		0.19		*0.06*		*0.74*		*0.22*		*0.06*		*0.05*		*0.07*		*70.1*	*26.5*	*98*
		Oscillatory zoning: light BSE bands																
	5	0.05-0.26	0	BDL-0.04	2	0.19-0.54	0	BDL-0.1	1	BDL-BDL	5	BDL-0.13	3	BDL-0.04	3	70.3-72.2	26.7-27.4	98.1-100
		0.13		*0.02*		*0.34*		*0.07*				*0.07*		*0.04*		*71.5*	*27.2*	*99.4*
		Oscillatory zoning: dark BSE bands																
	6	0.13-0.56	0	BDL-0.09	1	0.58-1.4	0	0.14-0.5	0	BDL-BDL	6	BDL-0.04	3	BDL-0.13	4	68.8-71.4	25.8-27.0	97.0-99.6
		0.46		*0.03*		*1.08*		*0.31*				*0.04*		*0.11*		*69.6*	*26.2*	*98*

Type-D	11	0.15-0.4 *0.25*	0	0.05-0.12 *0.07*	0	0.46-0.97 *0.74*	0	0.09-0.19 *0.14*	0	BDL-0.15 *0.11*	7	0.03-0.24 *0.15*	0	BDL-0.05 *0.03*	6	66.6-68.4 *67.4*	25.1-25.8 *25.5*	93.2-95.5 *94.5*
Mariela																		
Type-α	23	BDL-0.23 *0.1*	2	0.01-0.13 *0.05*	0	BDL-0.54 *0.17*	0	BDL-0.14 *0.06*	1	BDL-0.98 *0.45*	0	0.63-2.28 *1.62*	0	BDL-0.22 *0.11*	4	62.0-69.3 *66.8*	23.4-26.3 *25.3*	87.3-97.7 *94.8*
Type-β	9	0.18-0.37 *0.22*	0	0.05-0.15 *0.11*	0	0.10-0.50 *0.25*	0	0.03-0.25 *0.11*	0	BDL-0.18 *0.13*	1	1.64-2.11 *1.92*	0	BDL-0.09 *0.06*	3	65.0-66.5 *65.6*	24.6-25.2 *24.9*	92.4-94.6 *93.5*
Type-γ	28	BDL-0.15 *0.08*	1	BDL-0.06 *0.03*	3	0.01-0.45 *0.08*	0	BDL-0.20 *0.04*	6	BDL-0.18 *0.08*	15	0.38-0.85 *0.69*	0	BDL-0.80 *0.1*	6	63.1-70.6 *67.7*	23.9-26.9 *25.8*	88.6-98.6 *94.7*
Type-δ	20	BDL-0.11 *0.03*	2	0.15-0.46 *0.25*	0	BDL-0.18 *0.04*	1	BDL-0.13 *0.03*	8	BDL-0.28 *0.14*	10	0.89-1.19 *1.06*	0	BDL-0.16 *0.08*	3	66.4-69.1 *68.3*	25.2-26.2 *25.9*	93.5-95.9 *95.9*
El Laco																		
Magnetite-S	324	BDL-2.04 *0.56*	279	BDL-1.37 *0.12*	157	BDL-1.93 *0.32*	0	BDL-0.55 *0.14*	67	0.005-0.03 *0.006*	0	BDL-0.18 *0.06*	3	BDL-0.17 *0.04*	90	64.7-72.7 *69.1*	26.4-28.5 *27.7*	95.0-101 *97.6*
Magnetite-Z	33	0.1-0.89 *0.73*	*0*	0.09-0.22 *0.18*	0	0.01-0.09 *0.05*	0	BDL-0.06 *0.1*	29	0.09-0.18 *0.13*	0	0.16-0.2 *0.19*	0	BDL-0.06 *0.04*	14	67.8-70.9 *70.2*	26.8-28.1 *27.8*	95.7-100 *99.3*
Magnetite-X	38	0.44-1.24 *0.64*	*0*	0.18-0.91 *0.44*	0	0.01-0.39 *0.07*	0	BDL-0.2 *0.05*	20	0.12-0.56 *0.24*	0	0.16-0.22 *0.19*	0	BDL-0.09 *0.04*	5	69.0-71.1 *70.5*	27.4-28.8 *28.1*	98.1-102 *100*
Magnetite-Y	42	0.56-1.75 *0.9*	42	0.39-0.98 *0.52*	0	0.04-1.71 *0.5*	0	BDL-0.66 *0.2*	1	0.17-0.75 *0.29*	0	0.16-0.20 *0.18*	0	BDL-0.10 *0.05*	3	65.2-70.6 *69.1*	28.0-29.1 *28.3*	98.2-101 *100*
Magnetite-γ	12	BDL-0.65 *0.35*	4	0.08-0.42 *0.19*	0	0.01-0.81 *0.29*	0	BDL-0.08 *0.04*	8	0.04-0.19 *0.12*	0	0.20-0.39 *0.25*	0	0.01-0.01 *0.01*	12	66.9-69.6 *68.5*	26.7-27.1 *26.9*	95.6-96.5 *96.5*
Magnetite-α	28	0.07-0.75 *0.29*	0	0.21-0.82 *0.5*	0	0.01-0.96 *0.1*	0	BDL-0.30 *0.12*	21	0.38-1.66 *0.76*	0	0.21-0.32 *0.26*	0	0.01-0.03 *0.01*	0	66.7-71.2 *69.9*	27.7-28.3 *27.3*	98.4-100 *99.7*
Magnetite β. β1. β2	24	0.16-0.96 *0.6*	0	0.07-0.58 *0.41*	0	0.01-0.61 *0.09*	0	BD-0.43 *0.14*	*13*	0.06-1.54 *0.57*	0	0.01-0.29 *0.26*	0	0.01-0.1 *0.03*	24	67.9-71.3 *69.5*	27.1-28.4 *27.9*	97.4-100 *99.7*

Note: The range indicates the minimum and maximum concentration. The average is shown in italics.
N=number of analyses. n=number of analyses BDL for Mg. Al. Si. Ca. Ti . V and Mn.
*Representative concentrations for magnetite Type-1. -2 and -3 from Los Colorados drill-core LC-05-129. Many magnetite grains do not exhibit Type-3 and in many cases the concentrations of Type-1 and -2 overlap.
** Concentrations calculated from all data from Knipping et al. (2015a. b). Data not sorted by magnetite type.
Data source: Los Colorados (Knipping et al.. 2015a.b; Deditius et al.. 2018); Cerro Negro Norte (Salazar et al.. 2019); El Romeral (Rojas et al.. 2018b; this study).

Table 7. Data summary of the most relevant trace elements (in ppm) determined by LA-ICP-MS spot analyses in magnetite types from Cerro Negro Norte, El Romeral, Carmen, Fresia and Mariela.

	Cerro Negro Norte								El Romeral							
									Deep (~347 m)				*Shallow (~ 10 m)*			
Element	n	*Type-I* (N=28)	n	*Type-II* (N=26)	n	*Type-III* (N=37)	n	*Type-IV* (N=55)	n	*Type-I* (N=26)	n	*Type-II* (N=13)	n	*Type-I* (N=26)	n	*Type-II* (N=24)
Mg	0	32.6-4,050	0	17.2-1,850	0	44.1-2,690	0	8.54-4,360	0	82-7,130	0	53.2-7,640	0	71-1,620	0	26.2-1,590
		1,405		*419*		*724*		*913*		*3,361*		*2,243*		*676*		*347*
Al	0	130-3,010	0	180-1,910	0	481-2,650	0	67.3-1,290	1	BDL-2,290	0	156-1,470	0	86.8-1,050		84.9-1,900
		924		*669*		*1,406*		*280*		*1,384*		*763*		*562*		*323*
Ti	0	70-1,990	0	54.7-936	0	101-870	22	BDL-509	0	103-3,920	0	65-1,020	0	71-1,220	0	45-1,100
		330		*327*		*340*		*72.8*		*803*		*342*		*571*		*222*
V	0	1,247-2,090	0	1,230-2,113	0	887-1,370	0	8.38-562	0	3.5-2,792	0	2,500-2,864	0	1,017-1,495	0	1,045-1,493
		1,398		*1,737*		*1,099*		*215*		*2,489*		*2,683*		*1,261*		*1,277*
Cr	27	BDL-6.7	26	-	37	-	53	BDL-9.20	25	BDL-218	0	BDL-BDL	26	BDL-BDL	26	BDL-BDL
		6.7		-		-		*6.6*		*218*						
Mn	0	37.5-230	0	18.9-195	0	33.2-214	0	54.7-153.8	0	45.6-357	0	186-308	0	416-561	0	441-598
		134		*107*		*110*		*82.4*		*272*		*238*		*510*		*499*
Co	0	18.3-37.1	0	18.4-33.5	0	20.6-43.7	0	9.18-129	0	40.4-57.5	0	40.5-51.8	0	16.5-25.3	0	13.6-24.7
		25.7		*25.5*		*27.9*		*21.9*		*45.6*		*51.8*		*21*		*19.3*
Ni	0	53.5-178	0	58.4-176	0	26.2-145	0	18.7-428	0	0.3-64.7	0	48.9-92	0	68.6-123	0	79.5-144
		96.2		*99*		*61,0*		*105*		*54.7*		*60.1*		*92.6*		*112*
Cu	13	BDL-7.47	22	BDL-1.88	22	BDL-228	33	BDL-203	4	BDL-9.5	10	BDL-4.6	23	BDL-2.47	22	BDL-2,300
		3.19		*1.17*		*41.7*		*15.7*		*4.81*		*3.55*		*2.04*		*1,151*
Zn	9	BDL-31.3	18	BDL-13.9	23	BDL-15.4	25	BDL-19.1	4	BDL-53.3	10	BDL-13	0	8.3-31.5	6	BDL-29
		12.1		*9.15*		*9.34*		*7.9*		*12.4*		*9.9*		*19.4*		*14.4*
Ga	0	29.1-59.0	0	27.9-53.1	0	21.1-42.9	0	11.2-26.5	1	BDL-60.2	0	49.9-60.9	0	17.09-20.7	0	17.1-30.3
		39.2		*37*		*27.9*		*15.3*		*54.3*		*54.1*		*18.86*		*20.1*
Sn	22	BDL-2.45	24	BDL-0.87	31	BDL-1.02	45	BDL-1.11	6	BDL-4.4	6	BDL-25.6	4	BDL-2.55	18	BDL-2.27
		1.19		*0.87*		*0.9*		*0.8*		*1.56*		*5.89*		*1.47*		*0.7*

	Carmen						Fresia						Mariela							
Element	n	*Type- I* (N=40)	n	*Type-II* (N=10)	n	*Type-III* (N=44)	n	*Type-A* (N=35)	n	*Type-B* (N=44)	n	*Type-C* (N=34)	n	*Type-α* (N=39)	n	*Type-β* (N=25)	n	*Type-γ* (N=40)	n	*Type-δ* (N=30)
Mg	0	1,990-5,710	0	1,213-2,240	1	BDL-1,666	0	1,061-3,940	0	39.2-1,980	0	635-4,297	3	BDL-2,970	0	864-3,990	0	271-8,340	0	135-1,750
		3,842		*2,811*		*965*		*2,214*		*460*		*2,019*		*617*		*1,988*		*1,695*		*465*
Al	0	299-1,770	0	460-925	0	196-1,223	0	309-4,680	0	682-2,549	0	38.5-1,215	0	196-1,045	0	211-1,036	0	114-571	0	443-3,680
		1,036		*744*		*560*		*1,71*		*1824*		*305*		*435*		*739*		*250*		*2,367*
Ti	0	445-2,510	0	437-2,240	0	131-4,120	0	206-2,106	0	414-9,100	6	BDL-523	20	BDL-6,850	0	383-196,000	0	159-4,760	0	446-3,870
		1,108		*1,032*		*794*		*893*		*2,921*		*63.7*		*1,038*		*23,419*		*680*		*1,316*
V	0	1900-2,160	0	1930-2,096	1	BDL-2,710	0	435-828	0	1,659-1,879	0	18.3-405	0	4790-15230	0	11,570-16,800	0	4,760-6,810	0	9,120-9,910
		2,013		*2,010*		*2,411*		*595*		*1,756*		*146*		*9049*		*13,880*		*5,874*		*9,384*
Cr	40	BDL-BDL	10	BDL-BDL	44	BDL-BDL	34	BDL-5.5	44	BDL-BDL	34	BDL-BDL	1	BDL-51.2	4	BDL-38.5	25	BDL-18.7	6	BDL-24.7
								5.5						*23.7*		*12.3*		*11.2*		*14*
Mn	0	376-691	0	274-610	0	906-1,248	0	230-468	0	399-1,160	0	245-778	0	133-8,400	0	198-3,390	0	152-1,628	0	227-2,250
		500		*375*		*1,077*		*321*		*559*		*395*		*745*		*731*		*651*		*552*
Co	0	108-127	0	106-130	0	93.4-105	0	19.8-46.3	0	15.3-63.4	0	17.5-64	5	BDL-14	0	3.39-29.7	0	3.51-259	0	14.7-32.8
		115		*116*		*99.3*		*27.7*		*28.4*		*34.3*		*6.45*		*14.7*		*35.3*		*24.3*
Ni	0	265-338	0	293-327	0	250-303	0	153-184	0	242-283	0	110-164	0	123-266	0	167-268	0	150-402	0	224-338
		305		*309*		*283*		*165*		*260*		*144*		*204*		*222*		*283*		*292*
Cu	26	BDL-73.5	8	BDL-23	39	BDL-2.7	34	BDL-1.45	28	BDL-35.6	15	BDL-50.7	0	1.22-1,161	0	4.5-580	0	31.3-1,620	29	BDL-10
		9.47		*12*		*1.74*		*1.45*		*8.14*		*17.8*		*315*		*135*		*723*		*10*
Zn	0	19.3-136	0	17.7-108	0	16-165	0	6.4-48	0	16.6-163	0	10.9-74	0	4.2-103	0	7.4-63.8	0	7.7-57	0	5.5-63.4
		64.2		*43.7*		*58.6*		*20.5*		*69.7*		*32.9*		*27.6*		*20.9*		*20.3*		*24*
Ga	0	29.3-43.5	0	31.5-36.8	0	28.8-42.9	0	24.6-51.9	0	17.3-42.7	0	9.83-21.8	0	21.7-46.9	0	34.3-51.8	0	32.1-52.7	0	21.4-68.3
		38.5		*34.9*		*33.4*		*35*		*31.9*		*14.9*		*39.4*		*44*		*40.2*		*48.5*
Sn	0	1.15-5.26	0	1.15-2.75	0	0.26-3.57	0	2.09-4.69	2	BDL-2.79	0	5.07-18.0	18	BDL-17.4	0	0.39-6.91	37	BDL-0.37	9	BDL-1.16
		2.83		*1.83*		*1.21*		*3.25*		*0.94*		*9.85*		*3.86*		*1.48*		*0.28*		*0.6*

Note: The range indicates the minimum and maximum concentration. The average is shown in italics.
N=number of analyses, n=number of analyses below the detection limit (BDL).
The data correspond to: Los Colorados (Knipping et al., 2015a,b; Deditius et al., 2018); Cerro Negro Norte (Salazar et al., 2019); El Romeral Carmen, Fresia and Mariela (this study).
Detection limits for El Romeral, Carmen, Fresia and Mariela analizes are reported in the SM.

Table 8. Data summary of the most relevant trace elements (in ppm) determined by LA-ICP-MS spot analyses in magnetite types from El Laco.

	Cristales Grandes		Rodados Negros		San Vicente Alto		Laco Norte									
		Outcrop		*Drill-core*		*Drill-core*		*Outcrop*	*Drill-core*							
Element	n	*Magnetite-S* (N=118)	n	*Magnetite-S* (N=105)	n	Magnetite-S (N=67)	n	Magnetite-S (N=29)	n	Magnetite-α (N=9)	n	Magnetite-β (N=20)	n	*Magnetite-X and -Y* (N=21)	n	*Magnetite-Z* (N=14)
Mg	0	4,120-14,600 *9,141*	0	6,100-11,490 *7,706*	0	180-8,580 *3,623*	0	503-14,800 *9795*	0	881-4,490 *2,534*	0	5,610-10,130 *8,125*	0	5,750-14,240 *9,442*	0	5,520-9,740 *7,422*
Al	0	604-6,140 *2,419*	0	155-3,620 *1,067*	0	64.4-974 *488*	2	BDL-717 *255*	0	4,870-6,960 *6,128*	0	5,086-6,350 *5,864*	0	3,660-9,100 *6,492*	0	1,562-2,670 *2,069*
Ti	0	99-7,650 *2,526*	0	60-1,840 *452*	0	17.7-350 *173*	21	BDL-191 *125*	0	6,540-20,200 *11,537*	0	7,680-9,870 *8,654*	0	2,040-5,240 *3,363*	0	BDL-2,040 *1,411*
V	0	1,397-2,100 *1,781*	0	311-1,499 *1,104*	0	532-1,095 *913*	0	370-842 *578*	0	2,580-3,690 *2,978*	0	2,690-3,400 *2,957*	0	1,688-2,590 *2,028*	0	1,830-2,410 *2,159*
Cr	89	BDL-57.9 *18,7*	94	BDL-30.7 *BDL*	67	BDL-BDL	28	BDL-3.8 *3.8*	4	BDL-42.7 *8.13*	9	BDL-10.0 *4.69*	18	BDL-6.8 *BDL*	12	BDL-5.20 *BDL*
Mn	0	411-1,420 *857*	0	723-1,520 *1,055*	0	38.7-746 *336*	0	55.3-496 *278*	0	55.6-186 *115*	0	441-872 *607*	0	313-829 *562*	0	122-677 *428*
Co	0	617-154 *105*	0	100-166 *132*	0	78.6-156 *123*	0	60.5-168 *122*	0	141-174 *160*	0	121-171 *149*	0	144-170 *155*	0	89-162 *138*
Ni	0	39.9-147 *82,8*	0	96.8-150 *123*	0	175-293 *244*	1	175-253 *220*	0	402-476 *440*	0	344-428 *392*	0	272-338 *306*	0	278-350 *305*
Cu	68	BDL-48.2 *13,5*	99	BDL-20.8 *BDL*	34	BDL-93.4 *20.1*	16	BDL-34.3 *12.9*	3	BDL-9.40 *1.93*	16	BDL-2.68 *BDL*	21	BDL-BDL *BDL*	14	BDL-BDL *BDL*
Zn	0	51.9-201 *130*	0	89.7-266 *154*	0	18.5-95.4 *58.8*	0	15.6-20.2 *47.7*	0	64.2-90.6 *74.1*	0	65.4-127 *93.6*	0	21.1-112 *47.8*	0	41.5-107 *70.4*
Ga	0	9.2-47.5 *29.2*	0	6.5-19.4 *11.2*	5	BDL-4.07 *2.48*	5	BDL-5.9 *3.37*	0	29.2-38.5 *34.5*	0	39.7-50.5 *45.5*	0	34.2-57.5 *46.3*	0	25.0-30.2 *27.3*
Sn	0	3.6-29.4 *10.7*	0	3.9-8.5 *5.43*	0	2.85-5.64 *3.87*	0	5.72-24.3 *13.1*	0	3.26-6.28 *4.93*	20	3.49-5.80 *4.56*	0	4.58-8.10 *6.00*	0	4.03-7.20 *5.44*

Laco Sur

	Outcrop+drill-core		*Drill-core*					
Element	n	*Magnetite-S* (N=130)	n	*Deep* (N=34)	n	*Intermediate depths* (N=21)	n	*Shallow depth* (N=17)
Mg	10	BDL-12170	0	2,570-10,680	0	1,333-13,270	0	6,270-9,060
		6747		*5,396*		*5,853*		*7,464*
Al	22	BDL-2280	0	2,050-5,280	0	1,929-21,060	0	546-1,348
		664		*3,386*		*5,803*		*849*
Ti	37	BDL-1,165	0	1,790-112,000	0	3,160-10,100	0	226-653
		255		*15,322*		*6,099*		*406*
V	0	179-1,360	0	1,480-2,930	0	2,400-5,810	0	2,182-2,580
		846		*2,129*		*3,281*		*2,335*
Cr	128	BDL-3.9	6	BDL-495	9	BDL-151	16	BDL-3.29
		3.9		*68.4*		*35.6*		*3.29*
Mn	4	BDL-488	0	299-2290	0	93.2-781	0	34.9-432
		274		*753*		*403*		*163*
Co	0	24.7-144	0	80.4-137.4	0	41.3-140	0	108-118
		101		*116*		*107*		*112*
Ni	0	140-319	0	157-354	0	242-492	0	327-371
		251		*300*		*351*		*349*
Cu	71	BDL-305	13	BDL-48	7	BDL-10.1	5	BDL-2.81
		45.4		*5.25*		*4.23*		*2.78*
Zn	10	BDL-98	0	59.9-183	0	33.3-145	0	30.3-88.7
		39.5		*115*		*73.8*		*48.5*
Ga	51	BDL-4.3	0	12.8-37.9	0	20.8-37.2	0	6.39-9.93
		2.06		*27.0*		*26.7*		*7.57*
Sn	0	1.22-124	0	1.88-72.6	0	4.30-397	0	4.58-6.48
		11.7		*8.30*		*32.1*		*5.53*

Note: The range indicates the minimum and maximum concentration. The average is shown in italics.
N=number of analyses, n=number of analyses below the detection limit.
Data from La Cruz et al., (under review)

3.10. FIGURES

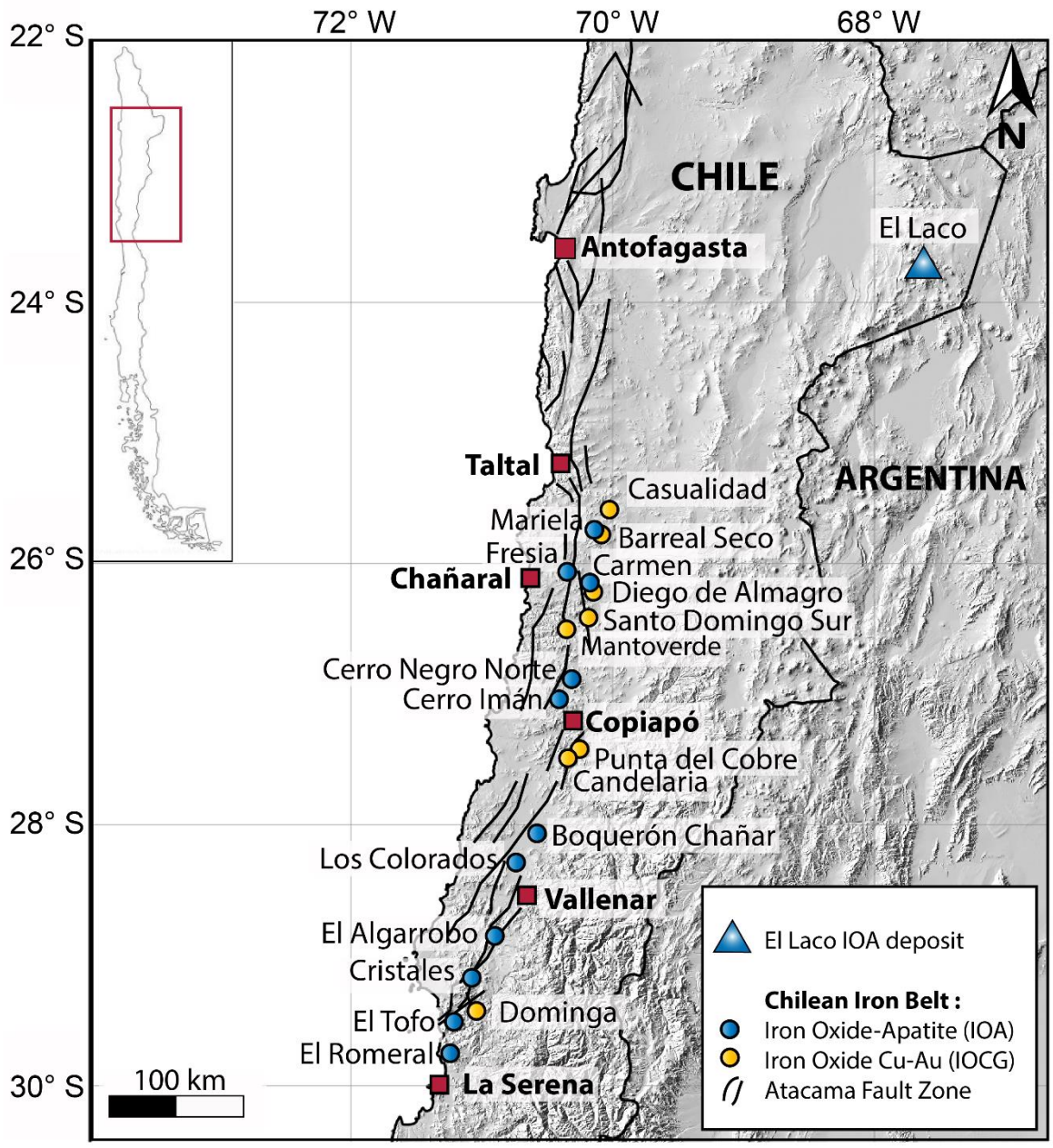

Figure 17. Map showing the location of main IOCG and IOA deposits in the Jurassic–Early Cretaceous Central Andean IOCG Province of the Coastal Cordillera (25-31°S) and El Laco IOA deposit (23°48´S) in the high Andes of northern Chile. Modified after Barra et al. (2017).

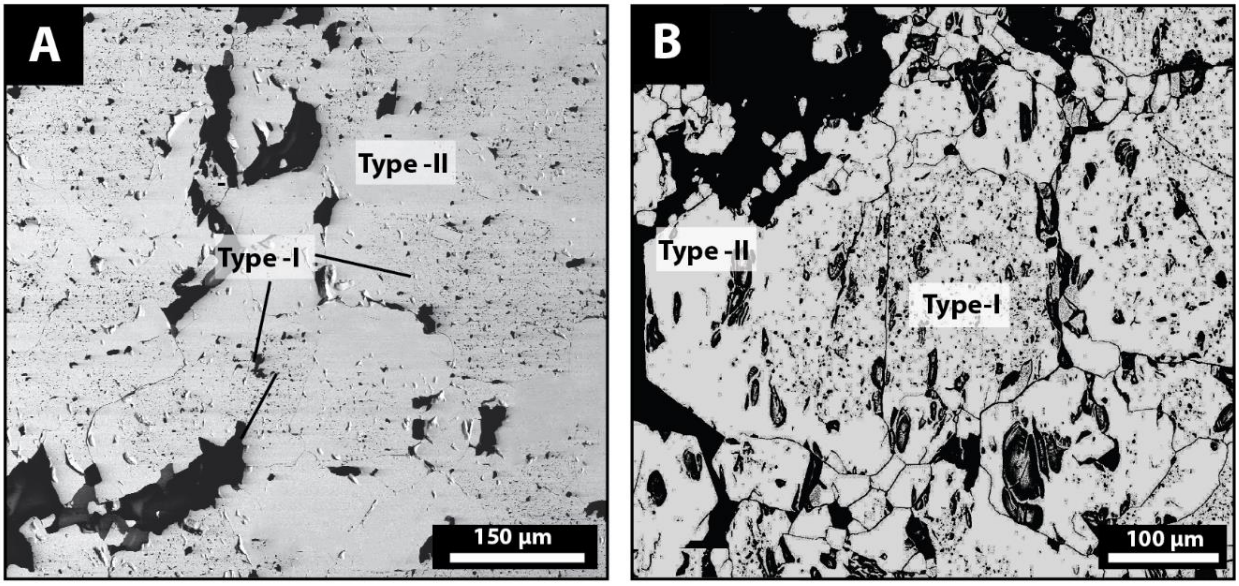

Figure 18. Back-scattered electron images of inclusion-rich Type-I magnetite surrounded by inclusion-poor Type-II magnetite from El Romeral deposit. (A) Sample collected from the massive ore body at ~347 m depth. (B) Sample collected from the massive ore body at 10 m depth. The images correspond to the magnetite grains analyzed by EMPA and LA-ICP-MS (this study).

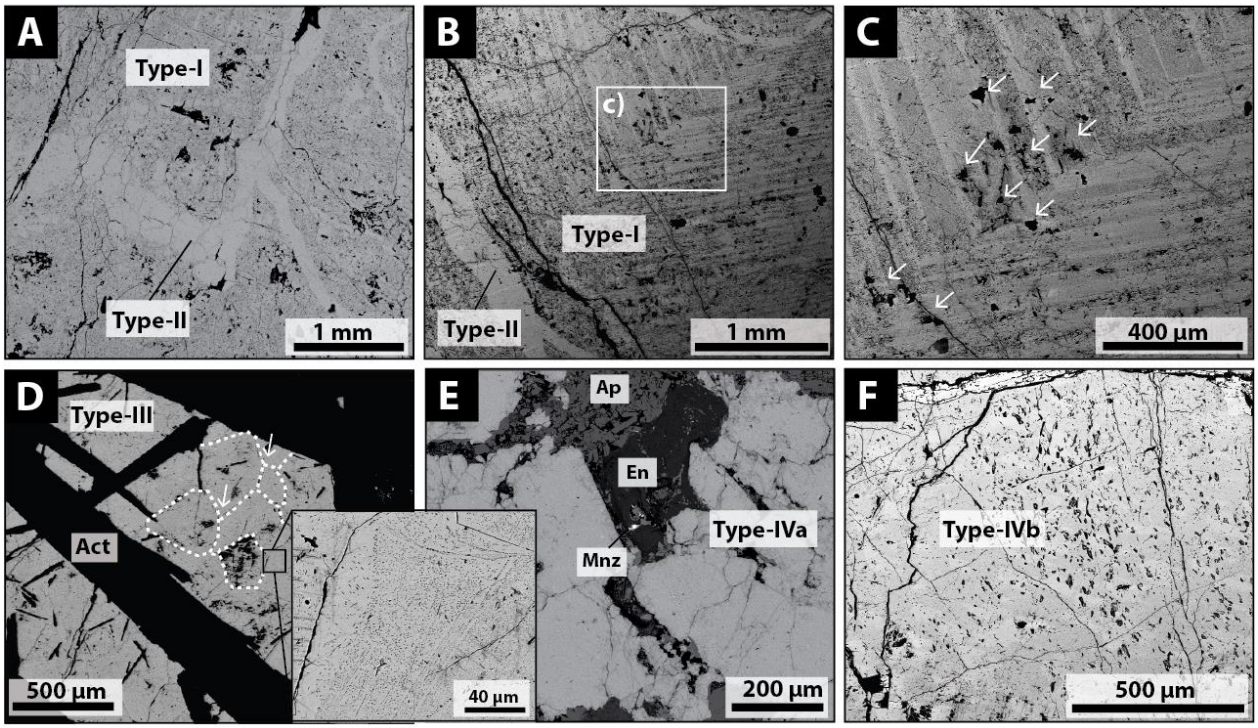

Figure 19. Back-scattered electron images of magnetite types from the Carmen deposit. (A) Inclusion-rich Type-I magnetite crosscut by pristine, inclusion-free Type-II magnetite veinlets; (B) Type-I magnetite showing oscillatory zoning with alternating dark and light bands crosscut by Type-II magnetite veinlet; (C) Detail of oscillatory zoning in Type-I magnetite. The white arrows indicate mineral inclusions that are distributed preferentially within the dark bands; (D) Type-III magnetite intergrown with actinolite (Act) crystals. Early magnetite was recrystallized to fine-grained aggregates of Type-III magnetite in a mosaic texture with triple junctions (white dotted lines and arrows). The inset shows a magnetite grain with numerous nano- to micron-sized inclusions; (E) Inclusion-poor Type-IVa magnetite veinlet associated with Cl-rich apatite (Ap), monazite (Mnz) and enstatite (En). The veinlet crosscuts Type-III magnetite; (F) Type-IVb porous magnetite veinlet.

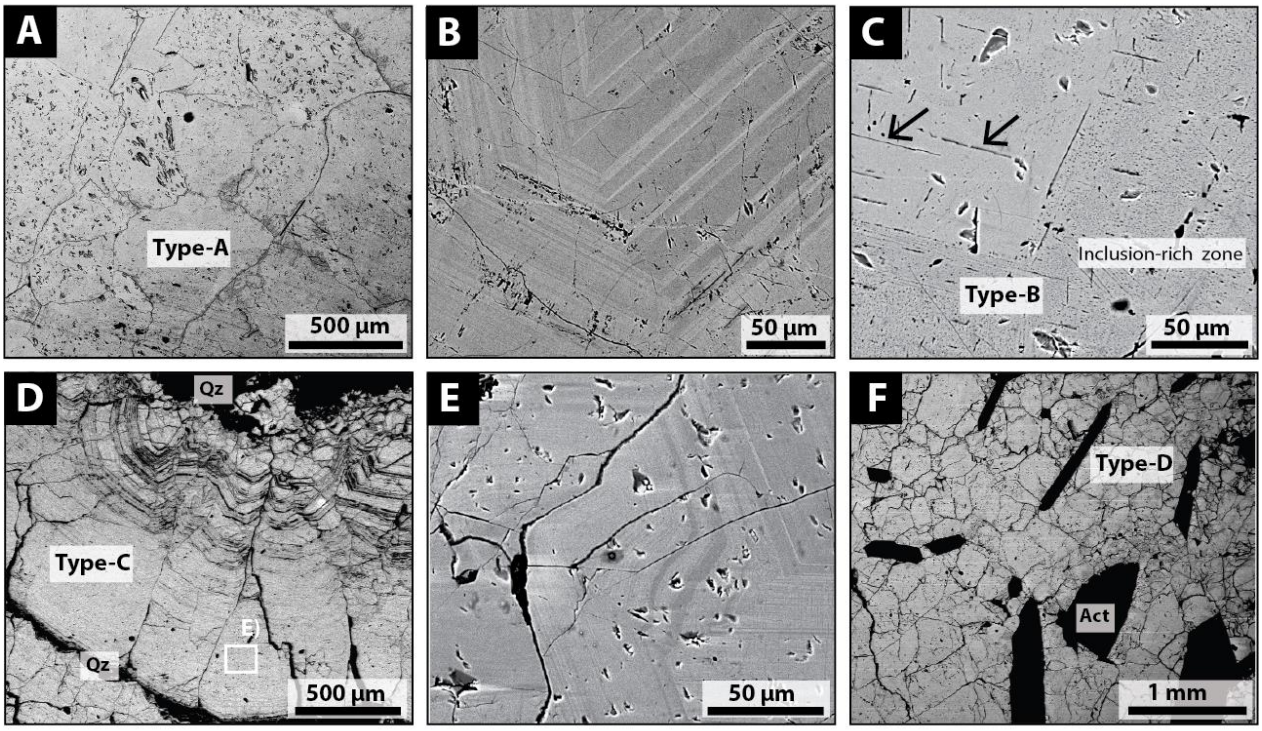

Figure 20. Back-scattered electron images of magnetite types from the Fresia deposit. (A) Recrystallized grains of Type-A magnetite. Note the presence of pores in some grains and the hematite replacement (BSE-dark) along rims; (B) Well-developed oscillatory zoning in Type-A magnetite. Note the absence of mineral inclusions and the presence of pores in some areas; (C) Type-B magnetite that exhibits exsolution lamellae of a Ti-bearing phase (black arrows) and numerous nano-inclusions oriented along magnetite crystallographic planes; (D) Crustiform-colloform banding in Type-C magnetite with quartz (Qz); (E) Detail from (D) showing the oscillatory zoning texture in Type-C porous magnetite; (F) Porous, recrystallized Type-D magnetite intergrown with large actinolite (Act) crystals in veinlet that crosscuts the altered host rock at the margin of the Fresia deposit.

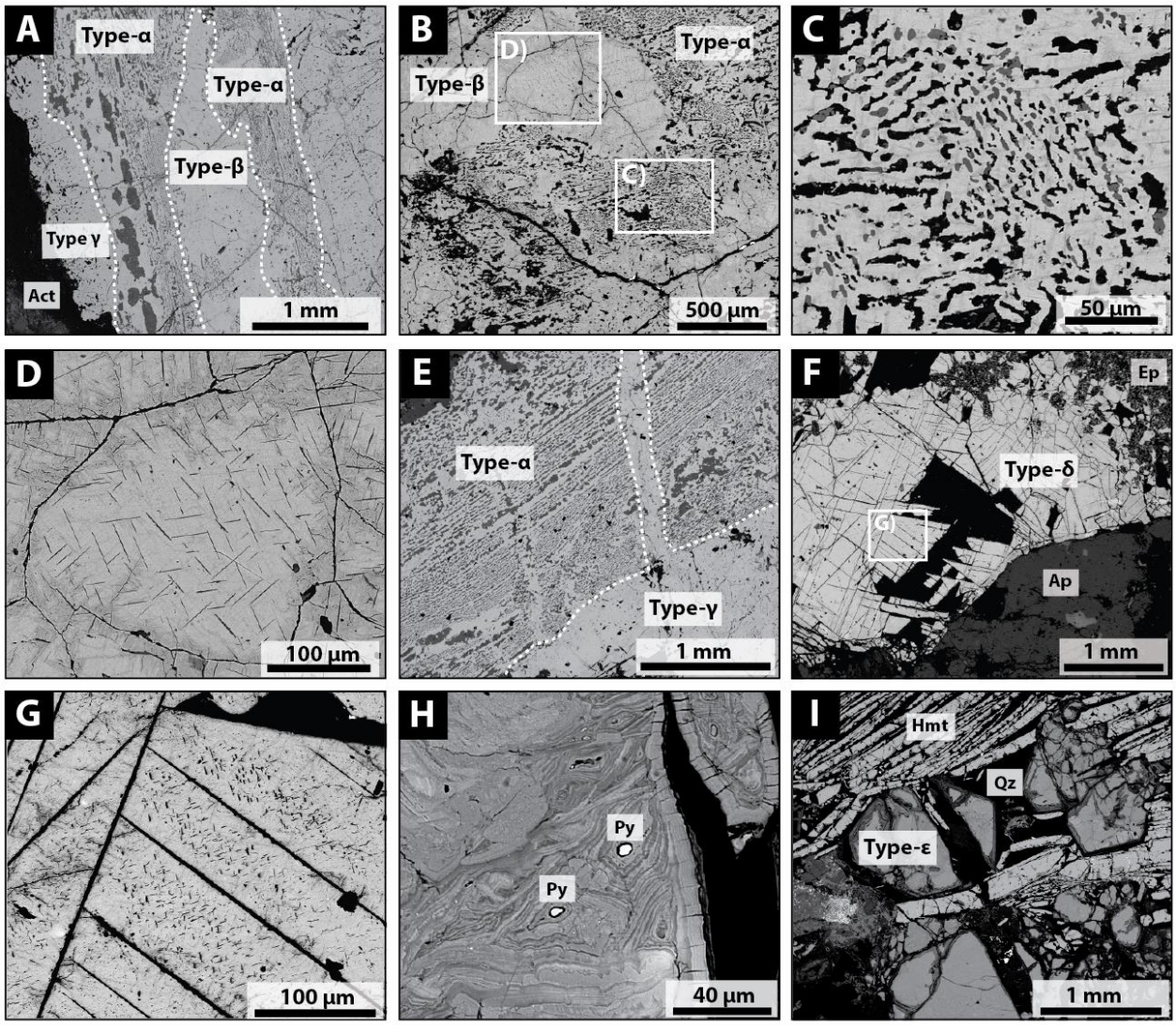

Figure 21. Back-scattered electron images of magnetite types from the Mariela deposit. (A) General view of Type-α, -β and -γ magnetite in contact with actinolite (Act); (B) Type-α magnetite with symplectite texture and fractured Type-β magnetite. The white rectangles indicate the areas corresponding to Figures C and D. (C) Symplectite texture composed of interstitial magnetite and vermicular rutile (BSE-light grey) altered to titanite (BSE-black). Note that magnetite is replaced by hematite along crystallographic planes; (D) Type-β magnetite exhibiting ulvöspinel/ilmenite exsolution lamellae. Note that magnetite is replaced by hematite along fractures; (E) Type-α magnetite crosscut by a later veinlet of Type-γ magnetite; (F) Type-δ magnetite veinlet which displays a well-defined cubic cleavage associate with epidote (Ep) and Cl-rich apatite (Ap). The white rectangle indicates the area of Figure G; (G) Type-δ magnetite showing abundant ilmenite exsolution lamellae; (H) Type-ε magnetite grain exhibiting a fluidal texture with bands of different shades of gray, which represent variable Fe and Si contents. Note the small pyrite grains (Py) hosted within Type-ε magnetite. (I) Type-ε Si-rich magnetite intergrown with specular hematite (Hmt) and quartz (Qz).

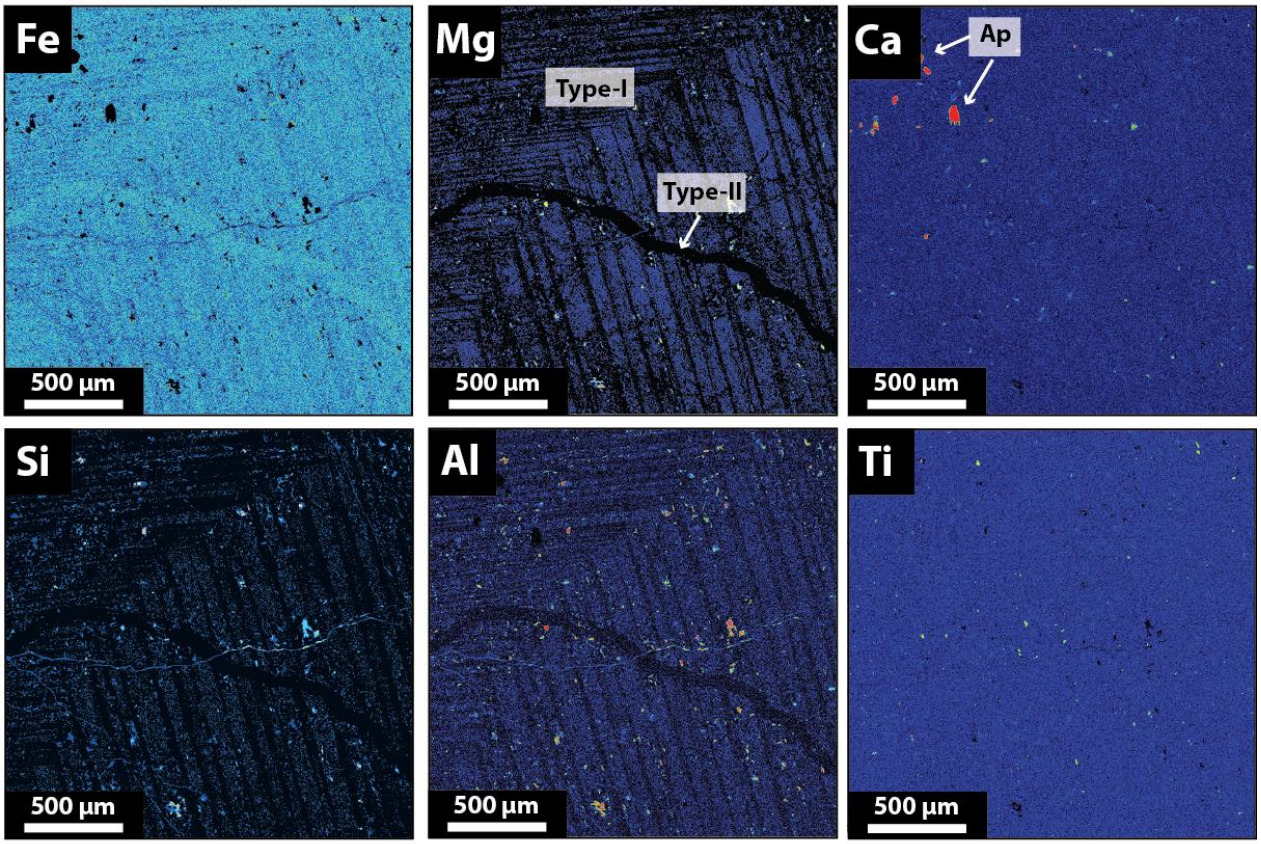

Figure 22. WDS maps for selected elements in Type-I and -II magnetite from the Carmen deposit. Note the oscillatory zoning and the presence of scarce apatite (Ap) inclusions.

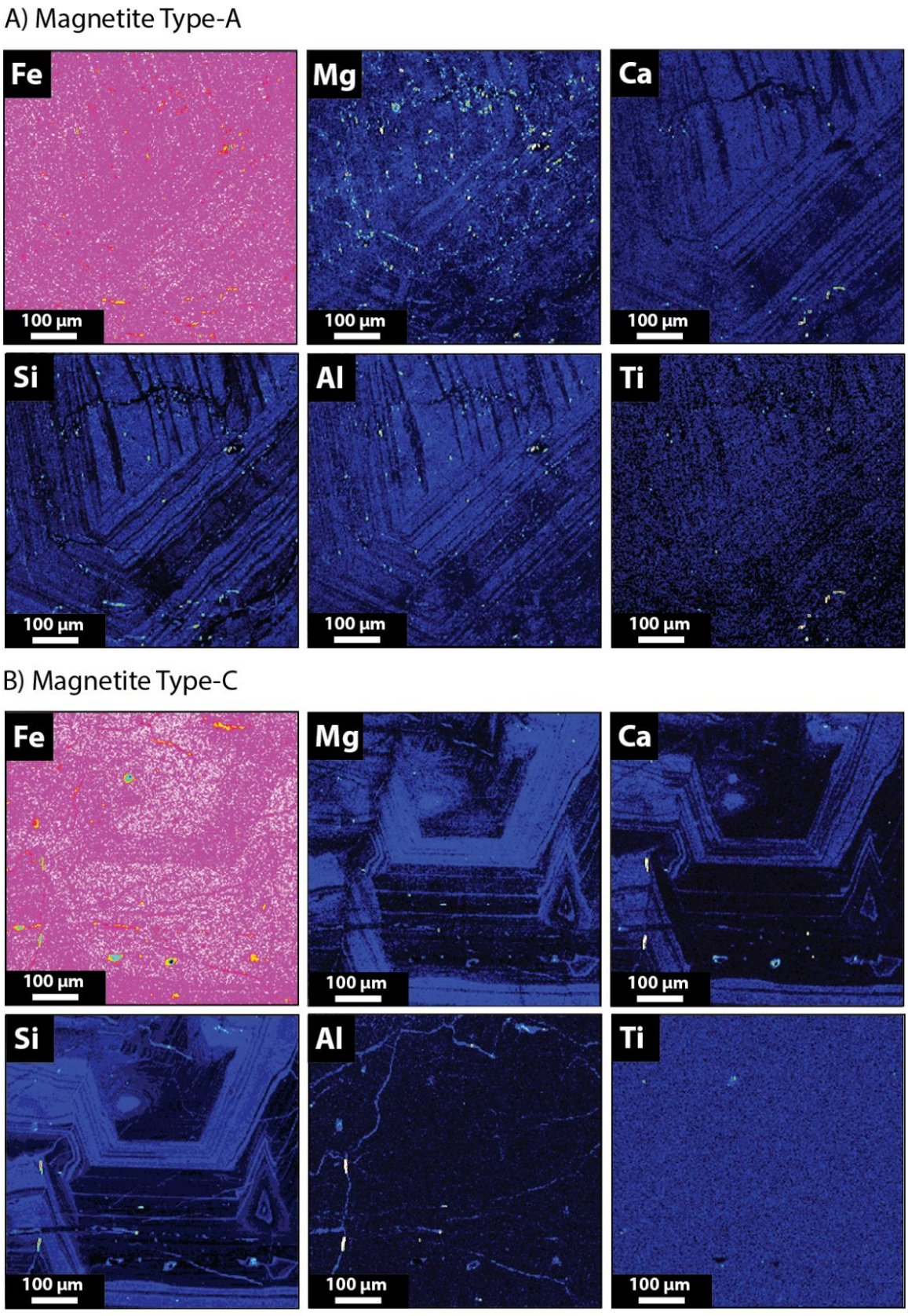

Figure 23. WDS maps for selected elements in Type-A (same as Fig. 4B) and Type-C magnetite from the Fresia deposit. Note the oscillatory zoning and the presence of abundant Mg-rich inclusions in Type-A magnetite.

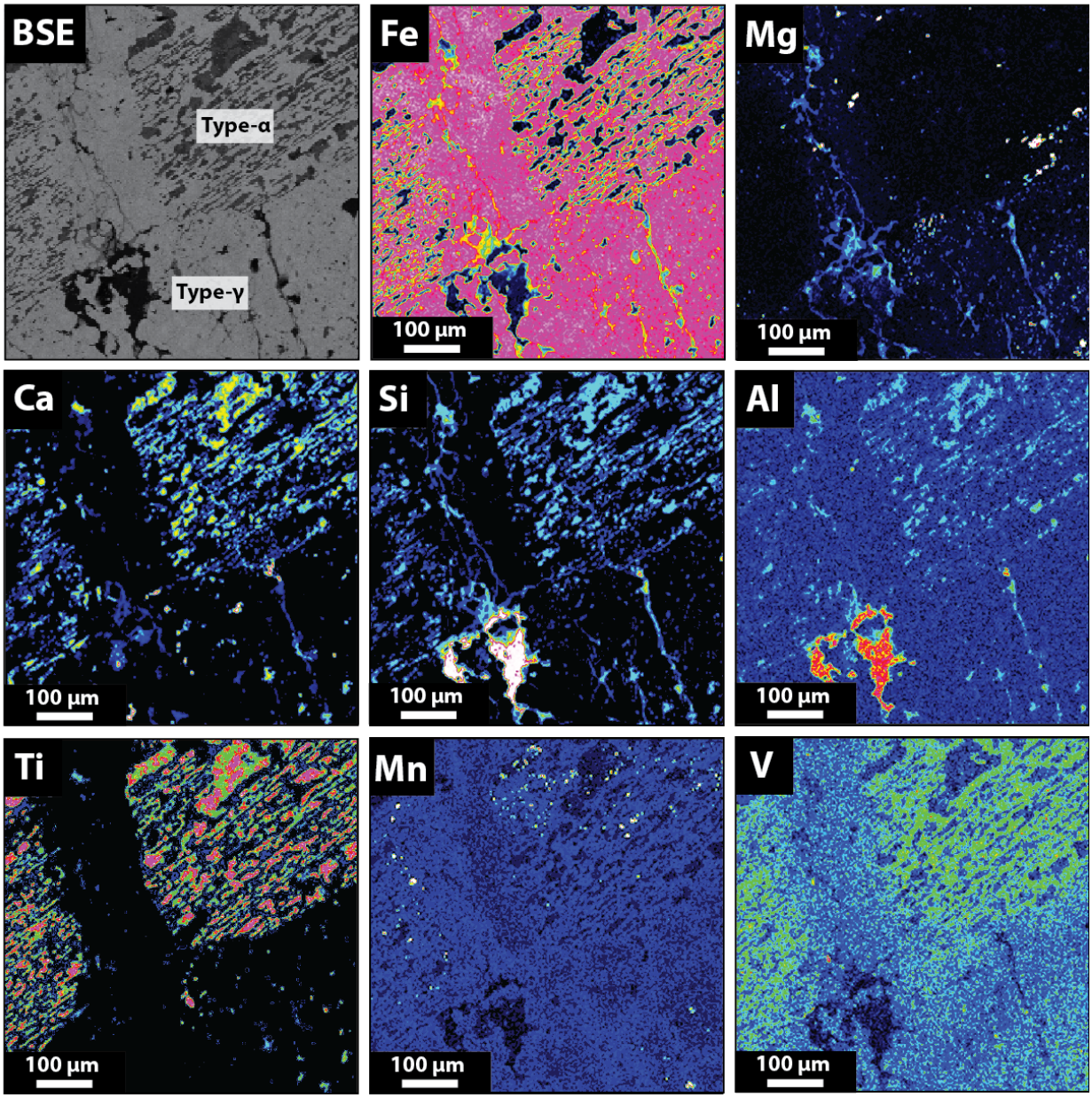

Figure 24. Back-scattered electron (BSE) image and WDS maps for selected elements in Type-α and -γ magnetite from the Mariela deposit.

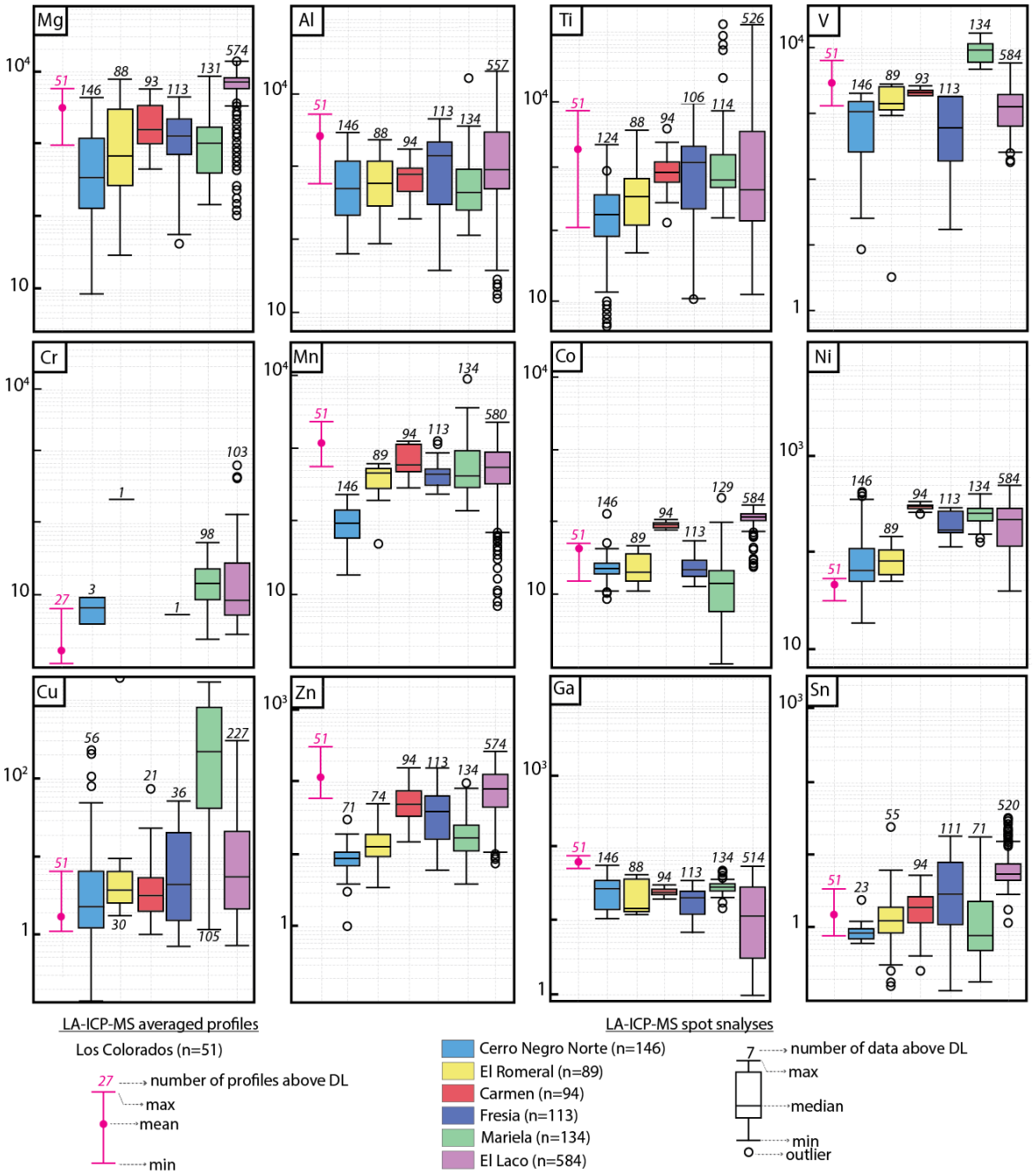

Figure 25. Statistical summary of the most important trace element concentrations (per deposit) in magnetite from Cerro Negro Norte (Salazar et al., 2019); El Romeral (Rojas et al., 2018b and this study); Carmen, Fresia, Mariela (this study); and El Laco (La Cruz et al., under review) determined by using LA-ICP-MS.

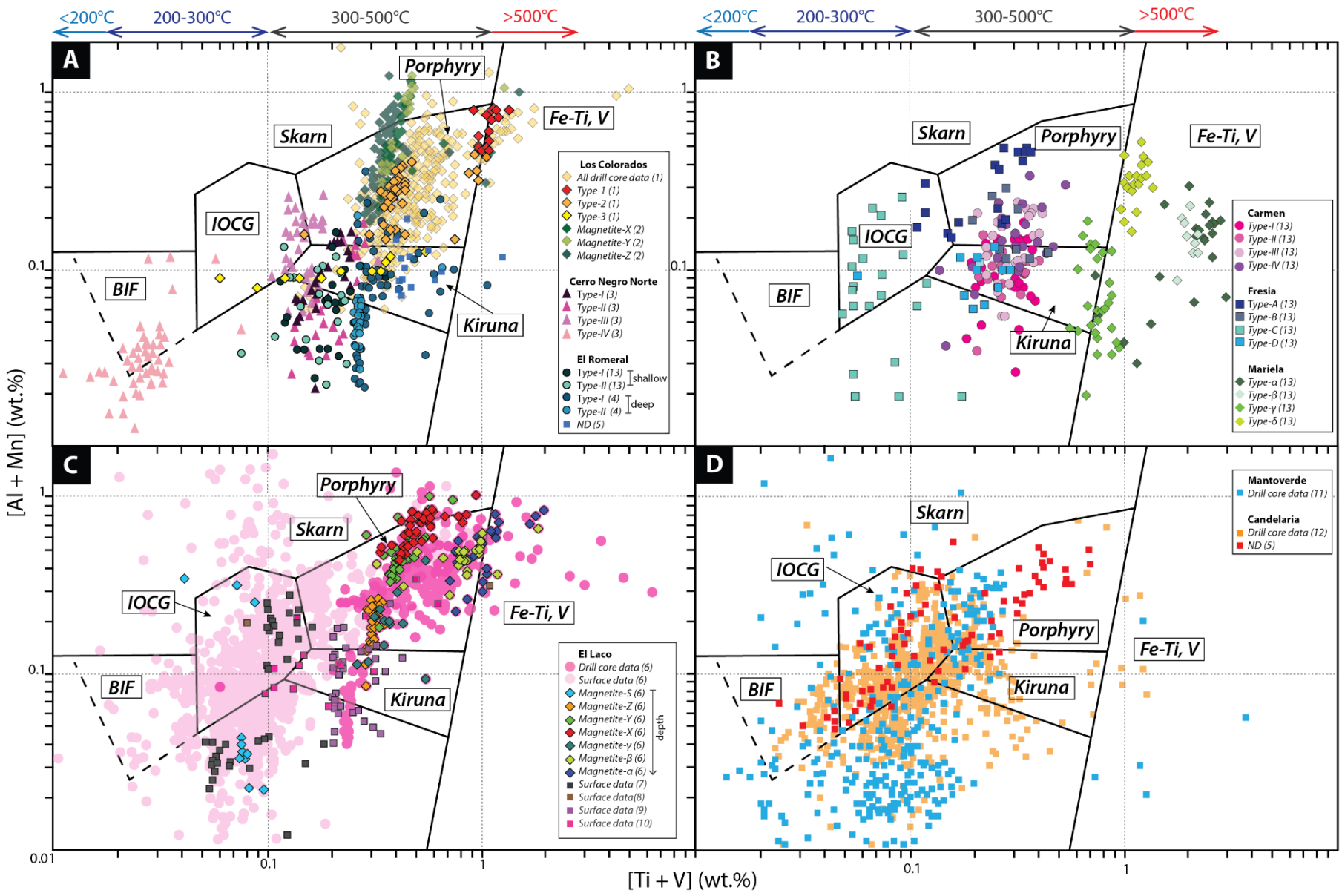
<200°C
200-300°C
300-500°C
>500°C
A
B
C
D
Porphyry
Skarn
Fe-Ti, V
IOCG
BIF
Kiruna
Los Colorados
All drill core data (1)
Type-1 (1)
Type-2 (1)
Type-3 (1)
Magnetite-X (2)
Magnetite-Y (2)
Magnetite-Z (2)
Cerro Negro Norte
Type-I (3)
Type-II (3)
Type-III (3)
Type-IV (3)
El Romeral
Type-I (13)
Type-II (13)
shallow
Type-I (4)
Type-II (4)
deep
ND (5)
Carmen
Type-I (13)
Type-II (13)
Type-III (13)
Type-IV (13)
Fresia
Type-A (13)
Type-B (13)
Type-C (13)
Type-D (13)
Mariela
Type-α (13)
Type-β (13)
Type-γ (13)
Type-δ (13)
El Laco
Drill core data (6)
Surface data (6)
Magnetite-S (6)
Magnetite-Z (6)
Magnetite-Y (6)
Magnetite-X (6)
Magnetite-γ (6)
Magnetite-β (6)
Magnetite-α (6)
depth
Surface data (7)
Surface data(8)
Surface data (9)
Surface data (10)
Mantoverde
Drill core data (11)
Candelaria
Drill core data (12)
ND (5)
[Al + Mn] (wt.%)
[Ti + V] (wt.%)
1
0.1
0.01

Figure 26. Chemical discrimination diagram after Dupuis and Beaudoin (2011) and modified by Nadoll et al. (2014) for all magnetite types from Andean IOA deposits and the Candelaria and Mantoverde IOCG deposits. (A) Los Colorados, Cerro Negro Norte and El Romeral; (B) Carmen, Fresia and Mariela; (C) El Laco; (D) Candelaria and Mantoverde. Data source: (1) Knipping et al. (2015a,b); (2) Deditius et al. (2018); (3) Salazar et al. (2019); (4) Rojas et al., (2018b); (5) Huang and Beaudoin (2019); (6) Ovalle et al. (2018); (7) Broughm et al. (2017); (8) Velasco et al. (2016); (9) Dare et al. (2015); (10) Nyström et al. (1994); (11) Simon et al. (2018); (12) Rodríguez et al. (under review); (13) This study; ND (not determined).

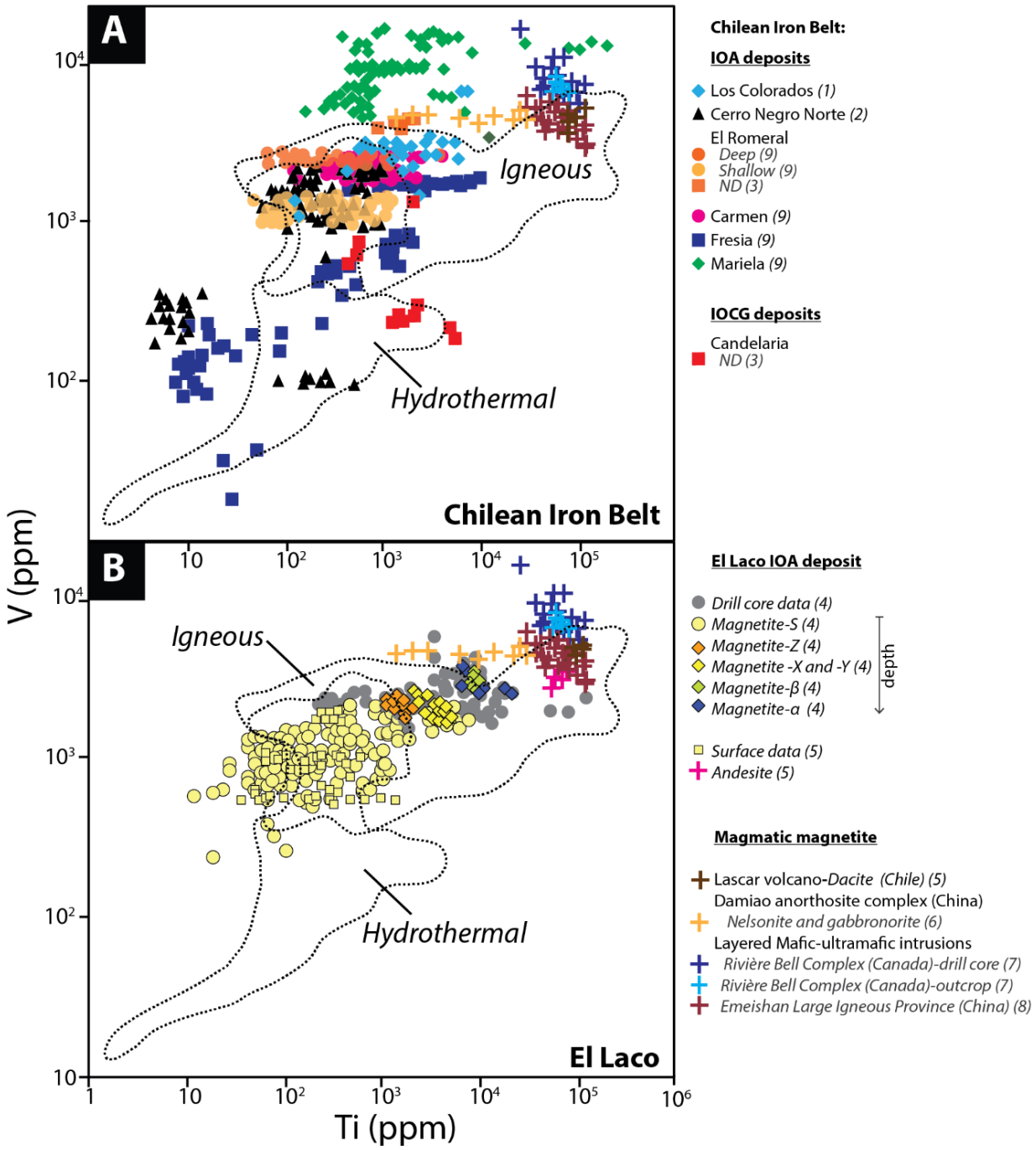

Figure 27. Concentration of Ti vs. V in magnetite from (A) Chilean Iron Belt and (B) El Laco. Magmatic magnetite data from the literature is also shown. The igneous and hydrothermal fields are from Nadoll et al. (2014). Note the overlapping area between the igneous and hydrothermal field. Data source: (1) Knipping et al. (2015a,b); (2) Salazar et al. (2019); (3) Huang and Beaudoin (2019); (4) La Cruz et al. (under review); (5) Broughm et al. (2017); (6) He et al. (2016); (7) Polivchuk (2017); (8) Liu et al. (2014); (9) This study. ND (not determined).

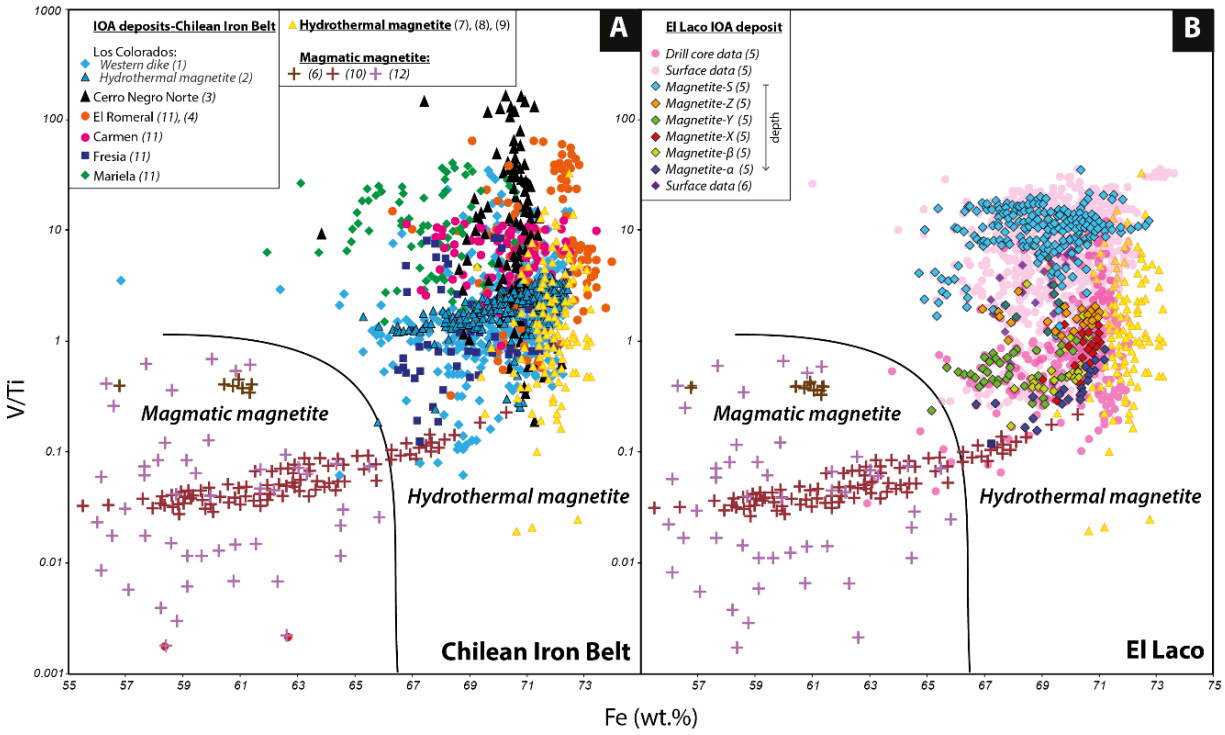

Figure 28. Fe vs. V/Ti discrimination diagram (Wen et al., 2017) for the Chilean Iron Belt (A) and El Laco (B). Data from magmatic and hydrothermal magnetite reported in the literature are also plotted. Data source: (1) Knipping et al. (2015a,b); (2) Deditius et al. (2018); (3) Salazar et al. (2019); (4) Rojas et al. (2018b); (5) Ovalle et al. (2018); (6) Broughm et al. (2017); (7) Nadoll (2011); (8) Nadoll et al. (2014); (9) Nadoll et al. (2015); (10) Liu et al. (2014); (11) This study; (12) References of igneous data in Wen et al. (2017).

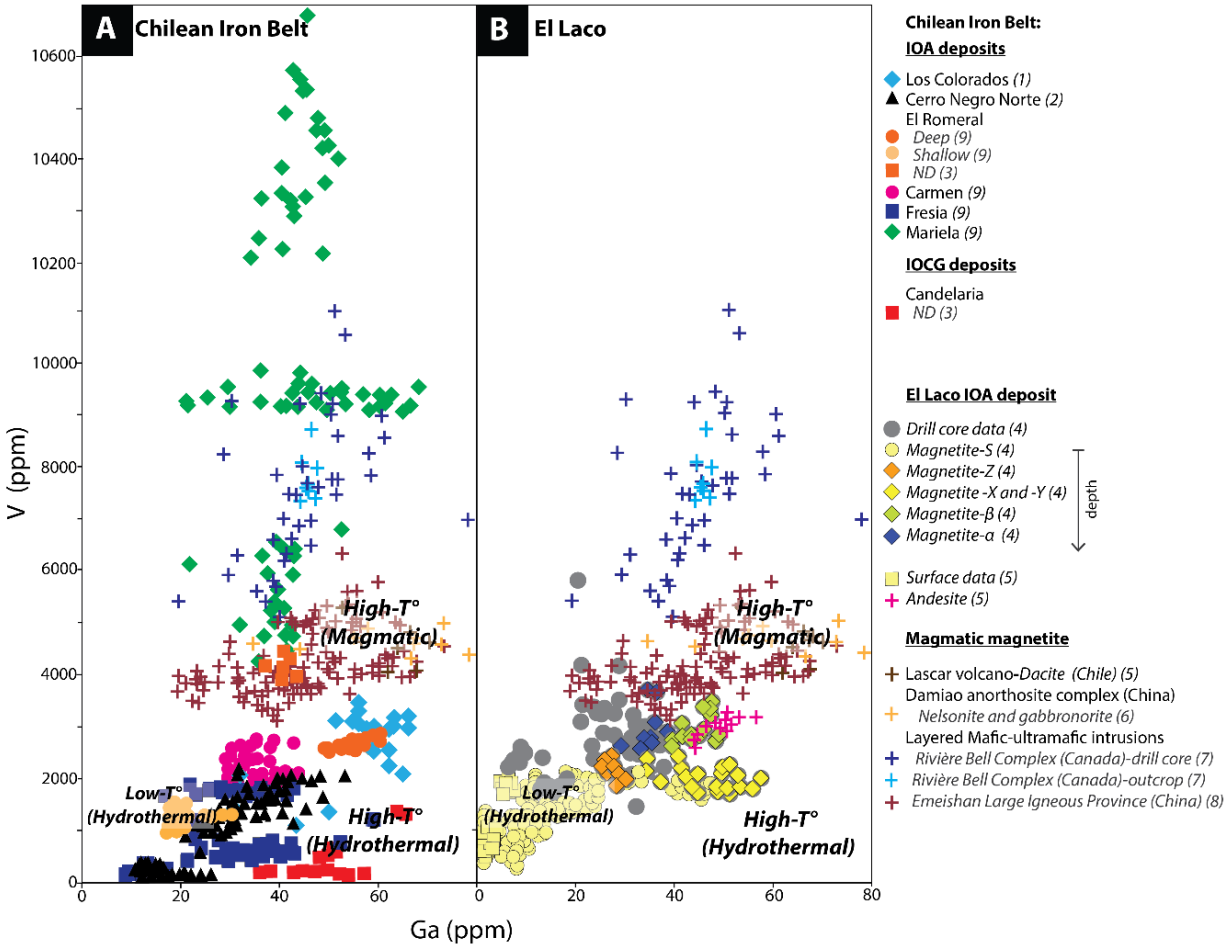

Figure 29. Concentration of Ga vs. V (per deposit) in magnetite from the Chilean Iron Belt (A) and El Laco (B). Data source: (1) Knipping et al. (2015a, b); (2) Salazar et al. (2019); (3) Huang and Beaudoin (2019); (4) La Cruz et al. (under review); (5) Broughm et al., (2017); (6) He et al. (2016); (7) Polivchuk (2017); (8) Liu et al. (2014); (9) This study. ND (not determined). See text for discussion.

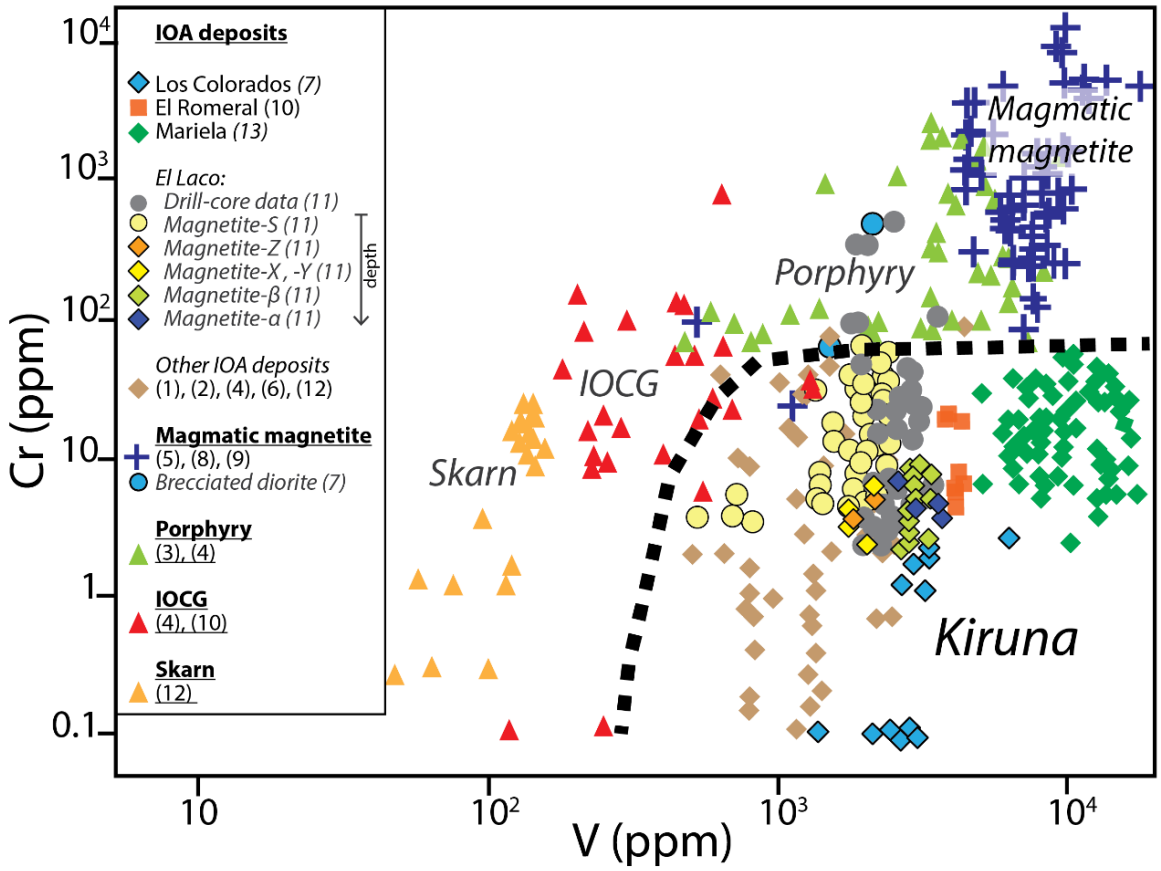

Figure 30. Concentration of V vs. Cr discrimination diagram modified from Knipping et al. (2015b). Magnetite from IOA deposits can be distinguished from other deposits such as porphyry, IOCG, skarn and magmatic magnetite. Higher V concentrations in magnetite indicate in general a more significant magmatic source. Data source: (1) Loberg and Horndahl (1983); (2) Nyström and Henríquez (1994); (3) Core (2004); (4) Dupuis and Beaudoin (2011); (5) Dare et al. (2014); (6) Dare et al. (2015); (7) Knipping et al. (2015a,b); (8) He et al. (2016); (9) Polivchuk (2017); (10) Huang and Beaudoin (2019); (11) La Cruz et al. (under review); (12) Sun et al. (2019); (13) This study.

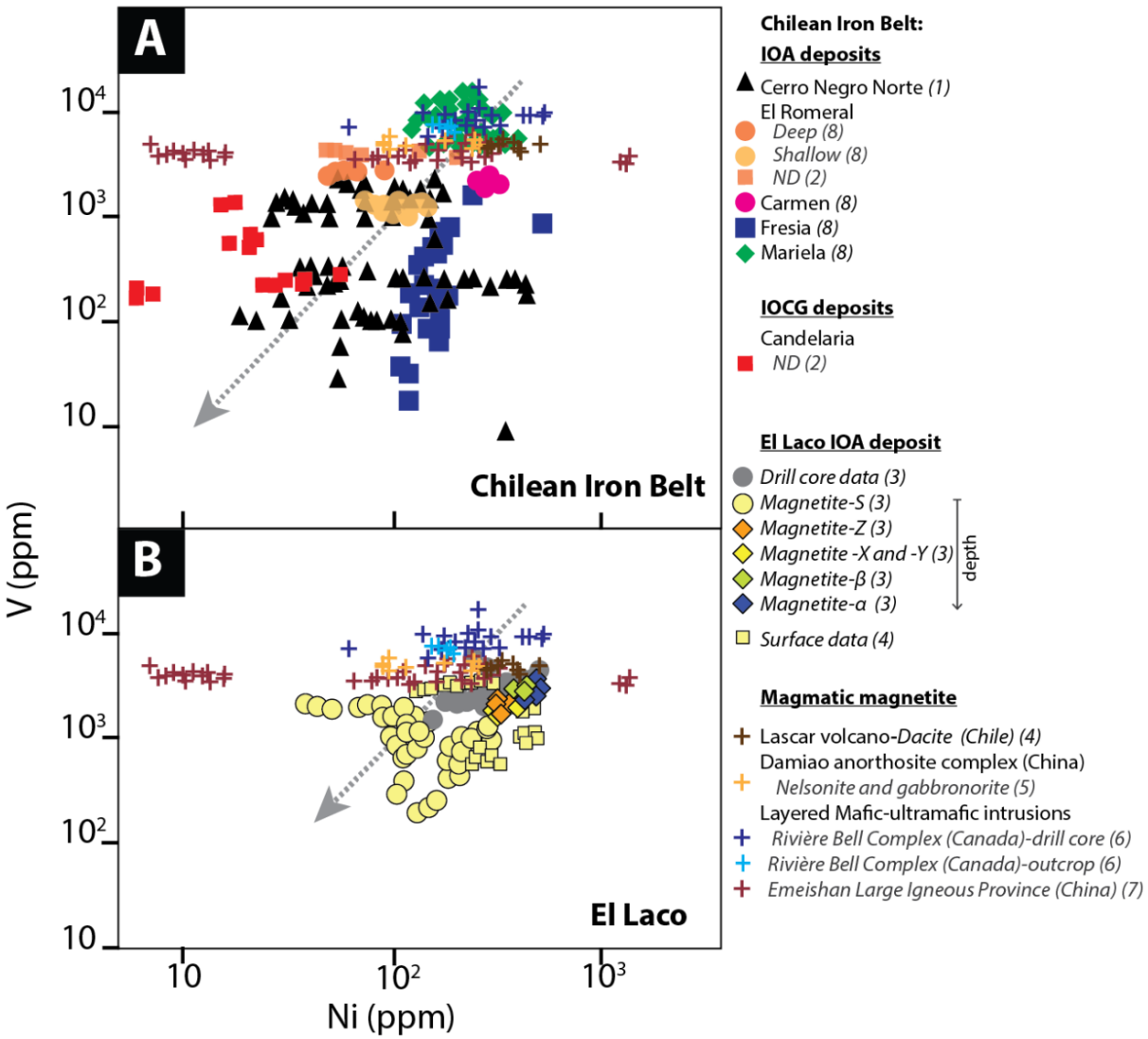

Figure 31. Concentration of Ni vs. V in magnetite from the Chilean Iron Belt (A) and El Laco (B). Data source: (1) Salazar et al. (2019); (2) Huang and Beaudoin (2019); (3) La Cruz et al. (under review); (4) Broughm et al. (2017); (5) He et al. (2016); (6) Polivchuk (2017); (7) Liu et al. (2014); (8) This study.

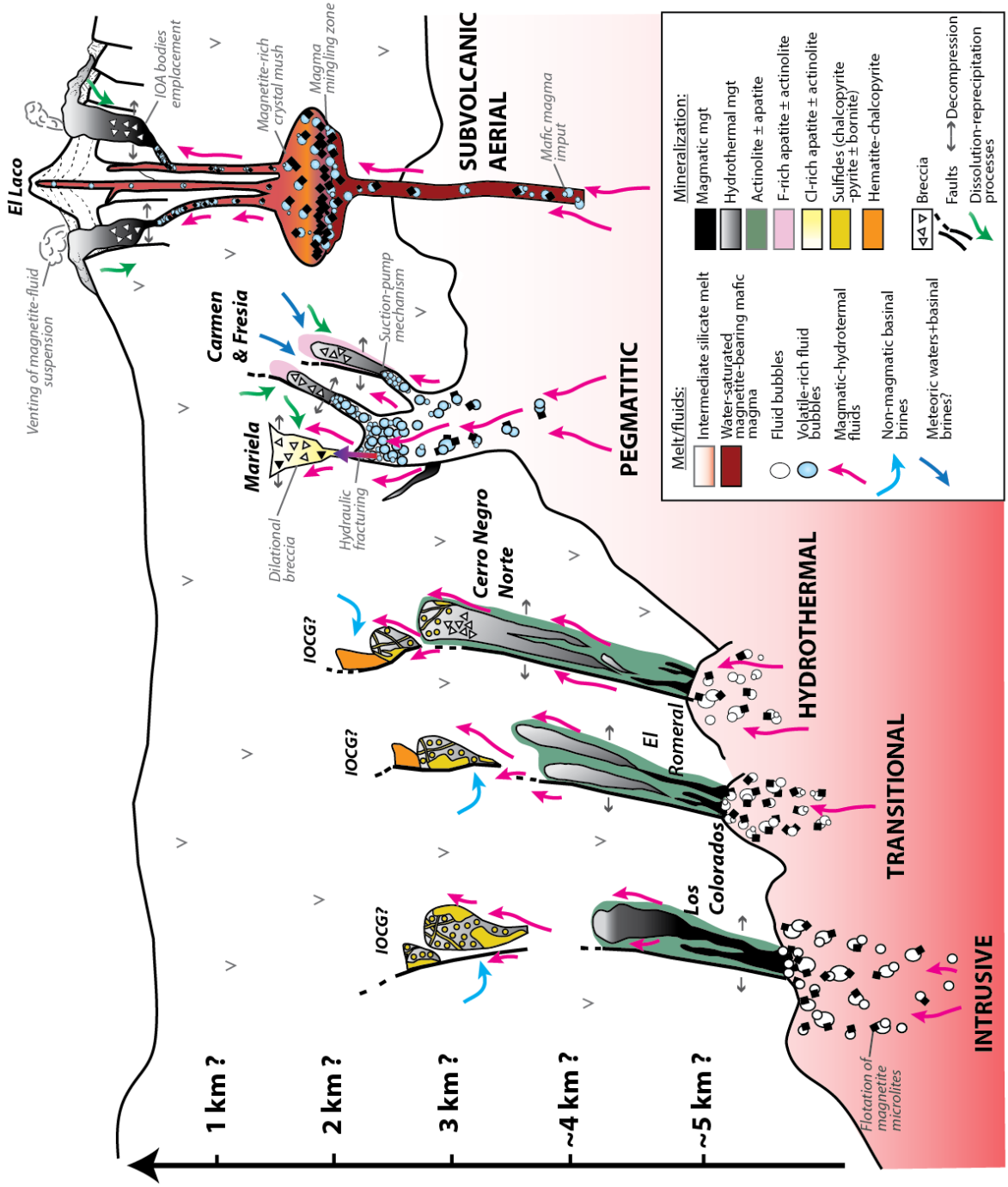

Figure 32. Schematic genetic model for the formation of Chilean IOA deposits from the Chilean Iron Belt and El Laco. The figure shows diferent styles or subtypes of IOA mineralization depending on the depth of emplacement: deep, intrusive-like (e.g., Los Colorados); transitional (e.g., El Romeral); intermediate, hydrothermal-like (e.g., Cerro Negro Norte); pegmatitic, apatite-rich (Carmen, Fresia and Mariela); and shallow, subvolcanic/subaerial (e.g., El Laco) deposits. These different IOA subtypes are controlled fundamentally by the depth of formation, the presence of structures/faults that cause decompression, the composition of the host rock, the source and flux rate of hydrothermal fluids, and the infiltration of non-magmatic fluids such as meteoric waters and possible basinal brines. The *flotation model* (Knipping et al., 2015a,b) provides a general framework to explain the origin of Chilean IOA subtypes and the observed genetic link between IOA and IOCG mineralization. See text for discussion.

CAPÍTULO 4

CONCLUSIONES

En este trabajo de tesis se han caracterizado las microtexturas y la química de los apatitos y magnetitas de los depósitos de tipo magnetita-apatito o *iron oxide-apatite* (IOA) Carmen, Fresia y Mariela, ubicados en la Franja Ferrífera Chilena del Jurásico-Cretácico Temprano de la Cordillera de la Costa del norte de Chile. Estos depósitos corresponden a cuerpos de magnetita masiva con una alta proporción de apatitos (~20-40 % modal) y menor proporción de actinolita, con cristales de centímetros a metros de largo, que desarrollan texturas pegmatíticas, y fuertemente controlados por estructuras extensionales asociadas al Sistema de Falla de Atacama (SFA).

Los depósitos Carmen y Fresia, corresponderían a vetas extensionales de magnetita masiva. Específicamente, la mineralización tipo IOA se formó en zonas de intersección de fallas, asociadas a sistemas de dúplex extensionales, las cuales acopladas con desplazamientos transtensionales crearon zonas de dilatación, donde los fluidos mineralizadores fueron inyectados formando cuerpos de magnetita-apatito con texturas tipo *com*b. La precipitación mineral se habría gatillado por caídas abruptas de presión a niveles corticales someros (< 4km), donde la migración de los fluidos ocurriría por el fracturamiento de la roca, asociado con la actividad misma de la falla, y no por la sobrepresión de los fluidos (mecanismo de bomba de succión).

Los apatitos y las magnetitas de Carmen y Fresia presentan evidencias de reequilibrio textural y composicional que se asocian a eventos de alteración post-cristalización.

Las microtexturas de reemplazo y de reequilibrio en los apatitos y magnetitas, además de las inclusiones secundarias de monacita y menor xenotima en apatito, se relacionan a procesos de disolución-reprecipitación (DR) gatillados por fluidos. Sin embargo, los eventos de alteración/ reemplazo fueron más intensos o penetrativos (i.e., mayor razón fluido/apatito) en Fresia que en Carmen.

En general, los apatitos de Carmen y Fresia se encuentran zonados con respecto a F y Cl, mostrando un comportamiento desacoplado entre dominios microtexturales y composicionales de fluorapatito y cloroapatito. Adicionalmente, presentan concentraciones de REE que alcanzan los 7400 ppm. En Carmen, se reconocen núcleos de apatito primario compuestos de F-apatito (hasta 3.73 wt.% F), mientras que las zonas alteradas se restringen a Cl-OH-apatito (hasta 4.94 wt.% Cl) y Cl-apatito (hasta 6.5 wt.% Cl). Por otra parte, los apatitos de Fresia muestran una composición variable entre los miembros extremos F-apatito, Cl-apatito y OH apatito, los cuales alcanzan concentraciones de hasta un 2.62 wt.% F y un 6.45 wt.% Cl.

En ambos depósitos, dominios Cl-OH-apatito se encuentran enriquecidos en S, Na, Sr, Fe, Mg, V, Mn, Cu, As, Ba y Pb, pero empobrecidos en La, Ce, Th y U, respecto a los de F-apatito. Dicho empobrecimiento refleja la nucleación y crecimiento de inclusiones de monacita y menor xenotima tanto en los bordes de grano o en la interface entre Cl-OH-apatito y F-apatito, a partir de la DP del apatito primario.

Los apatitos de Carmen y Fresia, presentan altos valores de εNd y bajas razones de $^{87}Sr/^{86}Sr$ inicial (Sr_i), lo cual es compatible con una fuente mantélica con mínima contribución cortical. Así, los valores obtenidos para los apatitos de Carmen (εNd: +5.9 - +6.5; Sr_i: 0.7038- 0.7047) son consistentes con una signatura magmática para F-apatito. Por otra parte, los apatitos de Fresia presentan valores más negativos y dispersos de εNd (-0.3 a +4.1), además de razones de Sr_i (hasta 0.70590) relativamente mayores a las de Carmen. Dicha signatura reflejaría la interacción entre los apatitos de Fresia y fluidos posiblemente derivados de cuencas sedimentarias.

En efecto, las microtexturas y la composición de los apatitos primarios de Carmen y Fresia, es decir F-apatito, se habrían modificado a partir de la interacción con fluidos hidrotermales o aguas meteóricas ricas en Cl y S (e.g., salmueras de cuenca). Asimismo, se concluye una signatura magmática para el F-apatiuto e hidrotermal para el Cl- y Cl-OH-apatito de Carmen y Fresia.

Asimismo, las microtexturas de las magnetitas de Carmen y Fresia indican que la geoquímica original de estas fue modificada a causa de procesos de DR y/o reequilibrio con fluidos hidrotermales. Las concentraciones de Ti, V y Ga en las magnetitas de Carmen y Fresia alcanzan valores de hasta 0,28 y 0,29 wt.% ; 0.23 y 0.24 wt.% ; y 35.6 y 30.6 ppm en promedio, respectivamente. Los datos de magnetita graficados en los distintos diagramas de discriminación (e.g., Ti + V vs. Al + Mn y Ga vs. V) para magnetita, acoplados a las microtexturas, sugieren que las magnetitas primarias habría sido reequilibradas por la infiltración fluidos más tardíos, producto de procesos de DR. Posiblemente, fluidos oxidados como salmueras de cuenca, de igual forma que en ciertos skarns de Fe.

Por otra parte, Mariela correspondería a una brecha de dilatación, en que el fracturamiento de la roca dentro de una zona de dilatación, asociada a la curvatura de una falla de orientación NNE y movimientos transtensionales, ocurrió por la sobrepresión o inyección hidráulica de los fluidos mineralizadores. Las microtexturas y geoquímica de los apatitos y magnetitas de Mariela indican que los fluidos magmáticos-hidrotermales que formaron la brecha, habrían sido exsueltos desde un magma primitivo. Los cristales de magnetitas analizados en este estudio, provenientes desde una porción más profunda del depósito Mariela, habrían sido posteriormente emplazados o transportados hacia niveles más someros.

En el depósito Mariela, la mayoría de los apatitos presenta zonación tipo parche, compuesta principalmente por dominios de Cl-apatito (hasta 6.7 wt.% Cl) y Cl-OH-apatito (hasta 3.94 wt.% Cl). La ausencia de inclusiones de monacita es consistente con concentraciones homogéneas de LREE, Th y U, y patrones de REE sin empobrecimiento en LREE, entre los distintos dominios microtexturales y composicionales.

Los apatitos de Mariela presentan los valores más altos y acotados de εNd (+5.5 +6.0) y las razones más bajas de Sr_i (0.70390-0.70407) de los tres depósitos en estudio. Los datos sugieren una fuente magmática con signatura primitiva que dio origen a fluidos salinos-clorurados de alta temperatura.

Las microtexturas de las magnetitas de Mariela son completamente distintas a aquellas descritas para la mayoría de los depósitos IOA. Las magnetitas se encuentran asociadas a fases minerales de Ti como ilmenita, rutilo, titanita y ulvöespinela, y muestran microtexturas típicas

descritas en rocas máficas y ultramáficas, como exsoluciones laminares y simplectitas de magnetita-rutilo (±titanita± ulvöespinela).

La química de las magnetitas de Mariela refleja condiciones de formación puramente magmáticas (> 500°C), sustentado principalmente por sus altas concentraciones de V (hasta 2.28 wt.% V), y relativamente altas concentraciones de Ti (0.98 wt.% Ti en promedio) y Ga (45 ppm Ga en promedio).

La composición de los halógenos de los apatitos alterados apunta a que fluidos portadores de cloro fueron los responsables de la alteración metasomática. Asimismo, la concentración de Cl y OH en apatito depende del pH del fluido metasomático que controla la disponibilidad de OH en el fluido, y por ende, la incorporación de Cl y OH en la estructura del apatito. El control estructural del SFA parece tener un rol fundamental en la incorporación de altas concentraciones de Cl en apatito (> 3.4 wt.% Cl), con base en que la partición de Cl entre apatito-fundido/fluidos aumenta considerablemente con una fuerte caída de presión. Así, co-precipitación de magnetita y apatito en estos sistemas, se debe a que la precipitación de ambas fases minerales depende principalmente de la presión, favorecido por condiciones de rápida descompresión.

Por otra parte, la presencia de azufre (S) en apatito se atribuye a fluidos oxidantes portadores de SO_2 y la sustitución acoplada sulfato-sulfito durante la sobreimposición u *overprint* hidrotermal que conduce a la incorporación de S^{4+} y S^{6+} mediante reacciones redox que reducen el S^{6+} a S^{4+}.

Adicionalmente, en este trabajo de tesis se presentó una discusión crítica sobre el uso de la geoquímica de elementos traza en magnetita, además de constreñir las condiciones de formación de los depósitos IOA Andinos y sus principales controles de la mineralización. Para esto, se resumieron y compararon los datos microtexturales y geoquímicos de las magnetitas de Carmen, Fresia y Mariela; los nuevos datos químicos de las magnetitas de El Romeral, tanto para los niveles más profundos (~347 m) y más someros (~10 m) del depósito, obtenidos en este estudio; y datos recopilados de la literatura, obtenidos de estudios de los últimos cinco años, de los Colorados, El Romeral, Cerro Negro Norte (Franja Ferrífera Chilena) y El Laco (Altiplano Chileno).

Los diferentes depósitos de la Franja Ferrífera Chilena y El Laco, revelan distintos tipos de magnetita, las cuales muestran un amplio espectro de microtexturas, e.g., zonación oscilatoria, bandeamiento coloforme, texturas de reequilibrio, exsolución laminar y simplectita; e inclusiones minerales distribuidas aleatoriamente en los núcleos de magnetita, siguiendo planos cristalográficos o en bandas ricas en elementos traza. Cada una de estas texturas entrega información de los procesos de formación de las magnetitas, es decir, magmáticos, hidrotermales, metasomáticos o de reequilibrio. En general, estas microtexturas acopladas con la composición química de la magnetita apuntan a que los depósitos IOA se forman a partir de una combinación de procesos tanto magmáticos como hidrotermales, y que la magnetita es susceptible a múltiples eventos de reequilibrio textural y composicional durante la formación y evolución de estos depósitos.

La geoquímica de la magnetita refleja condiciones/eventos variables de formación para cada uno de los depósitos en estudio. Estas condiciones varían desde puramente magmáticas, de alta-temperatura (>600 °C) y reducidas (baja-fO_2); a condiciones moderadas, de menor

temperatura magmático-hidrotermal y fO_2 intermedia; a baja-temperatura (200-300 °C) y condiciones hidrotermales más oxidantes (alta-fO_2). Una clara transición continua, desde condiciones de alta-temperatura y baja-fO_2 en las porciones más profundas del depósito, a condiciones de baja-temperatura, alta-fO_2 hacia niveles más someros se reconoce en El Laco. Los elementos traza, tales como Al, Ti, V, Cr, Mn, Ni, Cu y Ga son incorporados en la magnetita magmática e hidrotermal. La concentración de estos elementos es función de la disponibilidad del elemento (fuente), fugacidad de azufre y oxígeno, co-precipitación de las fases minerales competentes, interacción fluido-roca, la ocurrencia de inclusiones de escala nano a micro, y de manera más importante, la temperatura.

Adicionalmente, la observación de texturas de reequilibrio en magnetita sugiere que la composición de la magnetita primaria habría sido modificada, lo cual dificulta el uso e interpretación de distintos diagramas de discriminación. En particular, la concentración de Ti en magnetita ha sido ampliamente utilizada como un indicador del origen magmático, sin embargo, el Ti parece comportarse de manera móvil en los depósitos IOA durante los procesos de alteración hidrotermal y/o reequilibrio. Asimismo, la presencia de exsoluciones laminares de óxidos de Fe-Ti y simplectitas, que se forman mediante procesos de oxidación-exsolución y decompresión, respectivamente, requiere de nuevos cálculos complejos para determinar la composición original de la magnetita. Por consiguiente, el V y el Ga son mejores discriminantes para determinar condiciones de temperatura y fO_2 en la cristalizacón de magnetita.

Las microtexturas y geoquímica de la magnetita de los depósitos IOA de la Franja Ferrífera Chilena y El Laco, pueden ser explicadas por medio del *modelo de flotación*, el cual corresponde a un mecanismo de trasferencia "basal" de hierro que da origen a un fluido hidrotermal que forma/afecta a la mayoría de los depósitos IOA. En este modelo una suspensión de magnetita-fluido- (±apatito) evoluciona desde un magma silicatado intermedio-máfico y asciende hacia la superficie a través de fallas corticales preexistentas (Franja Ferrífera Chilena) o alternativamente, a través de fisuras que se formaron durante el colapso de la estructura volcánica (El Laco).

El *modelo de flotación* permite una variación dentro de su marco general, para acomodar distintos estilos o subtipos de mineralización IOA dentro de los niveles superiores de la corteza. Las variaciones observadas en los depósitos IOA Andinos sugieren que estos yacimientos conforman un grupo o clan de depósitos con grados variables de signaturas magmáticas e hidrotermales. Desde lo profundo, tipo-intrusivo (e.g., Los Colorados); transicional (e.g., El Romeral); intermedio, tipo-hidrotermal (e.g., Cerro Negro Norte); tipo-pegmatítico y rico en apatito (Carmen, Fresia y Mariela); y somero, subvolcánico/aéreo (e.g., El Laco). Estos subtipos de IOA se encuentran controlados fundamentalmente por la profundidad de formación, la presencia de estructuras/fallas por descompresión, la composición de la roca hospedante, la fuente y tasa de flujo de los fluidos hidrotermales, e incluso la infiltración de fluidos no-magmáticos como aguas meteóricas y posiblemente salmueras de cuenca. El modelo de formación propuesto también apoya la conexión genética observada entre la mineralización IOA e IOCG en la Franja Ferrífera Chilena, en un continuo desde lo profundo, con mineralización de magnetita empobrecida en sulfuros (IOA), a una mineralización más somera de magnetita y sulfuros (IOCG).

BIBLIOGRAFÍA

Apukhtina O.B., Kamenetsky V.S., Ehrig K., Kamenetsky M.B., Maas R., Thompson J. and Cook N.J. (2017) Early, deep magnetite-fluorapatite mineralization at the Olympic Dam Cu-U-Au-Ag deposit, South Australia. *Econ. Geol*. **112**, 1531-1542.

Barra F., Reich M., Selby D., Rojas P., Simon A., Salazar E. and Palma G. (2017) Unraveling the origin of the Andean IOCG clan: a Re-Os isotope approach. *Ore Geol Rev*. **81**, 62–78.

Barton M. D. and Johnson D.A. (1996) Evaporitic-source model for igneous-related Fe oxide–(REE-Cu-Au-U) mineralization. *Geol.* **24**, 259-262.

Barton M. D. and Johnson D. A. (2004) Footprints of Fe-oxide (-Cu-Au) systems. University of Western Australia Special Publication, **33**, 112-116.

Barton M. D. (2014) Iron oxide (–Cu–Au–REE–P–Ag–U–Co) systems. In *Scott, S.D., ed., Treatise on Geochemistry* (second edition, volume 13): Amsterdam, Elsevier, 515–541.

Bea F., Pereira M. D. and Stroh A. (1994) Mineral/leucosome trace-element partitioning in a peraluminous migmatite (a laser ablation-ICPMS study). *Chem. Geol*. **117**, 291-312.

Benavides J., Kyser T.K., Clark A.H., Oates C.J., Zamora R., Tarnovschi R. and Castillo, B. (2007) The Mantoverde iron oxide-copper-gold district, III Región, Chile: the role of regionally derived, nonmagmatic fluids in chalcopyrite mineralization. *Econ. Geol*. **102**, 415-440.

Belousova E. A. (2000) Trace elements in zircon and apatite: application to petrogenesis and mineral exploration. PhD thesis. Macquare University, Australia.

Belousova E. A., Walters S., Griffin W. L. and O´Reilly S. Y. (2001) Trace element signatures of apatites from granitoids of Mount Isa Inlier, north-west Queensland, Australia. *Aust. J. Earth Sci.* **48**, 603-619.

Betkowski V., Harlov D. and Rakovan J. (2016) Hydrothermal mineral replacement reactions for an apatite-monazite assemblage in alkali-rich fluids at 300 - 600 °C and 100 MPa. *Am. Mineral.* **101**, 2620–2637.

Bilenker L.D., Simon A.C., Reich M., Lundstrom C.C., Gajos N., Bindeman I. and Munizaga R. (2016) Fe–O stable isotope pairs elucidate a high-temperature origin of Chilean iron oxide-apatite deposits. *Geochim. Cosmochim. Acta* **177**, 94-104.

Chen H., Clark A. H. and Kyser T. K. (2010) The Marcona magnetite deposit, Ica, south-central Peru: a product of hydrous, iron oxide-rich melts?. *Econ. Geol.* **105**, 1441-1456.

Childress T. M., Simon A. C., Day W. C., Lundstrom C. C. and Bindeman I. N. (2016) Iron and oxygen isotope signatures of the Pea Ridge and Pilot Knob magnetite–apatite deposits, southeast Missouri, USA. *Econ. Geol.* **111**, 2033-2044.

Daliran F., Stosch H. G., Williams P., Jamli H. and Dorri M. B. (2010) Early Cambrian Iron Oxide-Apatite-REE (U) Deposits of the Bafq District, East-Central Iran. In Exploring for Iron oxide copper-gold deposits: Canada and Global analogues (L. Corriveau & H. Mumin, eds.). *Geological Association of Canada Short Course Notes* **20**, 143–155.

Dare S.A., Barnes S-J. and Beaudoin G. (2012) Variation in trace element content of magnetite crystallized from a fractioning sulfide liquid, Sudbury, Canada: Implications for provenance discrimination. *Geochim. Cosmochim. Acta* **88**, 27-50.

Dare S.A., Barnes S-J., Beaudoin G., Méric J., Boutroy E. and Potvin-Doucet C. (2014) Trace elements in magnetite as petrogenetic indicators. *Miner. Deposita* **49**, 785-796.

Dare S., Barnes S. J. and Beaudoin. G. (2015) Did the massive magnetite "lava flows" of El Laco (Chile) form by magmatic or hydrothermal processes? New constraints from magnetite composition LA-ICP-MS. *Miner Deposita*. **50**, 607.

Day W.C., Slac, J.F., Ayuso R.A. and Seeger C.M. (2016) Regional geologic and petrologic framework for iron oxide±apatite±rare earth element and iron oxide copper-gold deposits of the Mesoproterozoic St. Francois Mountains terrane, southeast Missouri, USA. *Econ. Geol.* **111**, 1825-1858.

Deditius A.P., Reich M., Simon A.C., Suvorova A., Knipping J., Roberts M.P. and Saunders M. (2018) Nanogeochemistry of hydrothermal magnetite. *Contrib. Mineral. Petrol.* **173**, 46.

De Melo G.H.C, Monteiro L.V.S, Xavier R.P, Moreto C.P.N, Santiago E.S.B, Dufrane S.A, Aires B. and Santos A.F.F. (2017) Temporal evolution of the giant Salobo IOCG deposit, Carajás Province (Brazil): constraints from paragenesis of hydrothermal alteration and U-Pb geochronology. *Miner. Deposita* **52**, 709-732.

Dupuis C. and Beaudoin G. (2011) Discriminant diagrams for iron oxide trace element fingerprinting of mineral deposit types. *Miner. Deposita* **46**, 319-335.

Espinoza R.S., Véliz G.H., Esquivel L.J, Arias F.J. and Moraga B.A. (1996) The cupriferous province of the Coastal Range, northern Chile. Andean copper deposits: New discoveries, mineralization, styles and metallogeny, *SEG Sp. Pub*. **5**, 19-32.

Frutos J. and Oyarzún M. J. (1975) Tectonic and geochemical evidence concerning the genesis of El Laco magnetite lava flow deposits, Chile. *Econ. Geol.* **70**, 988-990.

Groves D.I., Bierlein F.P., Meinert L.D. and Hitzman M.W. (2010) Iron oxide copper-gold (IOCG) deposits through Earth history: Implications for origin, lithospheric setting, and distinction from other epigenetic iron oxide deposits. *Econ. Geol.* **105**, 641-654.

Hansen E. C. and Harlov D. E. (2007) Whole-rock, phosphate, and silicate compositional trends across an amphibolite-to granulite-facies transition, Tamil Nadu, India. *J. Petrol*. **48**, 1641-1680.

Harlov D. E., Förster H. J. and Nijland T. G. (2002a) Fluid-induced nucleation of REE-phosphate minerals in apatite: nature and experiment. Part I. Chlorapatite. *Am. Mineral.* **87**, 245-261.

Harlov D. E. and Förster H. J. (2003) Fluid-induced nucleation of (Y+REE)-phosphate minerals within apatite: Nature and experiment. Part II. Fluorapatite. *Amer. Min*. **88**, 1209–1229.

Harlov D. E., Wirth R. and Förster H. J. (2005) An experimental study of dissolution–reprecipitation in fluorapatite: fluid infiltration and the formation of monazite. *Contrib. Mineral. Petrol*. **150**, 268-286.

Hitzman M.W., Oreskes N. and Einaudi, M.T. (1992) Geological characteristics and tectonic setting of proterozoic iron oxide (Cu- U- Au- REE) deposits. *Precambr. Res.* **58**, 241-287.

Huang X.W. and Beaudoin G. (2019) Textures and chemical compositions of magnetite from iron oxide copper-gold (IOCG) and Kiruna-type iron oxide-apatite (IOA) deposits and their implications for ore genesis and magnetite classification schemes. *Econ. Geol.* **114**, 1-74.

Huang W.W., Sappin A.A., Boutroy E., Beaudoin G. and Makvandi S. (2019) Trace Element Composition of Igneous and Hydrothermal Magnetite from Porphyry Deposits: Relationship to Deposit Subtypes and Magmatic Affinity. *Econ. Geol.* **114**, 917-952.

Jonsson E., Persson-Nilsson K., Högdahl K., Troll V. and Hallberg A. (2010) REE distribution and mineralogy in a Palaeoproterozoic apatite-iron oxide deposit: Grängesberg, Bergslagen, Sweden. In *IMA 2010*, **6**, 234.

Kim Y., Koecke B., Fiege B., Simon A. and Becker U. (2017) An ab-initio study of the energetics and geometry of sulfide, sulfite and sulfate incorporation in apatite; The thermodinamic basis for using this system as an oxybarometer. *Amer. Min*. **102**, 1646-1656.

Knipping J. L., Bilenker L.D., Simon A.C., Reich M., Barra F., Deditius A. P., Lundstrom C., Bindeman I. and Munizaga R. (2015a) Giant Kiruna-type deposits form by efficient flotation of magmatic magnetite suspensions. *Geol.* **43**, 591-594.

Knipping J. L., Bilenker L. D., Simon A. C., Reich M., Barra F., Deditius A. P., Wälle M., Heinrich C. A., Holtz F. and Munizaga R. (2015b) Trace elements in magnetite from massive iron oxide-apatite deposits indicate a combined formation by igneous and magmatic-hydrothermal processes. *Geochim. Cosmochim. Acta* **171**, 15-38.

Knipping J., L., Fiege A., Simon A.C., Oeser-Rabe M., Reich M. and Bilenker L. (2019a) In-situ iron isotope analyses reveal igneous and magmatic-hydrothermal growth of magnetite at the Los Colorados Kiruna-type iron oxide-apatite deposit, Chile. *Am. Mineral*. **104**, 471–484.

Knipping J., Webster J.D., Simon A.C. and Holtz F. (2019b) Accumulation of magnetite by flotation on bubbles during decompression of silicate magma. *Sci. Rep*. **9**, 3852.

Konecke B., Fiege A., Simon A., Parat F. and Stechern A. (2017) Co-variability of S^{6+}, S^{4+}, and S^{2-} in apatite as a function of oxidation state: Implications for a new oxybarometer. *Amer. Min.* **102**, 548–557.

La Cruz N.L., Simon A.C., Wolf A.S., Reich M., Barra F. and Gagnon J.E. (2019) The geochemistry of apatite from the Los Colorados iron oxide–apatite deposit, Chile: implications for ore genesis. *Miner. Deposita* **54**, 1143-1156.

Li X. and Zhou M-F. (2015) Multiple stages of hydrothermal REE remobilization recorded in fluorapatite in the Paleoproterozoic Yinachang Fe-Cu-(REE) deposit, Southwest China. *Geochim. Cosmochim. Acta* **166**, 53-73.

Maksaev V., Gardeweg M., Ramírez C. F. and Zentilli M. (1988). Aplicación del método trazas de fisión (fission track) a la datación de cuerpos de magnetita de El Laco e Incahuasi en el altiplano de la Región de Antofagasta. In *Congreso Geológico Chileno, No. 5, v. 1: B1-B23.*

Mumin A.H., Corriveau L., Somarin A.K. and Ootes L. (2007) Iron oxide copper-gold-type polymetallic mineralization in the Contact Lake belt, Great Bear magmatic zone, Northwest Territories, Canada: Explor. *Min. Geol*. **16**, 187–208

Nadoll P., Mauk J.L., Hayes T.S., Koenig A.E. and Box S.E. (2012) Geochemistry of magnetite from hydrothermal ore deposits and host rocks of the Mesoproterozoic Belt Supergroup, USA. *Econ. Geol.* **107**, 1275-1292.

Nadoll P., Angerer T., Mauk J. L., French D. and Walshe J. (2014) The chemistry of hydrothermal magnetite: a review. *Ore Geol. Rev.* **61**, 1-32.

Nadoll P., Mauk J.L., Leveille R.A. and Koenig A.E. (2015) Geochemistry of magnetite from porphyry Cu and skarn deposits in the southwestern United States. *Miner. Deposita* **50**, 493-515.

Naranjo J.A., Henríquez F. and Nyström J.O. (2010) Subvolcanic contact metasomatism at El Laco volcanic complex, central Andes. *Andean Geology*, **37**, 110-120.

Naslund H.R., Henríquez F., Nyström J.O., Vivallo W. and Dobbs F.M. (2002) Magmatic iron ores and associated mineralisation: examples from the Chilean high Andes and coastal Cordillera. In: *Hydrothermal Iron Oxide-Copper-Gold: A Global Perspective. T.M. Porter (Ed.)*, PGC Publishing, Adelaide, Australia, **2**, 207-226.

Nyström J. O. and Henríquez F. (1994) Magmatic features of iron ores of the Kiruna-type in Chile and Sweden: ore textures and magnetite geochemistry. *Econ. Geol.* **89**, 820-839.

Ovalle J.T., La Cruz N.L., Reich M., Barra F., Simon A.C., Konecke B.A. and Morata D. (2018) Formation of massive iron deposits linked to explosive volcanic eruptions. *Sci. Rep*. **8**, 14855.

Palma G., Barra F., Reich M., Valencia V., Simon A.C., Vervoort J., Leisan M. and Romero R. (2019) Halogens, trace element concentrations, and Sr-Nd isotopes in apatite from iron oxide-apatite (IOA) deposits in the Chilean iron belt: Evidence for magmatic and hydrothermal stages of mineralization. *Geochim. Cosmochim. Acta* **246**, 515-540.

Pan Y. and Fleet M. (2002) Compositions of the apatite-group minerals: substitution mechanisms and controlling factors. *Rev. Mineral. Geochem.* **48**, 13-50.

Patiño Douce, A.E., Roden, M.F., 2006. Apatite as a probe of halogen and water fugacities in the terrestrial planets. *Geochim. Cosmochim. Acta* **70**, 3173–3196.

Peng G., Luhr J. F. and McGee J. J. (1997) Factors controlling sulfur concentrations in volcanic apatite. *Amer. Min.* **82**, 1210-1224.

Perseil E. A., Blanc P. and Ohnenstetter D. (2000) As-bearing fluorapatite in manganiferous deposits from St. Marcel–Praborna, Val d'Aosta, Italy. *Can. Mineral.* **38**, 101-117.

Piccoli P. M. and Candela P. A. (2002) Apatite in Igneous Systems. In: Kohn, M.J., Rakovan., Hughes, J.M. (eds.), Phosphates: geochemical, geobiological, and materials importance. : *Rev. Mineral. Geochem.* **48,** 255-292.

Pollard P.J. (2006) An intrusion-related origin for Cu–Au mineralization in iron oxide–copper–gold (IOCG) provinces. *Miner. Deposita* **41**, 179.

Prowatke S. and Klemme S. (2006) Trace element partitioning between apatite and silicate melts. *Geochim. Cosmochim. Acta* **70**, 4513-4527.

Rakovan J., McDaniel D. K. and Reeder R. J. (1997) Use of surface-controlled REE sectoral zoning in apatite from Llallagua, Bolivia, to determine a single-crystal Sm-Nd age. *Earth Planet. Sci. Lett.* **146**, 329-336.

Reich M., Simon A.C., Deditius A., Barra F., Chryssoulis S., Lagas G. and Roberts M.P. (2016) Trace element signature of pyrite from the Los Colorados iron oxide-apatite (IOA) deposit, Chile: A missing link between Andean IOA and iron oxide copper-gold systems? *Econ. Geol.* **111**, 743-761.

Rhodes A. L. and Oreskes N. (1995) Magnetite deposition at El Laco, Chile: implications for Fe-oxide formation in magmatic-hydrothermal systems. Giant ore deposits-II: Controls on the scale of orogenic magmatic-hydrothermal mineralization Clark, AH, 582-622.

Rhodes A. L. and Oreskes N. (1999) Oxygen isotope composition of magnetite deposits at El Laco, Chile: Evidence of formation from isotopically heavy fluids. Geology and Ore Deposits of the Central Andes, Brian J. Skinner, ed., *Society of Economic Geologists Special Publication* **7**, 333-351.

Rieger A.A., Marschik R., Díaz M., Hölzl S., Chiaradia M., Akker B. and Spangenberg J.E. (2010) The hypogene iron oxide copper-gold mineralization in the Mantoverde district, northern Chile. *Econ. Geol.* **105**, 1271-1299.

Rieger A.A., Marschik R. and Díaz M. (2012) The evolution of the hydrothermal IOCG system in the Mantoverde district, northern Chile: new evidence from microthermometry and stable isotope geochemistry. *Miner. Deposita* **47**, 359-369.

Rojas P., Barra F., Reich M., Deditius A., Simon A., Uribe F., Romero R. and Rojo M. (2018a) A genetic link between magnetite mineralization and diorite intrusión at the El Romeral iron oxide-apatite deposit, northern Chile. *Miner. Deposita* 1-20.

Rojas P., Barra F., Deditius A., Reich M., Simon A., Roberts M. and Rojo M. (2018b) New contributions to the understanding of Kiruna-type iron oxide-apatite deposits revealed by magnetite ore and gangue mineral geochemistry at the El Romeral deposit, Chile. *Ore Geolog. Rev.* **93** 413-435.

Rusk B., Oliver N., Cleverley J., Blenkinsop T., Zhang D., Williams P. and Habermann P. (2010) Physical and chemical characteristics of the Ernest Henry iron oxide copper gold deposit, Australia; implications for IOGC genesis. In *Implications for IOGC Genesis; PGC Publishing: Adelaide, Australia.*

Salazar E., Barra F., Reich M., Simon A., Leisen M., Palma G. and Rojo M. (2019) Trace element geochemistry of magnetite from the Cerro Negro Norte iron oxide− apatite deposit, northern Chile. *Miner. Deposita* 1-20.

Sawka M. N. and Wenger C. B. (1988) Physiological responses to acute exercise-heat stress (No. USARIEM-M-14/88). Army research inst of environmental medicine natick ma.

Schettler G., Gottschalk M. and Harlov, D. E. (2011) A new semi-micro wet chemical method for apatite analysis and its application to the crystal chemistry of fluorapatite-chlorapatite solid solutions. *Am. Mineral.* **96**, 138-152.

Sha L. K. and Chappell B. W. (1999) Apatite chemical composition, determined by electron microprobe and laser-ablation inductively coupled plasma mass spectrometry, as a probe into granite petrogenesis. *Geochim. Cosmochim. Acta* **63**, 3861-3881.

Sillitoe R. H. and Burrows D. R. (2002) New field evidence bearing on the origin of the El Laco magnetite deposit, northern Chile. *Econ. Geol.* **97**, 1101-1109.
Sillitoe R. H. (2003) Iron oxide–copper–gold deposits: An Andean view. *Miner. Deposita* **38**, 787–812.

Simon A. C., Kniping J., Reich M., Barra F., Deditius A. P., Bilenker L. and Childress T. (2018) Kiruna-Type Iron Oxide-Apatite (IOA) and Iron Oxide Copper-Gold (IOCG) Deposits form by a combination of ignous and magmatic-hydrothermal processes:evidence from the Chilean Iron Belt. *SEG Special Publications*, **21**, 89-114.

Spear F. S. and Pyle J. M. (2002) Apatite, monazite, and xenotime in metamorphic rocks. *Rev. Mineral. Geochem.* **48**, 293-335.

Toplis M. J. and Dingwell D. B. (1996) The variable influence of P_2O_5 on the viscosity of melts of differing alkali/aluminium ratio: Implications for the structural role of phosphorus in silicate melts. *Geochim. Cosmochim. Acta* **60**, 4107-4121.

Tornos F., Velasco F. and Hanchar J.M. (2016) Iron-rich melts, magmatic magnetite, and superheated hydrothermal systems: The El Laco deposit, Chile. *Geology* **44**, 427–430.

Velasco F., Tornos F. and Hanchar, J.M. (2016) Immiscible iron-and silica-rich melts and magnetite geochemistry at the El Laco volcano (northern Chile): Evidence for a magmatic origin for the magnetite deposits. *Ore Geol. Rev.* **79**, 346-366.

Watson E. B. and Green T. H. (1981) Apatite/liquid partition coefficients for the rare earth elements and strontium. *Earth Planet. Sci. Lett.* **56**, 405-421.

Webster J. D. and Piccoli P. M. (2015) Magmatic apatite: A powerful, yet deceptive, mineral. *Elements* **11**, 177-182.

Westhues A., Hanchar J.M., Whitehouse M.J. and Martinsson O. (2016) New constraints on the timing of host-rock emplacement, hydrothermal alteration, and iron oxide-apatite mineralization in the Kiruna district, Norrbotten, Sweden. *Econ. Geol.* **111**, 1595-1618.

Westhues A., Hanchar J.M., LeMessurier M.J. and Whitehouse M.J. (2017a) Evidence for hydrothermal alteration and source regions for the Kiruna iron oxide–apatite ore (northern Sweden) from zircon Hf and O isotopes. *Geology* **45**, 571-574.

Westhues A., Hanchar J.M., Voisey C.R., Whitehouse M.J., Rossman G.R. and Wirth R. (2017b) Tracing the fluid evolution of the Kiruna iron oxide apatite deposits using zircon, monazite, and whole rock trace elements and isotopic studies. *Chem. Geol.* **466**, 303-322.

Williams P.J., Barton M.D., Fontbote L., de Haller A., Johnson D. A., Mark G., Marschik R. and Oliver N. H. S. (2005) Iron oxide-copper-gold deposits: Geology, space-time distribution, and possible modes of origin. *Economic Geology 100Th Anniversary Volume* 371–406.

Zaitsev A. and Bell K. (1995) Sr and Nd isotope data of apatite, calcite and dolomite as indicators of source, and the relationships of phoscorites and carbonatites from the Kovdor massif, Kola peninsula, Russia. *Contrib. Mineral. Petrol*. **121**, 324-335.

Zhao X., Zhou M. and Gao J. (2015) In situ Sr isotope analysis of apatite by La-MC-ICPMS: constraints on the evolution of ore fluids of the Yinachang Fe-Cu-REE deposit, Southwest China. *Miner. Deposita* **50**, 871-884.

Zeng L., Zhao X., Li X., Hu H., and McFarlane C. (2016) In situ elemental and isotopic analysis of fluorapatite from the Taocun magnetite-apatite deposit, Eastern China: Constraints on fluid metasomatism. *Amer. Min.***101**, 2468-2483.

ANEXOS

ANEXO A

MATERIAL SUPLEMENTARIO DEL CAPÍTULO 2

Halogens, trace element concentrations, and Sr-Nd isotopes in apatite from Iron Oxide-Apatite (IOA) deposits in the Chilean iron belt: Evidence for magmatic and hydrothermal stages of mineralization

Este archivo incluye:

A1. Structure and chemistry of apatite
A2. Geological background
A3. Geology of Carmen, Fresia and Mariela IOA deposits

Figures A1-A4

Otros materias suplementarios incluyen las siguientes tablas en formato Excel:

Table A0. LA-ICP-MS analyses for the Durango apatite reference material

Table A1. Apatite textures from Carmen, Fresia and Mariela deposits

Table A2: Statistical parameters for F-Cl-OH concentrations (formula values) in apatite from the Carmen, Fresia and Mariela deposits

Table A3: EPMA data for traverses across apatite domains from the Carmen, Fresia and Mariela deposits

Table A4: EPMA data for apatite types from Carmen

Table A5: LA-ICP-MS data for apatite types from Carmen, Fresia and Mariela

A.1. STRUCTURE AND CHEMISTRY OF APATITE

Apatite [$Ca_{10}(PO_4)_6(F, Cl, OH)$] has a hexagonal crystal structure formed by PO_4^{3-} tetrahedra that are arranged in two structural channels parallel to the crystal axis. Calcium is accommodated in two distinct structural sites: Ca(1) and Ca(2). Calcium atoms in the Ca(1) or columnar site account for 40% of the total Ca and bind to O, forming a nine-fold-coordination without F-Cl-OH coordination. These atoms join the PO_4^{3-} tetrahedra forming a three-dimensional network of tetrahedral PO_4^{3-} groups and columnar Ca^{2+} cations with channels passing around them. Calcium atoms in the Ca(2) or triangular Ca2+ cations correspond to the remaining 60% of the total Ca and are surrounded and coordinated with F-Cl-OH anions forming a seven-fold-coordination within the larger channel. For this reason, major structural changes due to exchanges in the anion column (F-Cl-OH) occur in the Ca(2) site (Elliot et al., 2002, Hughes and Rakovan, 2002; Pan and Fleet, 2002). The anion columns formed by F, Cl and OH anions are located in the center of the Ca(2) triangles, but at different levels in the structure for fluorapatite, chlorapatite and hydroxyapatite. Fluorine, which is the smallest of the anions (1.31 Å; Shannon, 1976), easily fits at the center of the Ca(2) triangles and is coplanar with Ca^{2+} cations. In contrast, the slightly larger OH^- (1.37 Å; Kusebauch et al., 2015) and the larger Cl^- (1.81 Å; Shannon, 1976) are located in a displaced position below or above the Ca(2) triangle, which causes a modification of the structure (Hughes et al., 1989). At magmatic temperatures above 500 °C these structural differences are allowed and the structure of chlorapatite and hydroxyapatite remain as hexagonal. However, at temperatures below 350 °C chlorapatite and hydroxyapatite acquire a monoclinic structure (Bauer and Klee, 1993).

The structure of apatite can accommodate other cations such as K^+, Na^+, Mn^{2+}, Fe^{2+}, Eu^{2+}, Ni^{2+}, $Cu^{2+,}$ Co^{2+}, Zn^{2+}, Sr^{2+}, Ba+, Pb^{2+}, Y^{3+}, $REEs^{3+}$, Th^{4+} and U^{4+} that substitute for Ca^{2+}, whereas anionic complexes such as AsO_4^{3-}, SO_4^{2-}, CO_3^{2-}, MnO_4^{3-}, VO_4^{3-} SiO_4^{4-} can replace the PO_4^{3-} group (Pan and Fleet, 2002). The radius of Ca^{+2} in Ca(1) and Ca(2) sites are 1.18 and 1.06 Å, respectively (Shannon, 1976), so divalent cations can be incorporated into the Ca(1) or Ca(2) site according to their size without any electrostatic compensation mechanism (Rakovan and Hughes, 2000; Pan and Fleet, 2002; Piccoli and Candela, 2002). It should be noted that Mn can enter the apatite structure as Mn^{2+} or Mn^{3+} depending on redox conditions, however, Mn^{2+} is more compatible in apatite than Mn^{3+} (Miles et al., 2014). Other cations including ($REEs^{3+}$ and Y^{+3}), U^{4+}, Th^{4+} and S^{6+}, require coupled substitutions to achieve charge balance. Although $REEs^{3+}$ have similar geochemical behavior, the small differences in their ionic radius results in LREEs entering the Ca(2) site (larger size, nine-fold coordination) whereas HREEs substitute into the Ca(1) site (smaller size, seven-fold coordination) (Hughes et al, 1991). The substitution of ($REEs^{3+}$ + Y^{3+}), U^{4+}, Th^{4+} and S^{6+} can be expressed as:

$(REE^{3+} + Y^{3+}) + Na^+ = 2Ca^{2+}$ (1)

$(REE^{3+} + Y^{3+}) + SiO_4+ = Ca^{2+} + PO_4^{3-}$ (2)

(Rønsbo, 1989; Fleet and Pan, 1995; Sha and Chappel, 1999, Chen et al., 2002; Pan and Fleet; 2002)

$(Th^{4+} + U^{4+}) + \bullet = 2Ca^{2+}$ (3)

(Hughson and SenGupta, 1964; Baumer et al., 1983, Pan and Fleet, 2002).

$SO_4^{2-} + SiO_4^{4-} = 2PO_4^{3-}$ (3)

$SO_4^{2-} + Na^+ = PO_4^{3-} + Ca^{2+}$ (4)

(Rouse and Dun, 1982; Peng et al., 1997; Sha and Chappel, 1999)

A2. GEOLOGICAL BACKGROUND

The Central Andes during the Late Jurassic to Early Cretaceous was characterized by an extensional tectonic setting with a Mariana-type subduction zone that produced a magmatic arc-backarc pair (Mpodozis and Ramos, 1990; Ramos, 2010). The eastward migration of the magmatic arc is reflected in several NS belts where remnants of the Jurassic arc are located at the current Pacific coastline and the Cretaceous arc is represented in the Coastal Cordillera (Scheuber and Reutter, 1992; Dallmeyer et al., 1996). The Jurassic-Cretaceous magmatic arcs were dominated by tholeiitic basaltic rocks, gabbros and mafic dikes associated with calc-alkaline andesites and basaltic andesite flows (Mpodozis and Ramos, 1990; Scheuber et al. 1994; Oliveros et al., 2006). A recent study demonstrated an origin of the Jurassic arc associated with subduction and not from a MORB-like source (Kramer et al., 2015). Plutonic complexes within the magmatic arc comprise hornblende-biotite gabbros, diorites, tonalites, granodiorites, and minor granites (Dallmeyer et al., 1996). The main structural feature along this convergent margin corresponds to the Atacama Fault System, an arc-parallel, sinistral strike-slip fault system that extends for over 1000 km (Brown et al., 1991a, 1993) and that formed in response to oblique subduction of the Aluk (Phoenix) plate during the Cretaceous period (Naranjo et al., 1984; Woodcock, 1986; Thiele and Pincheira, 1987; Reutter and Scheuber, 1988; Scheuber and Adriessen, 1990; Scheuber and Reutter, 1992).

A3. GEOLOGY OF CARMEN, FRESIA AND MARIELA IOA DEPOSITS

Carmen and Fresia deposits

The Carmen IOA deposit is an irregular magnetite-rich ore body with an EW orientation, approximately 50 m wide, 500 m long and at least 250 m vertical depth (Treloar and Colley, 1996). It is located ~20 km to the east of the Atacama Fault System (**Figure 2**), and is hosted by andesites of the Jurassic La Negra Formation (Godoy and Lara, 1998; Gelcich et al. 2005). The shape of the (now abandoned) open pit is marked by the intersection of an E-W trending set of steep faults with subhorizontal slickensides and a N-trending array of conjugate dip-slip faults (Treloar and Colley, 1993, 1996). The orientation and morphology of the Carmen deposit are related to its emplacement in a pull-apart structure formed during sinistral strike-slip movements during early stages of the Atacama Fault System (Cembrano et al., 2005). A quartz diorite stock with magnetite-apatite veins located at the northern end of the Carmen pit has been dated at 130.6 ± 0.3 Ma (U-Pb zircon age, Gelcich et al., 2005), which is consistent with a 131.0 ± 1.0 Ma U-Pb apatite age (Gelcich et al., 2005) obtained from a magnetite-apatite tabular body.

The Fresia IOA deposit, located ~25 km NW of Carmen, is emplaced close to the main trace of the Atacama Fault System (**Figure 2**). Fresia is an elongate, steep-sided massive magnetite body less than 20 m wide, and it has a sinuous shape, controlled by two sets of faults trending at 80° and 65°. The deposit is hosted by Lower Cretaceous andesitic rocks of Los Cerros Florida

Formation that comprises a series of thick lava flows intruded by andesitic dikes (Treloar and Colley, 1996).

The Fresia and Carmen deposits have similar ore textures. The ore bodies are dominated modally by massive magnetite with local hematite patches. The tabular magnetite bodies vary in size, with veins that are up to 20 m wide to veinlets no more than a few mm thick. Apatite commonly occurs as prismatic and acicular large crystals up to ~50 cm long (**Figure A1-a,c**), immersed in a magnetite matrix together with variable amounts of actinolite (**Figure A1-a**) and with a non-uniform distribution or perpendicular to vein walls or intrusion contacts (**Figure A1-c**). Some apatite grains have a color zonation with pink cores grading to pale pink or white rims, while others are replaced by elongated fine-grained apatite, or are crosscut by late magnetite and epidote veinlets. The massive magnetite-apatite bodies are brecciated and/or have banded structures with local development of flow-type textures (**Figure A1-b**), similar to those described for Kiruna deposits in Sweden (Frietsch, 1978). The host rocks are affected by a propylitic alteration (epidote-chlorite-calcite-actinolite-hematite), which is more pervasive in Fresia than in Carmen.

Treloar and Colley (1996) reported the following sequence of events for mineralization at Carmen and Fresia. The earliest stage was a propylitic alteration event that affected the host rocks followed by brecciation and magnetite precipitation in fractures, and as the breccia matrix forming fine layers of magnetite around clasts. Apatite and actinolite precipitated after magnetite, growing perpendicular from the breccia clasts and resembling the *stockscheider* structure of pegmatites described in evolved granites (Candela, 1997). The last event corresponds to late-stage veinlets with magnetite, hematite and epidote that crosscuts the previous events.

Mariela deposit

The Mariela deposit is located 90 km SE of Taltal and 3 km NW of the Barreal Seco IOCG deposit (**Figure 2**). It is hosted by a Cretaceous plutonic complex that intruded andesites of the Upper Jurassic-Lower Cretaceous Aeropuerto Formation. A granodiorite from the Coastal Batholith that outcrops west of the deposit has been dated at 112 ± 4 Ma (K-Ar biotite; Naranjo and Puig, 1984).

At Mariela, a regional weak propylitic alteration is overprinted by an apatite-actinolite event associated with a NNE orientation fault-related breccia pipe (**Figure A1-d**). The main apatite-actinolite mineralization-alteration stage is dominant in the central and eastern parts of the deposit, whereas apatite-magnetite predominates in the western part, and hornblende at depth. The breccia body is mainly composed of an apatite ± actinolite ± magnetite matrix with intrusive fragments strongly altered to chlorite and minor epidote. In contrast to Carmen and Fresia, apatite from Mariela is massive, forming large (up to 3 m wide) bodies (**Figure A1-d**). Within the apatite matrix, tabular to acicular crystals of actinolite are present with minor magnetite and hematite (2-15 cm). Large open spaces and smaller voids are often filled by cm-sized actinolite crystals. Minor copper mineralization in the form of oxides such as chrysocolla and atacamite, and trace amounts of sulfides (pyrite and chalcopyrite) are possibly related to a late hydrothermal sulfide event affected by supergene/oxidation processes.

References

Bauer M. and Klee W. E. (1993) The monoclinic-hexagonal phase transition in chlorapatite. Eur. J. Mineral. 5, 307-316 Rakovan, J., Hughes, J.M., 2000. Strontium in the apatite structure: Strontium fluorapatite and belovite-(Ce). Can. Mineral. 38, 839-845.

Baumer A., Caruba R., Bizzouard H. and Peckett A. (1983) Chlorapatite de synthésis: substitution et inclusions de Mn, Ce, U et Th traces. Can. Mineral. 21, 567-573.

Brown M., Dallmeyer R. D., Diaz F. and Grocott J. (1991a) Displacement history and tectonic significance of the Atacama Fault System (El Salado segment) N Chile: 40Ar/39Ar mineral age constraints: Eos (Trans. Am. Geophys. Union), 72/17, p. 263.

Brown M., Diaz F. and Grocott J. (1993) Displacement history of the Atacama Fault System, 25°00' S - 27°00' S, Northern Chile. Geol. Soc. America Bull. 105, 1165-1174.

Candela P. (1997) A review of shallow, ore-related granites: textures, volatiles and ore metals. J. Petrol. 38, 1619-1633.

Cembrano J., González G., Arancibia G., Ahumada I., Olivares V. and Herrera V. (2005) Fault zone development and strain partitioning in an extensional strike-slip duplex: a case study from the Atacama fault system, Northern Chile. Tectonophysics 400,105-125.

Chen F., Siebel W., Satir M., Terzioğlu M. and Saka K. (2002) Geochronology of the Karadere basement (NW Turkey) and implications for the geological evolution of the Istanbul zone. Inter. J. Earth Sci. 91, 469-481.

Dallmeyer R. D., Brown M., Grocott J., Taylor G. K. and Treloar P. J. (1996) Mesozoic Magmatic and Tectonic Events within the Andean Plate Boundary Zone, 26-27 30'S, North Chile: Constraints from Mineral Ages. J. Geol. 104, 19-40.

Elliott J. C. (2002) Calcium phosphate biominerals. Rev. Mineral. Geochem. 48, 427-453.

Hughes, J.M., Rakovan, J., 2002. The crystal structure of apatite, $Ca_5(PO_4)3(F, OH, Cl)$. Rev. Mineral. Geochem. 48, 1-12.

Fleet M. E. and Pan Y. (1995) Site preference of rare earth elements in fluorapatite. Amer. Min. 80, 329-335.

Frietsch R. (1978) On the magmatic origin of ion ores of the Kiruna type. Econ. Geol. 73, 478-485.

Gelcich S., Davis D. W. and Spooner E. T. (2005) Testing the apatite-magnetite geochronometer: U-Pb and 40Ar/39Ar geochronology of plutonic rocks, massive magnetite-apatite tabular bodies, and IOCG mineralization in Northern Chile. Geochim. Cosmochim. Acta, 69, 3367-3384.

Godoy E., and Lara L. (1998) Hojas Chañaral y Diego de Almagro, Región de Atacama. Mapas Geológicos Nº 5-6. Escala 1:100.000. SERNAGEOMIN, Santiago, Chile, 1998, 20 Pág.

Hughes J. M., Cameron M., and Crowley K. D. (1989) Structural variations in natural F, OH, and Cl apatites. Amer. Min. 74, 870-876.

Hughes J. M., Cameron M., and Mariano A. N. (1991) Rare-earth element ordering and structural variations in natural rare-earth bearing apatites. Amer. Mineral. 76, 1165-1173.

Hughson M. R. and SenGupta J. (1964) A thorian intermediate member of britholite-apatite series-physical+ chemical studies. Amer. Min. 49, 937-951.

Kramer W., Siebel W. M., Romer R., Haase G., Zimmer M. and Ehrlichmann R. (2005) Geochemical and isotopic characteristics and evolution of the Jurassic volcanic arc between Arica (18° 30´ S) and Tocopilla (22° S), North Chilean Coastal Cordillera. Chemie der Erde 65, 47–68.

Kusebauch C., John T., Whitehouse M. J., Klemme S., and Putnis A. (2015) Distribution of halogens between fluid and apatite during fluid-mediated replacement processes. Geochim. Cosmochim. Acta 170, 225-246.

Miles A. J., Graham C. M., Hawkesworth C. J., Gillespie M. R., Hinton R.W. and Bromiley G.D. (2014) Apatite: A new redox proxy for silicic magmas?. Geochim. Cosmochim. Acta 132, 101-119.

Mpodozis C. and Ramos V. A. (1990) The Andes of Chile and Argentina. In: Geology of the Andes and its Relation to Hydrocarbon and mineral Resources, Ericksen GE, Can˜as Pinochet MT, Ramos, V.A., 2010. The tectonic regime along the Andes: Present-day and Mesozoic regimes. Geol. J. 45, 2-25.

Naranjo J. A. and Puig A. (1984) Hojas Taltal y Chanaral: Servicio Nacional de Geología y Minería Carta Geológica de Chile No. 62-63, 140 p.

Oliveros V., Féraud G., Aguirre L., Fornari M. and Morata D. (2006) The early Andean magmatic province (EAMP): 40 Ar/39 Ar dating on Mesozoic volcanic and plutonic rocks from the Coastal Cordillera, Northern Chile. J. Volcanol. Geotherm. Res. 157, 311-330.

Pan Y. and Fleet M. (2002) Compositions of the apatite-group minerals: substitution mechanisms and controlling factors. Rev. Mineral. Geochem. 48, 13-50.

Peng G., Luhr J. F. and McGee, J. J. (1997) Factors controlling sulfur concentrations in volcanic apatite. Amer. Min. 82, 1210-1224.

Piccoli P. M. and Candela P. A. (2002) Apatite in Igneous Systems. In: Kohn, M.J., Rakovan., Hughes, J.M. (eds.), Phosphates: geochemical, geobiological, and materials importance. : Rev. Mineral. Geochem. 48, 255-292.

Reutter K-J. and Scheuber E. (1988) Relation between tectonics and magmatism in the Andes of northern Chile and adjacent areas between 21” and 25” S.V. Congr. Geol. Chileno, Actas, 1: A3455A363.

Rønsbo J. G. (1989) Coupled substitutions involving REEs and Na and Si in apatites in alkaline rocks from the Ilimaussaq intrusion, South Greenland, and the petrological implications. Amer. Min. 74, 896-901.

Rouse R. C. and Dunn P. J. (1982) A contribution to the crystal chemistry of ellestadite and the silicate sulfate apatites. Amer. Min. 67, 90-96.

Scheuber E. and Andriessen P. A. M. (1990) The kinematic and geodynamic significance Atacama fault zone, northern Chile. Jour. Struct. Geol. 12, 243-257.

Scheuber E. and Reutter K. J. (1992) Magmatic arc tectonics in the Central Andes between 21 and 25 S. Tectonophysics 205, 127-140.

Scheuber E., Bogdanic T., Jensen A. and Reutter K. J. (1994) Tectonic development of the north Chilean Andes in relation to plate convergence and magmatism since the Jurassic. In: Tectonics of the southern central Andes (pp. 121-139). Springer Berlin Heidelberg.

Sha L. K. and Chappell B. W. (1999) Apatite chemical composition, determined by electron microprobe and laser-ablation inductively coupled plasma mass spectrometry, as a probe into granite petrogenesis. Geochim. Cosmochim. Acta 63, 3861-3881

Shannon R. D. (1976) Revised effective ionic radii and systematic studies of interatomic distances in halides and chalcogenides. Acta Crystallogr. A32, 751-767.

Treloar P. J. and Colley H. (1993) Magnetite-apatite ores in the Atacama fault zone, El Salvador region, Northern Chile. In : Géodynamique andine : résumés étendus = Andean geodynamics : extended abstracts = Geodinamica andina : resumenes expandidos. Paris : ORSTOM, 487-490. (Colloques et Séminaires). Géodynamique Andine : Symposium International, 2., Oxford (GBR), 1993/09/21-23. ISBN 2-7099-1154-X.

Treloar P. J. and Colley H. (1996) Variations in F and Cl concentrations in apatites from magnetite-apatite ores in northern Chile, and their ore-genetic implications. Mineral. Mag. 60, 285-301.

Woodcock N. H. (1986) The role of strike-slip fault systems at plate boundaries. Royal Soc. (L Thiele, R., Pincheira, M., 1987. Tectónica transpresiva v movimiento de desgarre en el segmento sur de la Zona de Falla Atacama, Chile. Andean Geol. 31, 77-94.

Figure A1. Photographs of representative macroscopic apatite textures from the Carmen (a and b), Fresia (c), and Mariela (d) deposits. (a) Magnetite-apatite-actinolite assemblage. Apatite commonly occurs as elongated large crystals immersed in a magnetite matrix with actinolite. Note the pink color of apatite and magnetite veinlets crosscutting apatite and actinolite crystals; (b) Massive magnetite-apatite body with flow-type textures; (c) Apatite crystals oriented perpendicular to the sides of magnetite veinlets; (d) Yellow-white apatite-matrix breccia pipe with host rock fragments with propylitic alteration. Note the hammer as scale. Abbreviations: Ap= apatite, Mgt= magnetite, Act= actinolite.

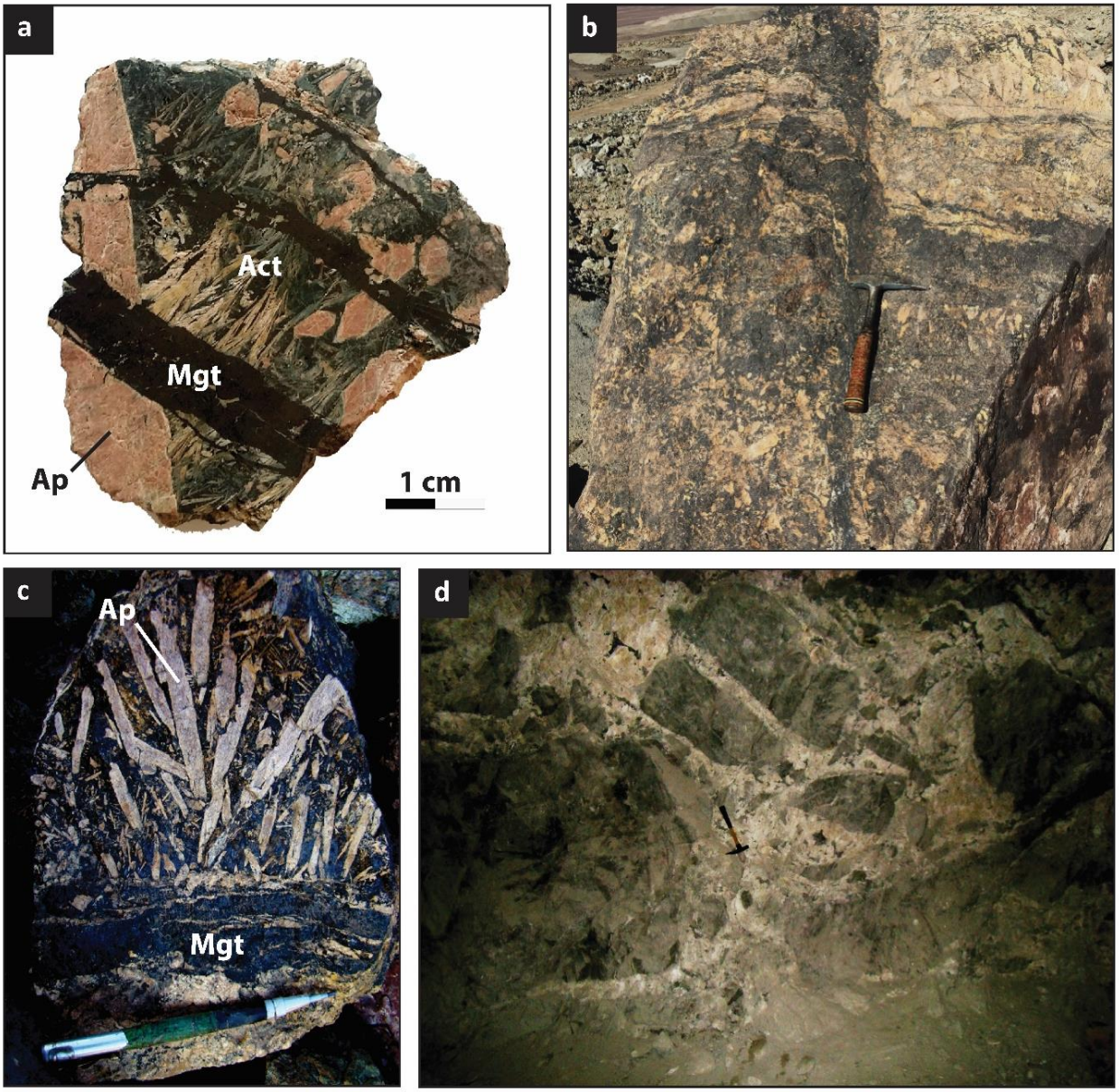

Figure A2. Binary plot of CaO versus P_2O_5 concentration (in wt.%) for each apatite type or domain analyzed in apatites from the Carmen, Fresia and Mariela deposits.

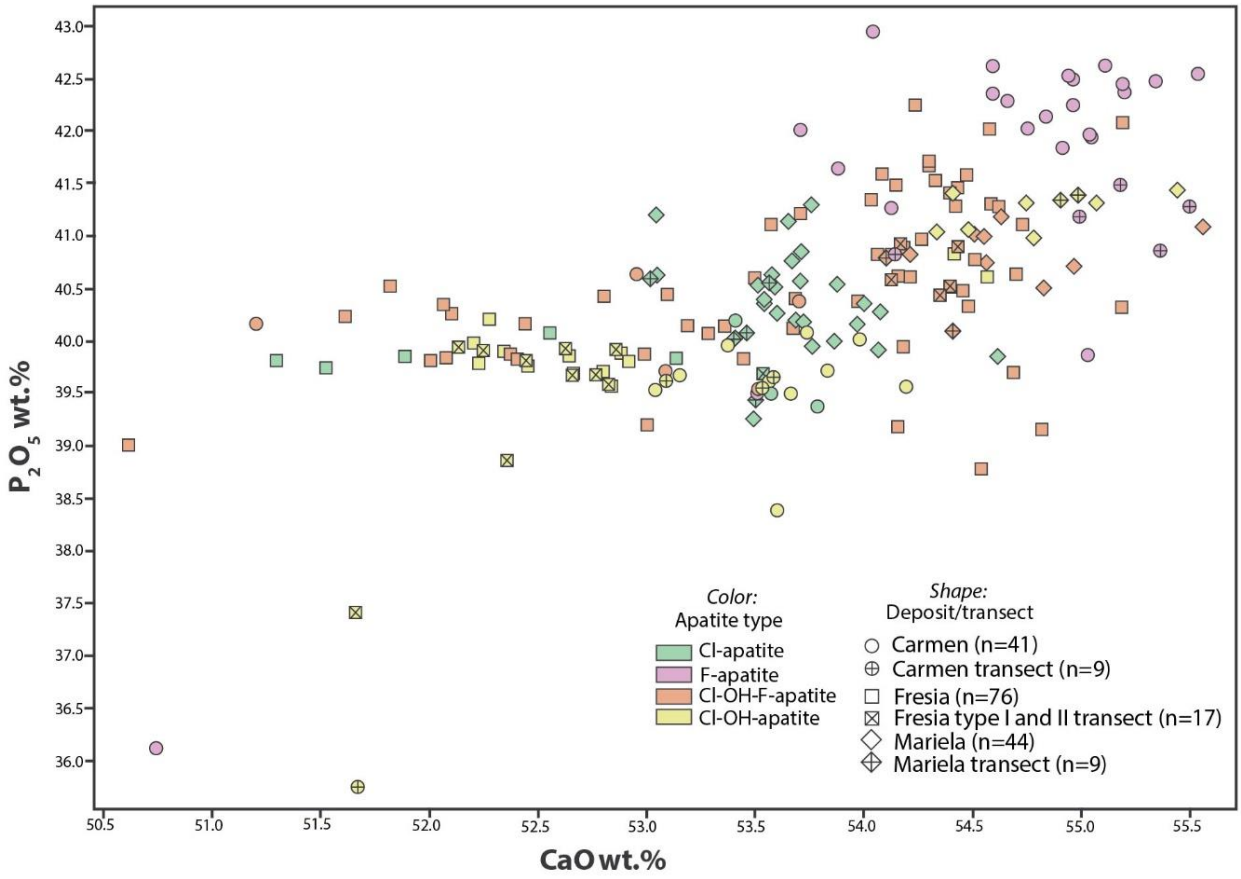

Figure A3. Binary plot of S versus Na (in apfu) for each apatite type identified in Carmen, Fresia and Mariela.

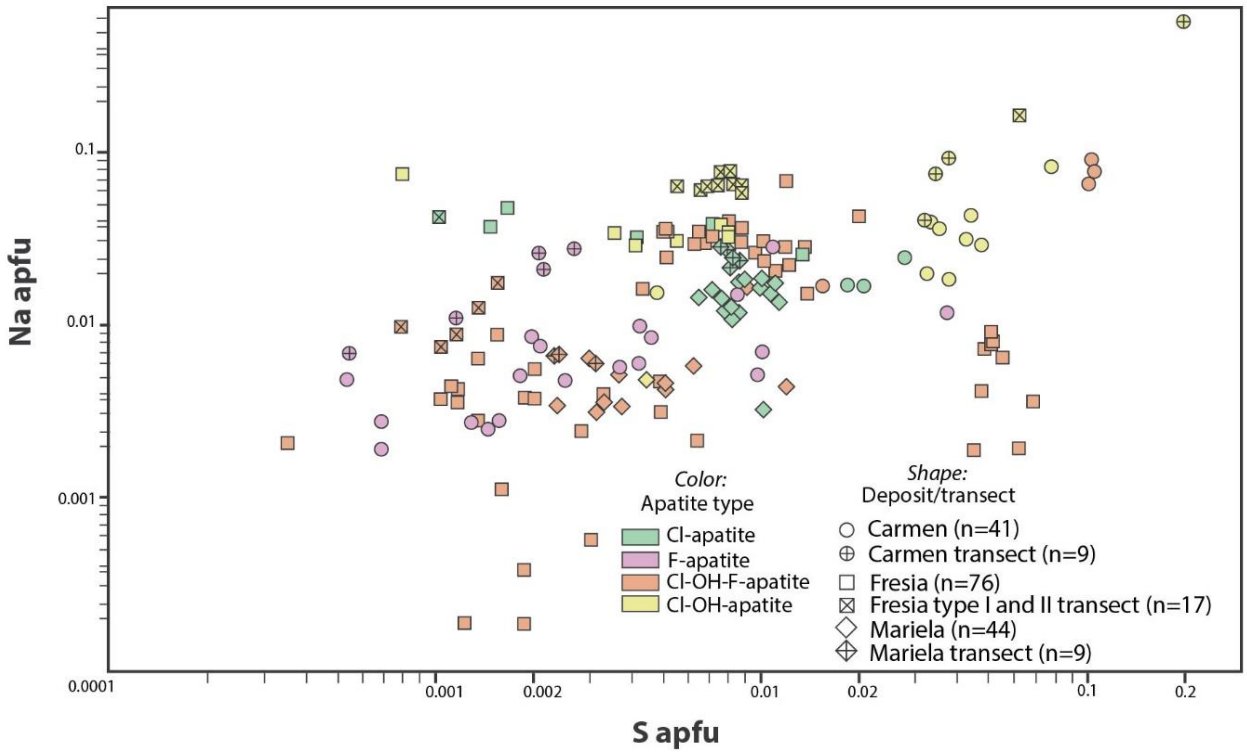

Figure A4. $^{87}Sr/^{86}Sr$ vs ε_{Nd} plot. Sr and Nd isotope ratios of apatite from Carmen, Fresia and Mariela were measured by TIMS and MC-ICPMS, respectively. The white hexagon corresponds to the apatite isotopic composition of the Durango IOA deposit (Mexico). The isotope composition of plutonic rocks of Coastal Cordillera northern Chile are shown. The isotopic composition of the bulk Earth (dashed gray line) lies at the ε_{Nd}=0 and $^{87}Sr/^{86}Sr$=0.705. See text for discussion.

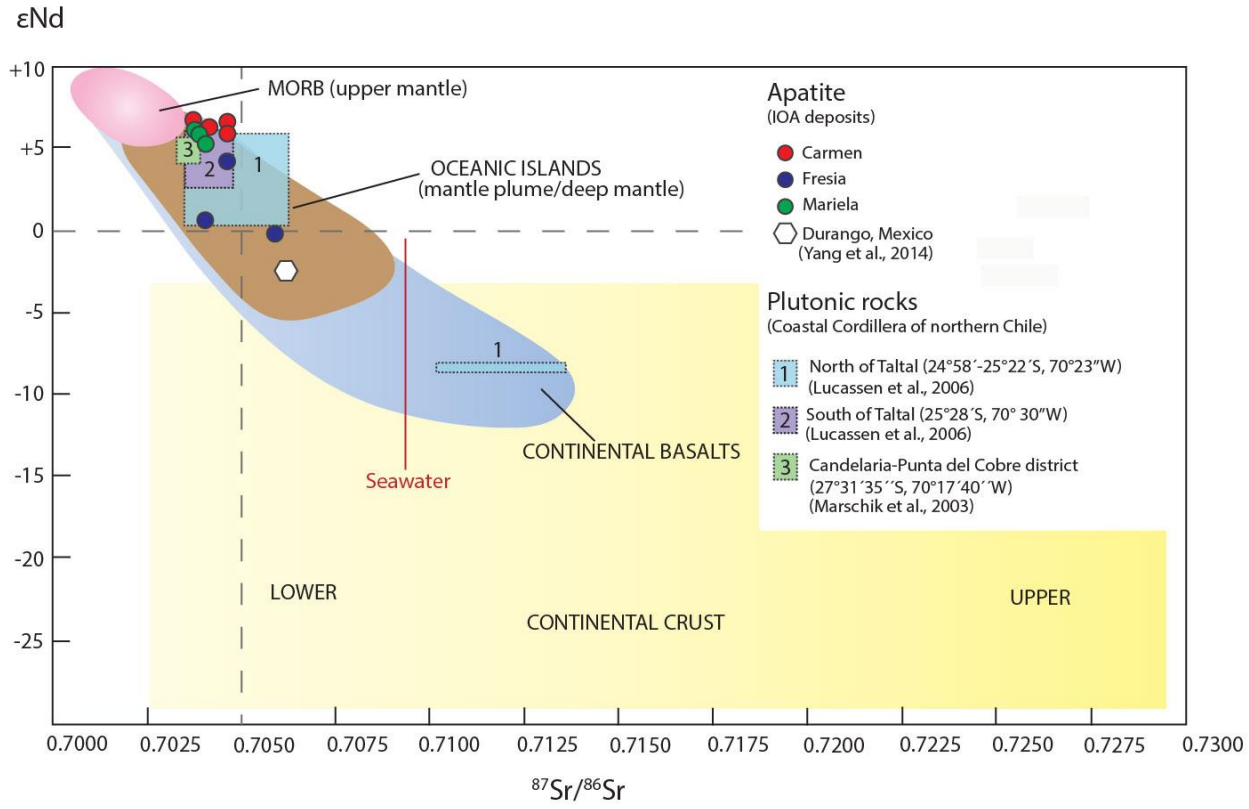

ANEXO B

MATERIAL SUPLEMENTARIO DEL CAPÍTULO 3

A review of magnetite geochemistry of Chilean Iron Oxide-Apatite (IOA) deposits and its implications for ore forming processes

Este archivo incluye:

B.1. Structure and chemistry of magnetite
B.2. Macroscopic magnetite textures from Carmen, Fresia and Mariela IOA deposits

Figures B1 to B10

Otros materias suplementarios incluyen las siguientes tablas en formato Excel:

Table B0: EPMA analytical conditions for magnetite and Fe-Ti oxides (ilmenite, rutile and titanite) analyses.

Table B1: LA-ICP-MS analyses for the GSD-1G reference material.

Table B2: Summary of EMPA analyses (all analyzed elements) for magnetite types from Carmen, Fresia, Mariela and El Romeral deposit (this study).

Table B3: Complete spot EMPA dataset from Carmen, Fresia, Mariela and El Romeral IOA deposits (this study).

Table B4: Fe-Ti oxides EMPA data from Mariela symplectite (this study.

Table B5: Summary of LA-ICP-MS analyses (33 elements) for magnetite types from Los Colorados, Cerro Negro Norte and El Laco deposits.

Table B6: Summary of LA-ICP-MS analyses (34 elements) for magnetite types from Carmen, Fresia, Mariela and El Romeral deposits (this study).

Table B7: Complete LA-ICP-MS data set from El Romeral, Carmen, Fresia and Mariela deposits (this study).

B.1. STRUCTURE AND CHEMISTRY OF MAGNETITE

Magnetite [$^{IV}Fe^{3+VI}(Fe^{2+}Fe^{3+)}O_4$] belongs to the space group F*d3m* and has an inverse spinel structure represented by the general formula AB_2O_4 (Bragg, 1915; Fleet, 1981), where A represent divalent cations such as Mg^{2+}, Fe^{2+}, Ni^{2+}, Mn^{2+}, Co^{2+}, Zn^{2+}, and B trivalent cation including Al^{3+}, Fe^{3+}, Cr^{3+}, V^{3+}, Mn^{3+} and Ga^{3+} which can be accomodated by isovalent substitutions in the magnetite structure (Lindsley, 1976; Wechsler et al., 1984). Cations with a different charge including both Ti^{4+} and Si^{4+} can enter to the magnetite structure via coupled substitutions with a divalent cation (Wechsler et al., 1984). Other cations have more than one possible oxidation state depending on fugacity conditions, e.g., V can be incorporated mainly as V^{3+} with minor amounts of V^{4+} in titanomagnetite (Toplis and Carrol, 1995; Balan et al., 2006; Bordage et al., 2011). In the magnetite structure the tetrahedral sites are occupied by ferric ions (Fe^{3+}), whereas octahedral sites by subequal numbers of ferric and ferrous (Fe^{2+}) ions (Lindsley, 1976; Waychunas, 1991; Wechsler et al., 1984).

In the system FeO-Fe_2O_3-TiO_2 many phase transitions occur between magnetite and other mineral of the spinel group. Notably ulvöspinel (Fe_2TiO_4) and magnetite present a continuous solid solution (SS) called titanomagnetite SS (above 600 °C) and their oxidation products (titanomaghemite); while hematite (Fe_2O_3) and ilmenite ($FeTiO_3$) also form solid solution between them (Buddington and Lindsley, 1964).

B.2. MACROSCOPIC MAGNETITE TEXTURES FROM THE CARMEN, FRESIA AND MARIELA IOA DEPOSITS

Carmen and Fresia

The Carmen and Fresia deposits have similar macroscopic ore textures. The magnetite ore bodies comprise aggregates of massive magnetite (>60% modal) with coarse apatite grains (up to 20-40% modal) and minor actinolite (**Figure B1**: Ca-8, Ca-2; **Figure B2**: Fre-10). They also occur as a magnetite matrix with coarse apatite and actinolite immersed in it (**Figure B1**: Ca-7, Ca-9; **Figure B2**: F-5). Late magnetite veins, which vary in width from a few mm thick up to ~20 m wide, crosscut the early massive magnetite-apatite-actinolite assemblage (**Figure B1**: Ca-7, Ca-9) or occur at the margins of the deposits crosscutting the altered (epidote-chlorite-calcite-actinolite-hematite) host rock (**Figure B2**: Fre-4). Locally, banded growth of magnetite and fine-grained apatite occur in Fresia (**Figure B2**: F-2). In Carmen the massive magnetite is locally replaced by hematite in the form of patches, while in Fresia where the hydrothermal alteration is more intense the replacement is more pervasive. Some parts of the ore bodies are brecciated and/or display banded structures with flow-type textures.

In Carmen, apatite commonly occurs as prismatic and acicular pink to white (core to rim) large crystals up to ~50 cm long, with a non-uniform distribution or perpendicular to magnetite vein walls (**Figure B1**). In Fresia, aggregates of yellow to white fine-grained apatite (**Figure B2**: Fre-

10, F-2) dominate over pink prismatic crystals (**Figure B2**: F-5). According to Palma et al. (2019) apatite from Carmen and Fresia is chemically zoned with respect F and Cl. Carmen apatite is mostly primary F-apatite (pink) replaced by hydrothermal Cl-OH-apatite (white), which is restricted to rims and fractures, whereas primary F-apatite from Fresia was partially to completely replaced by both fine-grained hydrothermal Cl-OH-apatite and minor Cl-apatite (Palma et al., 2019).

Mariela

The Mariela deposit corresponds to a breccia body mainly composed of an apatite ± actinolite ± magnetite matrix and intrusive fragments mainly altered to chlorite and epidote. The apatite-actinolite assemblage is dominant in the central and eastern parts of the deposit, whereas apatite-magnetite dominates in the western part. The yellow-white apatite from Mariela, dominantly Cl-apatite and Cl-OH-apatite (Palma et al., 2019), is mostly massive forming large apatite bodies up to ~3 m wide. Fibrous to acicular crystals of actinolite and aggregates of magnetite up to ~15 cm (**Figure B3**: Ma-10, Ma-11), and specular hematite (**Figure B3**: Ma-21) occur intergrown within the apatite matrix. Minor copper oxides including chrysocolla and atacamite (**Figure B3**: Ma-21) are possible related to a late hydrothermal sulfide event (pyrite and chalcopyrite) affected by oxidation/supergene processes. In addition to the apatite ± actinolite ± magnetite matrix, magnetite (veinlets or bands?) occurs crosscutting the altered host rock (**Figure B3**: Ma-1).

References

Balan, E., De Villiers, J.P.R., Eeckhout, S.G., Glatzel, P., Toplis, M.J., Fritsch, E., 2006. The oxidation state of vanadium in titanomagnetite from layered basic intrusions. Am. Mineral. 91, 953-956.

Bordage, A., Balan, E., Villiers, J.R., Cromarty, R., Juhin, A., Carvallo, C., 2011. V oxidation state in Fe-Ti oxides by high-energy resolution fluorescence-detected X-ray absorption spectroscopy. Phys. Chem. Miner. 38, 449-458.

Bragg, W.H., 1915. The structure of the spinel group of crystals. Philos. Mag. 30, 305-315.

Buddington, A.F., Lindsley, D.H., 1964. Iron-titanium oxide minerals and synthetic equivalents. J. Petrol. 5, 310-357.

Fleet, M., 1981. The structure of magnetite. Acta Crystallogr. B 37, 917-920.

Lindsley, D.H., 1976. The crystal chemistry and structure of oxide minerals as exemplified by the Fe-Ti oxides. In: Rumble III, D. (Ed.), Oxide Minerals. Rev. Mineral. Mineral. Soc. Am. , pp. L1-L60.

Palma, G., Barra, F., Reich, M., Valencia, V., Simon, A.C., Vervoort, J., Leisen, M., Romero, R., 2019. Halogens, trace element concentrations, and Sr-Nd isotopes in apatite from iron oxide-apatite (IOA) deposits in the Chilean iron belt: Evidence for magmatic and hydrothermal stages of mineralization. Geochim. Cosmochim. Acta 246, 515-540.

Toplis, M.J., Carrol, M.R., 1995. An experimental study of the influence of oxygen fugacity on Fe-Ti oxide stability, phase relations, and mineral –melt equilibria in ferro-basaltic systems. J. Petrol. 36, 1137-1170.

Waychunas, G.A. 1991. Crystal chemistry of oxides and oxyhydroxides. In: Lindsley, D.H. (Ed.), Oxide Minerals: Petrologic and Magnetic Significance. Mineralogical Society of America, pp. 11-61.

Wechsler, B.A., Lindsley, D.H., Prewitt, C.T., 1984. Crystal structure and cation distribution in titanomagnetites ($Fe_{3-x}Ti_xO_4$). Am. Mineral. 69, 754-770.

FIGURE B1: Photographs of representative magnetite-bearing rocks from the Carmen deposit selected for this study. Samples Ca-2 and Ca-8 are composed of massive magnetite with coarse apatite and minor actinolite crystals. Samples Ca-7 and Ca-9 consist of a magnetite matrix with coarse apatite and actinolite crystals of variable size. Late magnetite veinlets crosscut the primary magnetite-actinolite-apatite assemblage. Abbreviations: Act=actinolite, Ap=apatite and Mgt=magnetite.

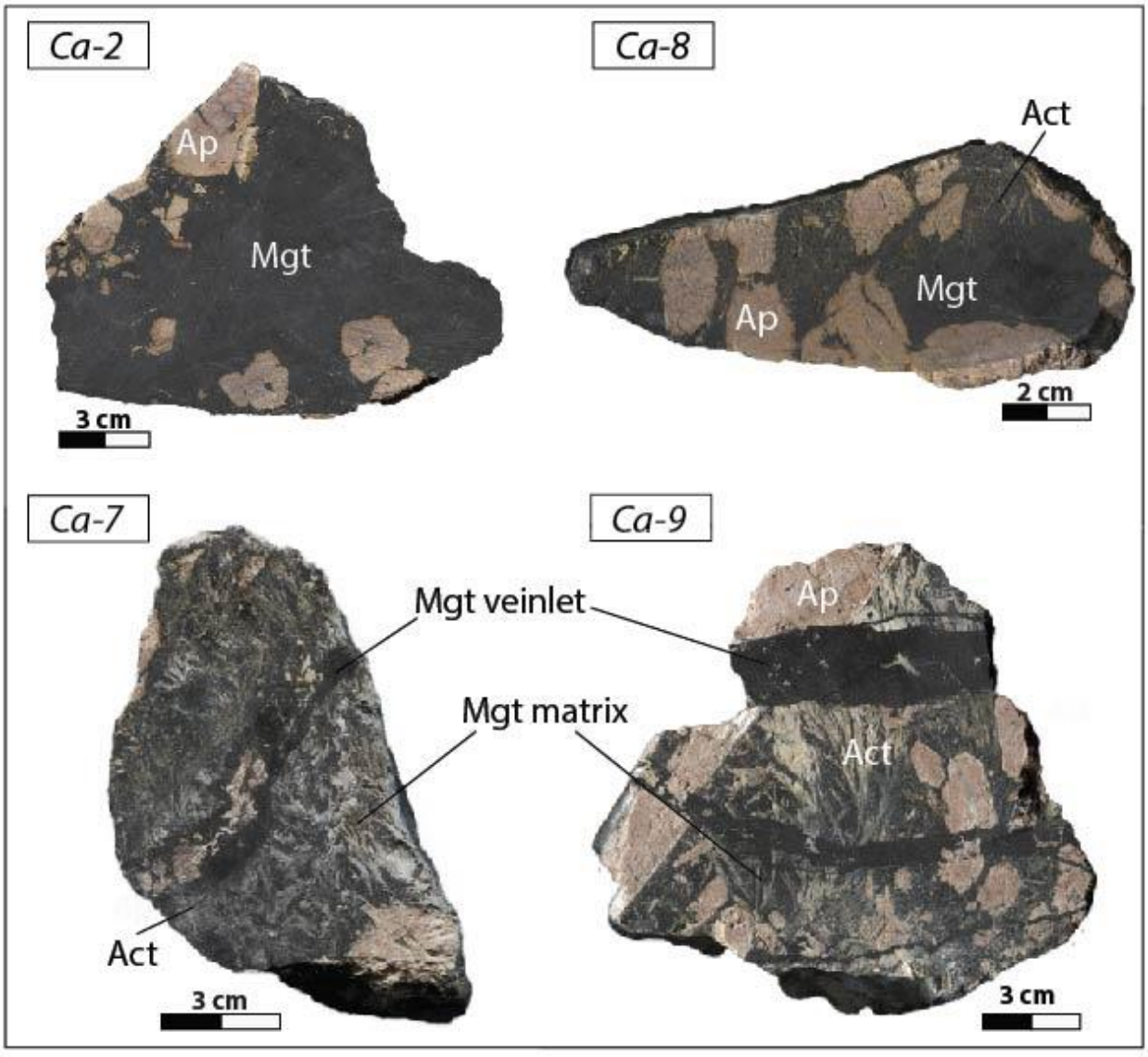

FIGURE B2: Photographs of representative magnetite-bearing rocks from the Fresia deposit selected for this study. Sample Fre-10 comprises massive magnetite with an aggregate of yellow Cl-rich apatite. Sample F-5 is composed of a magnetite matrix with pink apatite and actinolite crystals of variable size. Sample F-2 consists of banded magnetite and yellow fine-grained Cl-rich apatite. Note the central green band of an unknown mineral that could correspond to some type of pyroxene. Sample Fre-4 comprises magnetite veinlets that crosscut the altered host rock at the margin of the deposit. Abbreviations: Act=actinolite, Ap=apatite and Mgt=magnetite.

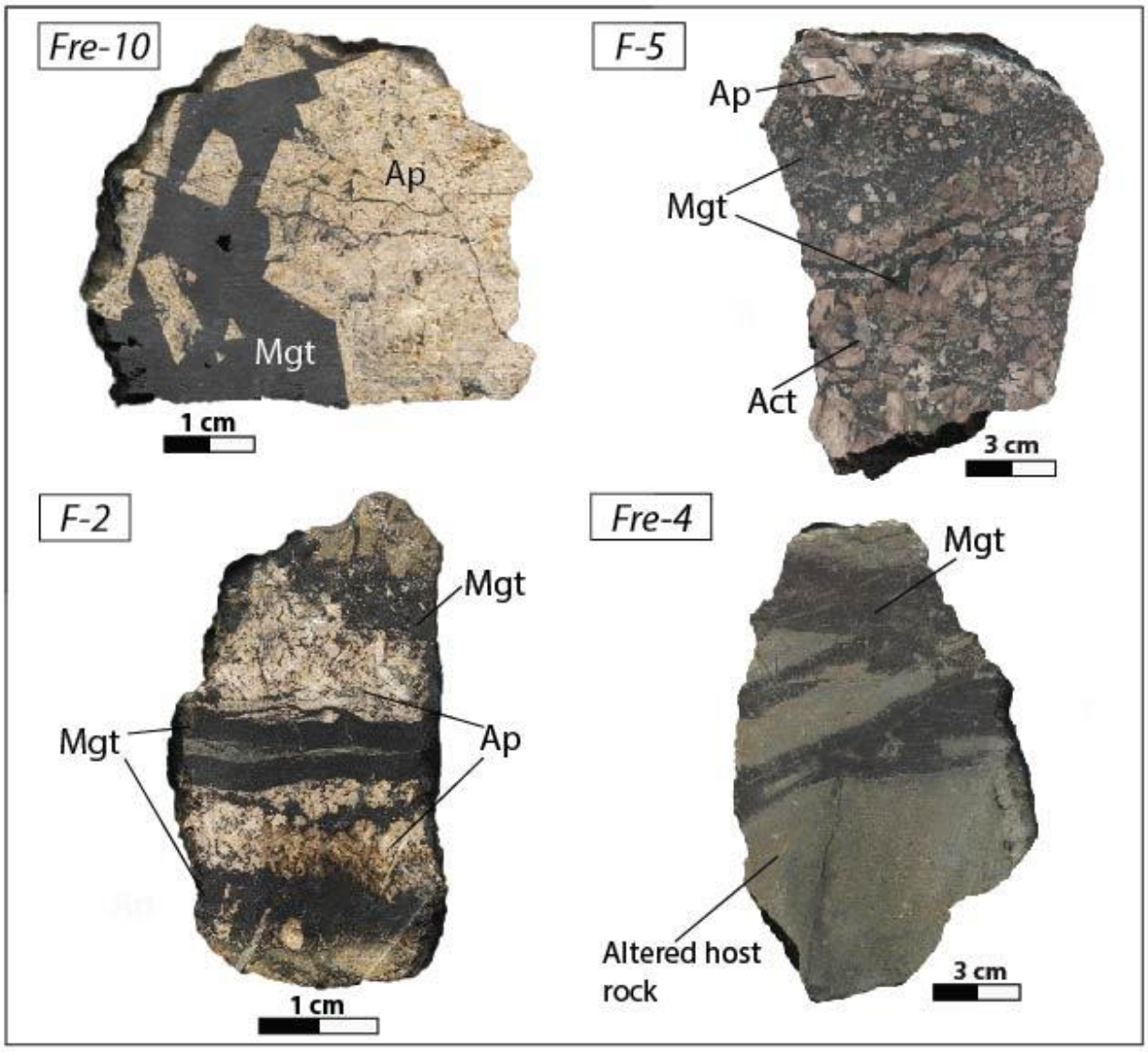

FIGURE B3: Photographs of representative magnetite-bearing rocks from the Mariela deposit selected for this study. Samples Ma-10 and Ma-11 consist of magnetite aggregates within a Cl-rich apatite matrix. Sample Ma-1 comprises a magnetite veinlet crosscutting the altered andesite host rock. Sample Ma-21 corresponds to magnetite replaced by specular hematite with minor copper mineralization. Abbreviations: Act=actinolite, Ap=apatite, Hmt=hematite, Mgt=magnetite and Qz=quartz.

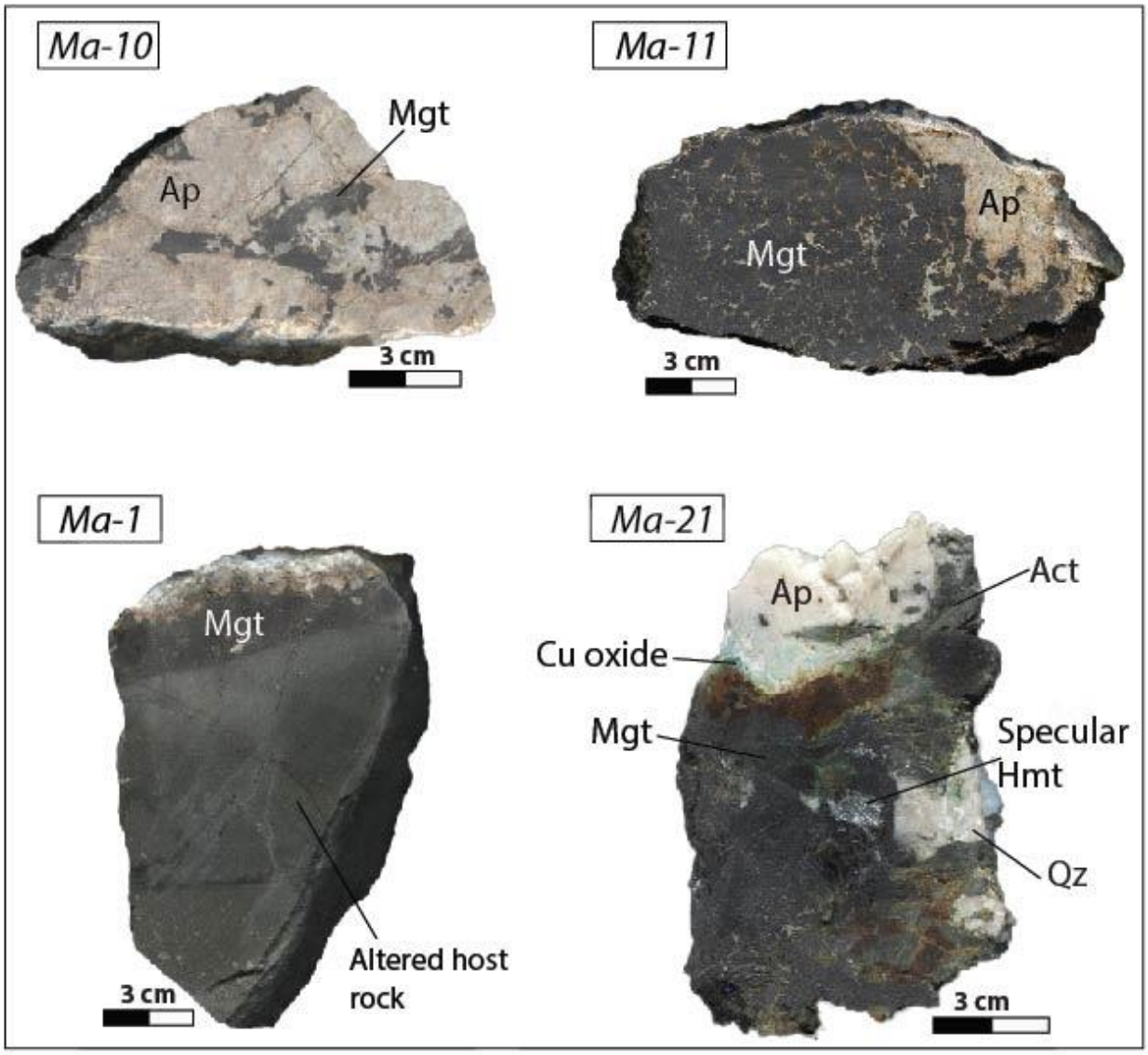

FIGURE B4: Back-scattered electron images of different magnetite types from the Los Colorados IOA deposit. (A) Different magnetite grains showing areas described as "cores" and rims". The darker gray areas (cores) ubiquitously contain mineral inclusions and higher concentrations of trace elements (Ti, Mn, Al) relative to lighter gray areas. The rims are generally inclusion-free. (B, C, D) Zoned, late-stage, hydrothermal Magnetite-X (B), -Y (C) and –Z (D). Darker gray areas correspond to trace-element rich zones and lighter gray areas to trace element-poor zones. Modified from Deditius et al. (2018) and Simon et al. (2018).

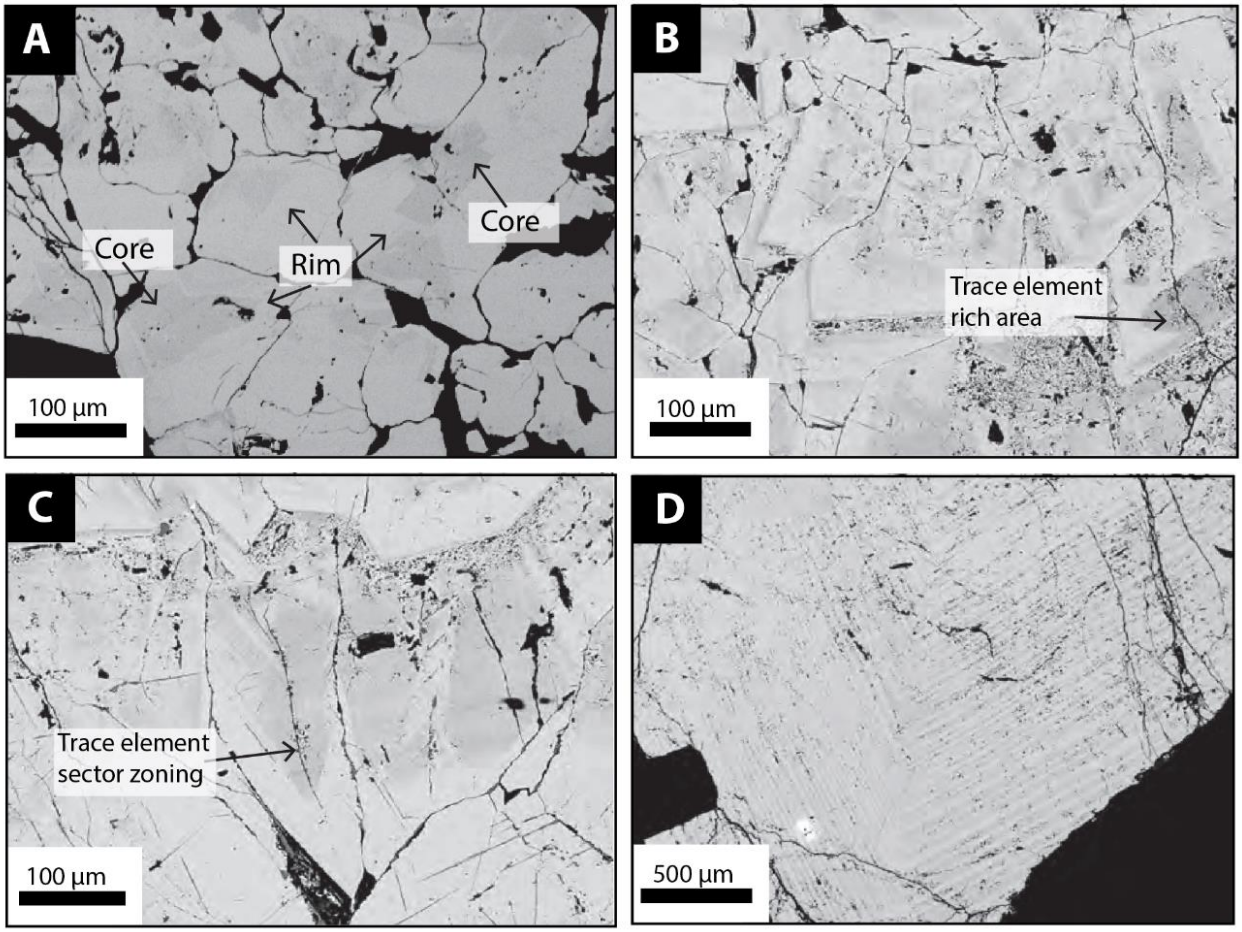

FIGURE B5: Back-scattered electron images of different magnetite types from the Cerro Negro Norte IOA deposit. (A) Magnetite grain with an inclusions-rich core (Type-I) and inclusion-free rims (Type-II). (B) Euhedral Type-III magnetite grain with a cryptic zonation towards the edge of the crystal. (C) Oscillatory and sinusoidal inclusion arrangement in Type-IV magnetite. Modified from Salazar et al. (2019).

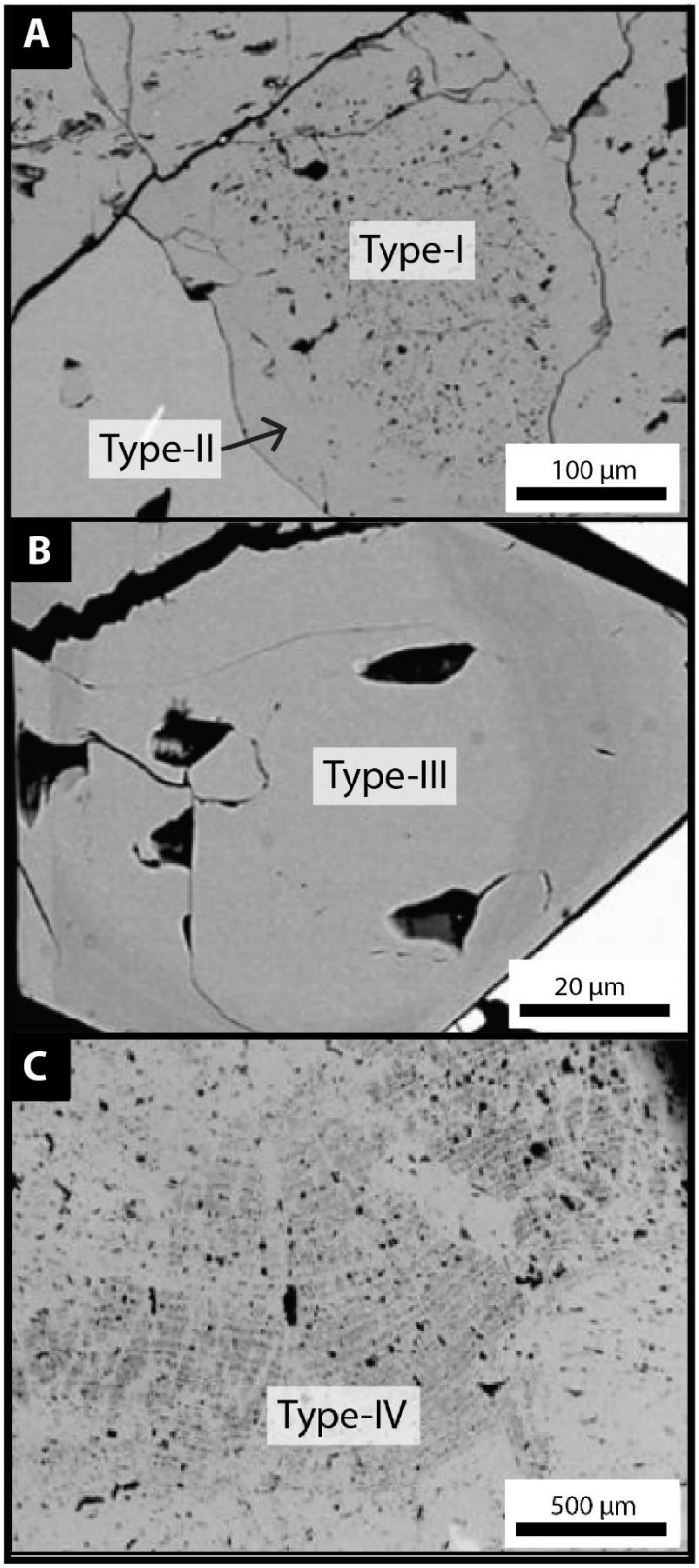

FIGURE B6: Back-scattered electron images of different magnetite types from Laco Norte. The average Ti concentration of magnetite grains from the surface to the base of the drill core is shown on the left. (a) Euhedral, altered and porous Magnetite-S grain showing pervasive replacement by hematite and goethite along grain boundaries, fractures and pores. (b) Aggregate of pristine Magnetite-Z grains, weakly oxidized to hematite. (c) Microcrystalline core of pristine Magnetite-X showing evidence of dissolution-reprecipitation processes. Magnetite-Y precipitates over Magnetite-X and exhibits alternating bands of Ti-bearing inclusions responsible for the increase in the magnetite Ti concentration at this level. (d) Ti-poor Magnetite-γ from pyrite-rich massive magnetite zone associated with gypsum veinlets. Magnetite-γ forms over inclusion-rich Magnetite-β and displays sector zoning with inclusion-rich areas. (e) Euhedral core of inclusion-rich Magnetite-β surrounded by a pristine inclusion-free-rim of Magnetite-β1. Both magnetite types have a high Ti content. Irregular grains of Ti-poor Magnetite-β2 associated with late gypsum veinlets developed over Magnetite-β1 rims. (f) Aggregate of Ti-rich Magnetite-α grains showing well-developed ilmenite exsolution lamellae, which exhibit both trellis and sandwich textures. Modified from Ovalle et al. (2018)

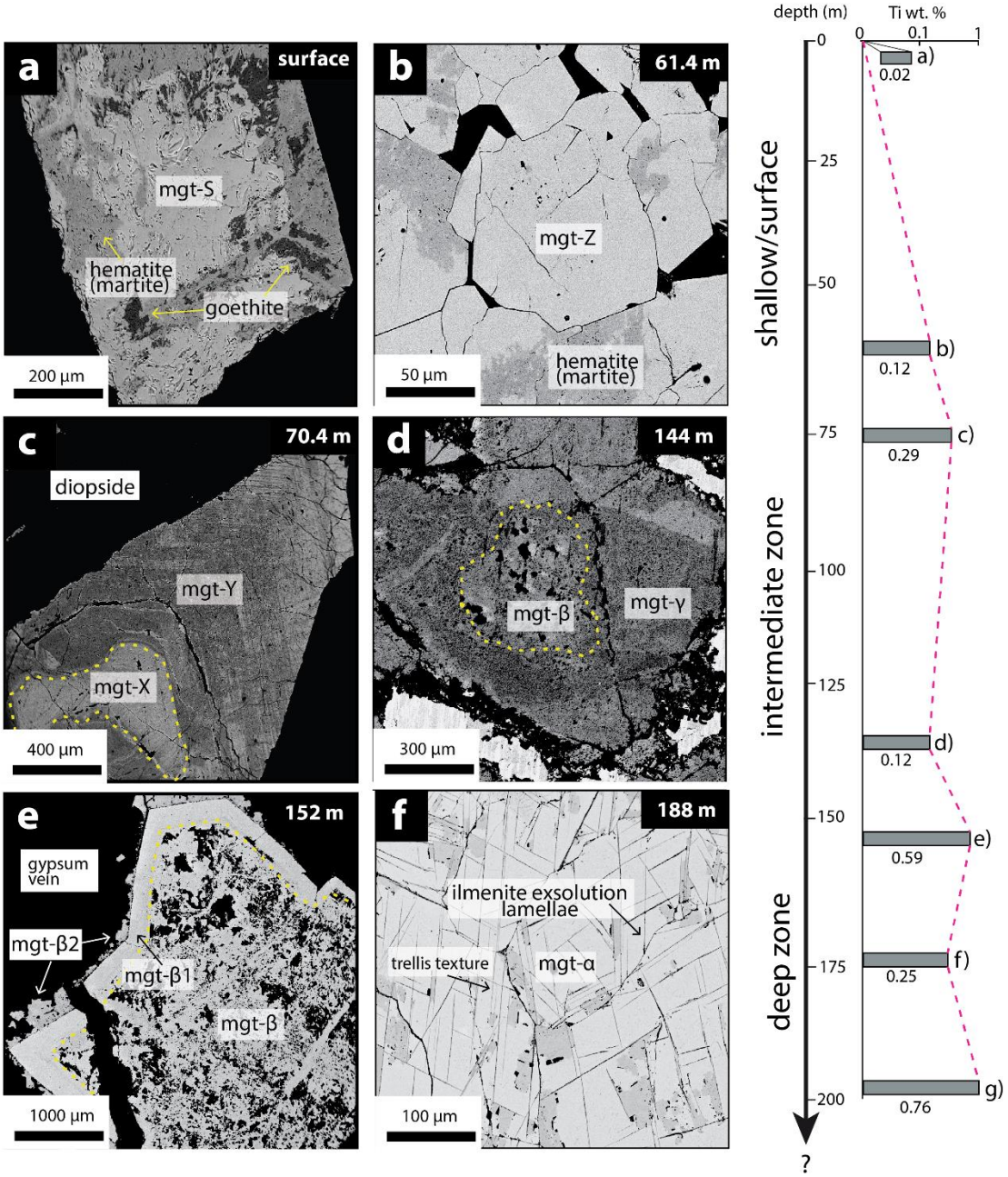

FIGURE B7: WDS elemental maps of selected trace elements in magnetite grains from Los Colorados (A, B) and Cerro Negro Norte (C). (A) Magnetite exhibiting clear Ti zonation with a Ti-rich inclusion-rich core (Type-1), a Ti-poor transition zone (Type-2), and a Ti-depleted inclusion-free rim (Type-3). (B) Magnetite-Z grain characterized by oscillatory zoning. The WDS maps reveal Ti-Mn particles in trace element-poor bands (zones depleted in Al, Mg, Si and Ca) but most elements are homogeneously distributed in the trace element rich bands. (C) Type-I magnetite grain (inclusion-rich core) showing abundant Si-Al inclusions surrounded by an inclusion-poor rim (Type-II) that contains Ti-, Al- and Si-enrichment zones. Modified from Knipping et al. (2015b), Deditius et al. (2018) and Salazar et al. (2019).

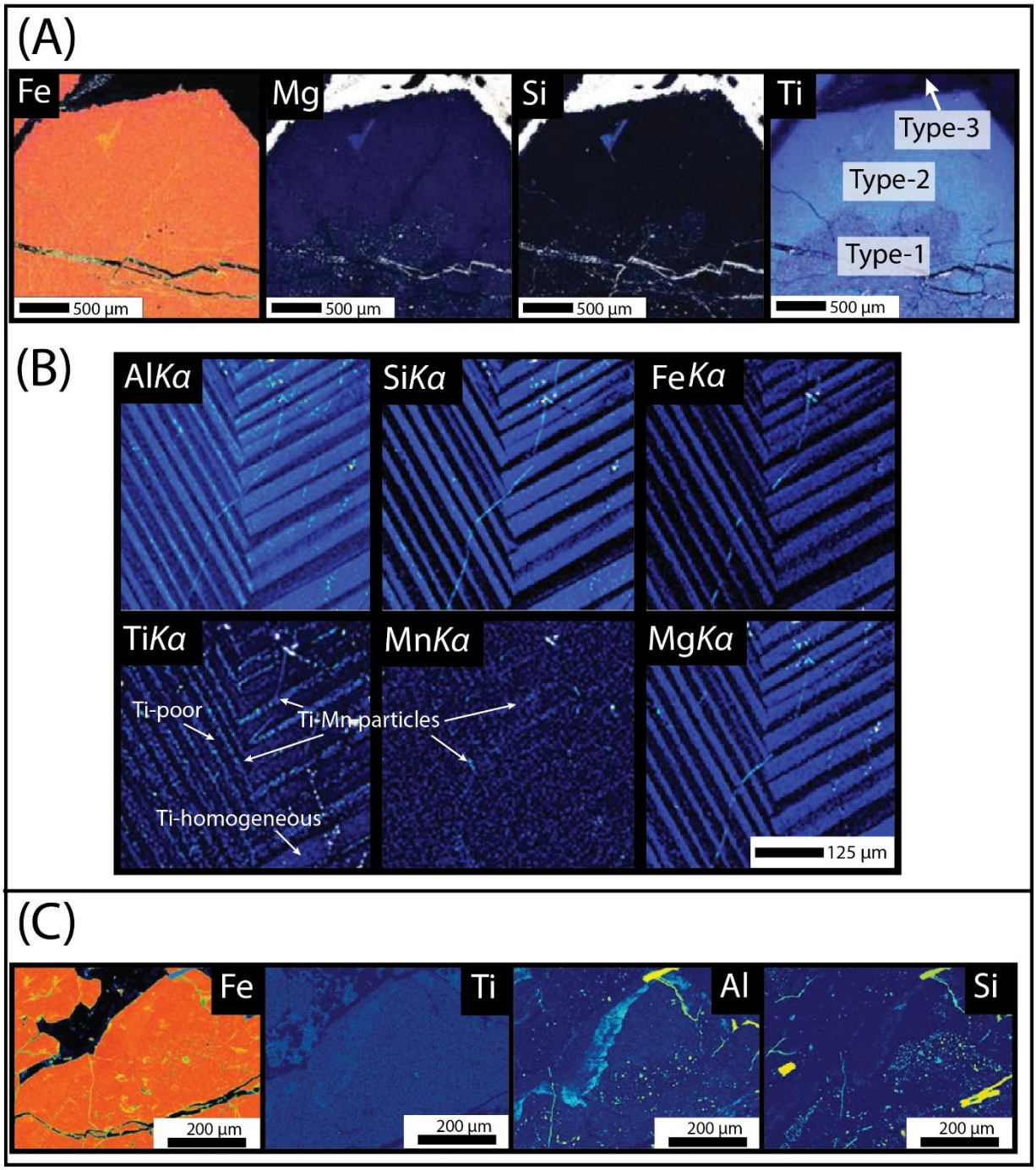

FIGURE B8: Composite ilmenite-ulvöspinel lamellae exsolution in Type-β magnetite from the Mariela IOA deposit. Nano-size mineral inclusions are observed in the vicinity of exsolution lamellae.

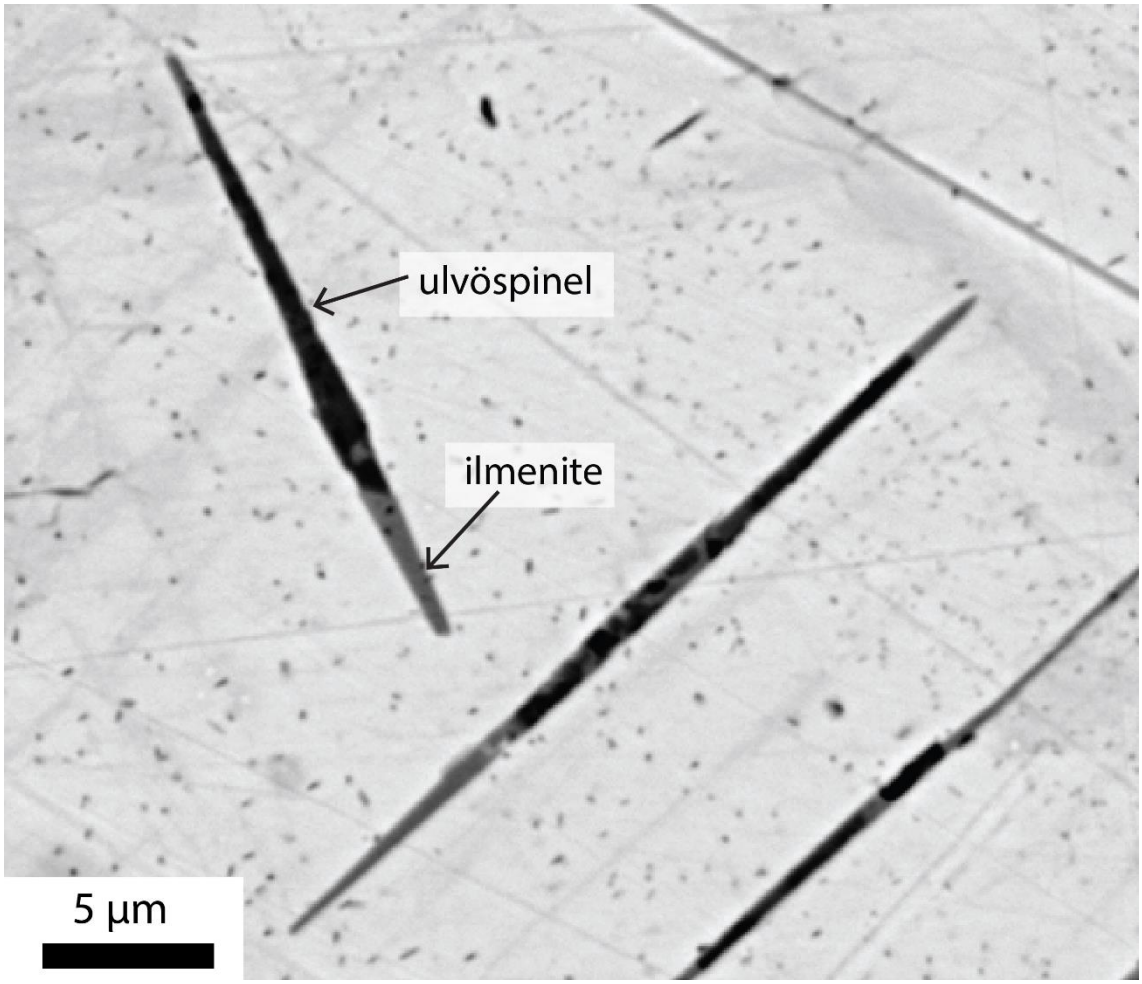

FIGURE B9: Ti vs. V concentration plot for different magnetite types from (A) Chilean Iron Belt and (B) El Laco. The igneous and hydrothermal field are defined based on the dataset of Nadoll et al. (2014). Note the overlapping area between the igneous and hydrothermal field. Numbers in parentheses refer to the source of the information. (1) Knipping et al. (2015a,b); (2) Salazar et al. (2019); (3) Huang and Beaudoin (2019); (4) This study.

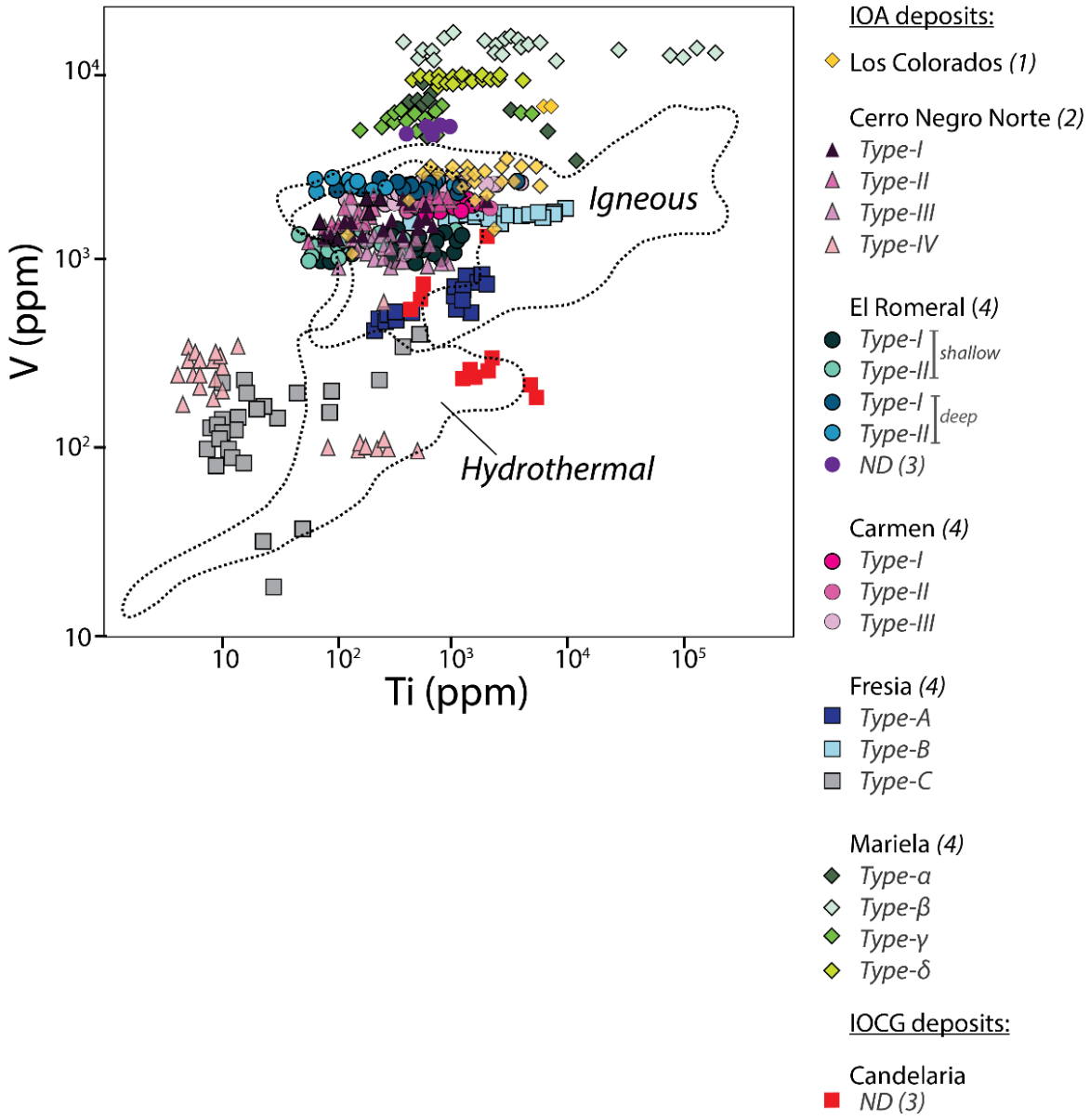

FIGURE B10: Ga vs. V concentration plot for different magnetite types from the Chilean Iron Belt. Numbers in parentheses refer to the data source: (1) Knipping et al. (2015a,b); (2) Salazar et al. (2019); (3) Huang and Beaudoin (2019); (4) This study.